Iron-based photoactive complexes : control of geometry and electronic properties

Ulises Carrillo Arcos

C2MP (Chimie-Mécanique-Matériaux-Physique)
L2CM (Laboratoire Lorrain de Chimie Moléculaire)

Thèse

Présentée et soutenue publiquement pour l'obtention du titre de

DOCTEUR DE l'UNIVERSITE DE LORRAINE

Mention : Chimie

par Ulises Alonso CARRILLO ARCOS

Iron-based photoactive complexes : control of geometry and electronic properties

03 mars 2023

Membres du jury :

Directeurs de thèse :	**M. Philippe GROS**	**Directeur de recherche CNRS** **Université de Lorraine, Nancy**
	Mme. Cristina CEBRIAN AVILA	**Maître des conférences** **Université de Lorraine, Metz**
Président et rapporteur :	**Mme. Carole DUBOC**	**Directrice de recherche CNRS** **Univ Grenoble-Alpes, Grenoble**
Rapporteur :	**M. Samuel DAGORNE**	**Directeur de recherche CNRS** **Institut de Chimie, Université de Strasbourg, Strasbourg**
Examinateur :	**M. Matteo MAURO**	**Maître des conférences** **Université de Strasbourg, Strasbourg**

UMR CNRS 7053, L2CM, Laboratoire Lorrain de Chimie Moléculaire, Faculté des Sciences et Technologies, Université de Lorraine BP 70239, F-54506 Vandœuvre-lès-Nancy

Acknowledgements

This work could not been able without the support and collaboration of several people, that in one way or another I'll take with me.

I would like to thanks to my directors Cristina and Philippe for always being there whenever I needed your advice and guidance.

To the members of my jury Carole, Samuel and Matteo for your nice disposition and being able to discuss and evaluate this work.

To all the technicians, people in the lab, co-workers many thanks for your support and assistance, as during my stay in Metz, to Gilbert, Stephany, Philippe, Kevin, Vero, Didier, Melanie, Herbé and in Nancy to Sabrina, Stephan, Mathilde, Anil, Nour, Lynda, Quarentin, Alexandre, Nathalie, Catherine, Sandrine, Emilian, Dylan.

To Stefan and Ronan in Strasbourg for all your pleasing and prompt support, measurements and for the exchange of ideas.

To Marine Desage-El Murr for the enjoyable exchange of ideas and contributions.

To Tony in Valencia for your pleasant collaboration and contributions.

To all the people in Paderborn starting with Mattias, Jackob, Athul, Lorena, Dirk, Tanja, Anabel, Yanik, Steffen, Marina.

Also to the great friends that I have the luck to meet Luan & Manos, Ameer, Gerardo, Bertille, René, Bruno, Alvaro, Cristian and Cristina, Mumo, Ernesto, Eduardinho, Hugo, Mehdi, Maria P, Juan D, Andrea, Lizeth, Dyn, Tang, Jaime, Ivan, Lucia, Hugo, Jairo, Pablo, Porter, Diana, Anne-Claire, Diana, Wlad, Jess, Edyely, Maria, Mau, Pinto, Aramis, Natalia, Filipe, Daniel, Camille, Fer, Pame.

To Laura for being with my being a support, a friend and much more, let's keep moving forward side by side.

To all my family, that in the distance, we are together. Thanks to my dad and mom, sister and brothers, and sister in law. To Cooper, Chulis, Muff, Canelo, Dona's, Baguiro. To my uncles and aunts, cousins and nieces. To my grand -father's and -mother's that I know, you're be proud of me.

Finally,

WE DID IT!

Thanks!

Résumé

Cette thèse de doctorat s'inscrit dans le domaine de la chimie organométallique, visant à développer des complexes photoactifs à base de fer en vue de leur utilisation dans des applications de conversion énergétique. L'un des objectifs actuels de l'humanité est la recherche d'alternatives aux combustibles fossiles comme principale source d'énergie, en raison de la production de déchets liée aux problèmes environnementaux (changement climatique, pollution de l'eau, du sol et de l'air). Les sources d'énergie renouvelables comme l'énergie éolienne, hydroélectrique et solaire, entre autres, constituent une nouvelle alternative. En particulier, l'énergie solaire est une alternative verte, durable et renouvelable. On calcule que le soleil fournit à la Terre l'énergie nécessaire pour une année entière en une heure environ (voir §I, Figure 1). Cette quantité d'énergie pourrait répondre aux besoins en électricité de l'humanité d'aujourd'hui et de demain. En fait, ce type d'énergie peut être transformé en électricité au moyen de cellules solaires, ou être utilisé comme énergie chimique dans des réactions photocatalytiques, par exemple. Une façon d'exploiter ce type d'énergie est d'utiliser des matériaux moléculaires, parmi lesquels les métaux nobles (Ru, Ir, Pt, etc.) et les terres rares (lanthanides) ont joué un rôle clé dans ce domaine en raison de leurs performances exceptionnelles et des propriétés photophysiques et électrochimiques de leurs complexes. Certaines de leurs caractéristiques englobent une forte absorption de la lumière visible, un comportement redox réversible, des états excités pertinents à longue durée de vie et une stabilité thermique.

Les métaux nobles ont été largement utilisés pour la conversion énergétique des marsouins avec différentes applications telles que la photothérapie dynamique, les diodes électroluminescentes organiques, les cellules solaires à colorant ou la catalyse par exemple. Pourtant, leur rareté, l'impact environnemental de leur extraction, de leur exploitation et de leur séparation, combinés à leur prix élevé, rendent leur application à grande échelle impossible. Pour ces raisons, on s'intéresse de plus en plus aux métaux de transition de la première rangée (fer, manganèse, chrome), car ils sont plus abondants, moins chers et leur processus d'extraction est moins agressif pour l'environnement (voir §1, Figure 3). Parmi les métaux de transition de la première rangée, le fer se distingue par le fait qu'il est le métal de transition le plus abondant sur la croûte terrestre et qu'il est environ 25 000 fois moins cher que le Ru, largement utilisé. Par conséquent, le développement de matériaux moléculaires photoactifs robustes et efficaces

basés sur des métaux abondants sur Terre constitue un véritable jalon pour remplacer les processus nuisibles à l'environnement par la durabilité. Cependant, le développement d'un photosensibilisateur basé sur un métal de transition 3d n'est pas trivial, le problème principal est que les métaux 3d font face à des champs de ligands plus faibles que les espèces 4d ou 5d ; par exemple, si nous comparons le **$[Ru(bpy)_3]^{2+}$** largement utilisé avec le 3d homologue **$[Fe(bpy)_3]^{2+}$**, le temps de vie de l'état excité est de 1μs et 150 fs respectivement (voir §I.1). De plus, les complexes 3d présentent des propriétés photophysiques qui ne sont pas appropriées à leur application en tant que composés photoactifs, ce qui constitue un défi auquel s'attaque la communauté scientifique, surtout au cours de la dernière décennie. Afin d'augmenter la force du champ du ligand, la stratégie consistant à utiliser des ligands fortement donneurs de C comme les carbènes N-hétérocycliques (l'un des plus étudiés, voir §I.2.3) a été appliquée. Comme l'ont rapporté Wärnmark et ses collègues dans leurs travaux précurseurs, où ils ont décrit le premier complexe de fer avec un MLCT (transfert de charge métal-ligand, voir §I.1) de 9 ps (voir §I.2.3, Figure 14) (presque deux ordres de grandeur plus long que **$[Fe(bpy)_3]^{2+}$**). Ce résultat exceptionnel a clairement mis en évidence l'importance primordiale d'une sphère de coordination conçue de manière rationnelle et a ouvert la porte des applications de conversion énergétique aux complexes à base de fer. Depuis lors, des résultats impressionnants ont été obtenus, y compris les premiers exemples de complexes de fer luminescents (voir §I.2.4, Figure 20). Cependant, si des concepts originaux ont été explorés, des développements supplémentaires sont encore nécessaires pour que les complexes à base de fer soient réellement compétitifs par rapport aux autres composés photoactifs.

Dans ce travail de doctorat, nous avons travaillé à deux niveaux différents. D'un point de vue fondamental, nous avons étudié le contrôle de la géométrie moléculaire dans les complexes azine-NHC Fe(II) bidentés par modification du ligand, ainsi que l'exploration d'unités de coordination (formellement) anioniques. En outre, nous nous sommes lancés dans une chimie plus appliquée, comme pour la synthèse de complexes Fe(II) hétéroleptiques en vue de la production de H_2 dans des réactions de fractionnement de l'eau.

En ce qui concerne la synthèse stéréosélective de complexes azine-NHC Fe(II) bidentés, nous avons développé une méthodologie à température ambiante pour accéder sélectivement aux complexes à géométrie faciale ou méridienne. Pour réaliser ce contrôle sélectif *fac/mer*, nous avons conçu plusieurs ligands avec une substitution modifiée de l'azine par des groupes de différents degrés d'encombrement tels que Mes et CH_3) (Voir §III.4, Schéma 9). Nous avons découvert que la sélectivité est étroitement liée à l'encombrement à proximité

de l'atome coordinateur N de l'azine. La meilleure sélectivité a été obtenue lorsque le CH3 (encombrement stérique plus faible) était en position alpha de l'azote coordonné au centre du fer (voir §III.4, Tableau 4). Il est intéressant de noter qu'en augmentant l'encombrement stérique dans cette position (série de dérivés 6-substitués), avec des substituants tels que des groupes isopropyle ou chlore, la même sélectivité a été obtenue (voir §III.4.3, tableau 6). En fait, on a souvent observé que des séquences de substitution comparables de ligands bidentés conduisaient à l'isomère mer, compte tenu de l'orientation commune de ces substituants. Dans le cas d'un groupe plus exigeant stériquement (Mes), une sélectivité mer n'a été obtenue qu'avec Mes en position 5 de l'azine (voir §III.4, Tableau 4). Pour évaluer la portée de notre méthodologie sélective fac/mer, nous avons utilisé des carbènes de nature électronique variée, allant de groupements plus acceptants (bIm) à des groupements plus donneurs (4MeIm). Nous avons observé que, quelle que soit la nature électronique du NHC, la sélectivité était maintenue, ce qui a permis d'obtenir un ensemble de complexes faciaux et méridiens avec différents carbènes (voir §III.4.1, tableau 5). Pour améliorer les propriétés optiques des complexes à base de pyridine, des ligands à base de quinoléine et de quinoxaline ont été préparés. De manière intéressante, la complexation avec ces deux ligands a permis d'obtenir la stéréosélectivité faciale exclusivement (voir §III.4.3, schémas 12 et 13). Comme dans la série substituée par la pyridine, nous avons étudié plus avant l'effet du NHC. La synthèse de deux ligands supplémentaires à base de quinoxaline avec bIm et 4MeIm comme NHC a été réalisée. Il est intéressant de noter que la complexation s'est déroulée avec une fac stéréosélectivité, ce qui est cohérent avec les résultats précédents (voir §III.4.3, schéma 14).

Malgré les calculs préliminaires effectués par le Dr. Antonio Francés Monerris (Valencia), la compréhension de la sélectivité fac/mer nécessite une étude plus approfondie du mécanisme de complexation, qui est actuellement en cours. Jusqu'à présent, la caractérisation structurelle a montré que les isomères fac présentent des sphères de coordination plus distordues (voir §III.4.4, Figure 42, Tableau 7) que les isomères mer, ce qui pourrait être délétère pour la dynamique de leur EE. Cependant, il est également concevable que la configuration faciale entraîne des interactions interligands qui ne sont pas présentes dans la configuration méridienne (voir §III.4.5, Figure 44, Tableau 8). Ces interactions dans la conformation faciale pourraient empêcher l'élongation de la liaison Fe-N, qui a été démontrée comme étant le facteur principal causant la désintégration des états excités de la MLCT. D'autre part, la nature de la NHC et de la π-conjugaison semble être le paramètre clé contrôlant leurs propriétés optiques et redox, les deux isomères présentant des comportements distincts (voir

§III.4.6). L'utilisation d'azines π-extendues est particulièrement pertinente en raison de leur collecteur MLCT de faible hauteur, ce qui entraîne une meilleure absorbance dans le spectre UV-vis (voir §III.4.6, Figures 46 et 47, Tableau 9). En outre, la réduction possible du couplage électronique avec les états MC pourrait contribuer à une durée de vie plus longue de la MLCT. A cet égard, une collaboration avec le Prof. Dr. Stefan Haacke à Strasbourg est en cours pour étudier l'influence sur la cinétique de l'EE. Cette partie de la thèse met en évidence le grand potentiel de ces complexes, qui peuvent profiter de l'effet synergique du couplage d'un motif de substitution spécifique à l'unité azine avec le NHC, est ainsi mis en évidence. Il en résulte une synthèse de complexes non labiles du fer(II) avec une stéréosélectivité vraisemblablement donnée par les interactions inter-ligands. De plus, les caractéristiques opto-électroniques qui peuvent être facilement modifiées en fonction de l'unité azine et de la partie NHC.

En ce qui concerne les complexes de Fe(III) portant des ligands anioniques tridentés, nous avons cherché à obtenir des complexes de fer ayant une durée de vie accrue des états excités à longue période. La stratégie consistait à utiliser des ligands donneurs forts tels que des amides et des unités de cyclométallisation afin d'induire un fort champ de ligand et de déstabiliser les états MC (voir §IV). Nous avons donc synthétisé et caractérisé différents ligands anioniques qui portent des unités NHC avec des donneurs N-amido (série carbazolate) (voir §IV.2.1, Schéma 15) ou avec des donneurs C-anioniques (série cyclométallisée) (voir §IV.4.2, Schéma 20). Concernant la série N-amido, nous avons rapporté la synthèse de trois complexes, un homoleptique (voir §IV.2.2, Schéma 16) et deux hétéroleptiques (voir §IV.3, Schéma 17) avec des interactions métal-ligand maximisées grâce à la formation de chélates à 6 membres. La force de la sphère de coordination a été modulée en fonction du nombre de ligands N-amido coordonnés, bien que dans tous les cas, des espèces Fe(III) aient été obtenues. Il est intéressant de noter que les composés homoleptiques et hétéroleptiques semblent avoir un mélange d'orbitales basé sur le métal et sur le ligand, comme le montre leur comportement en oxydation (voir §IV.4.4, Figure 57 et Tableau 12), ce qui suggère que ce type de ligands pourrait être utile pour obtenir une " inversion HOMO " complète telle que définie par Jakubikova. Des propriétés plus distinctes sont apparues dans leur comportement de réduction, avec les complexes hétéroleptiques présentant un premier potentiel de réduction remarquablement décalé anodiquement qui pourrait refléter l'ion métallique moins enrichi par rapport au complexe homoleptique. En outre, la réduction des fragments tpy a également été observée en raison de leur fort caractère d'accepteur. Il est intéressant de noter que les deux

séries de complexes ont montré des bandes de transfert de charge de nature différente presque sur toute la gamme visible et s'étendant jusqu'à la région IR.

Quant à la série C-anionique, lors d'un stage de 2 mois avec le Prof. Dr. Bauer à Paderborn dans le cadre du programme DrEAM de l'Université d'Excellence de Lorraine (LUE), nous avons développé une méthodologie qui nous a permis d'obtenir de nouveaux complexes Fe-CCC bis-cyclométallisés (Voir §IV.4.3, Schéma 22), sans utiliser de boîte à gants, de réactif transmétallant ou réducteur. Les propriétés de l'état fondamental des complexes homoleptiques obtenus ont été étudiées. Ces complexes présentent une unité pyrimidine cyclométallisante qui permet une stabilisation orbitale induite par le squelette pyrimidine et les substituants en position 2 (-Ph, -CF_3), lorsque le caractère attracteur d'électrons augmente, un décalage anodique est observé dans leurs ondes de potentiel de réduction. Les deux complexes présentent trois bandes d'absorption distinctes correspondant aux transitions π-π*, MLCT et LMCT qui se trouvent à une énergie plus faible par rapport à celle rapportée par Bauer avec un squelette phényle au lieu d'une pyrimidine. La présence du substituant phényle sur la pyrimidine conduit à une augmentation de l'intensité d'absorption (voir §IV.4.4, Figure 60, Tableau 14). Des calculs sont en cours en collaboration avec le Dr. Antonio Francés Monerris afin de mieux comprendre la nature des absorptions UV-vis observées pour les complexes de fer N-amido et cyclométallés. Des mesures complémentaires sont également effectuées en collaboration avec le Prof. Dr. Haacke à Strasbourg pour mesurer la dynamique de la relaxation de l'état excité (expériences TAS). Ensuite, une série de tests de réduction sera effectuée sur les complexes cyclométallisés afin d'obtenir des complexes Fe(II)-CCC, puis les propriétés de l'état fondamental et de l'état excité des complexes seront étudiées. Enfin, la synthèse de complexes hétéroleptiques avec des ligands push-pull sera tentée pour obtenir des complexes Fe(II)-CCC avec un flux électronique vectoriel.

Enfin, et c'est un aspect important de ce travail de doctorat, nous nous intéressons à la tendance croissante de la production d'hydrogène vert, en raison de son énorme densité énergétique (120 MJ kg-1) et de ses nombreuses applications industrielles (pharmacie, raffinage, agriculture, etc.), la poursuite de la production d'hydrogène vert sans empreinte carbone devient de plus en plus importante ces dernières années. Afin d'atteindre cet objectif, nous avons planifié la synthèse d'un ensemble de ligands afin de concevoir des dyades bimétalliques hétéroleptiques ditopiques Fe-Co qui seront testées comme photosensibilisateurs dans la réaction de séparation de l'eau dans la réduction des protons ($2H^+ + 2e^- \rightleftharpoons H_2\ E^0 = 0\ V\ vs\ RHE$). Cette partie de la synthèse des ligands a été réalisée dans notre laboratoire

(L2CM) tandis que la synthèse hétérolytique du complexe a été faite dans le cadre du programme DrEAM en Allemagne avec le Prof. Dr. Bauer.

Après différentes approches pour obtenir les ligands ciblés (voir §V.2.1, schémas 26, 27 et 29), nous avons réussi à obtenir deux des trois ligands : un qui se coordonnera de manière monodentée au Co, donnant une dyade (voir §V.2, Figure 68), et un qui se coordonnera de manière bidentée au cobalt, permettant l'accès à une dyade et une triade (voir §V.2, Figure 68). A l'heure actuelle, Bauer et ses collègues ont rapporté le complexe hétéroleptique avec l'un des ligands pour une coordination monodentée du Co (Voir §V.2.1, Schéma 27, ligand **H_2L29**). Par conséquent, nous nous sommes concentrés sur la synthèse des complexes homoleptiques et hétéroleptiques (voir §V.3, Schéma 30) avec le ligand ditopique à coordination bidentate pour le centre Co. Le complexe homoleptique **[Fe(L30)$_2$]$^{2+}$** a été obtenu (voir §V.3 Tableau 17). Ensuite, le complexe hétéroleptique a été obtenu en suivant une procédure rapportée par Bauer dans laquelle ils utilisent un ligand volumineux tridenté (**BuL**) pour inhiber cinétiquement la formation du complexe hétéroleptique. Le **[Fe(HMDS)$_2$(THF)]** en solution a été utilisé comme source combinée de fer et de base pour coordonner le **BuL**, puis le ligand **H_2L30** a été parallèlement déprotoné et ajouté à la solution de **[FeBuL]$^{2+}$**, ce qui a permis d'obtenir le complexe hétéropolitique **[Fe(BuL)(L30)]$^{2+}$** (voir §V.3, schéma 30). Il est intéressant de noter que dans les deux cas, nous coordonnons sélectivement le centre ferreux au tridenté parmi les deux sites de coordination possibles (C^N^C et N^N). Nous avons réussi à synthétiser un complexe ditopique hétéroleptique qui peut coordonner un ion cobalt en utilisant le protocole de Bauer. La caractérisation de l'état fondamental a révélé que la nature riche en électrons des unités dipyridyle semble favoriser le MLCT, impliquant un ligand **BuL** plutôt que **L30**, empêchant le transfert électronique cible vers le site de coordination du Co. En conséquence, alors que la coordination réelle du Co peut exercer un effet d'attraction suffisant, ces résultats démontrent clairement la nécessité d'augmenter les différences électroniques entre les ligands terminaux (push) et ditopiques (pull). Par exemple, l'utilisation d'un ligand terminal anionique et/ou l'introduction d'unités réservoirs d'électrons au sein du ligand ditopique pourraient être envisagées.

Le projet est actuellement en cours, ciblant les différences de caractère électronique entre le ligand terminal et ditopique afin de favoriser un transfert vectoriel d'électrons vers le site de coordination du Co. Quant à notre complexe, il sera coordonné au cobalt afin d'obtenir une triade (Voir §VI.5, Figure 78) et ainsi évaluer :

- La stabilité de la triade, la caractérisation de l'état fondamental et l'ESL.

- Leurs performances dans l'évolution photocatalytique de H_2 et comparer les activités entre la dyade et les triades.

Table of Contents

Abbreviation list

4’-pytpy = 4'-(pyridin-4-yl)-2,2':6',2''-terpyridine

4MeIm = 4-methylimidazole

ACN = Acetonitrile

bIm = Benzimidazole

bim-pyr = (4-pyrene-2,6-diyl)bis(1-methylimidazol-2-ylidene)

BuL = Bulky ligand

Bpy = Bipyridine

Btz = 3,3’-dimethyl-1,1’-di-*p*-tolyl[4,4’bis-(1,2,3-triazol-5-ylidene

CB = Conduction band

cpbmi = (carboxypyridine-2,6-diyl)bis(1-methyl-imidazol-2-ylidene)

dcpp = 2,6-bis(2-carboxypyridinyl)-pyridine

ddpd = N,N’-dimethyl-N,N’-dipyridin-2-ylpyridine-2,6-diamine)

DFT = Density Functional Theory

DIPP = Diisopropylamine

DMF = N,N-Dimethyformamide

DMSO = Dimethylsulfoxide

dpmi = Di(pyridine-2-yl)(3-methylimidazol-2-yl)methane

dqp = 2,6-di(quinoline-8-yl)pyridine)

DSSC = Dye-sensitized solar cell

Dtapbmi = 1,10-(4-(di(p-tolyl)amino)pyridine-2,6-diyl) bis(methylimidazole-2-ylidene))

EDTA = Ethylenediaminetetraacetic acid

ER = Electron relay

ES = Excited state

ESD = Estimated Standard Deviations

ESL = Excited-state lifetime

EtOAc = Ethyl acetate

GS = Ground State

HImP = 1,1’-(1,3- phenylene)bis(3-methyl-1-imidazol-2-ylidene

HOMO = Highest occupied molecular orbital

IC = Internal conversion

Im = Imidazole

ISC = Intersystem crossing

L^{bi} = 2,5-bis(3,5-di-tert-butyl-2-isocyanophenyl)thiophene

LLCT = Ligand-to-ligand charge-transfer

LMCT = Ligand-to-metal charge-transfer

L^{tri} = 5,5'-(2-isocyano-5-methyl-1,3-phenylene)bis(2-(3,5-di-tert-butyl-2-isocyanophenyl)thiophene)

LUMO = Lowest unoccupied molecular orbital

MC = Metal centered

MLCT = Metal-to-ligand charge-transfer

NHC = N-heterocyclic carbenes

NIR = Near-infrared

o-DCB-*d4* = Tetra-deuterated 1,2-dichlorobenzene

OLEDS = Organic light-emitting diodes

PALCT = $\pi_{\text{anti-bonding}}$-to-ligand charge transfer'

pbbi = (pyridine-2,6-diyl)bis(1-tert-butyl)-imidazol-2-ylidene

pbbi = (pyridine-2,6-diyl)bis(1-tert-butyl)-imidazol-2-ylidene)

pbmbi = (pyridine-2,6-diyl)bis(1-methyl-benzimidazol-2-ylidene

pbmi = (pyridine-2,6-diyl)bis(1-methyl-imidazol-2-ylidene)

pbpy = 6-phenyl-2,2′-bipyridine

pdmmi = 3,3'-pyridine-2,6-diyl(methylene)bis(1-methylimidazolylidene)

PDT = Photodynamic therapy

$PhB(MeIm)_3)_2$ = Bis(tris(methylimidazolin-2-ylidene)(phenyl)borate)

pqa = Phenanthidin-4-yl)(quinolin-8-yl)amido

PRC = Proton reduction catalyst

PS = Photosensitizer

pzbhbi = (pyrazine-2,6-diyl)bis(1-hexyl-benzimidazol-2-ylidene)

pzbmi = (pyrazine-2,6-diyl)bis(1-hexyl-benzimidazol-2-ylidene)

RHE = Reversible hydrogen electrode

ROS = Reactive oxygen species

bim-ant = (4-anthracene-2,6-diyl)bis(1-methylimidazol-2-ylidene)

SET = Single electron transfer

SNAr = Nucleophilic aromatic substitution

SR = Sacrificial Reductant

TAS = Transient absorption spectroscopy

^{t}Bu = Tert-butyl

TCE-*d2* = Bis deuterated trichloroethylene

TEOA = Triethanolamine

TFA = Trifluoroacetic acid

TFBP = Tetrakis[3,5-bis(trifluoromethyl) phenyl]borate

THF = Tetrahydrofuran

TMC = Transition metal complexes

TMSA = Trimethylsilylacetylene

Tol = Toluene

tpy = Terpyridine

TTET = Triplet-triplet energy transfer

UV = Ultra-violet

WGS = Water-gas-shift

WS = Water splitting

Δ_0 = Ligand field splitting parameter

I. General Introduction

I. General Introduction

Already since several decades, the modern societies are in their quest for stopping their dependence on non-renewable fossil fuels as a principal energy source, that arises up to 90% of energy consumed by humankind,[1] which is around 18 TW and it is predicted to reach 43 TW in 2100. The use of fossil fuels produces a large quantity of pollutants and greenhouse gases related to serious environmental problems (climate change, water, soil and air pollution).[2] As an alternative to avoid fossil fuels, the scientific community has searched for alternative renewable energy sources like solar, wind power and hydroelectric among others. (Figure 1).[3]

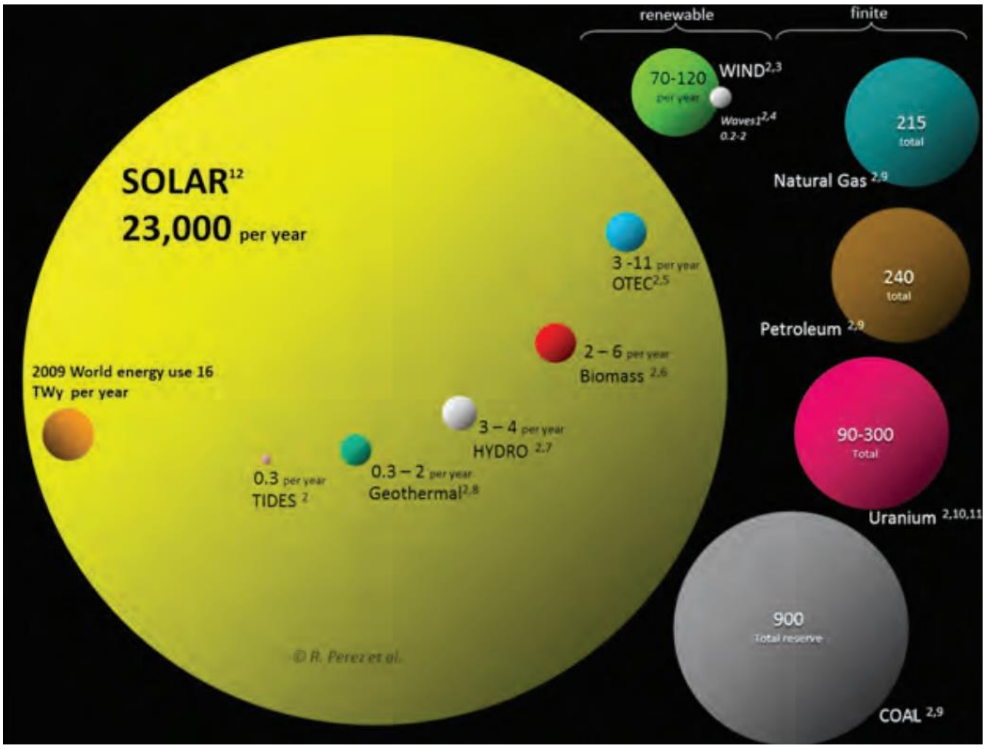

Figure 1. Estimate of finite and renewable energy reserves (Terawatt-years) taken from reference 3.

The solar energy is a green, sustainable, and renewable option. Actually, the sun delivers to the Earth the energy needed for a whole year in about one hour. Thus, such an extraordinary and practically limitless power could easily supply the electricity needs of our society, nowadays and in the future.[4] In fact, sunlight can be easily transformed into electricity

by means of solar cells.[5] Furthermore, it can be also converted into chemical energy through, for instance, photocatalytic reactions for storage reasons due to its intermittent and diffuse character.[6] In both cases, when molecular materials are considered, noble (Ru, Ir, Pt, Au) and rare-Earth metals (lanthanides) have played a key role due to their outstanding performances stemming mainly from the ideal photophysical and electrochemical properties of their complexes. These properties encompass strong visible light absorption, reversible redox behaviour, long-lived relevant excited states (ES) and thermal stability.

Noble and rare metals have been used in photo dynamic therapy (PDT),[7] as light emitters organic light-emitting diodes (OLEDs),[8] phosphorescent organic light-emitting diodes (PhOLEDs),[9] dye-sensitizer solar cells (DSSCs),[10] catalysis and energy conversion reactions.[6,11] However, the scarcity and high cost of these elements are detrimental to their sustainable application on a large scale. In addition to this, geopolitical issues are to be considered since there are often only few countries that mine and produce them. For instance, in Figure 2 it is shown the global production for rare earth oxides in the second half of the last century, being controlled by the United States of America and then by China.[12] In addition, the environmental impact for mining, extraction, separation and earth remediation produces a huge amount of toxic waste and consumes enormous quantities of water.[13]

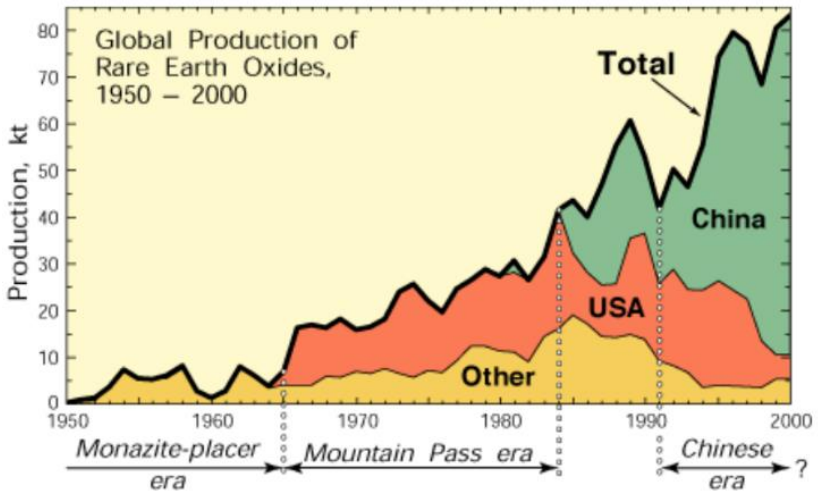

Figure 2. Global production of rare earth oxides from 1950 to 2000. Taken from reference 12.

In recent years, an increasing interest in switching from rare metals to first-row transition (3d) metals like iron, manganese, vanadium or chromium instead of noble metals, since they are remarkably more abundant[14] and generally cheaper (Figure 3).[15] Actually, significant and successful strategies have been reported for 3d transition metals. In this regard iron takes a special role since it is the most abundant transition metal in Earth-crust and cheaper in comparison to noble metals. In comparison, iron is approximately 25000 times cheaper than Ru,[16] one of the most widely used for photocatalytic applications. Moreover, its extraction process is more sustainable and efficient, since the remediation and by-products are less toxic.[17] As a result, the development of robust and efficient photoactive molecular materials based on Earth-abundant metals constitute a genuine milestone to replace environmentally harmful process towards sustainability.[18]

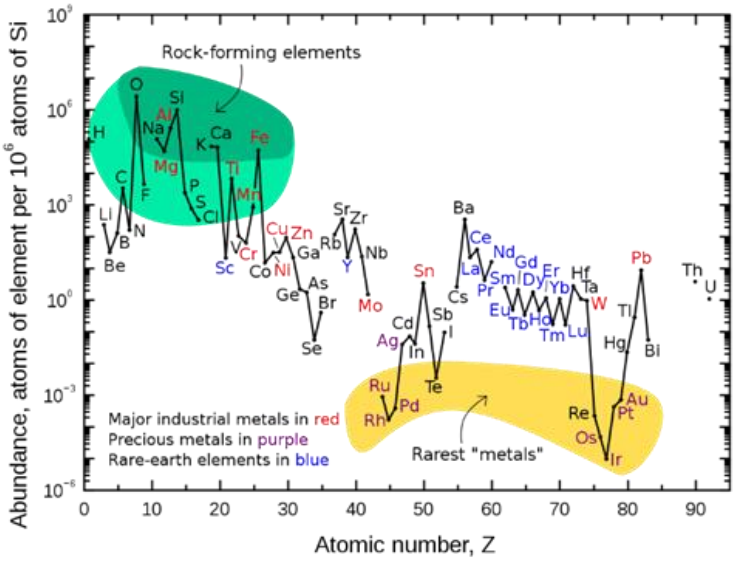

Figure 3. Abundance (atom fraction) of the chemical elements in Earth's crust as a function of atomic number. Graphic taken from reference 15.

However, developing photosensitizers based on 3d transition metal complexes (TMC) that can contend with those based on noble metals is a real challenge.[19,20] The main issue is that 3d-metals face weaker ligand fields than 4d- or 5d- species, since 3d orbitals are more compact than those of 4d- or 5d- metals. In consequence, the overlap between ligand and metal orbitals is weaker in the former case and, as a result, the corresponding ligands tend to be more labile than those of 4d- or 5d- complexes (Fig 4a). Moreover, 3d- complexes present a large number

of metal-centered (MC) states of similar energy close to the electronic ground state (GS) energy level. Access to these excited MC states results typically in more distorted molecular structures respect to that of the GS as a consequence of the elongation of the metal-ligand bonds,[21] favoring a nonradiative relaxation process from the MC states to the GS (Fig 4b). Concerning 4d- and 5d- metal complexes, they present stronger ligand fields leading to larger energy gaps between the MC states. In some cases, it is worth noting that the energy gap of the lowest MC and the GS can be large enough to avoid a non-radiative relaxation. In a such scenario, the lowest MC state can become luminescent and photochemically active,[21] as well there are reports of 3d complexes with MC state emitters.[20]

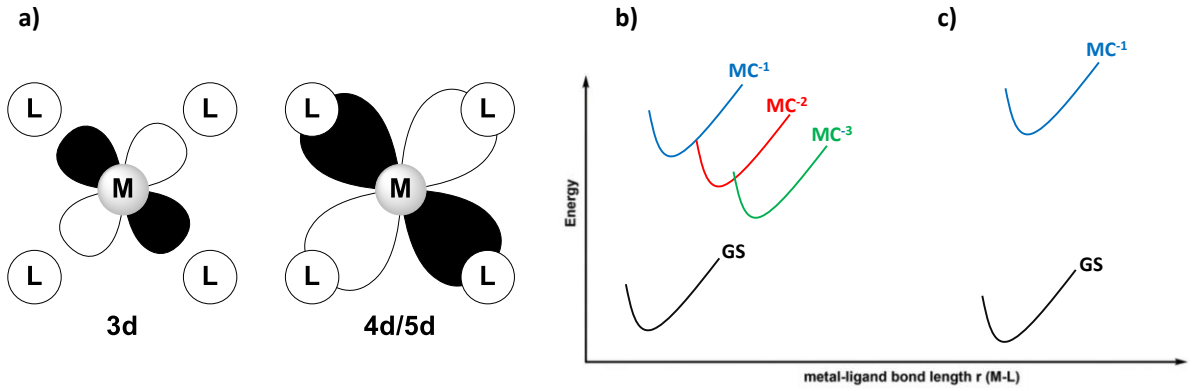

Figure 4. a) Overlap between metal d-orbitals and ligands. b) Simplified potential energy surface for 3d-metal complexes c) Simplified potential energy surface for 4d- or 5d-metal complexes.

Notwithstanding their inherent small ligand fields, important advances for photoactive 3d TMC has been made in recent years achieving stable compounds with sufficiently long-lived relevant excited states and even presenting luminesce.[18,20] As mentioned before, among the transition metals, iron is the most abundant and the fourth most common element in the Earth's crust. Besides the concomitant advantages regarding its low price and accessibility, iron is placed in the same column as ruthenium in the periodic table and thus, similar properties could have been expected for iron complexes while offering a greener and cheaper alternative. Unfortunately, their photophysical behavior is rather different, spurring the scientific community in the last decade to contribute to this very important field of chemistry. In the following sections we will first describe and compare the photophysical properties of Fe(II)

and Ru(II) complexes that will allow for a better understanding of the subsequently explained design of ferrous compounds explored so far to address the issues regarding light conversion applications.

I.1 Photophysical properties of Fe(II) and Ru(II) complexes.

In order to rationalize the design of photoactive complexes, it is imperative to understand the fundamentals of their photophysics and photochemistry. To begin with, it is helpful to identify the possible low-lying electronic ES arising from one-electron excitations.[22] In the case of metal complexes bearing π-conjugated ligands, four main electronic states can be identified:

i) Metal-centred (MC) states, involving electronic transitions within the d orbitals (d-d) and whose energy directly depends on the ligand-field splitting parameter Δ (Figure 5, MC).

ii) Ligand-centred (LC) states, which result from transitions between occupied and empty π orbitals (π-π*) of the ligands (Figure 5, LC).

iii) Metal-to-ligand charge transfer (MLCT) states, arising from transitions between occupied metal d orbitals and unoccupied ligand orbitals (d-π*) (Figure 5, MLCT).

iv) Ligand-to-metal charge transfer (LMCT) states, associated to excitations from occupied π ligand orbitals and unoccupied metal d orbitals (π-d) (Figure 5, LMCT).

Even though MC transitions are Laporte forbidden, they become partially allowed by dynamic symmetry lowering, in complexes with lower symmetry or in heteroleptic complexes without inversion of symmetry.[23]

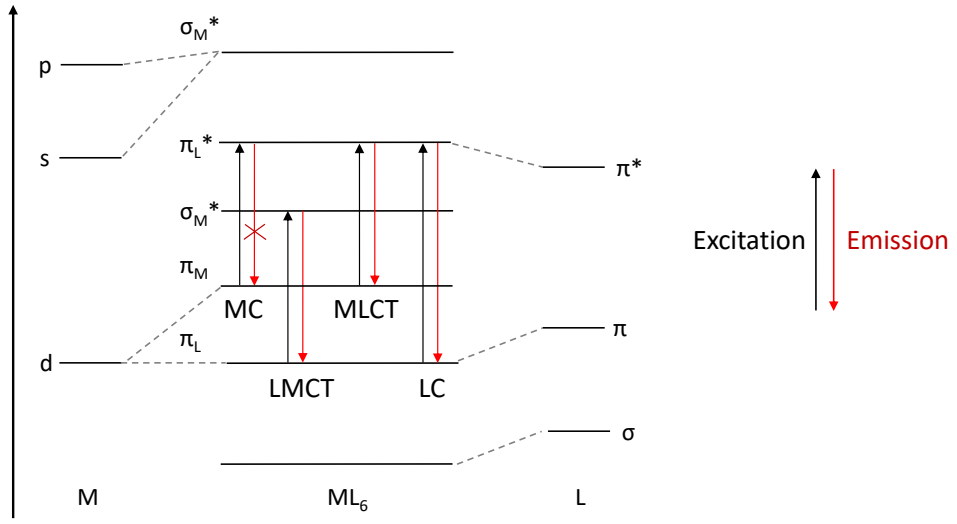

Figure 5. Molecular orbital diagram for an octahedral transition metal complex. MC, LMCT, MLCT and LC transitions based on localized MO configurations.

To understand the photophysical differences between **[Ru(bpy)$_3$]$^{2+}$** and **[Fe(bpy)$_3$]$^{2+}$** complexes, Tanabe-Sugano diagrams can be an important tool (Figure 6). These diagrams provide information on the relative order of the different spectroscopic states as a function of the field splitting of the complex. Moreover, in the case of d^6 complexes, a drastic change in the state ordering is observed as a consequence of the spin configuration. The Fe-complex is found very close to the high/low spin barrier, consequently presenting metal-centred states ($^5T_2$, $^3T_1$) lower in energy than the MLCT states. In contrast, the Ru analogue has a higher Δ/B value, hence the MC states are more destabilized, leaving the MLCT states as the lowest-lying.

For sake of explanation, a representation of ligand field splitting in **[Ru(bpy)$_3$]$^{2+}$** and **[Fe(bpy)$_3$]$^{2+}$** complexes is depicted in Figure 6b and 6c respectively. With an assumed octahedral symmetry and a simplified $4d^6$ electronic structure, upon **[Ru(bpy)$_3$]$^{2+}$** complex formation, the metal-centred d orbitals split in three low-energy orbitals with t_{2g} symmetry and two high-energy orbitals with e_g symmetry. As a consequence of the high Δ_0 value for this 4d complex, a $(t_{2g})^6$ low spin ground-state configuration is privileged. The highest occupied molecular orbital (HOMO) being localized on the t_{2g} system and the lowest unoccupied molecular orbital (LUMO) on the empty π* orbitals. Upon light absorption (λ = 452 nm) **[Ru(bpy)$_3$]$^{2+}$** complex lead to the population of ^{1}MLCT states, followed by fast intersystem crossing (ISC) to the energetically lower ^{3}MLCT state (Figure 7, left).

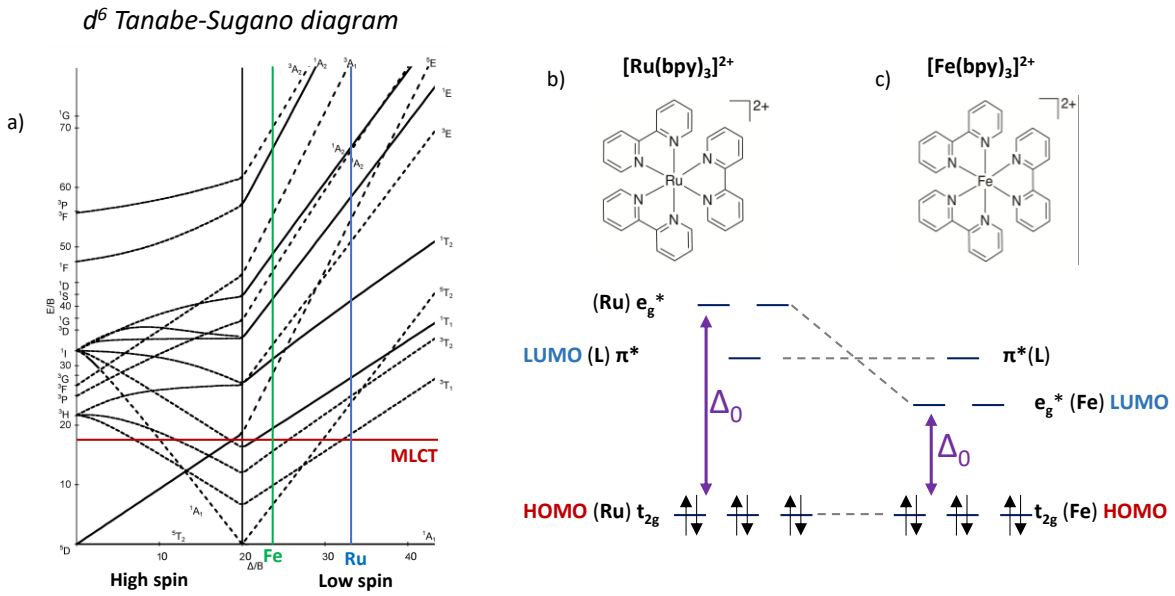

Figure 6. a) Tanabe-Sugano diagram for the d^6 electron configuration. Simplified molecular orbital diagrams of b) **[Ru(bpy)$_3$]$^{2+}$** and c) **[Fe(bpy)$_3$]$^{2+}$** complexes.

The weakly distorted ^{3}MLCT state is long enough (τ_{MLCT} = 1μs) to perform an oxidizing/reducing single electron transfer (SET) or to allow a phosphorescent decay.[24] The small distortion favours the radiative excited-state relaxation against the nonradiative deactivation. In sharp contrast, although having the same type of orbitals, the MLCT lifetime of **[Fe(bpy)$_3$]$^{2+}$** is several orders on magnitude shorter. The weaker ligand field exerted by Fe(II) implies that the e_g orbitals are less destabilized and lie consequently at lower energies than the π* ligand orbitals (Figure 6b). After light absorption, **[Fe(bpy)$_3$]$^{2+}$** populates the ^{1}MLCT state, followed by ISC into ^{3}MLCT state. Due to the small ligand field splitting, MC states are energetically lower to MLCT states leading to an ultrafast relaxation (~ 150 fs) from the ^{3}MLCT into $^{3/5}$MC states, followed by vibrational relaxation on a time scale of few ps into the ^{1}GS (Figure 7, right).[25–27] As a result, Fe(II) complexes as **[Fe(bpy)$_3$]$^{2+}$** are unsuitable for applications seeking to exploit the MLCT state, having been mostly studied for spin-crossover applications.

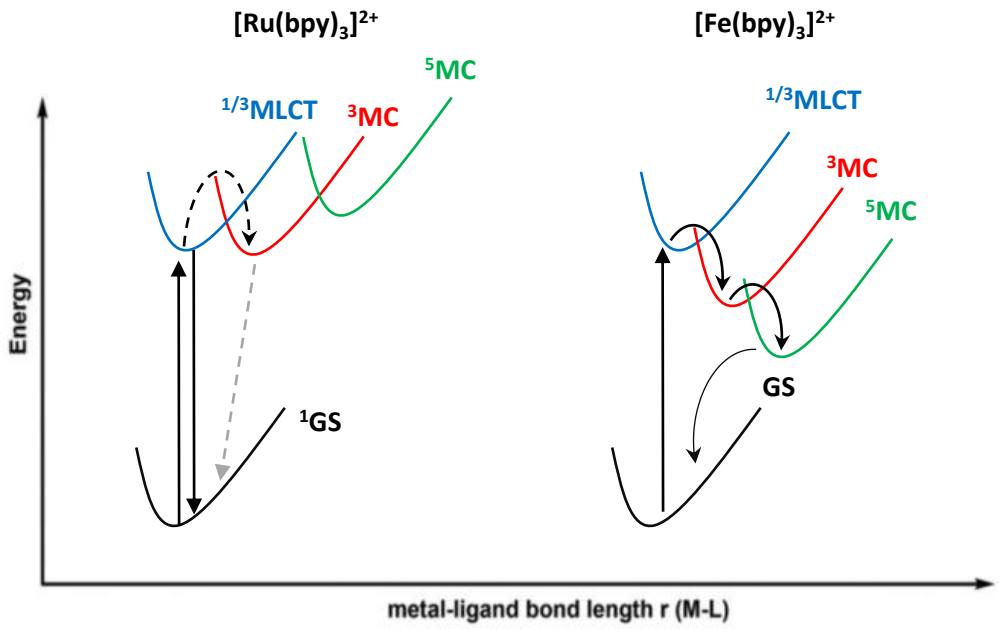

Figure 7. Simplified potential energy surface diagrams with key electronic states in **[Ru(bpy)$_3$]$^{2+}$** (left) and **[Fe(bpy)$_3$]$^{2+}$** (right).

The strategies to avoid this detrimental non-radiative deactivation, and thus to increase luminescent or photocatalytic properties, rely on preventing (or slowing down) the MC states population upon their destabilization together with a further stabilization of the MLCT states. Increase of the ligand field strength can be attained by using strong ligands such as N-heterocyclic carbenes (NHC),[28] cyanides[29] or cyclometalating units[30] which has proven the most successful way to increase the MLCT excited-state lifetimes in Fe(II) complexes. Additionally, improving metal-ligand interaction further enhances the effects exerted by a certain ligand.

Indeed, when the frontier orbitals are spatially separated, an notable stabilization of the $^{1/3}$MLCT states can be induced upon introduction of electron-withdrawing groups[31] or increase of the π-conjugation at the LUMO (π* orbital)[32]. In the case of heteroleptic complexes with push/pull ligands, the MLCT manifold can be lowered, with the concomitant appearance of even lower ligand-to-ligand charge-transfer (LLCT) states.[33] However, although this way of reasoning is very helpful when designing a complex, it is important to bear in mind that most ligand modifications will likely affect both the MC and MLCT manifolds.

I.2 Strategies towards Iron(II)-based complexes with long-lived MLCT

Several synthetic approaches have been explored to increase the MLCT lifetimes in ferrous complexes, including modifying the nature of the coordinating units, improving the geometry depending on the type of ligand chelation or strain of the coordination sphere. In the following sub-sections, the main strategies will be reviewed in detail, where the examples have been selected so as to better illustrate the parameter being discussed.

I.2.1 Maximizing M–L interaction: ligand chelation

Maximizing the overlap between metal and ligand orbitals is key for enhancing the ligand field. In the case of an octahedral coordination, the optimal interaction is found between the axially aligned e_g metal system (orbitals $d_{x^2-y^2}$, d_{z^2} over the axes x,y,z, Figure 8) with the sigma ligand orbitals due to symmetry, achieving maximal values when bond angles approach those of the ideal octahedron (90° for L-M-L cis angles and 180° for L-M-L trans angles). This interaction will impact the e_g^* level, being more destabilized as the interaction upon complex formation gets stronger. This can be nicely illustrated when comparing bidentate and tridentate coordination as in **$[Ru(bpy)_3]^{2+}$** and **$[Ru(tpy)_2]^{2+}$** (tpy= 2,2':6',2''-terpyridine), respectively. While **$[Ru(bpy)_3]^{2+}$** is emissive at room temperature, **$[Ru(tpy)_2]^{2+}$** is rather non-emissive.[34] This is a consequence of the poor interaction between the tpy and metal d orbitals, due to a smaller N-Ru-N angles as shown in Figure 9. This strategy has also been applied to iron complexes, of which some examples will be described in Chapter 2.

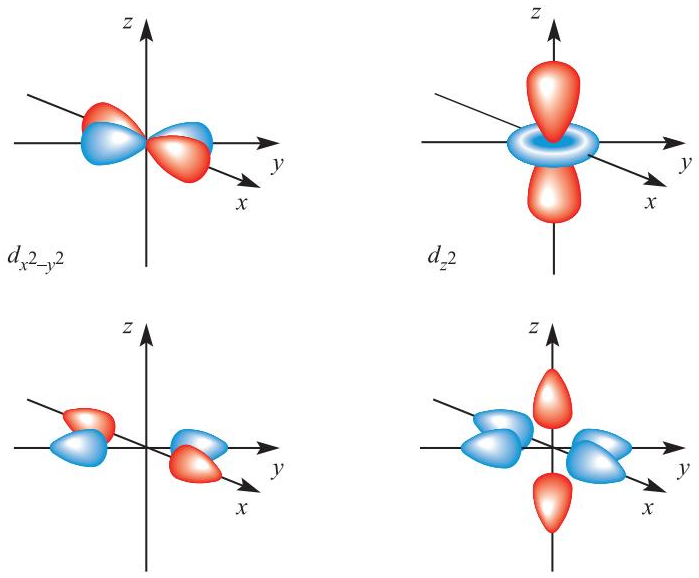

Figure 8. Metal atomic orbitals $d_x{}^2$-y^2, $d_z{}^2$ matched by symmetry with ligand group orbitals for an octahedral complex with only σ-bonding picture taken from reference 35.

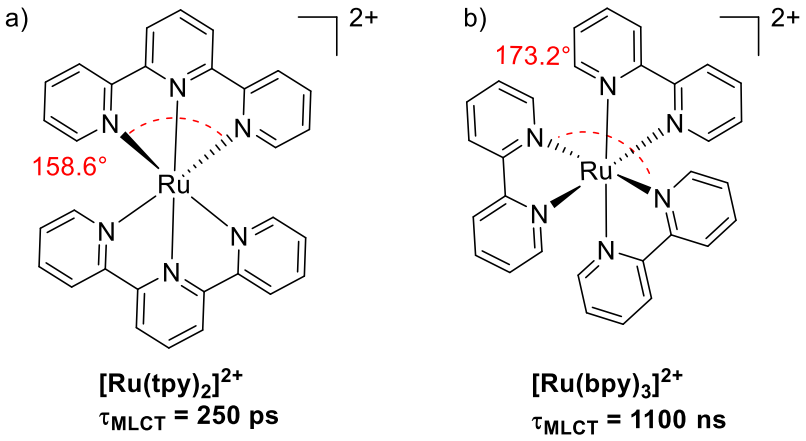

Figure 9. Structure, angles and MLCT lifetimes of a) **[Ru(bpy)$_3$]$^{2+}$** and b) **[Ru(bpy)$_3$]$^{2+}$** complexes.

Apart from the ligand denticity, changing the ring chelation also allows for tuning the metal-ligand orbital overlap. McCusker and co-workers reported **[Fe(dcpp)$_2$]$^{2+}$** (dcpp=2,6-bis(2-carboxypyridinyl)-pyridine),[36] a ferrous complex bearing a tridentate ligand with a N-Fe-N trans angle of 178.3° (Figure 10a). The improvement of the bite angle was accomplished by expanding the tpy ligand with carbonyl bridges between the pyridine units. The electron withdrawing character of these groups contributed to a concomitant stabilization of the π*

orbitals that allows for a better interaction with the t_{2g} system, thereby further increasing Δ. These modifications of the metal-ligand interaction can be nicely observed in the ESL that increases up to 280 ps at room temperature. However, in spite of the improvement, it was found that the excited state corresponds to a ^{3}MC state instead of MLCT state.[37] Following this train of thought, Heinze and co-workers applied this concept to obtain the heteroleptic complex **[Fe(dcpp)(ddpd)]$^{2+}$** (ddpd= N,N'-dimethyl-N,N'-dipyridin-2-ylpyridine-2,6-diamine) with N-Fe-N trans angles 178.4° (Figure 10b).[38,39] Apart from the more appropriate coordinating geometry of the six-membered chelating rings, the push-pull character afforded by the electron-withdrawing dcpp with the electron-rich ddpd ligand resulted in lower MLCT states with a ^{3}MC of 548 ps -double in comparison with that of McCusker- and no participation of ^{5}MC state due to higher destabilization attributed to ligand push-pull design. It is worth to note the concomitant appearance of an even lower-lying ligand-to-ligand charge-transfer (LLCT) states.

Gros and co-workers reported the synthesis of **[Fe(dqp)$_2$]$^{2+}$** (dqp=2,6-di(quinoline-8-yl)pyridine) complex (Figure 10c).[40] This pincer-type ligand combined an improved coordination of the metal centre (N-Fe-N bite angle of 178.4°) with the lower π* orbitals of the quinoline moieties, together with a reduced flexibility respect to the aforementioned expanded tpy ligands. As a result, an improvement of the photophysical properties was expected. Yet, the complex presented a ^{3}MLCT lifetime of 0.45 ps, which is just slightly longer than that observed for **[Fe(tpy)$_2$]$^{2+}$**. This result can be ascribed to the weaker ligand field created by the six Fe–N bonds that stabilizes the ^{5}MC, which participates actively in the relaxation process unlike **[Fe(dcpp)$_2$]$^{2+}$** and **[Fe(dcpp)(ddpd)]$^{2+}$** complexes.

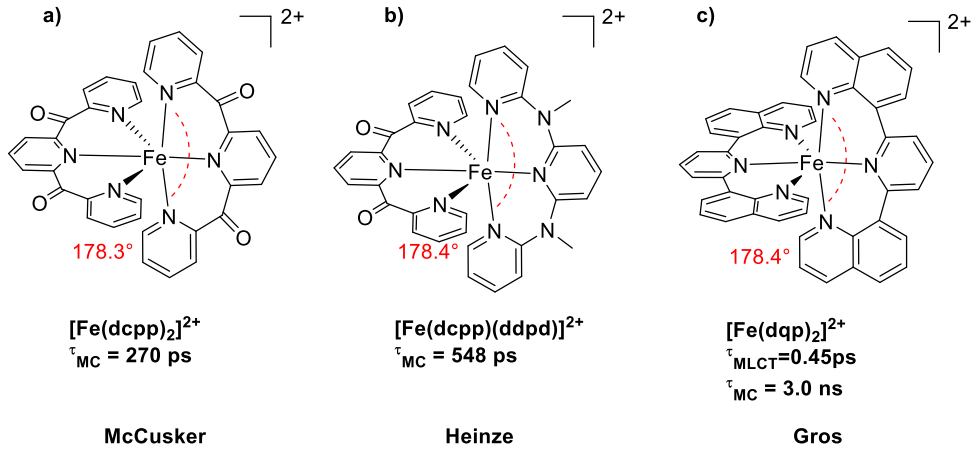

Figure 10. Structure, angles, MLCT and MC lifetimes of **[Fe(dcpp)$_2$]$^{2+}$**, **[Fe(dcpp)(ddpd)]$^{2+}$**, and **[Fe(dqp)$_3$]$^{2+}$** complexes.

From these results it is evident that improving the coordinating symmetry at the metallic center is not enough to efficiently destabilize the MC states. In addition to this, the increase of flexibility results in non-radiative vibrational relaxations that appear to rule the ES dynamics.

I.2.2 Rigidity increase

An interesting example of the improvement of the ES dynamics on increasing the rigidity was reported by McCusker and coworkers, comprising the macrocyclic cage ligand shown in Figure 11.[41] Following the initial complexation of Fe(II) by the bpy units, the additional coordination of two Cu(I) ions at the amine-imine sites contributed to the rigidification of the structure. More importantly, the vibrational modes associated to the MLCT relaxation were reduced, leading to an impressive ESL for the MLCT state of 2.6 ps, which is more than 20-fold longer than the analogous unconnected **[Fe(bpy)$_3$]$^{2+}$** (100 fs).

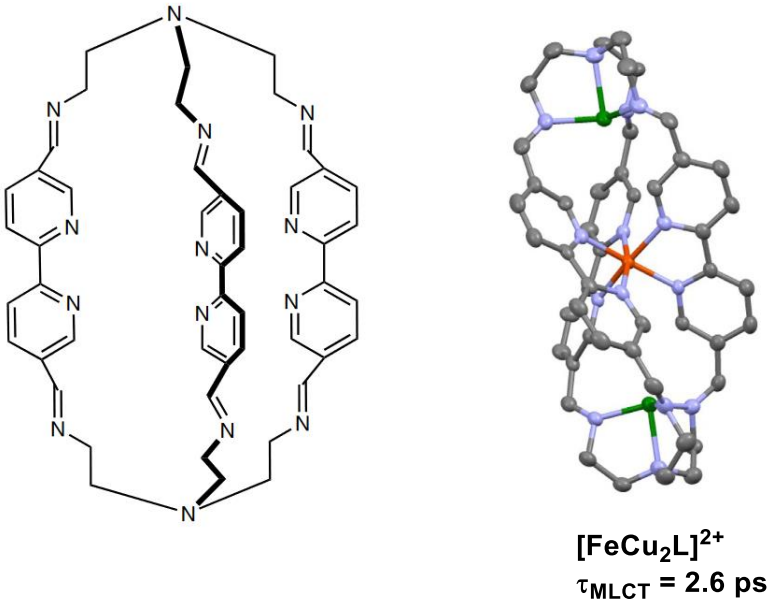

Figure 11. Structure of ligand **L**. Single-crystal X-ray structure of the cation of **[FeCu$_2$(L)](PF$_6$)$_4$** with MLCT lifetime. For the metal ions, color coding is as follows: Fe, red; Cu, green; N, purple; C, grey. All hydrogen atoms and counteranions have been removed for clarity. Taken from reference 41.

I.2.3 Strong field ligands

The increase of the ligand field strength can be alternatively be reached by using strong C-donor ligands,[42] which proved to be the most successful way to alter the order of MC and MLCT levels to increase the MLCT excited-state lifetimes in Fe(II) complexes. Graffney and co-workers have reported the effect of strong donor ligands in the **$[Fe(bpy)(CN)_4]^{2-}$** complex (Figure 12).[29] They measured a 20 ps MLCT lifetime which, in comparison to that of **$[Fe(bpy)_3]^{2+}$**, is two orders of magnitude longer. Furthermore, no experimental evidence of ^{3}MC and ^{5}MC excited states was found, suggesting a significant destabilization of the MC excited states relative to the ^{3}MLCT manifold.

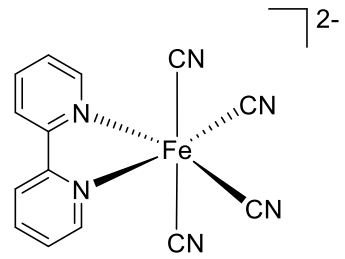

$[Fe(CN)_4(bpy)]^{2-}$
τ_{MLCT} = 20 ps

Figure 12. Structure of **$[Fe(bpy)(CN)_4]^{2-}$** complex and ^{3}MLCT lifetime.

Nevertheless, the most studied C-donor ligands are certainly N-heterocyclic carbenes (NHC). A carbene is a neutral carbon species with only six electrons in its valence shell.[43] Carbenes are classified as singlet (spin paired) (Figure 13a) or triplet (unpaired spin) (Figure 13b) as a function of their electronic structure. In general, the carbon possesses a sp^2 hybridization with an empty orbital p (p_π) and one full σ orbital (according to different authors is a p_x with strong σ character). Most carbenes are bent but in extreme case carbenes with linear geometry can be found (Figure 13c).[43] Another sub-type of carbenes, the so-called persistent carbenes (also known as stable carbenes) is a type of carbene which demonstrate particular stability, it can either be of triplet or singlet nature as well. A widely studied type of persistent carbenes are the NHCs, relevant in coordination chemistry for their air stability[44] and their easily tunable electronic and steric properties.[45] In particular, NHC have an out-of-plane empty p orbital and a full σ-orbital (Figure 13d). Thus, they are neutral ligands, with a strong σ-donor

character and a varying π-acceptor character as a function of the π-donation exerted by the nitrogen atoms adjacent to the carbenic carbon.

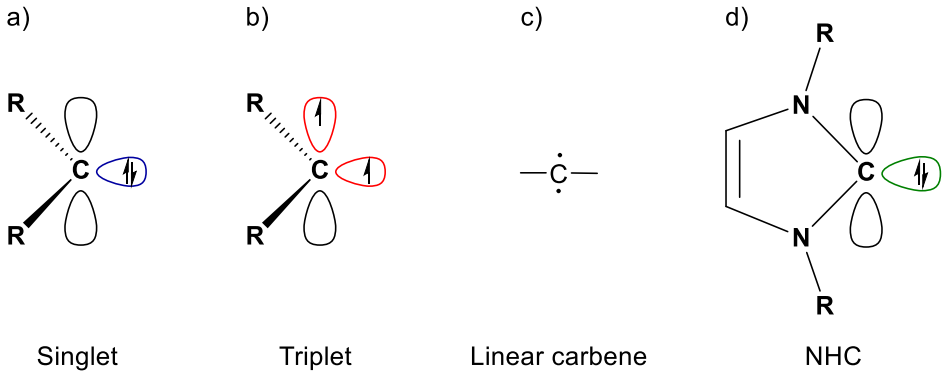

Figure 13. a) singlet carbene structure, b) triplet carbene structure, c) linear carbene, d) NHC-carbene structure (singlet).

Although first described in 1969,[46] iron NHC complexes have received increasing interest since the 2000s, especially for their successful application in catalysis.[47] However, it was not until 2013 that Wärnmark and co-workers investigated he photophysics of this type of complexes.[28] These authors reported a series of homoleptic complexes, **[Fe(pbmi)$_2$]$^{2+}$** and **[Fe(pbbi)$_2$]$^{2+}$**, comprising tridentate pyridine-bis(NHC) ligands (pbmi = (pyridine-2,6-diyl)bis(1-methyl-imidazol-2-ylidene) and (pbbi=(pyridine-2,6-diyl)bis(1-tert-butyl)-imidazol-2-ylidene)) (Figure 14a and 14b). The presence of the strong NHC units in the coordination sphere resulted in an outstanding increase of the ^{3}MLCT lifetime up to 9 ps, which is almost two orders of magnitude compared to that of **[Fe(tpy)$_2$]$^{2+}$**. Moreover, the quaternizing substituent of the NHC moiety was shown to play a significant role in the MLCT lifetime. In fact, the tert-butyl groups (^{t}Bu) present in **[Fe(pbbi)$_2$]$^{2+}$** reduced the ^{3}MLCT lifetime to 300 fs in comparison to **[Fe(pbmi)$_2$]$^{2+}$**, where methyl groups were introduced. This result was attributed to the higher steric demand of ^{t}Bu, that impedes the metal coordination with longer Fe-L bond distances, which results in a photophysical behavior resembling that of the classic Fe-polypyridine complexes.[48,49]

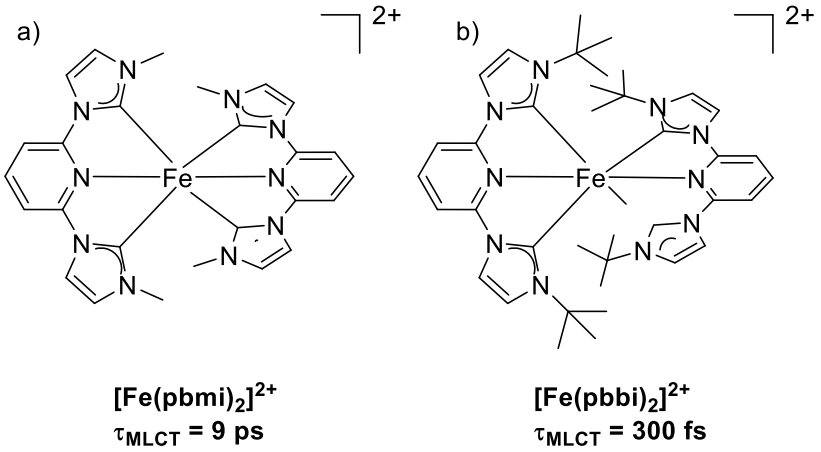

Figure 14. Structure and MLCT lifetimes of a) **[Fe(pbmi)$_2$]$^{2+}$** and b) **[Fe(pbbi)$_2$]$^{2+}$** complexes.

Electronic modification within the tridentate scaffold was thoroughly investigated by Gros, Haacke and coworkers.[40,50] These authors prepared **[Fe(cpbmi)$_2$]$^{2+}$** (cpbmi=(carboxypyridine-2,6-diyl)bis(1-methyl-imidazol-2-ylidene)), a complex bearing a carboxylic acid group in the pyridine seeking to stabilize the MLCT states, as well to examine the possibility of engaging it in electron transfer processes (Figure 15a).[51] Nicely, the introduction of these electron withdrawing groups led to an increase of the ^{3}MLCT lifetime to **16.5** ps due to the stabilization of the π* ligand orbitals. More interestingly, sensibilization of a TiO_2 semiconductor surface with this COOH-based complex led for electron injection,[52,53] allowing for the generation of a photocurrent in a dye-sensitized solar cell (DSSC) device. This result was of paramount importance since it opened the door to the development of materials for solar energy conversion based on Earth-abundant elements.

On the other hand, replacement of the imidazole-based NHC by a more π-conjugated benzimidazole afforded **[Fe(pbmbi)$_2$]$^{2+}$** (pbmbi=(pyridine-2,6-diyl)bis(1-methyl-benzimidazol-2-ylidene) (Figure 15b), which also resulted in an increased ^{3}MLCT lifetime of 16 ps. The increase in the MLCT lifetime is attributed to an enhanced charge transfer character as well as a destabilization of the MC level due to the more π -accepting character of the BIm units. The same group reported the complex **[Fe(cpbmbi)$_2$]$^{2+}$** (cpbmi=(carboxypyridine-2,6-diyl)bis(1-methyl-benzimidazol-2-ylidene)) by mixing -COOH and BIm units affording an even more increased ^{3}MLCT lifetime of 26 ps (Figure 15b).

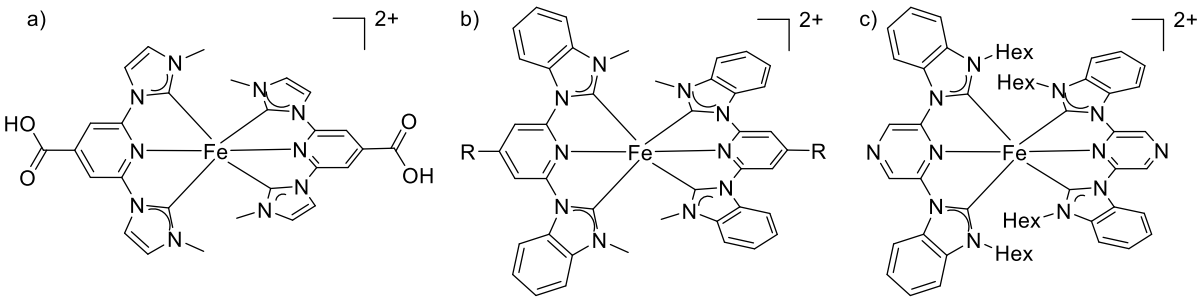

$[Fe(cpbmi)_2]^{2+}$
τ_{MLCT} = 16.5 ps

$[Fe(pbmbi)_2]^{2+}$, R=H
τ_{MLCT} = 16 ps
$[Fe(cpbmbi)_2]^{2+}$, R=CO_2H
τ_{MLCT} = 26 ps

$[Fe(pzbhbi)_2]^{2+}$
τ_{MLCT} = 32 ps

Figure 15. Structures and MLCT lifetimes of a) **$[Fe(cpbmi)_2]^{2+}$**, b) **$[Fe(pbmbi)_2]^{2+}$**, b) **$[Fe(cpbmbi)_2]^{2+}$** and c) **$[Fe(pzbhbi)_2]^{2+}$** complexes.

Furthermore, Gros and Haacke attempted both MLCT stabilization and MC destabilization within a series of azine-modified ferrous complexes.[54] As a result of a judicious design combining pyrazine and benzimidazole units, **$[Fe(pzbhbi)_2]^{2+}$** (pzbhbi=(pyrazine-2,6-diyl)bis(1-hexyl-benzimidazol-2-ylidene)) attained a ^{3}MLCT lifetime of 32 ps, which is the actual record for NHC-based Fe(II) complexes (Figure 15c). Apart from the electron accepting character of the tridentate ligand, an essential role was attributed to the hexyl chains since it has a double action; at first the hexyl chains can interact with the diazine rings of the other ligand, this interaction may hinder the puckering motion and thus structural relaxation. At second, it can shield the complex to reduce the ligand-solvent interaction, diminishing the dynamic solvation and preventing a faster relaxation.

Bauer and coworkers showed that increasing the number of NHC groups coordinating the Fe center leads to a destabilization of the MC states (HOMO), as well this leads to a destabilization of the π^* orbitals (LUMO) due to the lower number of pyridines coordinated.[55] Moreover, a clear correlation between the ^{3}MLCT lifetime and the number of Fe-NHC bonds was found. While one and two NHC donors led to ^{3}MLCT lifetimes below 100 fs, the ^{3}MLCT reached 3.6 ps and 8.1 ps with three and four NCH units, respectively. However, Bauer and Heinze later probed that only 2 NHC are enough to achieve comparable lifetimes (9.2 ps) on improving the M–L interaction (Figure 16).[56] They used a tripodal CNN ligand dpmi (dpmi=(di(pyridine-2-yl)(3-methylimidazol-2-yl)methane)) with 6-membered chelated rings with in the complex **$[Fe(dpmi)_2]^{2+}$** leading to close to 90° bite angles enhancing iron-ligand orbital overlap.

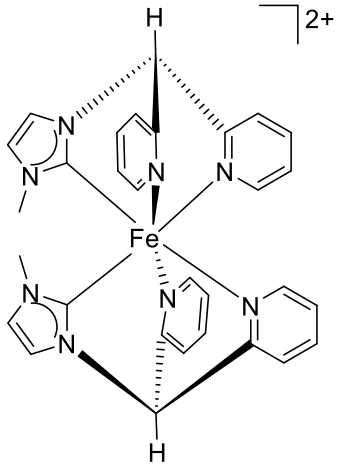

[Fe(dpmi)$_2$]$^{2+}$
τ_{MLCT} = 9.2 ps

Figure 16. Structure and MLCT life time of **[Fe(dpmi)$_2$]$^{2+}$** complex.

Other attempts to increase even more the ligand field splitting with other types of carbenes have been made. For instance, mesoionic carbenes (MICs) have a stronger σ-donor character and better π-accepting capability thanks to their structure and increased number of N atoms in its structure.[57–59] In this regard, the groups of Sundström, Wärnmark and co-workers coordinated the mesoionic ligand btz (btz=3,3'-dimethyl-1,1'-di-*p*-tolyl[4,4'bis-(1,2,3-triazol-5-ylidene) to **Fe(bpy)Cl$_2$**, affording the heteroleptic complex **[Fe(btz)$_2$bpy]$^{2+}$** with a ^{3}MLCT lifetime of 13 ps (Fig 17a).[60] These authors described as well the corresponding homoleptic complex **[Fe(btz)$_3$]$^{2+}$** (Fig 17b). As a result of the very strong coordination sphere due to the 6 carbene units, an impressive ESL of 528 ps was obtained for the ^{3}MLCT state, being still one of the longest achieved so far for a Fe(II) complex.[61] Bauer's group included this 1,2,3-triazole-based MIC in a tridentate ligand with a pyridine unit in the middle. The resulting complex **[Fe(btp)$_2$]$^{2+}$** (btp=4,4′-(pyridine-2,6-diyl)bis(1-ethyl-3-methyl-1,2,3-triazol-5-ylidene)) exhibited a comparable ^{3}MLCT lifetime to **[Fe(btz)$_2$bpy]$^{2+}$**, which could be regarded as a geometrical isomer of the former (Figure 17c).[62]

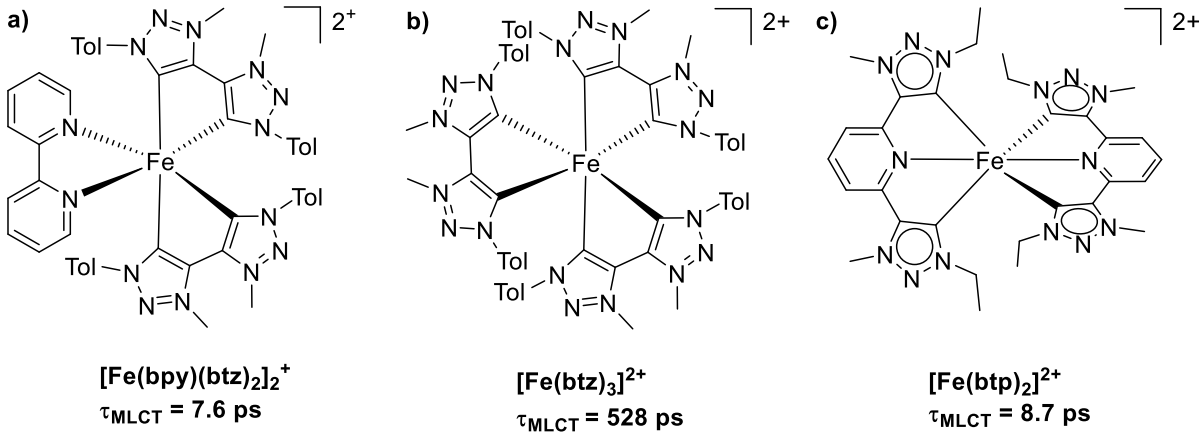

Figure 17. Structures and MLCT lifetimes of **[Fe(bpy)(btz)$_2$]$^{2+}$, [Fe(btz)$_3$]$^{2+}$**, and **[Fe(btp)$_2$]$^{2+}$** complexes

A different way for extending the ^{3}MLCT lifetimes can be achieved by introducing additional chromophore units on the coordinating ligands,[63] as successfully applied for Ru(II)[64] and Cu(I)[65] complexes. The presence of close-lying excited states from the chromophore (^{3}Chrom) allow for a thermal equilibrium with the ^{3}MLCT state, acting as a reservoir for the excitation energy and contributing to slow down the excited state relaxations. In the case of Fe(II) complexes, a theoretical study of octahedral NHC-based complexes bearing an anthracene at 4 position of the central pyridine, connected by different linkers as electron acceptor unit was carried out by Monerris *et al* (Figure 18).[66] These authors predicted the lowest energy triplet state to be localized on the anthracene. Depending on the spacer the absorption capacities increases or decrease. Among the spacers, the alkynyl one allows a large pi-delocalization over the NHC ligand and anthracene. Thus it may act as an energy reservoir for an excited state population delaying the excited-state decay of the complexes, leading to possible extended excited-state lifetimes and enhanced luminescence.

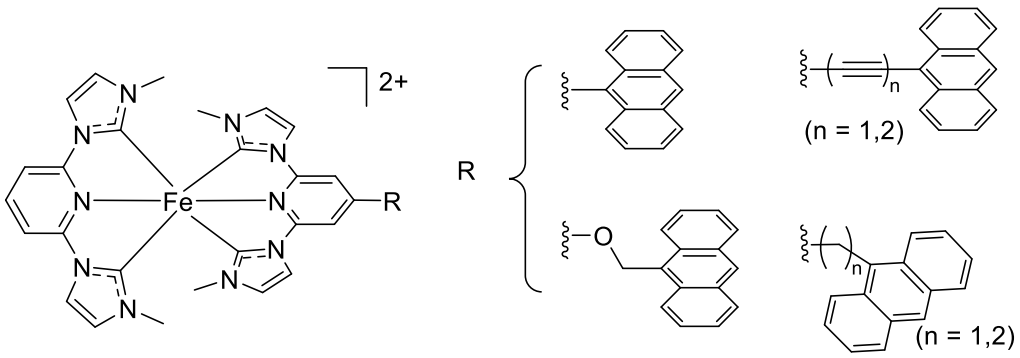

Figure 18. Structures of different Fe(II) heteroleptic complexes with different spacers linked to anthracene.

To experimentally explore this concept, Bauer and co-workers reported two complexes **[Fe(bim-ant)$_2$]$^{2+}$** (bim-ant=(4-anthracene-2,6-diyl)bis(1-methylimidazol-2-ylidene)) and **[Fe(bim-pyr)$_2$]$^{2+}$** (bim-pyr=(4-pyrene-2,6-diyl)bis(1-methylimidazol-2-ylidene)) (Figure 19).[67] Unfortunately, no electronic reservoir was observed by equilibrium between ^{3}MLCT and ^{3}Chrom, with both complexes presenting ^{3}MLCT lifetimes ≈ 13 ps. Nevertheless, an antenna effect from ^{1}Chrom to the ^{1}MLCT via internal conversion (IC) was reported.

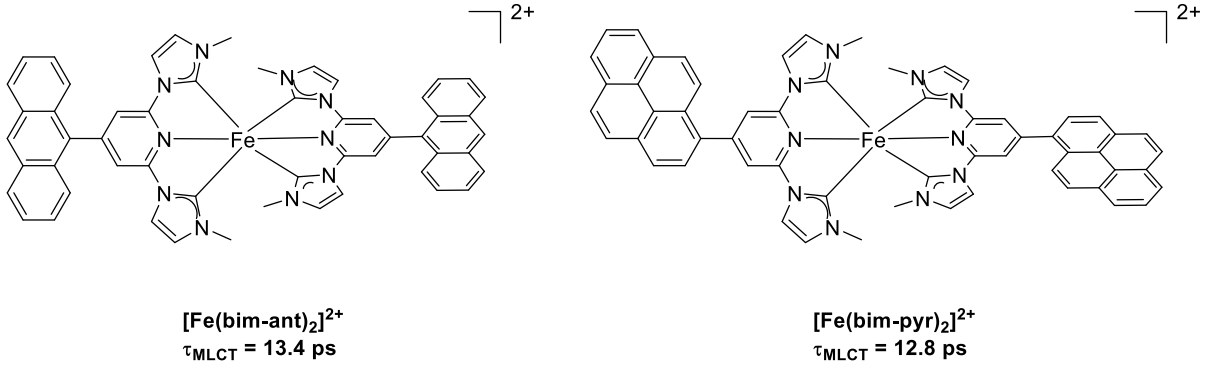

Figure 19. Structure and MLCT lifetime of **[Fe(bim-ant)$_2$]$^{2+}$** and **[Fe(bim-pyr)$_2$]$^{2+}$** complexes.

Alternatively, Dixon and co-workers reported in 2015 a theoretical investigation of the effects of cyclometallating ligands on the photophysical properties of Fe(II) complexes as an alternative to NHC ligands.[68] Interestingly, a possible inversion of the ^{3}MC and ^{3}MLCT states was predicted with tridentate phenyl-bipyridine C^N^N ligands where a double cyclometallation is possible. Additionally, the ^{5}MC states are not be populated in the relaxation

cascade. Experimentally, Bauer and co-workers initially reported a mono-cyclometalated polypyridine Fe(II) version, **[Fe(pbpy)(tpy)]$^{2+}$** (pbpy=6-phenyl-2,2′-bipyridine) (Figure 20a).[30] This mono-cyclometalated complex yielded a ^{3}MLCT lifetime of 0.8 ps, which represents a significant increase compared to **[Fe(tpy)$_2$]$^{2+}$** (145 fs), demonstrating its beneficial effect. However, the photophysical characterization revealed that single cyclometallation is no sufficient to reverse the ^{3}MC-^{3}MLCT, and only a long-lived ^{3}MC state (12 ps) was found to be populated in the relaxation cascade.

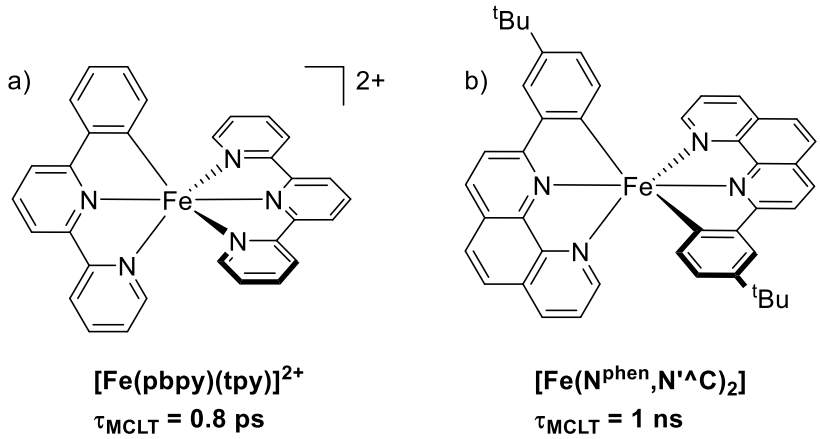

Figure 20. Structure and MLCT life time of a) **[Fe(pbpy)(tpy)]$^{2+}$** and b) **[Fe(N^{phen}N'^C)$_2$]** complexes.

Berkefeld and co-workers succeeded in synthesizing the complex **[Fe(N^{phen}N'^C')$_2$]** with two cyclometallated units (Figure 20b).[69] The phenylphenanthroline-derived complex has a strong-field that promotes an MLCT ESL of 1 ns in solution and an outstanding 2.4 ns ESL in the solid state, experimentally proving the computational investigation of Dixon and co.

I.2.4 HOMO inversion

The concept of HOMO inversion, introduced by Jakubikova and co-workers in 2017, was initially conceived to improve the light-absorption properties of Fe(II) species.[70] This theoretical work clearly highlights the importance of the π-donation properties of the ligand. As previously stated, in Fe(II)-polypyridine complexes, the HOMO possesses a metal-localized

t_{2g} character with lower-energy π orbitals (Figure 21, left). Introduction of π-conjugated donor groups entails the destabilization of ligand-centered π orbitals up to about the t_{2g} level, favouring their mixing and resulting in a mixed-character (p+d) HOMO (Figure 21, centre). Further destabilization of π orbitals can lead to invert the order with t_{2g} metal levels (Figure 21, right) making the HOMO based in the ligand π orbitals.

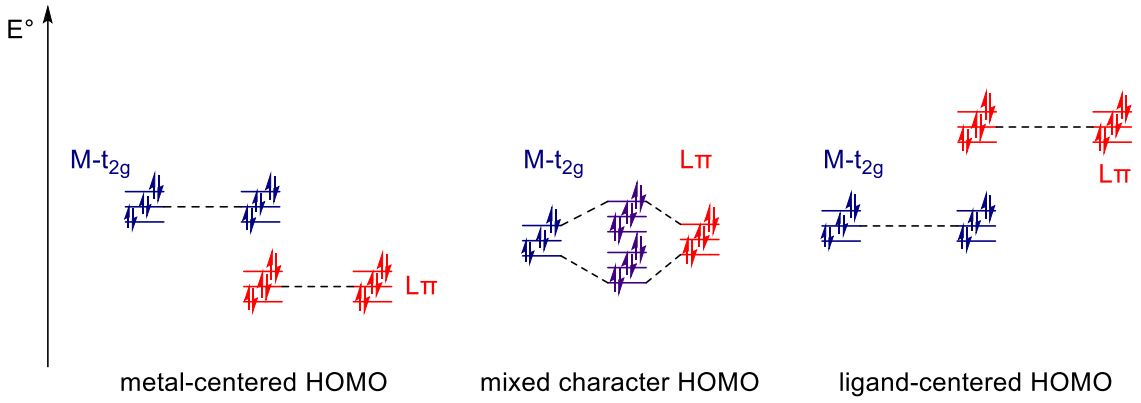

Figure 21. Interactions between Fe centered t_{2g} orbitals with ligand centered π orbitals (HOMO metal-centered, left). Mixed character between Fe centered t_{2g} orbitals with ligand centered π orbitals (HOMO with mixed character, middle). Interactions between Fe centered t_{2g} orbitals with ligand centered π orbitals (HOMO ligand-centered, right). Inspired from reference 70.

This HOMO inversion could lead to a panchromatic absorption in Fe(II) complexes. This was recently experimentally demonstrated by Gros and coworkers reporting a series of complexes with variable number of thiophene moieties, which permit the delocalization of the MLCT states on the ligands resulting in an elongation of excited state lifetimes, an increase the molar extinction coefficient and a panchromatic absorption effect (Figure 22).[71]

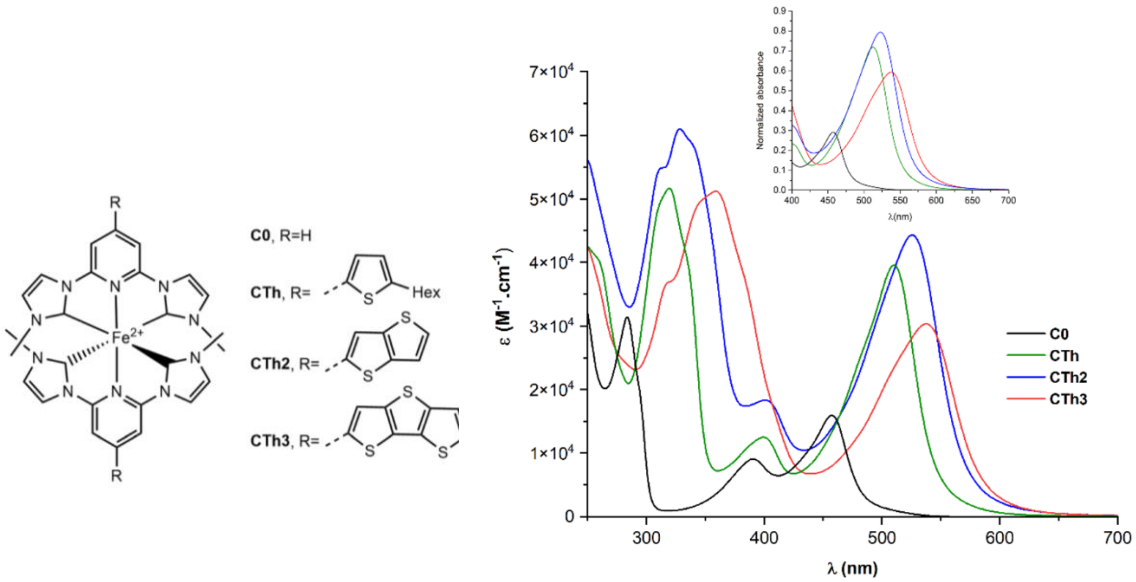

Figure 22. Structures of complexes **C, CTh, CTh2, Ch3** and UV-Vis spectra of complexes in acetonitrile. Inset: normalized absorbance for the lowest energy band. Picture taken from reference 71.

The work of Jakubikova allows us to better understand the work of Herbert and co-workers that designed two complexes by mixing anionic strong σ-donor amido groups with benzannulated N-heterocyclic acceptor units.[72] Interestingly, the complexes **[Fe(pqa)$_2$]** (pqa= phenanthidin-4-yl)(quinolin-8-yl)amido, R= -^{t}Bu or -CF_3) (Figure 23) presented a panchromatic absorption, which correlated well with the idea proposed by Jakubikova. In addition, this remarkable destabilization of the ligand-centered π orbitals also dramatically impacts the excited state relaxation kinetics. Indeed, these complexes exhibit nanosecond charge transfer excited state lifetimes. DFT calculations showed that the HOMO in these complexes has a ligand-metal π antibonding [π*(p+d)] character as a result of a linear combination of the N(2p) lone pair and the filled Fe(t_{2g}) orbitals, which would correspond to the intermediate case represented in Figure 23. Since a high destabilization of the MC states is ensured by the strong σ-donating character of the amido ligands, the orbital splitting results in a panchromatic absorption with contribution from $\pi_{antibonding}$-to-ligand charge transfer (PALCT). Transient absorption spectroscopy (TAS) suggests that the nanosecond CT lifetimes can be attributed to the decay of ^{3}PALCT (τ_{PALCT}= 2.6 ns) which is mixed with MLCT state. It is worth noting that the lifetimes achieved for Herbert are the best so far for Fe(II) complexes.

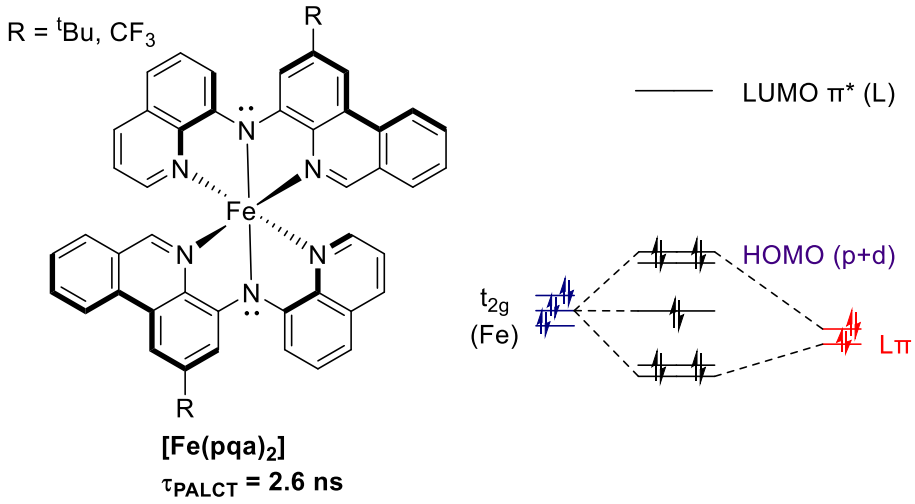

Figure 23. Structure of **[Fe(pqa)$_2$]** complex with excited lifetime and simplified molecular orbital diagram showing a partial HOMO-inversion character by mixing the orbitals metal-based t_{2g} and π ligand orbitals.

I.3 Alternatives to photoactive MLCT Fe(II) complexes

As we have seen, enormous advances have been achieved concerning photoactive Fe(II) complexes, with MLCT ESL attaining even the nanosecond regime. These complexes have proven useful in electron transfer applications (see section §IV.1). However, only the complex reported by Berkefeld exhibits luminescence.[69]

In the search for alternative $3d^6$ MLCT complexes, in 2017, Wenger and co-workers synthesized Cr(0) and Mo(0) complexes with chelating isocyanide ligands: the tris(diisocyanide)-chromium complex **Cr(CN^{tBu}Ar$_3$NC)$_3$**[73] and the tris(diisocyanide)-molybdenum complex **Mo(CNAr$_3$NC)$_3$**[74] (Figures 24a and 24b). The **Cr(CN^{tBu}Ar$_3$NC)$_3$** complex has a low-spin $3d^6$ configuration as a result of a large ligand field splitting provided by the isocyanides. Consequently, the MC states are at sufficiently high energy to avoid non-radiative deactivation process allowing ^{3}MLCT states with lifetime of 2.2 ns, showing phosphorescence emission at room temperature with an emission quantum yield of $\varphi_{em}=10^{-5}$. This lifetime is long enough to allow energy transfer reactions from the ^{3}MLCT state to photon emission by triplet-triplet annihilation up-conversion with anthracene. The Mo^0 complex presents even better properties than its homolog Cr^0 as a consequence of the $4d^6$ electronic configuration that confers on it a stronger ligand field than that of the $3d^6$ Cr(0) species. In fact,

the complex **Mo(CNAr$_3$NC)$_3$** presents a ^{3}MLCT lifetime of 225 ns and a phosphorescence quantum yield of φ_{em}=0.045. The oxidation potential of the ^{3}MLCT is -2.5V (vs Fc/Fc$^+$), which makes it a strong photoreductant, even stronger than **[Ru(bpy)$_3$]$^{2+}$** and **Ir(ppy)$_3$**, which are widely used in photoredox chemistry.

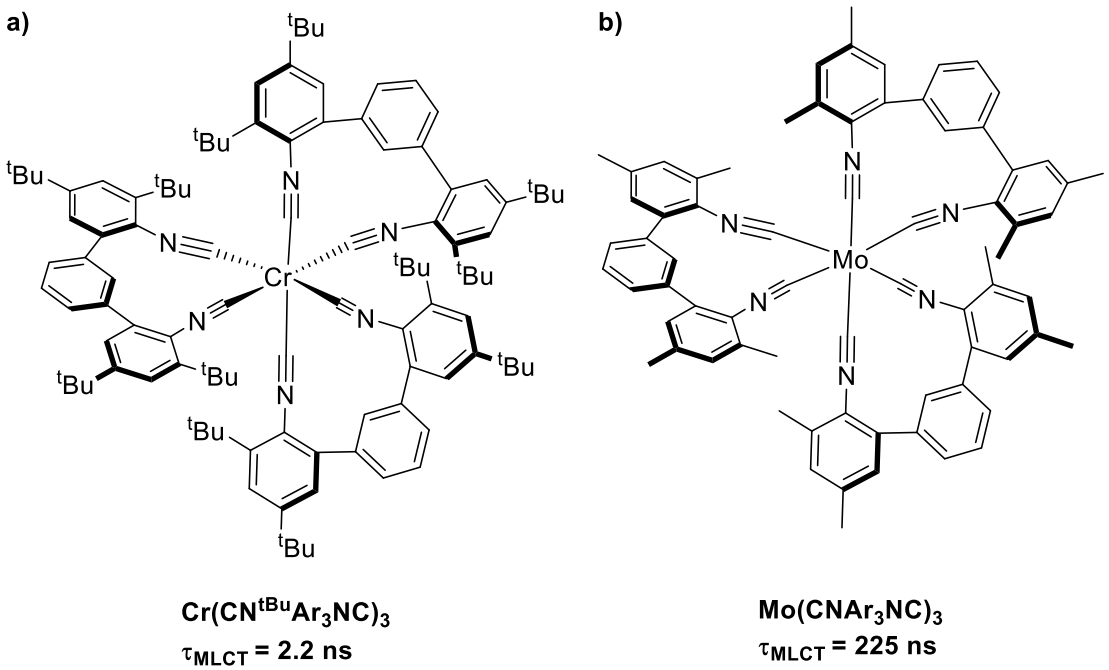

Figure 24. Structures and MLCT lifetime of a) **Cr(CN^{tBu}Ar$_3$NC)$_3$** and b) **Mo(CNAr$_3$NC)$_3$** complexes.

Another example developed by Wenger's group in 2021 concerns 3d^6 Mn(I) complexes with MLCT luminescence in solution at room temperature and photoreactivity.[75] These complexes comprised either bidentate or tridentate isocyanide chelate ligands giving access to air-stable complexes. The complexes **[MnL^{bi}]$^+$** (L^{bi}=2,5-bis(3,5-di-tert-butyl-2-isocyanophenyl)thiophene) (Figure 25a) and **[MnL^{tri}]$^+$** (L^{tri}=5,5'-(2-isocyano-5-methyl-1,3-phenylene)bis(2-(3,5-di-tert-butyl-2-isocyanophenyl)thiophene)) (Figure 25b). Both complexes display phosphorescence with quantum yield of φ=0.05% for **[MnL^{bi}]$^+$** and φ=0.03% **[MnL^{tri}]$^+$** that surpass the isocyanide Cr-complex **Cr(CN^{tBu}Ar$_3$NC)$_3$** (Figure 22a). Complex **[MnL^{bi}]$^+$** has a ^{3}MLCT lifetime of 740 ps and the tridentate version **[MnL^{tri}]$^+$** presents a ^{3}MLCT of 1730 ps both complexes were able to perform photoinduced electron transfer derived for the ^{3}MLCT. Further characterization of the excited states suggests the

existence of a lower energy $^3(\pi$ -$\pi^*)$ state (Figure 25c) which is the responsible for triplet-triplet energy transfer (TTET) observed in presence of triplet quenchers meanwhile the ^{3}MLCT luminescence remained unchanged.

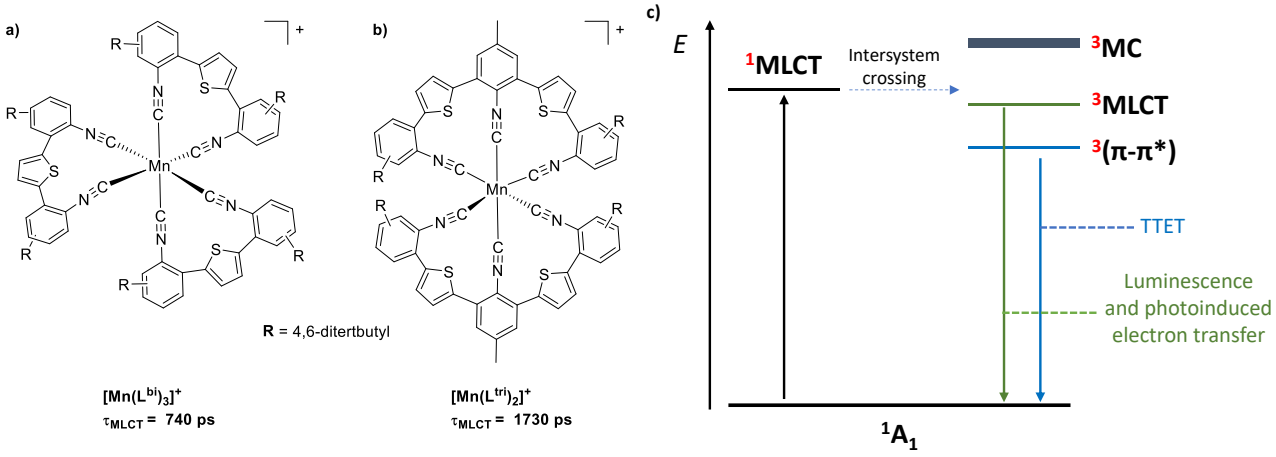

Figure 25. Structures and MLCT-lifetime of a) **[MnL^{bi}]$^+$**and b) **[MnL^{tri}]$^+$** complexes. c) Simplified energy level scheme for **[MnL^{bi}]$^+$**and **[MnL^{tri}]$^+$** complexes with relevant electronic states.

These new isocyanide Mn-complexes contributed to luminescent and photoactive MLCT 3d^6 transition metal complexes. As well they demonstrate that aside MC, MLCT and LMCT excited states, other excited states ($^3\pi$-π^*) can be responsible of luminescence and can undergo bimolecular TTET to substrates, this is unexpected and photochemically relevant. This is a nice step on first-row transition metal complexes besides iron of abundant earth-crust metals, highlighting the fact that the excited states of this group of metals is diverse and we are still discovering it.

As well cobalt complexes have been studied. Zysman-Colman and co-workers described two cobalt(III) complexes bearing tridentate imine σ-donor ligands that featured deep-blue emissions with ^{3}LMCT character (**[Co(L1)$_2$]$^{3+}$**=5.7 ns and **[Co(L2)$_2$]$^{3+}$**=2.31 ns) (Figure 26a).[76] Persson and Wärnmark also reported in 2021 a Co(III) luminescent example, **[Co(PhB(MeIm)$_3$)$_2$]$^+$** (PhB(MeIm)$_3$)$_2$=bis(tris(methylimidazolin-2-ylidene)(phenyl)borate)), bearing an anionic tripodal borate ligand with three carbenes. Most interestingly, the complex

presents a rather unusual microsecond emission (≈0.8 μs) from a ^{3}MC state that can be explained as a consequence of the remarkably strong ligand field (Figure 26b).[77]

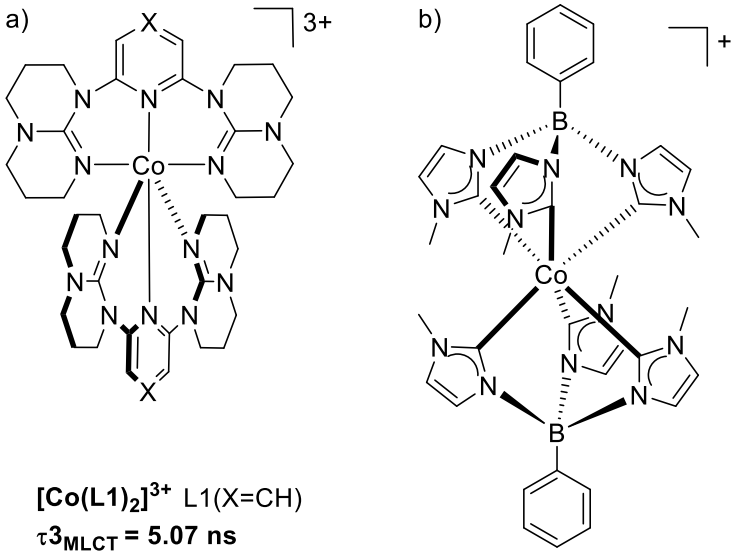

Figure 26. Structures and excited lifetimes of a) $[Co(L1)_2]^{3+}$, $[Co(L2)_2]^{3+}$ and, b) $[Co(PhB(MeIm)_3)_2]^{+}$ complexes.

I.4 Fe(III) complexes

Very recently, remarkable progress has been achieved with Fe(III) d^5 complexes and their photochemical applications, constituting a genuine alternative to previously described Fe(II) d^6 complexes. While essentially having the same frontier molecular orbitals, the partially filled t_{2g} orbitals in low-spin Fe(III) complexes enable low-energy LMCT transitions from a filled ligand π-orbital (Figure 27).[78]

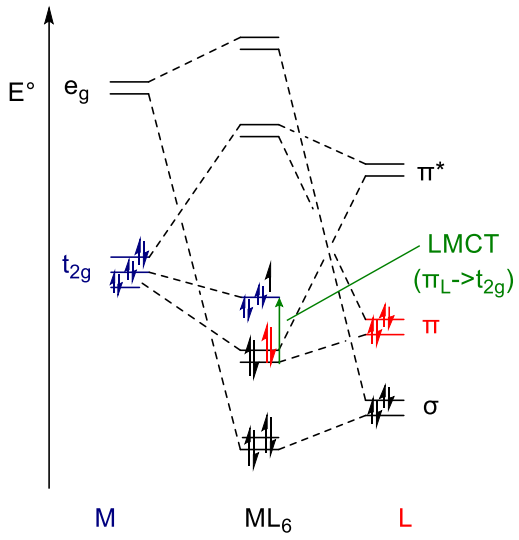

Figure 27. Schematic molecular orbital diagram for a prototype low-spin d^5 complex exhibiting σ- and π-back donation interactions. The green arrow indicates a LMCT transition from a ligand π-orbital to metal-based t_{2g} orbital.

A nice example of Fe(III) d^5 complex is **[Fe(btz)$_3$]$^{3+}$** reported by Wärnmark and co-workers using the ligand btz (btz=3,3'-dimethyl-1,1'-di-*p*-tolyl) (Figure 28a).[79] Even though **[Fe(btz)$_3$]$^{2+}$** presented outstanding photophysical properties,[61] the properties of the Fe(III) analogue are even more interesting. According to Mössbauer spectroscopy **[Fe(btz)$_3$]$^{3+}$** has a low-spin $3d^5$ electron configuration with a $^2T_2$ ground state (Figure 28c). Due to its electronic configuration, the complex **[Fe(btz)$_3$]$^{3+}$** exhibits a LMCT transition with absorption bands peaking at 528 and 558 nm. Excitation of these bands promoted a ^{2}LMCT emission at room temperature with a lifetime of 100 ps and a quantum yield of 3 x 10^{-4} in MeCN becoming the first iron complex that exhibit photoluminescence from a charge transfer state. As for the LMCT state, it presents a weak distortion with respect to the GS, which limits the efficiency of non-radiative relaxation (Figure 28d).

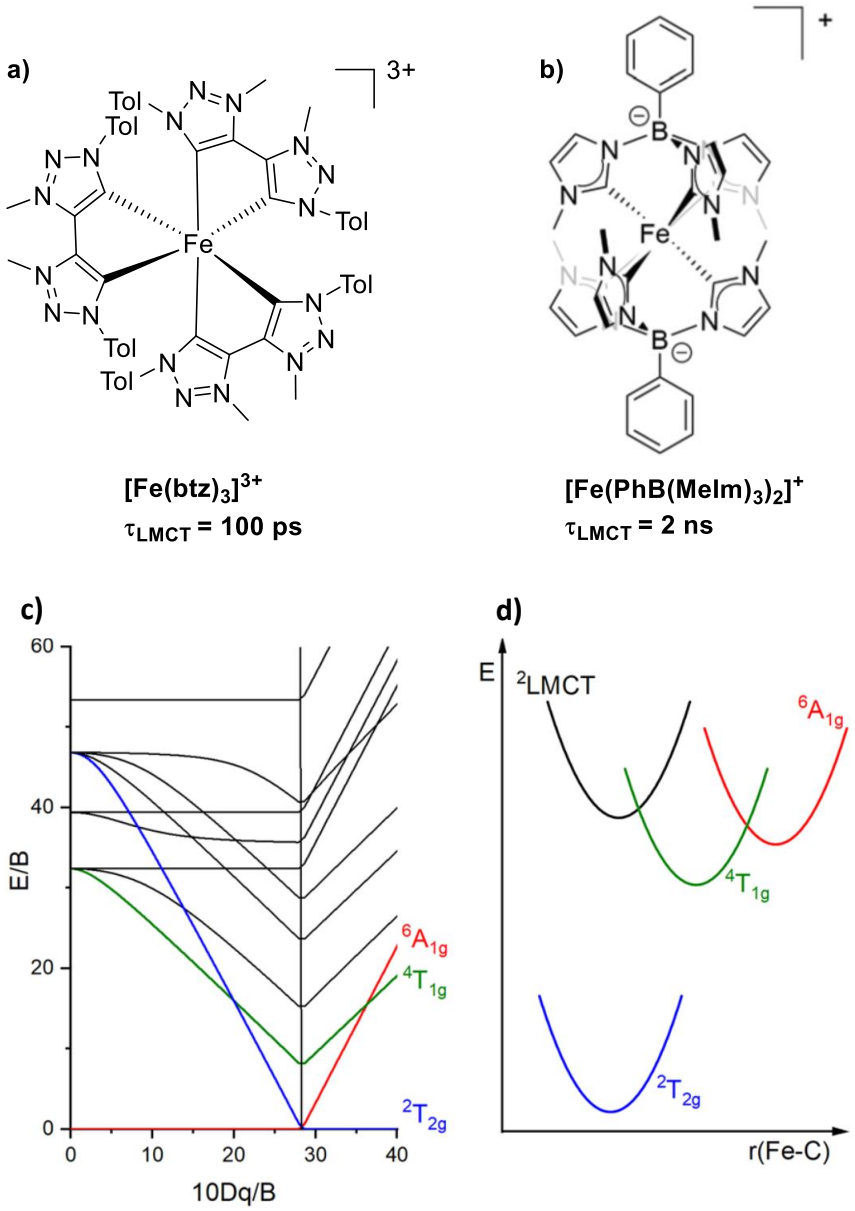

Figure 28. a) Structure and MLCT-lifetime of **[Fe(btz)$_3$]$^{3+}$** complex. b) Structure and MLCT-lifetime of **[Fe(PhB(MeIm)$_3$)$_2$]$^+$** complex. c) Tanabe-Sugano diagram for a d^5 configuration octahedral ML_6 complex. d) Simplified potential energy surface diagram with relevant electronic states for a d^5 configuration octahedral FeL_6 complex. Taken from reference 20.

The same group described shortly after in 2018 another example of a photoluminescent Fe(III) complex, **[Fe(PhB(MeIm)$_3$)$_2$]$^+$**, on coordinating the previously mentioned NHC-based borate ligand (Figure 28b).[80] This complex presents a room temperature photoluminescence from a ^{2}LMCT state with a lifetime of 2.2 ns and a quantum yield of 2%. The anionic nature of the ligand combined with a nearly perfect octahedral NHC coordination and a good metal-

ligand orbital overlap account for these impressive results. With respect to **[Fe(btz)$_3$]$^{3+}$**, the MC states ($^4T_{1g}$ and $^6A_{1g}$) in **[Fe(PhB(MeIm)$_3$)$_2$]$^+$** are pushed to higher energies, reducing the ISC from the ^{2}LMCT to the ^{4}MC and ^{6}MC states (Figure 28d). In addition, **[Fe(PhB(MeIm)$_3$)$_2$]$^+$** in the ^{2}LMCT excited state is a strong oxidant and reductant with excited state redox potentials of $E_{1/2}$*([Fe^{III}]*/[Fe^{II}]) = 1.0 V and $E_{1/2}$*([Fe^{IV}]*/[Fe^{III}]*) = -1.29V. As a result, this complex has been employed in several photochemical investigations, raising the prospect of applying Fe-complexes as an truly sustainable alternative to Ru(II) polypyridines complexes.[81,82]

I.5 Use and application of photoactive molecules

Thanks to the reactivity of photoactive molecules with light they can be used in several fields by generating ES that lead to radiative first-order decays such as fluorescence or phosphorescence. When the ES lifetimes are long enough, the molecules can be engaged in second-order processes with other entities such as charge transfer or chemical reactions as in the case of the so-called photosensitizers. Indeed, it is worth saying that electronic ES are much more reactive and with drastically altered properties in comparison to the corresponding GS. Thus, the coupling of appropriate excited states with appropriate partners can lead to applications in various fields, which range from dye-sensitized solar cells, photochemical catalysis, and phototherapy among others. The next part we detail the most relevant applications.

I.5.1 Dye-sensitized solar cells (DSSCs)

Dye-sensitized solar (DSSCs) are considered good candidates for the next generation of photovoltaic technologies.[83] These devices are easily fabricated and offer multiple possibilities for modulation. Since the seminal work of Grätzel and O'Regan in 1991,[84] the design of DSSCs has attracted tremendous research interest, improving their efficiency up to a certified 13.5%.[85] There are four key components of the DSSCs that can be modified[86] (Figure 29a): **i)** the photosensitizer (or dye), that is aimed at absorbing and converting the solar energy into electrical one, and is chemically bound to the semiconductor; **ii)** the semiconducting

photoanode, where the oxidation takes place, usually made of a mesoporous oxide layer over a glass substrate with a transparent conducing oxide (TCO) layer (commonly titanium dioxide –TiO_2–); **iii)** the redox mediator, which is needed for the dye regeneration -generally the redox couple iodide/triiodie (I^-/I_3^-) solution- ; and **iv)** the counter electrode, with those based on platinum being widely used. Modification of each of the components will have an impact on the final performance of the device. However, due to the mutual interdependence of all four components, optimization of the device performance must be tackled as a whole.[86]

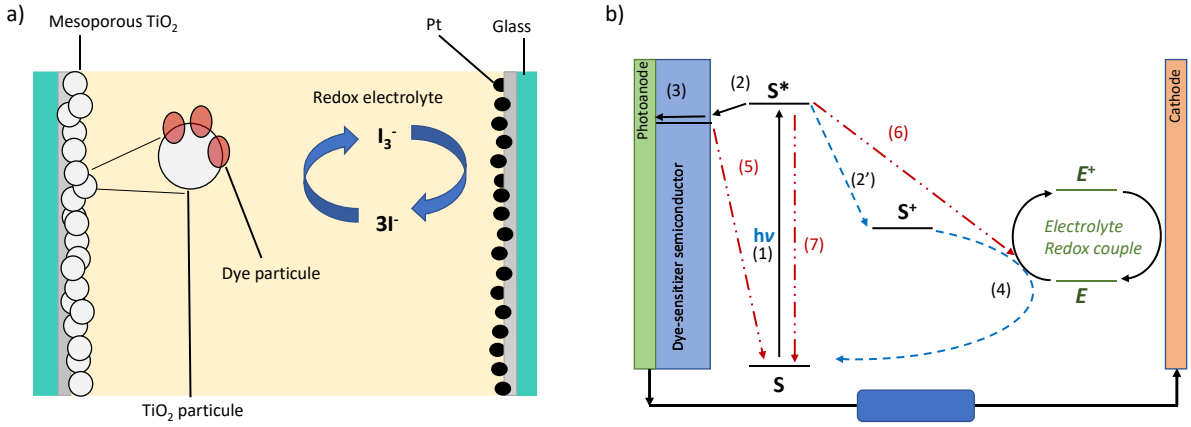

Figure 29. a) Schematic overview of a dye-sensitized solar cell. b) Simplified operating diagram for a DSSC. The basic electron transfer processes are indicated by numbers (1-7).

The operational mechanism of a DSSC[86] begins with the device interacting with light, where the sensitizer (S) is promoted from the ground state to an excited state (S*) (Figure 29b, process 1). After excitation, the excited dye S* injects an electron into the conduction band (CB) of the semiconductor (Figure 29b, process 2) towards the photoanode (Figure 29b, process 3), giving an oxidized dye S^+ (Figure 29b, process 2'). The redox couple reacts with the oxidized dye, thus recovering S in its original form (Figure 29b, process 4). The electronic charge accumulated in the photoanode is transferred to the cathode at which the redox couple is regenerated, thus completing the electric circuit. Since the total electron transfer process in a DSSC is regenerative, the net charge is zero.[86] However, the efficiency of a DSSC depends on the relative energy levels of the components,[86] *e.g.* the chromophore should be prone and able to inject the electrons into the semiconductor. Thus, it is important to note the side mechanisms that lead to the deactivation of the DSSC. Once the electron density that is

generated after injection of electrons from the S* to the semiconductor, the reduction of S^+ can happen by reverse electron donation from the CB (Figure 29b, process 5). Similarly, the charge that is in the CB can interact with the oxidized form of the redox couple (Figure 29b, process 6). Furthermore, the excited chromophore may just simply get relaxed in a non-radiative way (Figure 29b, process 7).

Considering the pivotal role of the dye in DSSCs, great efforts have been made to improve DSSC efficiencies by means of dye optimization. Ruthenium-based dyes are far the most widely studied due to their excellent performances. Already in 1993, Nazeeruddin *et al.*[87] reported the **N3** dye as standard model of efficient charge transfer sensitizer for TiO_2-based DSSCs (Figure 30a). Using N3 as photosensitizer allowed to reach of a photovoltaic efficiency up to 10%, which can be attributed to its absorption from the visible to the near-infrared region. Moreover, **N3** complex shows an efficient photoexcited electron injection into the semiconductor layer via carboxylate anchoring groups. Another remarkable example of the same group is the so-called **"black dye"**, which is a Ru(II) complex bearing thiocyanato and a carboxylated terpyridine leading to an efficiency of 10.4% in a DSSC (Figure 30b).[87] In 2005, these authors reported a partially deprotonated **N3** dye that led to an improved conversion efficiency up to 11.2%,[10,87–89] the so-called dye **N719** (Figure 30c), which has become one of the most common benchmarking dyes for DSSCs.[83,90]

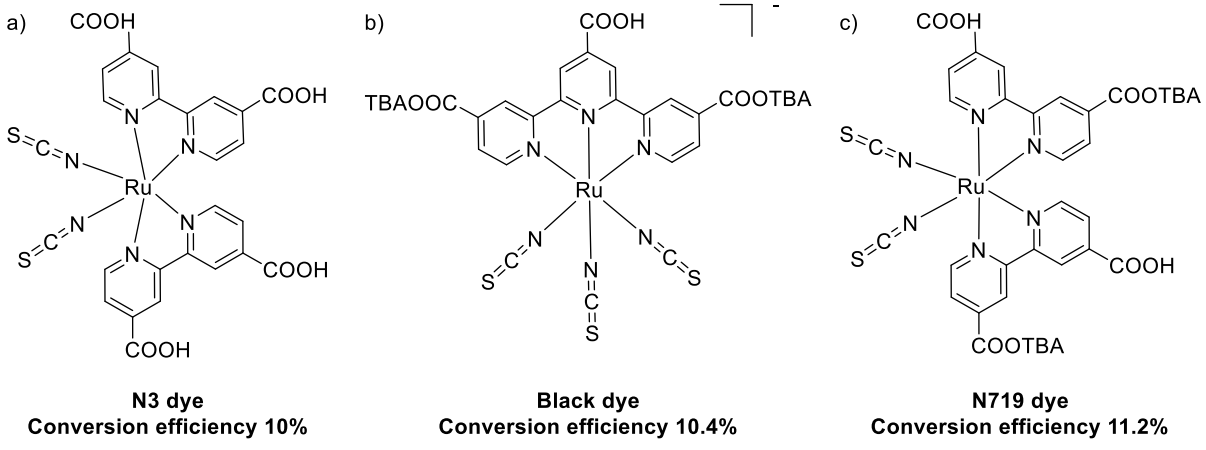

Figure 30. Structure and energy conversion efficiency of a) **N3 dye**, b) **black dye** and c) **N719 dye**. TBA=tetrabutylammonium.

Many efforts focused on the engineering of the DSSCs, by ligand design of the chromophores seeking to improve their efficiency and stability,[91] replacing the anchoring groups by other anions, incorporating like carboxylate, phosphonate or functionalized ancillary groups[92,93] have been reported. Moreover, the efficiency of Ru(II)-based DSSCs has remained unchanged over the past ten years.[83] Even though this kind of DSSCs are stable and reports relatively high efficiency, the complicated synthesis and purification and the high cost of the metals have motivated the development of new types of photosensitizers.

In the case of Fe-based photosensitizers, the group of Gros demonstrated in 2015 the feasibility of the employment of this kind of dyes by reporting the generation of a photocurrent, though very modest (0.13%), with $[\mathbf{Fe(cpbmi)_2}]^{2+}$ under solar irradiation. However, on optimizing the device and the electrolyte, including MgI_2 and GuNCS (guanidium thiocyanate) to improve interfacial charge generation and reducing recombination, a photovoltaic performance of 1% was achieved.[94] Following a computational study to understand and improve the dye-to-TiO_2 electron injection,[95] the authors kept working on heteroleptic dyes to favor a vectorial electronic transfer into the semiconductor.

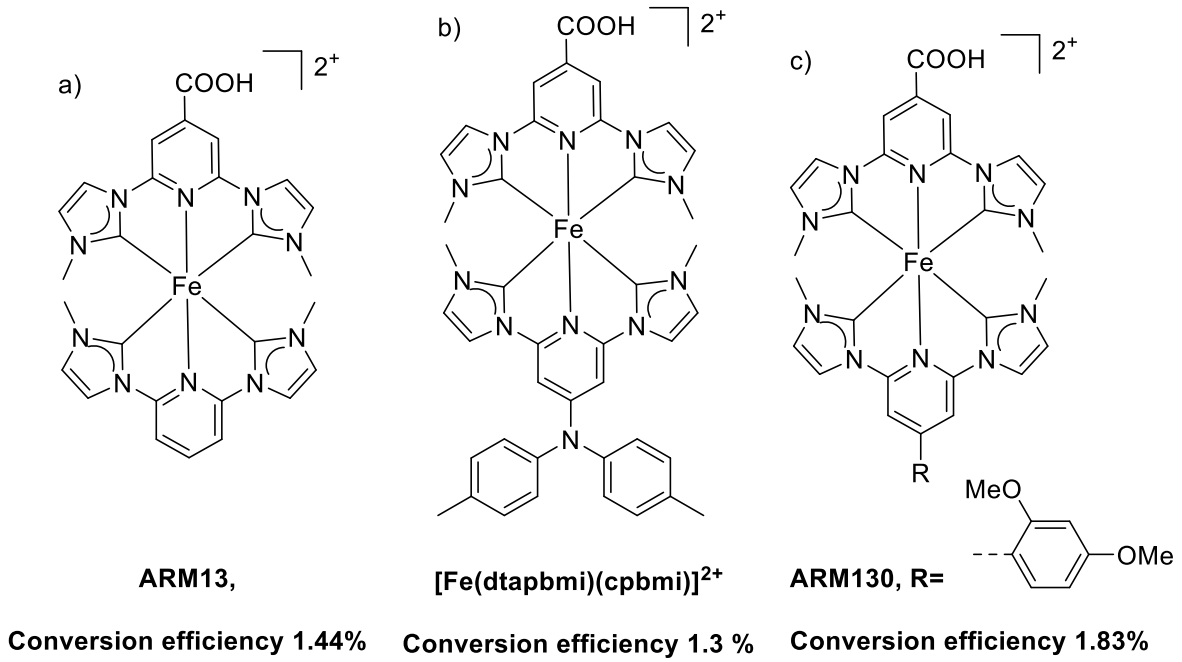

Figure 31. Structure and conversion efficiency of a) **ARM13**, b) **$[\mathbf{Fe(cpbmi)(dtapbmi)}]^{2+}$** and c) **ARM130** complexes.

As a result, **ARM13** reached power conversion efficiency of 1.44%[71] while **ARM130** bearing a dimethyloxyphenyl group in the ancillary ligand reached 1.83%[93], which is the highest performance reported so far (Figures 31a and 31c respectively). It is worth noting that an interesting performance of 1.3% was also reported by the group of Wärnmark thanks to the complex **[Fe(dtapbmi)(cpbmi)]$^{2+}$** (cpbmi=1,10 -(4-carboxypyridine-2,6-diyl)bis(3-methylimidazole-2-ylidene)), dtapbmi=1,10-(4-(di(p-tolyl)amino)pyridine-2,6-diyl) bis(methylimidazole-2-ylidene)) (Figures 31b).[96]

I.5.2 Visible light photoredox catalysis

The term *Photoredox catalysis*, first used by Michael Grätzel et al. in 1982, refers to a type of catalysis system that can accelerate redox reactions by electron transfer between a photocatalyst and an organic substrate, driven by light.[97] To date ruthenium(II)[98] and iridium(III)[99] complexes are the most popular PS due to their intrinsic properties (light absorption in the visible region, long-lived photoexcited states).[24,100]

The principle is the same, after the photosensitizer absorbs a photon in the visible region, an electron of the photocatalyst's on the HOMO t_{2g} metal-centered orbital is promoted to a ligand-centered π^* orbital (MLCT). The ^{1}MLCT goes under ISC to a lower energy ^{3}MLCT state that should be long-lived enough to engage a SET. This photoexcited triplet states has the property of being more oxidizing and more reducing than the ground-state species. As an example, in oxidative quenching the half reaction is described by the reduction reaction **[Ru(bpy)$_3$]$^{3+}$** + e^- -> **[Ru(bpy)$_3$]$^{2+*}$** with reduction potential of -0.81 V ($E_{1/2}^{III/*II}$ vs the saturated calomel electrode (SCE). This means that the excited-state **[Ru(bpy)$_3$]$^{2+*}$** is stronger reductant than the ground-state **[Ru(bpy)$_3$]$^{2+}$** ($E_{1/2}^{III/II}$ = +1.29 V vs SCE).[101] On the other hand, the reduction potential of the excited state **[Ru(bpy)$_3$]$^{2+*}$** + e^- -> **[Ru(bpy)$_3$]$^{+}$** ($E_{1/2}^{*II/I}$ = +0.77 V vs SCE) meaning that this species is a stronger oxidant than the ground state ($E_{1/2}^{II/I}$ = -1.33 V vs SCE).[101] Thanks to these unique properties **[Ru(bpy)$_3$]$^{2+*}$** may proceed either by oxidative or reductive quenching (Scheme 1).[24] This has been exploited in catalysis in redox reactions, C-C bond formations, isomerizations and coupled with other metals to perform several organic transformations.

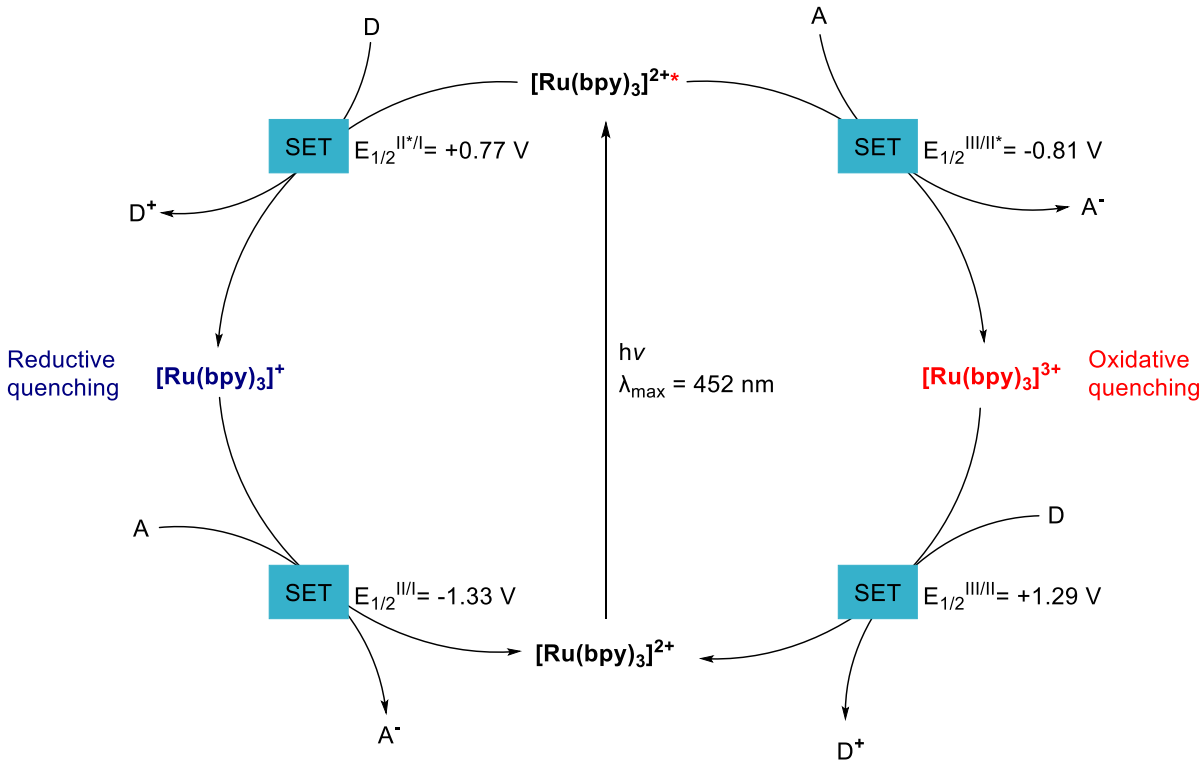

Scheme 1. Oxidative and reductive quenching cycles of **[Ru(bpy)$_3$]$^{2+}$**.

One example, is the merge reaction of photoredox Ru-complex with a high-valent copper catalyst in the trifluoromethylation of arylboronic acids,[102] this reaction is desirable due to the utility of the -CF_3 group in medicinal chemistry. The reaction starts with the excitation of **[Ru(bpy)$_3$]$^{2+}$** complex to generate the excited species **[Ru(bpy)$_3$]$^{2+*}$** that makes a single electron transfer (SET) to oxidize the **Cu^{I}X** to **Cu^{II}X$_2$**, subsequently the reduced **[Ru(bpy)$_3$]$^{+}$** reacts with **CF$_3$I** to form the radical ·**CF$_3$** and regenerate the photocatalyst. Then the **Cu^{II}X$_2$** intermediate is oxidized to **Cu^{II}X-CF$_3$** upon addition of the radical ·**CF$_3$** after those steps a transmetalation occurs between the **Cu^{II}X-CF$_3$** and the phenylboronic acid proceed to give a high-valent aryl-Cu^{III} intermediate, which undergo reductive elimination to forge the aryl-CF_3. In this reaction the photocatalyst serves not only to generate the radical ·**CF$_3$** but also plays an integral role in the oxidation of the copper catalytic cycle via SET (Scheme 2). It is notable the role of both metals since the absence of **[Ru(bpy)$_3$]$^{+}$/CuOAc** or both the reaction is inhibited.

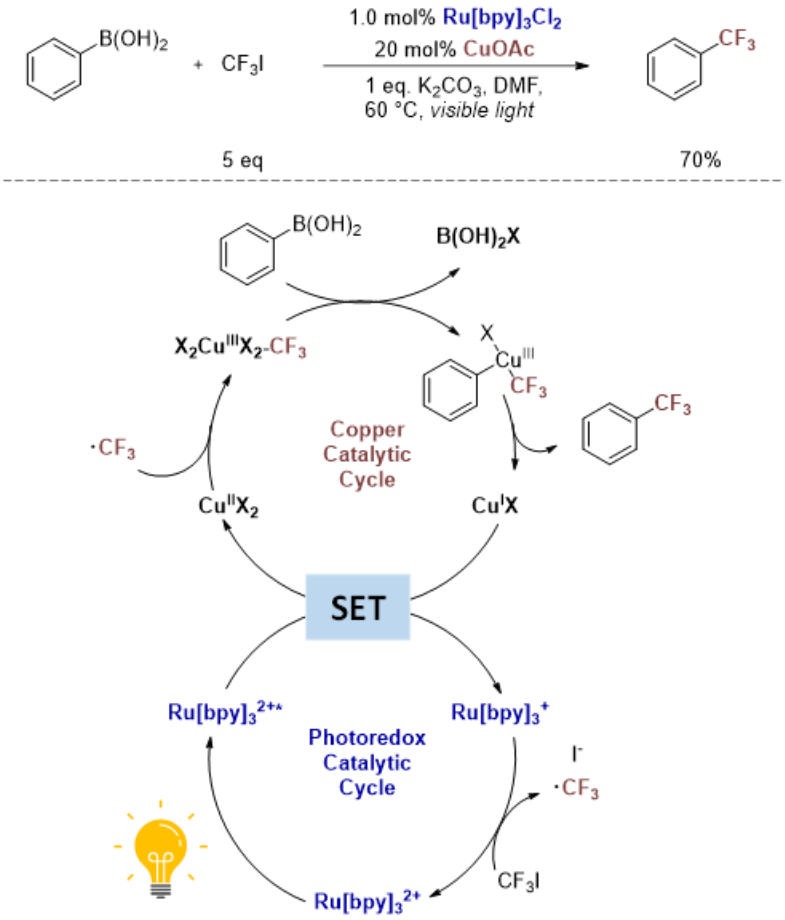

Scheme 2. Dual proposed mechanism in trifluoromethylation reaction via photoredox and high-valent copper catalysis.

Very recently Wärnmark reported a protocol of addition of alkyl halides to alkenes and alkynes using an Fe-based complex as photoredox catalysis.[103] They took advantage of the long-lived excited state of the ^{2}LMCT-,^{3}MLCT-states and $Fe^{3+/2+}$ oxidation states via two-photon mechanisms. So far this is the only report where an iron complex is quenched via charge transfer to the ES. The last years, reports of Fe-based photocatalysts have increased finding more application in catalysis. Yet, there are still several challenges to face in order to replace noble metals. First, most of the excited Fe-complexes presents short excited state lifetimes. Second, most of the reports relay on light-induced electron transfer or atom transfer rather than energy transfer like for the noble metals. Although there is room to improvement to make the 3d earth abundant metals attractive alternatives in this field.[104]

I.5.3 Photodynamic therapy

Photosensitizers can be exploited in the field of medicinal chemistry, as for instance in photodynamic therapy (PDT). This therapy relies on the fact that, upon light irradiation, a photosensitizer absorbs one photon and generates an excited state, which triggers the formation of cytotoxic species such as reactive singlet oxygen ($^1O_2$) and/or other reactive oxygen species (ROS), causing damage in the vicinity of the cell and eventual cell death (Figure 32).[7,105] Importantly, the photosensitizer should be inactive in the absence of light, allowing for a localized activation and a reduction of the possible side-effects. As general requirements of a PS for PDT are: i) a long-lived electronic excited state, which is responsible of the production of the $^1O_2$/ROS, ii) minimal cytotoxicity of the non-irradiated PS iii) accumulation of PS in targeted cells (diseased tissue), vi) absorption of the light in the range of relative tissue transparency (700-1100 nm), v) chemical and photochemical stability, vi) prompt PS clearance from the body. In addition, the PS can undergo two-photon excitation (TPE) using NIR light, in this case, the depth of light penetration is greater and the intra cellular components won't be affected by NIR light.[106] The limitations for two-photon PDT include the lack of optical technology for light delivery.[107]

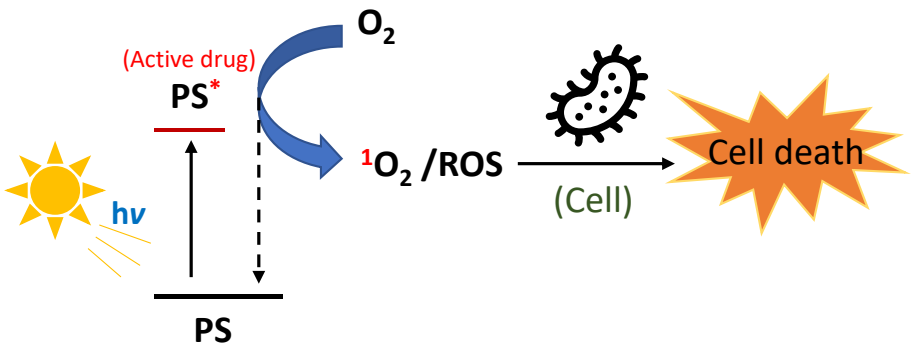

Figure 32. Schematic representation of process and mechanism of PDT. Light irradiation to the PS, formation of active drug (PS*) that produces ROS leading to targeted cell death.

In the 70-80 decades, the research of highly reactive photosensitizers has focused on organic PS like porphyrins, the most popular being Photofrin (HpD) (Figure 33a)[108] Ru-based

transition complexes have recently proved to be effective in chemotherapy treatment. Thanks to established synthetic procedures allowing a rational ligand design, different functions can be tuned, including solubility, charge distribution, cellular uptake efficiency and/or electrochemical properties. In 2015, applying a fine-tuning of the PS properties, the groups of Turro and Gasser disclosed a Ru(II)-based complex **TLD1433** (Figure 33b).[109,110] This compound entered in clinical trials in early 2017.[111,112]

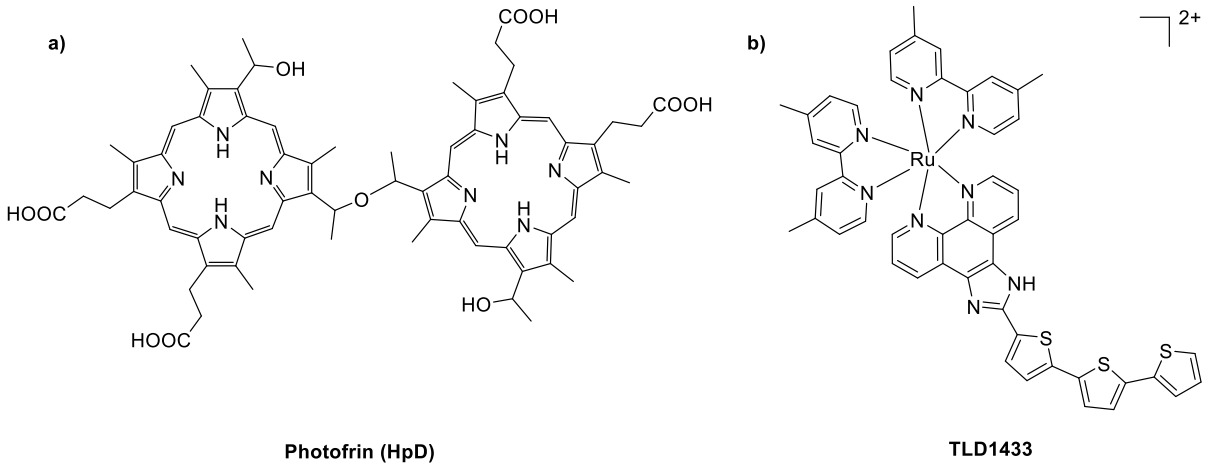

Figure 33. a) structure of **Photofrin**/**HpD** (the actual structure of Photofrin is a complex mixture of ester- and ether-linked dimers and oligomers). b) structure of **TLD1433**.

To date, thanks to their long excited state lifetimes only heavy TM are used has been explored in this field like Ir(III), Os(II), Pt and Re(I) showing that the metal-based PS are promising candidates for PDT.[7] However, there is no record of any Fe-based complexes in this field. This is another reason to keep in the quest of having Fe-based chromophores with excited long lifetimes.

II. Thesis objectives

II. Thesis objectives

As detailed in the introduction, especially during the last decade, there has been a continuously growing interest in developing Earth-abundant metal-based photosensitizers as an alternative to noble metals. So far, the most important advances concern the photophysics of 3d TMC of Cr(0), Mn(I), Fe(II/III) or Co(III) have been achieved, exhibiting long-lived EE of varying nature ranging from MLCT, LMCT, PALCT, or even $^3(\pi\text{-}\pi^*)$ in the case of manganese. The case of iron-based compounds is particularly appealing for low-cost devices and industrial applications since it is the most abundant metal on the Earth crust. As a result, research on photoactive iron complexes continues to stimulate the scientific community due to their particularly challenging ultrafast non-radiative deactivation. While remarkable achievements have been made as it has been previously evocated, systematic studies relating chemical structure and the resulting photophysical properties are still rare. Moreover, most of the reported compounds are cationic complexes bearing tridentate NHC-based ligands. Therefore, this PhD thesis aims at preparing photoactive iron complexes with a controlled coordination sphere and including original ligand motifs in order to rationalize their photophysical properties, providing thus important guidelines for their successful use in energy conversion applications.

This manuscript is divided in three main parts:

- **Bidentate azine-NHC Fe(II) complexes.**

Bidentate ligands instead of tridentate represents an improvement in the interaction between the ligand and the metal, hence a higher destabilization of the MC states could be achieved in order to reduce their deleterious non-radiative EE deactivation. A big challenge that addresses the use NHC-py bidentate ligands in Fe complexes is the non-separable mixture of facial and meridional isomers -Statistically 1:3 *fac:mer* ratio- (Figure 34). Henceforth, development of a selective protocol for a facial and/or meridional isomer is pivotal to study the impact of the geometrical influence in the photophysical and photochemical properties.

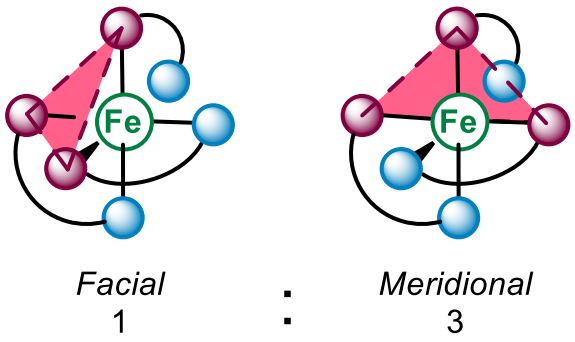

Figure 34. Representation of *fac*-FeL_3 and *mer*-FeL_3 complexes.

- **Fe(III) complexes bearing tridentate anionic ligands.**

In order to increase the lifetime of the excited states the use of strong donor ligands would be applied, whether amides or carbanions will be subject of study in tridentate ligands (Figure 35). Moreover, the possibility of the improvement in the symmetry and interaction between ligand and metal by ligand design. The homoleptic and heteroleptic versions will be tackled.

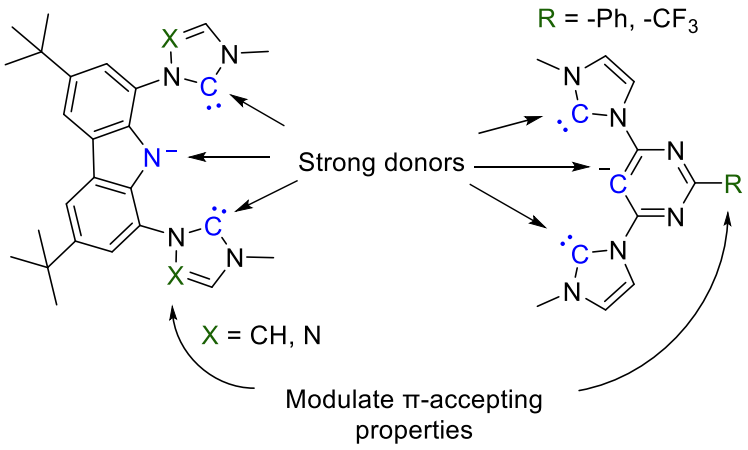

Figure 35. Schematic representation of tridentate anionic ligands

- **Iron complexes as photosensitizers towards H_2-evolving bimetallic photocatalysts.**

In parallel to the fundamental studies developed previously, this last chapter deals with a more target-oriented work. In fact, capitalizing on previous results on photoactive tridentate iron(II)-NHC complexes from our laboratory, and in the frame of a French-German

consortium, we targeted the preparation of Fe-Co dyads as photocatalysts for solar H_2 production. It is desirable that all these compounds, strategies and techniques would be applied to solve a problematic. The problematic addressed will be the search of production of molecular H_2 by using solar light as an energy source. We will design supramolecular, heteroleptic and ditopic catalysts (Figure 36). That would be constituted by a photosensitizer and linked to a catalyst. That further solar irradiation would perform energy transfer from the Fe-chromophore through the liker into the catalyst that will perform the H_2 formation.

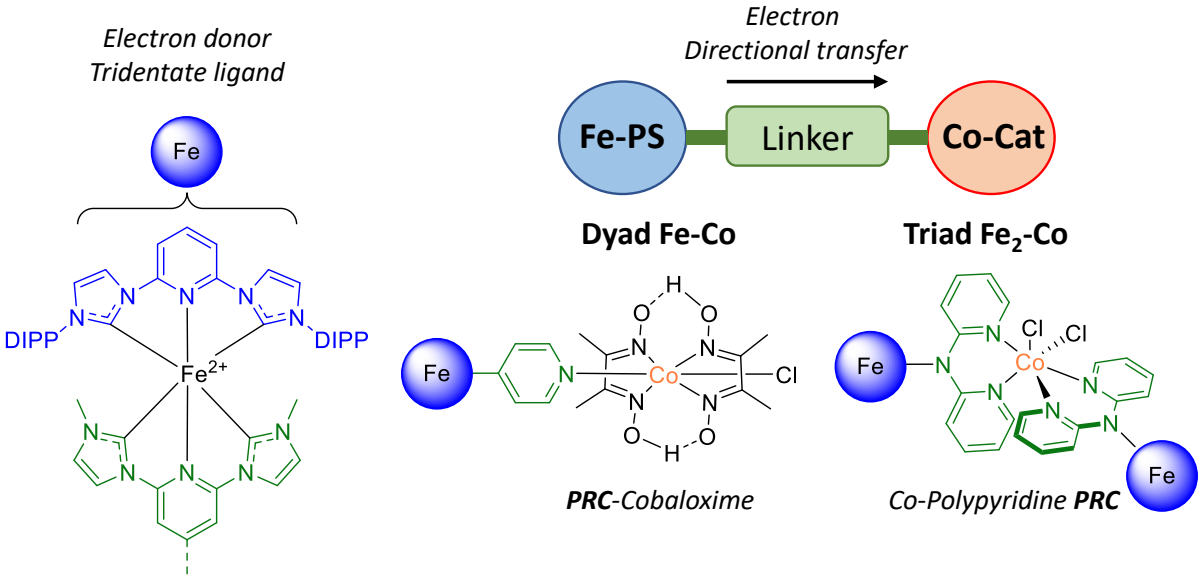

Figure 36. Schematic representation of Fe-L-Co dyads for H_2 production

III. Bidentate azine-NHC Fe(II) complexes

III. Bidentate azine-NHC Fe(II) complexes.

III. 1 Introduction

The stereoselective synthesis of octahedral complexes with unsymmetrical bidentate ligands $M(A\text{^}B)_3$ is attractive due to the intrinsic relationship between molecular structure and resulting properties. Indeed, it is well-known that the coordination of this type of ligands often results in a mixture of facial and meridional stereoisomers in a statistical 1:3 ratio (Figure 37).[113] However, these isomers can have different photophysical, electrochemical and magnetic properties,[114–118] with appealing applications in OLEDs,[114,119,120] catalysis[120,121] or supramolecular chemistry[122–124]. Considering that isolation of these isomers can be extremely challenging,[113] especially in the case of labile complexes, attaining control over the *fac*/*mer* stereoisomerism is thus of great importance.

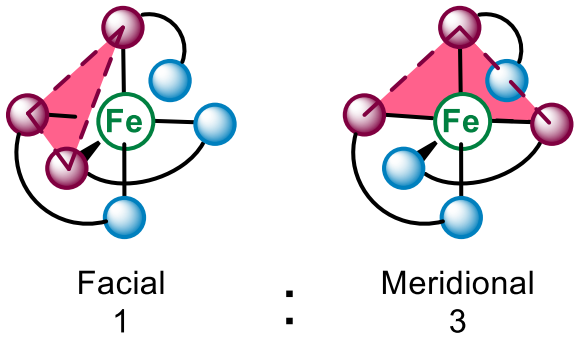

Figure 37. Representation of *fac*-FeL_3 and *mer*-FeL_3 complexes.

Especially in the case where the nature of donor atoms are remarkably different, selectivity towards a specific isomer can be achieved more easily. Among the parameters controlling the stereoisomerism, temperature is frequently used since it does not require any chemical modification of the complexes. In 2003, Thompson reported a synthesis of tris-cyclometalated Ir(III) complexes ($Ir(C\text{^}N)_3$) in which they manage to control the isomerism thorough temperature.[118] The meridional isomers were obtained at low temperature, suggesting that their formation was kinetically favored, the facial isomers were obtained at higher temperatures, indicating a thermodynamic control in this latter case (Scheme 3a).

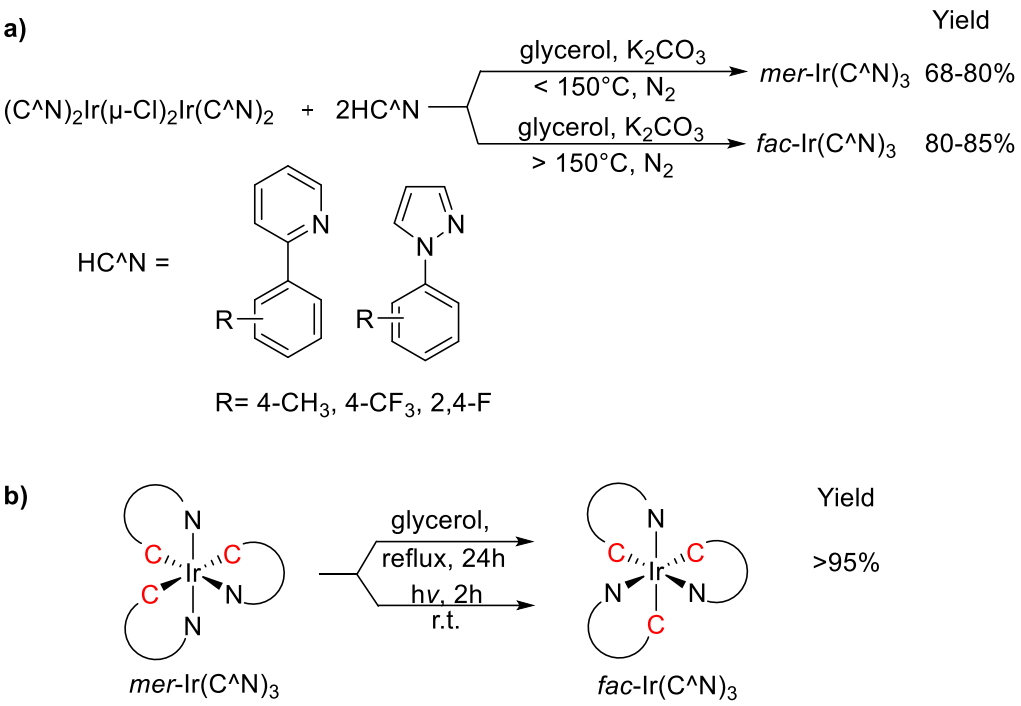

Scheme 3. a) Synthesis of *mer*-Ir(C^N)$_3$ and *fac*-Ir(C^N)$_3$. b) Thermal and light triggered isomerization reactions from *mer*-Ir(C^N)$_3$ to *fac*-Ir(C^N)$_3$.

Once the complexes are formed, isomerization conversions can be performed as well upon heating (with or without acid-base catalysis) or light irradiation.[125] In this regard, the same group reported isomerization reactions from a *fac*:*mer* mixture towards single isomer (Scheme 3b). In particular, the authors succeeded in the *mer*→*fac* isomerization by refluxing the *mer* isomer in glycerol, supporting the idea that the facial isomer is the compound thermodynamically favored. An explanation of this is that the meridional configuration places phenyl groups trans to each other, which has a strong trans-effect and destabilizes the compounds,[126] while in the facial complexes all the three phenyl groups are opposite pyridyl or pyrazolyl groups (Scheme 3b). Interestingly, they also reported the *mer* → *fac* isomerization by photochemical conversion using an UV lamp for 2h at room temperature.

Other factors such as steric or additional intra-/intermolecular interactions can further modulate the *fac*/*mer* ratio, with effects that can largely counterbalance that of the trans-effect, especially in the case of bidentate ligands composed of similar coordinating units,[127] Scott in

2011 reported a nice example where intermolecular interactions rules the stereoisomerism.[128] Facial Fe(II)-complexes are obtained thanks to inter-ligand π-π stacking interactions between phenyl and pyridine moieties. As well, they reported the same results for other metals like Mn(II), Co(II/III), Ni(II) and Zn (II) (Figure 38).

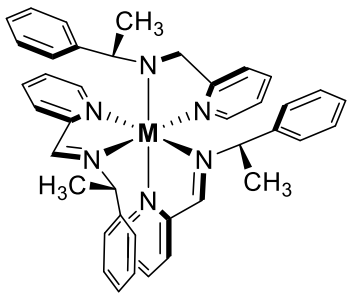

fac-$[ML_3]^{2+}$

M = Fe(II), Mn(II), Co(II/III), Ni(II), Zn(II)

Figure 38. Structure of *fac*-$[ML^3_3]^{2+}$.

Alternatively, the template strategy has been used also for aligning non-symmetric ligands around a metal center.[129,130] In 1998 Weizman three tethered bipyridine units to a benzene scaffold using ester linkages, giving at the end a tripodal ligand.[131] After coordination with Ru^{III}, the ester was hydrolyzed affording a tris-bidentate **2-Ru-D** complex with a facial ligand orientation (Scheme 4). This kind of strategy is very useful for so-called "inert" late transition metal with diimine ligands. This strategy takes relevance when the metal ion belongs to the first-row transition due to their higher lability. Thus, the formation of a (hemi)cage complex impedes the rapid equilibration *fac*-*mer* in solution.

A different strategy to isolate either *mer* of *fac* complex can relies upon either selective crystallization or differential solubility.[127] Although either form can be favored in some cases, a dual action of the anion and solvent permitted selective isolation of fac isomers.[132]

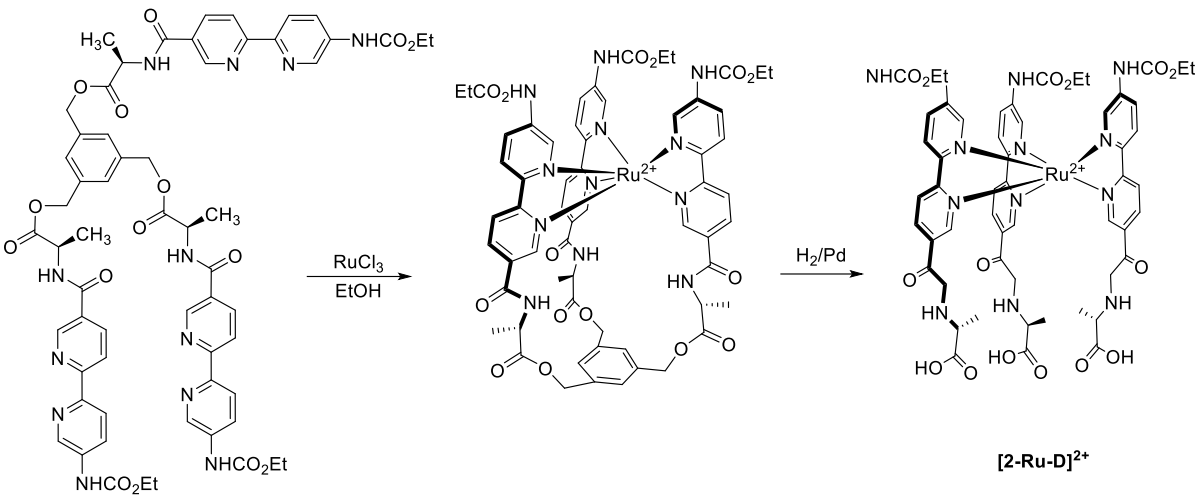

Scheme 4. Synthetic procedure to **[2-Ru-D]**$^{2+}$ complex using a template ligand.

Recently Nabeshima and co-workers reported a *fac/mer* isomerization with tripodal ligands, where they revealed that the *fac:mer* ratio depends on the solvents.[123] Interestingly, the solvent-dependent selectivity does not relies on the counteranion, metal center and the substituents on the bipyridine (Table 1). In this contribution solvation plays an important role in supramolecular systems that adapt their structures in response to the environmental change. They conclude that the dispersion term δ_d of the Hansen solubility parameter (HSPs) showed a good correlation with G of the *fac:mer* isomerization.

Table 1. Schematic representation of the interconversion between. Ratios of the *fac:mer* isomers of **[2bFe](TFPB)**$_2$. (TFBP=tetrakis[3,5-bis(trifluoromethyl) phenyl]borate.

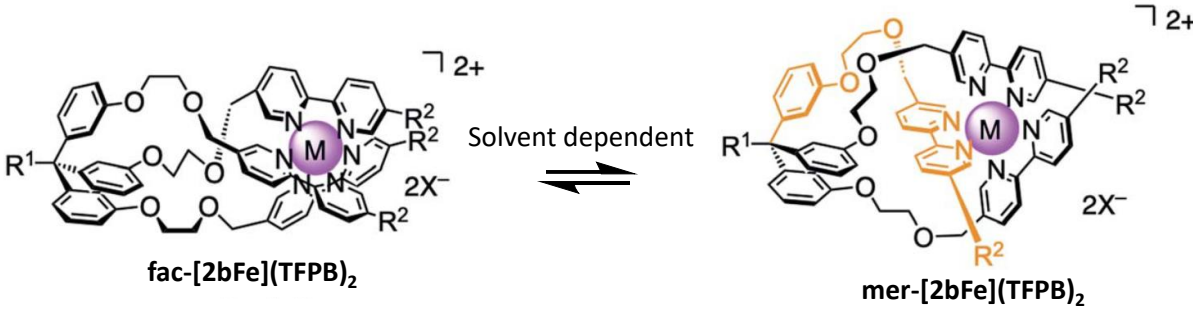

Solvent	TCE-d_2	$CDCl_3$	*o*-DCB-d_4	Dioxane-d_8	DMF-d_7	THF-d_8
fac:mer	10:90	10:90	13:87	20:80	32:68	34:66
Solvent	CD_2Cl_2	CD_3CO_2D	CD_3OD	Acetone-d_6	CD_3CN	
fac:mer	40:60	53:47	64:36	69:31	71:29	

Following the research line of our laboratory dealing with photoactive Earth-abundant metals, iron(II) complexes bearing bidentate pyridyl-NHC were initially studied during the PhD work of Kévin Magra (Scheme 5).[133] Interestingly, these complexes exhibited MLCT excited state lifetimes of up to 20 ps that compare well with those of their tridentate analogs (Figures 14, see §I.2.3) in spite of having one NHC unit less. These results can be interpreted as a result of the better M–L interaction afforded by the bidentate ligands, highlighting their interest to afford photoactive iron complexes. However, the asymmetry of these bidentate ligands resulted in the formation of *fac*/*mer* complexes. For instance, in the case of the ligand reference (Scheme 5) comprising pyridine-imidazol-2-ylidene ligands (**L0**/**C0**), a 1 *fac* to 14 *mer* ratio was obtained.[134] In sharp contrast to typical Fe^{II} complexes, no lability was observed for this kind of complexes. Unfortunately, it was not possible to isolate these geometric isomers. Therefore, molecular modeling was chosen to offer some insights into the photophysical properties of these distinct species, particularly regarding their excited state properties. These results showed that, upon electronic excitation, the meridional configuration leads to faster relaxation kinetics, resulting in shorter excited state lifetimes than the facial isomer.[134]

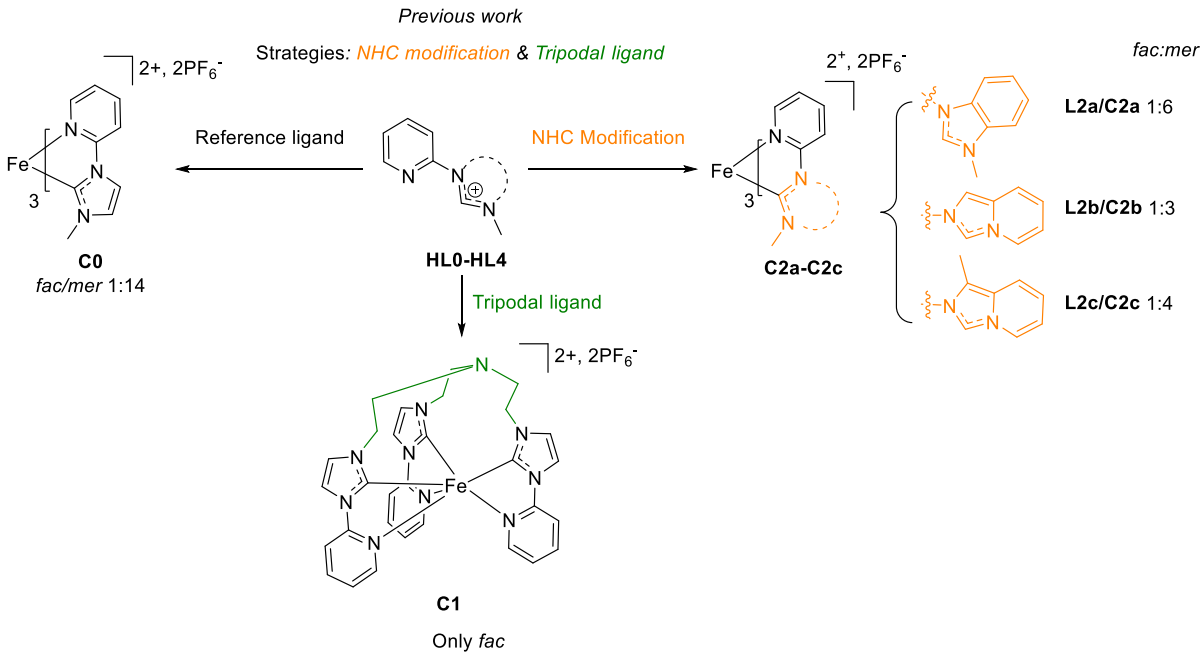

Scheme 5. Overview of previous ligand designs explored in the group and their impact on the *fac*/*mer* ratio of the corresponding iron(II) complexes.

Prompted by these results, an alternative strategy was selected to favor facial coordination. This geometry was nicely achieved by means of the tripodal ligand afforded complex **C1** thanks to the preorganized bidentate units (Scheme 5).[135] A longer excited-state MLCT lifetime (up to 20 ps) was obtained in comparison to that of the mostly *mer* iron(II) complex bearing **C0** (10 ps), which confirms the crucial role of the *fac:mer* isomerism in the overall decay process. However, the influence of the connecting scaffold and the increased rigidity on the final properties of the facial isomer cannot be ruled out.

In a subsequent study, Kévin Magra selected a series of isomeric bidentate ligands **L2a-2c** with increased π-conjugated systems.[136] The conjugation of the benzannulated ring have a distinct effect on the energies of the frontier orbitals, as reflected in cyclic voltammetry and UV-Vis spectroscopy. Noteworthy, the increased steric demand of the ligands leads to a modification of the stereoselectivity towards higher *fac:mer* ratios respect **L0** (Scheme 5), highlighting the importance of rational ligand design. Taking into account the interesting photophysical properties of pyridine-NHC iron(II) complexes, the necessity of developing a stereoselective methodology for the preparation of these geometrical isomers became clear to us, that would subsequently preclude the isomer isolation issues. To tackle this challenging objective, the synthesis of these complexes was carried out:

i) on modifying the reaction conditions;

ii) upon modulation the stereo-electronic properties of the ligands.

III. 2 Synthesis of Fe(II) complexes with pyridine-NHC ligands.

The prototypical ligand precursor **HL0**, was selected for our first coordination study. Its synthesis was carried out following two steps. First, a nucleophilic aromatic substitution of the *in-situ* generated imidazolate part on the 2-fluoropyridine at 180ºC for 18 h afforded the 2-(1*H*-imidazol-1-yl)pyridine intermediate. The imidazole scaffold was subsequently quaternized with MeI in DMF at 110ºC overnight, and final anion exchange upon addition of aqueous saturated solution of KPF_6 to improve the ligand solubility in organic solvents yielded precursor **HL0** in 70% yield (Scheme 6).

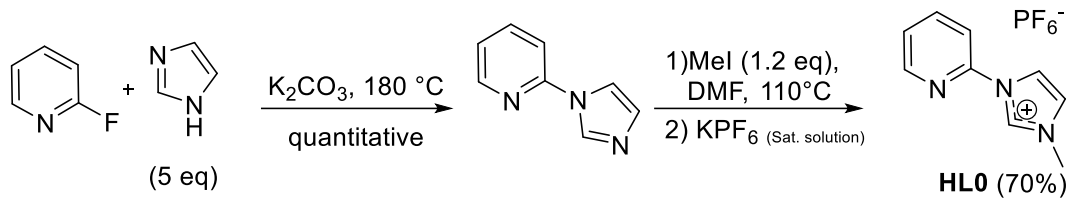

Scheme 6. Synthesis of the ligand precursor **HL0**.

With **HL0** in hand, the complexation conditions previously established in our group (See scheme 7) were applied i.e. the use of $FeCl_2$ as iron source, DMF as solvent and t-BuOK as the base and 1 h of stirring at room temperature under Argon atmosphere (Schlenk). Under these conditions, **C0** was obtained in 40% yield with a 6:94 *fac*:*mer* ratio.

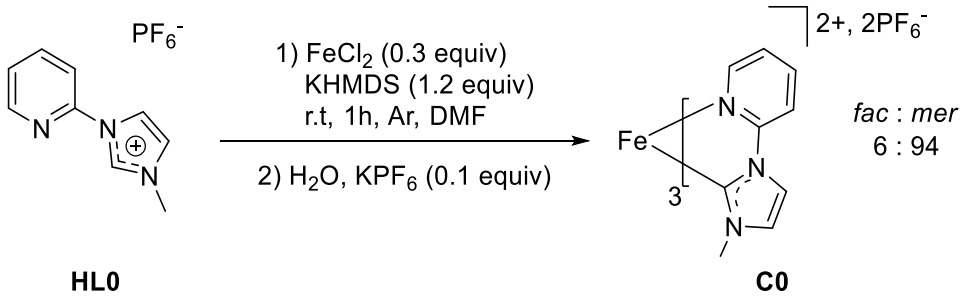

Scheme 7. Reaction conditions for synthesis of complex **C0**.

The ratio between *fac:mer* isomers can be easily determined by comparing the ^{1}H-NMR spectra of **HL0** and **C0**. In figure 28 on top (green) there is the ^{1}HNMR of the ligand precursor **HL0**, and at the bottom that of the complex **C0** (red). After the complexation reaction the proton "**a**" (≈ 9.26 ppm, singlet) corresponding to the proton of the pre-carbenic carbon disappears, signing the formation of the NHC. Then proton "**b**" (≈ 3.96 ppm, singlet) assigned to the methyl group undergoes a high field shift and gets desymmetrized displaying a unique singlet for the facial isomer due to its symmetry and three singlets for the meridional isomer (Figure 39). The peak integration gives a quick access to the *fac:mer* ratio showing here a large preference for the *mer* isomer (6:94).

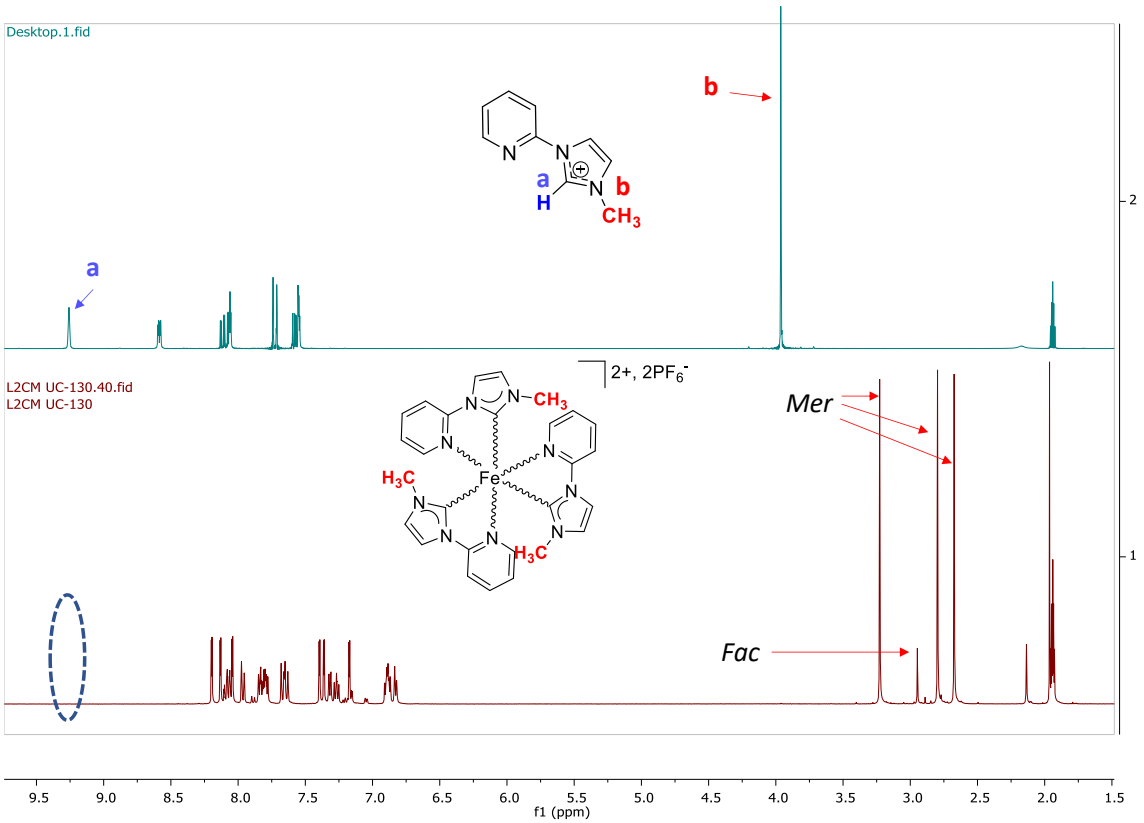

Figure 39. ^{1}NMR spectra of **HL0** (top) and mixture of *fac:mer*-**C0** complex (bottom) in CH_3CN-d_3 (or CD_3CN).

III. 2.1 Modification of the reaction's conditions

From this first experiment favouring almost exclusively the meridional isomer, we moved to the investigation of the impact of the reaction conditions on the selectivity. Several relevant parameters were varied such as the solvent, the base and the reaction temperature. The main results are collected in Table 2.

Table 2. Modification of parameters in complexation reaction conditions.

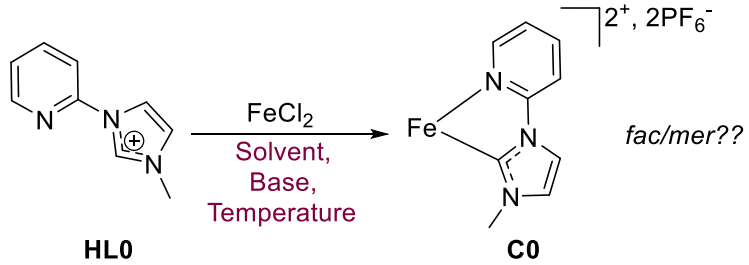

Entry	Solvent	Base	T (°C)	Yield(%)[a]	*fac*:*mer*[b] *(%)*
1	DMF	*t*-BuOK	r.t.	40	6:94
2	Tol	*t*-BuOK	r.t.	No reaction	No reaction
3	THF	*t*-BuOK	r.t.	20	8:92
4	MeCN	*t*-BuOK	r.t.	25	14:86
5	DMSO	*t*-BuOK	r.t.	27	25:75
6	DMF	KHMDS	r.t.	44	25:75
7	DMF	Cs_2CO_3	r.t.	–	–
8	DMSO	KHMDS	r.t.	45	17:83
9	DMSO	KHMDS	180	64	44:56
10[c]	THF	LiHMDS	-20	40	25:75

[a]Isolated Yield; [b]*fac*/*mer* ratio determined by ^{1}H-NMR; [c]Reaction carried at -20°C.prior deprotonation of the ligand with LiHMDS and $FeCl_2$ addition and temperature allowed to reach r.t.

As already mentioned complex **C0** was obtained in 40% yield with a 6:94 *fac*:*mer* ratio (Table 2, entry 1) using $FeCl_2$ as metallic source, *t*-BuOK as base and DMF as solvent, with the reaction being performed at room temperature overnight.[137] We have screened several solvents (entries 2–5). Complex **C0** was obtained in slightly lower yield (20-27%) except when using toluene in which the reaction was inhibited (entry 2). Interestingly, the solvent was found to modify the isomers ratios. In fact, the formation of the more apolar meridional isomer appeared to be less favored in solvents such as CH_3CN or DMSO, yielding a 25:75 *fac:mer* mixture. Changing the base also plays an important role, (entries 1, 6 and 7). While no complex was observed with Cs_2CO_3, the use of KHMDS resulted in an increased facial isomer amount (25:75) respect to that of the reported condition with *t*-BuOK (6:94) (Entries 1 and 6). From these results, combining DMSO and KHMDS was expected to further favour the formation of the facial isomer (entry 8) but a lower *fac:mer* ratio (17:83) was obtained instead. Performing this same reaction at high temperature had the most noticeable impact in the stereoselectivity (entry 9). In fact, mixing the ligand and $FeCl_2$ at 180° for 20 min before the addition of the base

afforded **C0** as a facial-enriched mixture (*fac:mer* 44:56) reinforcing the hypothesis that the facial isomer is indeed the thermodynamic product.

We envisioned that the presence of the carbene unit prior to the addition of the metallic source might have had an impact in the coordination mechanism (entry 10). Indeed, in the previous experiments, the carbene was only formed after a likely initial coordination of the pyridine unit to the metal center. The carbene preformation reaction was carried out in THF at -20°C using LiHMDS as the base, further addition of $FeCl_2$ and stirring for 1h. The coordination resulted in a statistical *fac:mer* ratio with **C0** in 40% yield. An effect favouring facial complex is observed. This can be attributed to the change of the base, as entry 3 where the *fac* percentage increases from 8% to 25%, or to the preformation of the carbene prior to iron addition (entry 10). However, the statistical ratio does not mean that there is no preference for any of the isomers.

Despite of having changed several parameters, we did not succeed in achieving selectivity neither in favour of the *fac* or the *mer* isomers. The reported protocol (Scheme 7) remained the most selective, in this case, towards a meridional configuration. The best selectivity towards the facial configuration were achieved with DMSO as a solvent, KHMDS as a base and at high temperature (180°C), attaining an almost equimolar *fac/mer* mixture. Temperature is an important factor to favour one isomer over another however, total selectivity was not achieved, and it was not a determinant factor as for other metals.[118]

III. 2.2 Isomerization reactions

As stated in the introduction of this chapter, it is possible to convert a kinetic isomer into the thermodynamic one, which frequently corresponds to respectively meridional and facial configurations. Thus, we decided to investigate such *mer* → *fac* isomerization in our case.

The isomerization process was first attempted applying some protocols based on either protic[138] or aprotic acid activation with UV-light.[139] Table 3 shows the results with malonic and trifluoro acetic acids (TFA) chosen as protic acids (HA). **C0** was first solubilized in EtOAc), then the acid was added and the mixture heated at 70°C (Table 3, entries 1–2). Even after 6 days of stirring, we did not observe any change in the *fac:mer* ratio. In the case of aprotic

acid, **C0** was dissolved in CH_3CN-d_3 and SiO_2 was added. Then the mixture was irradiated with UV-light (at 254 and 366 nm)) during 6h at r.t.. No signs of interconversion between isomers could be observed (Table 3, entries 3–4). Of great interest here is the non-lability of the PyNHC ligands in this complex, which is unexpected by comparison with the bipyridine analogue.[113]

Table 3. Isomerization reactions with protic/aprotic acids.

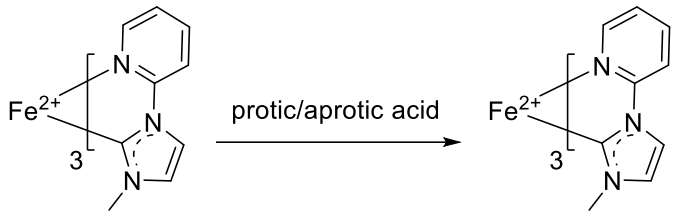

Entry	Conditions	Solvent	Time	After *fac:mer*[a]
1	Malonic acid (10 eq)	EtOAc	6 days	25:75
2	TFA (10 eq)	EtOAc	6 days	25:75
3	SiO_2 (hv = 254 nm)	ACN-d_3	6 h	25:75
4	SiO_2 (hv = 366 nm)	ACN-d_3	6 h	25:75

[a]Fac:mer ratio determined by ^{1}H-NMR.

The thermal conversion of **C0** (7:93 *fac:mer* ratio) was also investigated. The ^{1}H-NMR spectra recorded in DMSO-d_6 at various temperatures are depicted in Figure 40. The mixture was heated at 150 °C and analyzed over time. Interestingly, the *fac:mer* ratio evolved into 13:83 ratio after 12h (green spectrum), 30:70 ratio after 24h (cyan blue spectrum) and 58:42 *fac*:*mer* ratio after six days (purple spectrum). These results confirm, in agreement with our previous investigations, the lower thermodynamic stability of the meridional ligand arrangement. Unfortunately, total conversion could not be reached after extended periods of time where decomposition of the complex occurred.

Even though a total conversion was not achieved, it is remarkable that through thermal conversion, the facial isomer increases its proportion more than 800% from going from 7% to 58% (6 days). On the other hand, this study proved the remarkable thermal stability of **C0**.

Since we failed in isomerizing or achieving a selective synthesis by modifying the reaction conditions, we decided to develop a ligand-controlled selective synthesis.

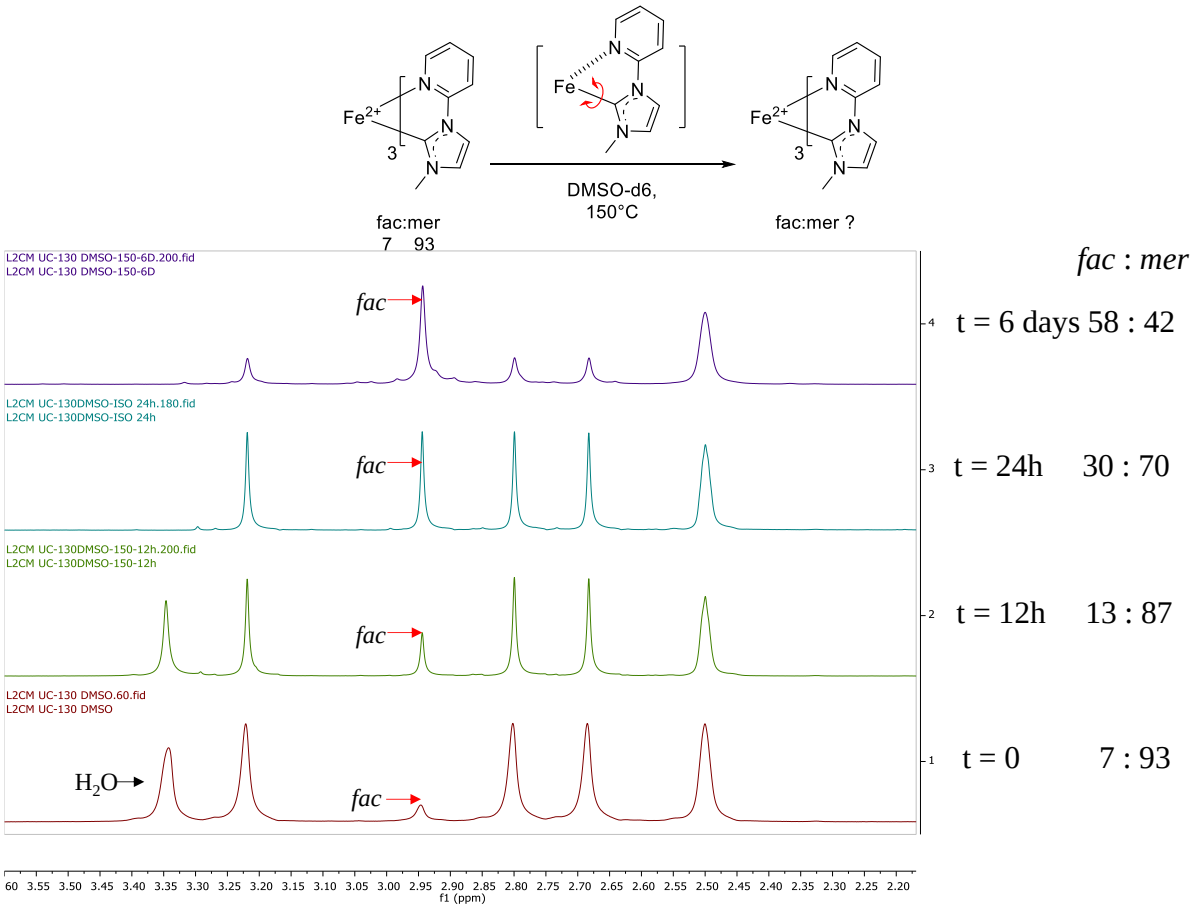

Figure 40. ^{1}H-NMR monitoring of the mer → fac conversion in **C0** as a function of the temperature in DMSO-d_6. Only the 2.20– 3.60 ppm window is shown for clarity.

III. 3 Influence of the stereoelectronic properties of the ligands on the complexation reaction

Modification of py-NHC ligands was previously investigated in the group, but only at the NHC unit, where the steric hindrance seemed to play a key role.[140] Assuming that the azine unit may coordinate the Fe(II) ion on the first place if the carbene is not preformed (Table 2, entry 10), we reasoned that modifications of this coordination site could have a prominent impact on the stereoselectivity. Thus, we decided to explore the effects of modifying both the substitution nature and pattern in the azine unit on the final complex configuration as shown in Scheme 8. Also, we studied the modification of the carbene unit to ascertain if the selectivity was further affected by its nature.

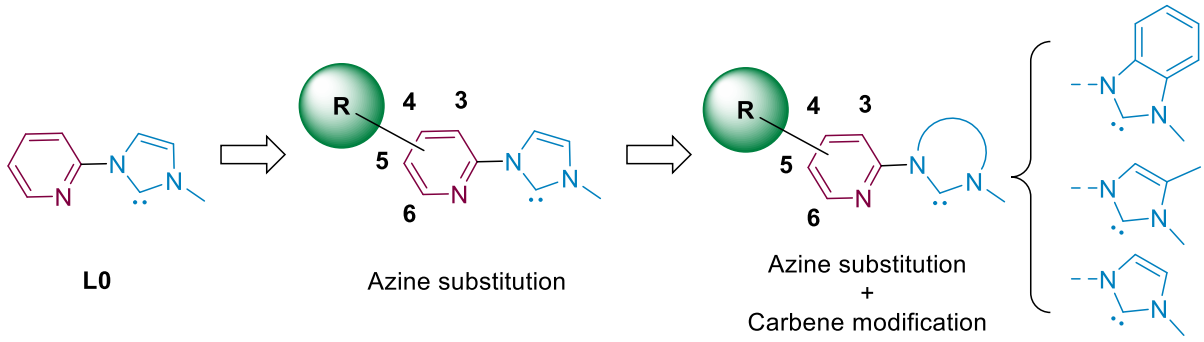

Scheme 8. General overview of the modification strategy of ligand **L0**.

III. 4 Substituent-induced control of *fac/mer* isomerism in azine-NHC Fe(II) complexes.

To begin with, a systematic substitution pattern over the pyridine was planned. For this purpose, two different substituents intended to impulse two levels of steric hindrance were targeted. A low steric hindrance, methyl (**HL3**-**HL8**) was selected in order to minimize the inductive or resonance effects (Scheme 9a). As a high level, mesityl (Mes) group (**HL6**-**HL8**) was chosen instead, not only due to its high steric demand, but also because of the additional

possibility of promoting π-stacking interactions (Scheme 9b).[141] The introduction of the substituents was done at position 4,5 and 6 of the pyridine moiety, since an anticipated weaker metal coordination could be anticipated for functionalization at position 3 due to a reduction of ligand coplanarity.[117]

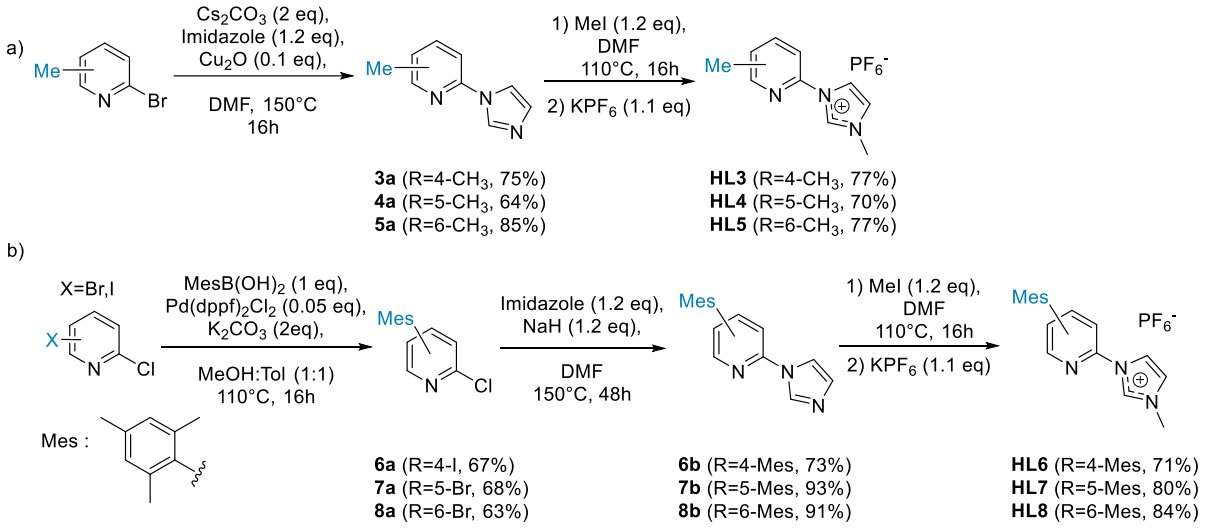

Scheme 9. Synthesis of (a) methyl-substituted ligands **HL3-HL5**, and (b) mesityl-substituted ligands **HL6-HL8**.

The synthesis of Me-based ligands **HL3-HL5** started with the precursors **3a-5a**, which were obtained in good yields by an Ullmann coupling within the imidazole on the corresponding methylated bromopyridine, then a quaternization with iodomethane in DMF at 110°C and finally metathesis with potassium hexafluorophosphate (Scheme 9a). Mes-based ligands **HL6**–**HL8** were prepared from the appropriate halogenated 2-chloropyridines. After the initial selective introduction of the mesityl group by means of a Suzuki coupling affording the intermediates **6a-8a**. The imidazole unit was introduced via a S_NAr mechanism at the Cl-substituted pyridine position (**6b-8b**). Once the imidazole was introduced, the quaternization with MeI was carried out followed by I^- to PF_6^- counterion metathesis. The target precursors were obtained in good yields (71-84%, Scheme 9b).

Based on our previous study on the reaction conditions with unsubstituted ligands (see §III.2.1), we selected $FeCl_2$ as iron source, DMF as solvent and KHMDS as the base since the target complex was obtained in good yield with no preference for any of the isomers, which

could thus allow to better evaluate the neat ligand effect. The complexation results of **HL3-HL8** precursors are collected in Table 4. All the ligands coordinated successfully, except **L8**. The overall yield for complexes **C3-C8** is around 45% regardless the ligand nature. However, a clear impact in the *fac:mer* selectivity was observed depending on the substituent. For the methyl series, the methyl group at position 4 and 5 (**L3**, **L4**) did not influence the selectivity, affording **C3** and **C4** with near statistic 25:75 *fac:mer* ratio (entries 1 and 2). In sharp contrast, the presence of the methyl group in position 6, adjacent to the pyridinic N atom (**L5**) led to the exclusive formation of the facial isomer *fac*-***C7*** despite a non-negligible steric hindrance towards the iron center (entry 3). We can consider this result as atypical and unexpected since the coordination of 6-methyl-2,2'-bipyridine with iron resulted in complexes with meridional isomerism.[142] As well, the complex presents a low-spin configuration, which differs as well from other similarly substituted facial complexes.[143,144] On the other hand, the Mes group did not show any influence in the final configuration when substituted at position -4 (**L6**), we can explain this due to its outward directionality. The corresponding **C6** complex showed a statistical 25:75 ratio (entry 4). Howbeit, the presence of the Mes group at position -5 results in a sterically hindered environment, particularly in facial configuration. As a result, a direct impact on the final configuration leads to almost exclusively *mer*-**C7** complex was after coordination of **L7** (entry 5).

The coordination of **L8** with the Mes group in position 6 next to the pyridinic N atom did not proceed, even heating the reaction or performing the carbene before addition of the iron source, the coordination was unsuccessful (entry 6). It is worth to note that similar substitutions at the 5-membered NHC moiety in related Fe^{II} Py-NHC complexes have been described.[141] However, the smaller angle formed between the Mes group and the Fe–N bond due to the 6-membered pyridine ring is likely to increase the steric hindrance to such an extent that coordination is completely inhibited.

Table 4. Effect of the ligand steric demand on Fe^{II} complex formation.

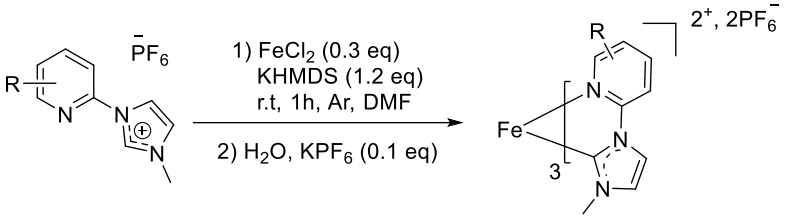

Entry	Ligand precursor	Yield (%)[a]	*fac*:*mer* ratio[b]	Complex
1	**HL3** (4-Me)	44	25:75	**C3**
2	**HL4** (5-Me)	44	20:80	**C4**
3	**HL5** (6-Me)	45	98:2	*fac*-**C5**
4	**HL6** (4-Mes)	48	25:75	**C6**
5	**HL7** (5-Mes)	45	4:96	*mer*-**C7**
6	**HL8** (6-Mes)	–	–	–

[a]Isolated yield. [b]*fac*/*mer* ratio determined by ^{1}H-NMR.

III. 4.1 Influence of the NHC unit

Having identified the excellent selectivity promoted by the 6-Me (**L5**) and 5-Mes (**L7**) substitutions towards respectively fac and mer geometries, , the impact of the NHC electronic nature was then evaluated. Thus, two carbene precursors were envisaged for each series derived from benzimidazole (bIm) and 4-methylimidazole (4-MeIm) to afford more π-acceptor and more σ-donor NHC units respectively. In Scheme 10 is depicted the synthesis of these new ligand precursors **HL9**–**HL12**.

The coordination reactions were performed under the same conditions as in section §II.2.1, and the results are collected in Table 4. The coordination of **L9**–**L12** ligands led to the expected complexes **C9**–**C12** in moderate yields (40–49%) (Table 5). The electronic nature of the NHC unit did not affect the facial configuration selectivity with a 6-Me substitution (entries 1–3) or the meridional selectivity in the case of the 5-Mes substitution (entries 4–6), attaining even a complete selectivity for both configurations while keeping the facial or meridional congeners remaining at best below the detection limit in ^{1}H-NMR. Therefore, these results nicely indicated that the final configuration of the system is mostly determined by the azine substitution pattern in py-NHC complexes.

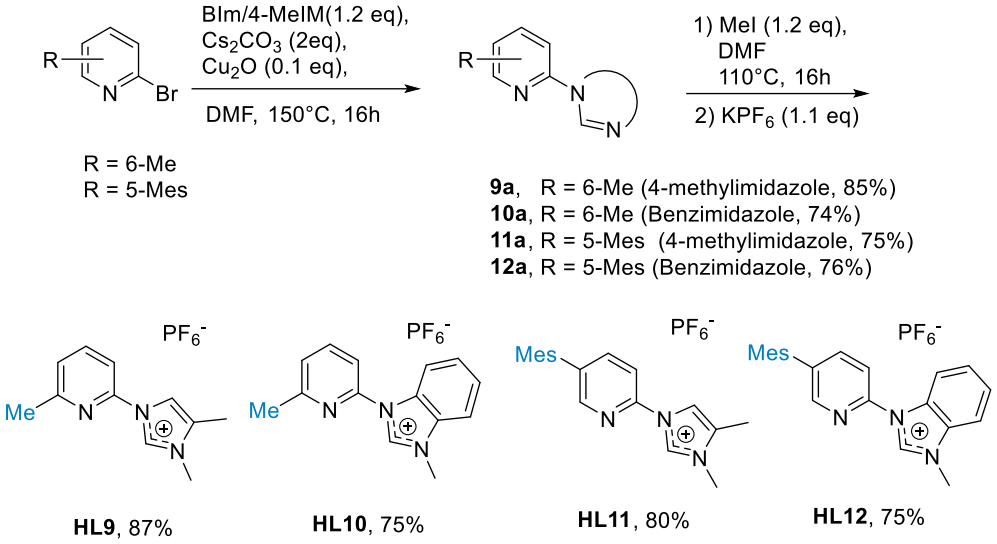

Scheme 10. Synthesis of ligands **HL9**–**HL12.**

Table 5. Effect of the nature of the NHC unit on the Fe^{II} complex formation. Data from **HL7** and **HL19** are presented for comparison reasons.

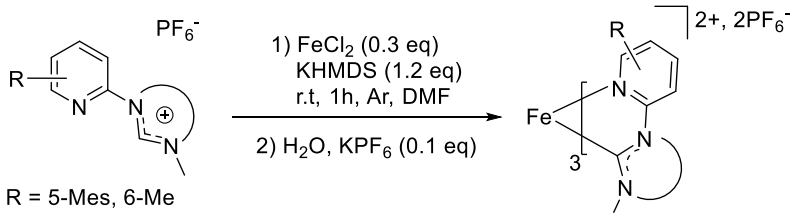

Entry	Ligand precursor	Yield (%)[a]	*fac*:*mer* ratio[b]	Complex
1	**HL5** (6-Me, Im)	45	98:2	*fac*-**C5**
2	**HL9** (6-Me, 4-MeIm)	48	100:0	*fac*-**C9**
3	**HL10** (6-Me, bIm)	43	100:0	*fac*-**C10**
4	**HL7** (5-Mes, Im)	45	4:96	*mer*-**C7**
5	**HL11** (5-Mes, 4-MeIm)	49	1: 99	*mer*-**C11**
6	**HL12** (5-Mes, bIm)	40	1: 99	*mer*-**C12**

[a]Isolated Yield. [b]*fac*/*mer* ratio determined by ^{1}H-NMR.

III. 4.2 Substituent nature variation at position 6

The counterintuitive and unanticipated facial selectivity exerted by the 6-Me substituted ligands **L5**, **L9** and **L10** encouraged us to investigate the exact role played by this group,

allowing us to understand if a possible agostic interaction between 6-Me with a pyridine group or another non-covalent interaction was the reason of facial selectivity. As a result, a new series of ligand precursors was prepared with varying functionalities at this position. The introduction of a more sterically hindered isopropyl (^{i}Pr) chain was performed by reacting 2,6-dibromo pyridine with iPrMgCl. The introduction of imidazole via an Ullman coupling followed by quaternization and I^-/PF_6^- exchange gave ligand **HL13** (Scheme 11). Ligands **HL14**–**HL16** bearing halogenated substituents (CF_3, F, Cl) and **HL17** with a dimethylamino (NMe_2) group were also prepared to examine the impact of the electronic effect. The synthesis of these ligands is described in Scheme 11. The synthetic protocols were similar to those previously described starting from the appropriate 2-halogenopyridine except for **HL17** where the previous introduction of the NMe_2 groups was necessary.

Precursors **HL13**–**HL17** were subsequently involved in the iron coordination step (Table 6). The introduction of the ^{i}Pr group induced the same selectivity as the methyl group, *i.e.* the exclusive facial isomerism, affording *fac*-**C13** in 30% yield (entry 1). With electron-withdrawing halogenated substituents, the results were different (entries 2–4). No complex was obtained with **L14** (6-CF_3) and **L15** (6-F) attributable to an excessively reduced coordinating ability of the pyridine due to high-electron withdrawing character of the substituents, while **L16** (6-Cl) led exclusively to *fac*-**C16** albeit in poor yield (18%). This latter example is, however, of particular interest since it would allow for complex functionalization via cross-couplings or S_NAr reactions for instance. In presence of the electron-donating NMe_2 group, no coordination complex could be obtained (entry 5). A possible origin of such a fate could be coordination by the amino group competing with those of the NHC moiety. From these results we can infer that facial selectivity is not necessarily led by an agostic interaction between the hydrogens of the methyl group and the pyridine ring since the selectivity was not compromised with –Cl and –^{i}Pr substituents.

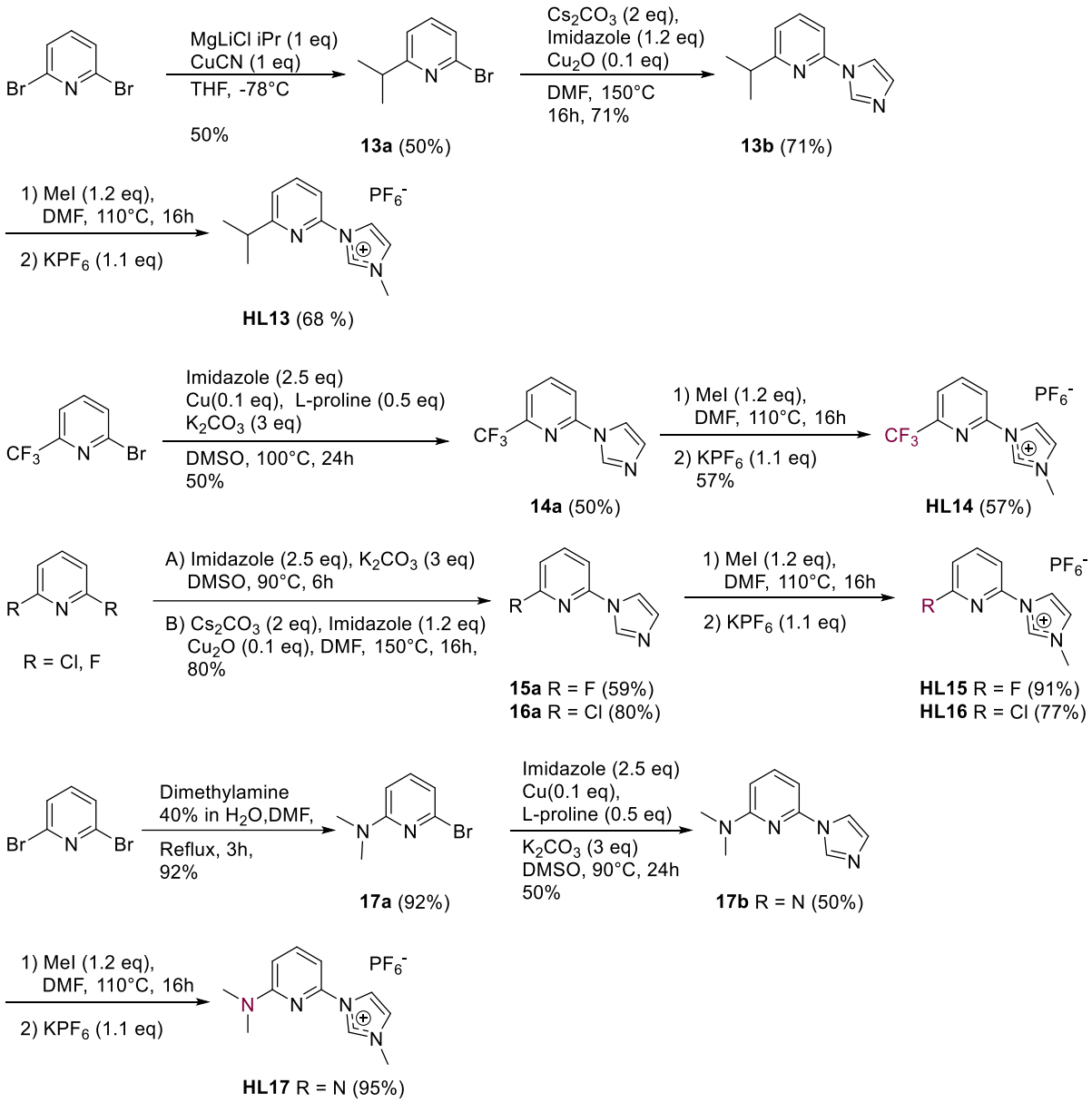

Scheme 11. Synthesis of ligands **HL13-HL17**.

Table 6. Coordination with different substituents at position 6 on the pyridine moiety.

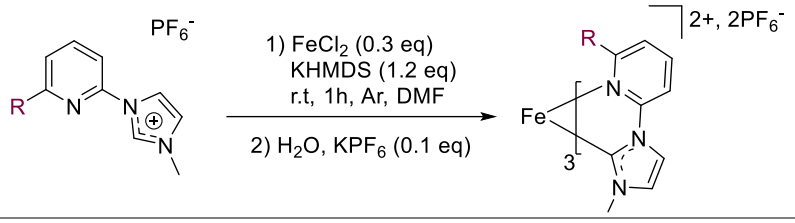

Entry	Ligand precursor	Yield (%)[a]	*fac*:*mer* ratio[b]	Complex
1	**HL13** (R=iPr)	40	100:0	*fac*-**C13**
2	**HL14** (R=CF_3)	–	–	–
3	**HL15** (R=F)	–	–	–
4	**HL16** (R=Cl)	18	100:0	*fac*-**C16**
5	**HL17** (R=NMe_2)	–	–	–

[a]Isolated Yield. [b]*fac*/*mer* ratio determined by ^{1}H-NMR, with ≥1% as detection limit.

III. 4.3 Use of π-extended azines

In order to evaluate the scope of this unprecedented ligand-induced stereoselectivity, we anticipated that the steric hindrance afforded by a -CH- unit of a benzannulated ring could be comparable to that of the 6–CH_3 (Figure 41). thus, we have prepared quinoline and quinoxaline-based ligand precursors (Scheme 12), together with one based on isoquinoline for comparison reasons (Scheme 13). However, it is worth nothing that other bidentate quinoline-based ligands such as 2-pyridin-2yl)quinoline lead to the exclusive formation of the meridional iron(II) complex.[145]

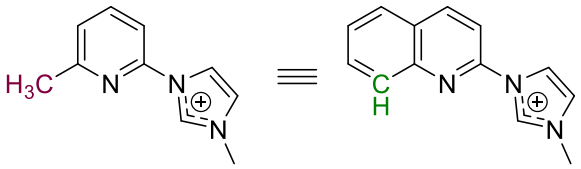

Figure 41. Steric hindrance of CH_3 compared to aromatic CH.

HL18 and **HL19** were prepared as we previous ligand precursors by means of a SNAr reaction. However, while **HL18** was prepared stepwise in good yield by reacting 2-

chloroquinoline with in-situ generated potassium imidazolate followed by quaternization with MeI, **HL19** was directly obtained from 2-chloroquinoxaline with N-methylimidazole in 77% yield due to the higher reactivity of this azine. An isoquinoline-based ligand (**HL20**) was also synthesized with the study the effect of having a conjugated aromatic ring in positions 3 and 4 of the pyridine (Scheme 12) and elucidate if the facial or meridional preference could be guided by having an aromatic ring in these positions. Possibly, the substitution pattern of the isoquinoline can lead to a series of intra or inter ligand interactions conferring certain selectivity allowing us to reach a plausible explanation for the facial selectivity. The synthesis of **HL20** was performed via the previously described Ullmann coupling to afford **20a**, then a later quaternization to give the target ligand precursor in 77% yield.

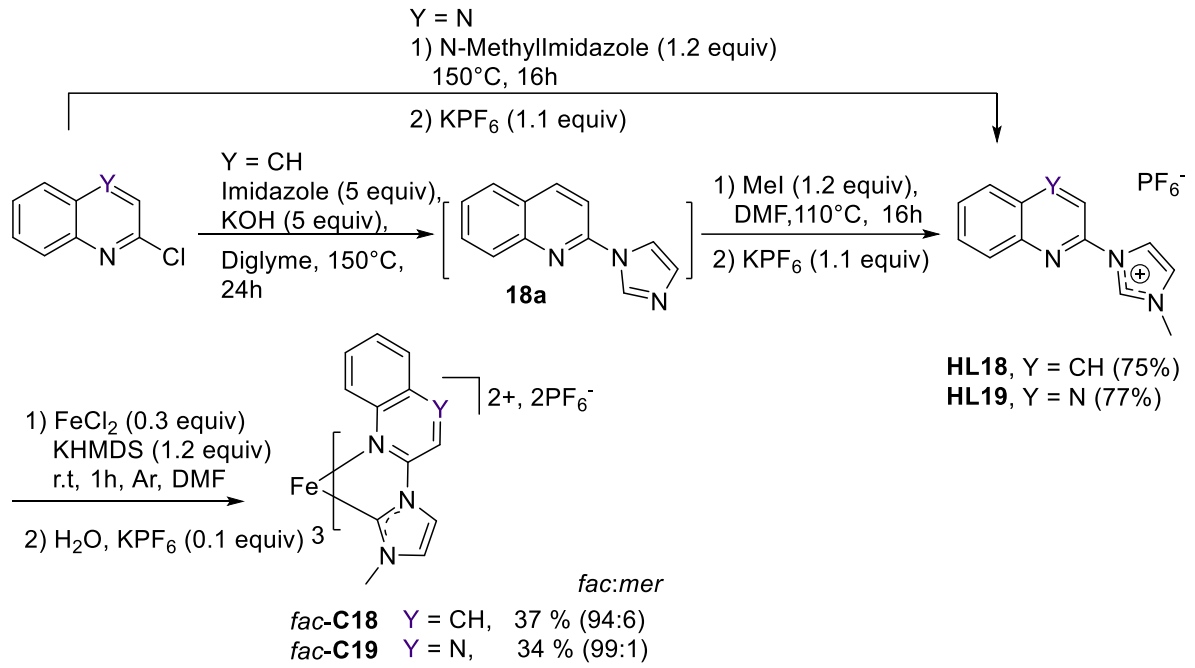

Scheme 12. Synthesis of ligand precursors **HL18** and **HL19** and synthesis of complexes *fac*-**C18** and *fac*-**C19**.

The complexation of both π-extended H**L18H–HL20** precursors was carried out under the aforementioned conditions using $FeCl_2$ and KHMDS in DMF at r.t. (Table 4). Complexation of **L18** and **L19**, which implies an important steric hindrance close to the metal, resulted in an almost complete selectivity towards the facial isomer, affording exclusively *fac*-**C18** and *fac*-**C19** complexes in 37% and 34% yield, respectively. Gratifyingly, complex **C20**

was obtained instead as a mostly meridional mixture (8:92 *fac*:*mer*), which allowed us to validate our hypothesis (Figure 41).

As in the pyridine-substituted series, we further investigated the effect of the NHC unit for these type of ligand precursors. The synthesis of two additional quinoxaline-based precursors **HL21** and **HL22** is presented in Scheme 14, together with their complexation reactions. Selection of the quinoxaline derivatives was based on their improved optical properties respect to pyridine-based complexes (see §III.4.6). Interestingly, complexation was achieved with full stereoselectivity in both cases, affording *fac*-**C21** and *fac*-**C22** in 37% and 34% yield, respectively, and being completely consistent with previous results.

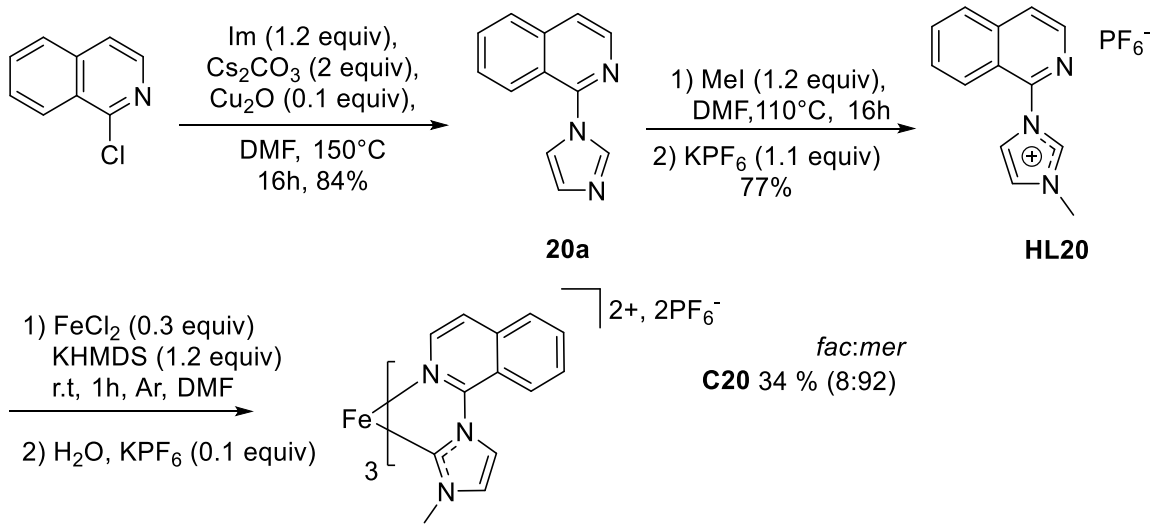

Scheme 13. Synthesis of ligand **HL20** and complex **C20**.

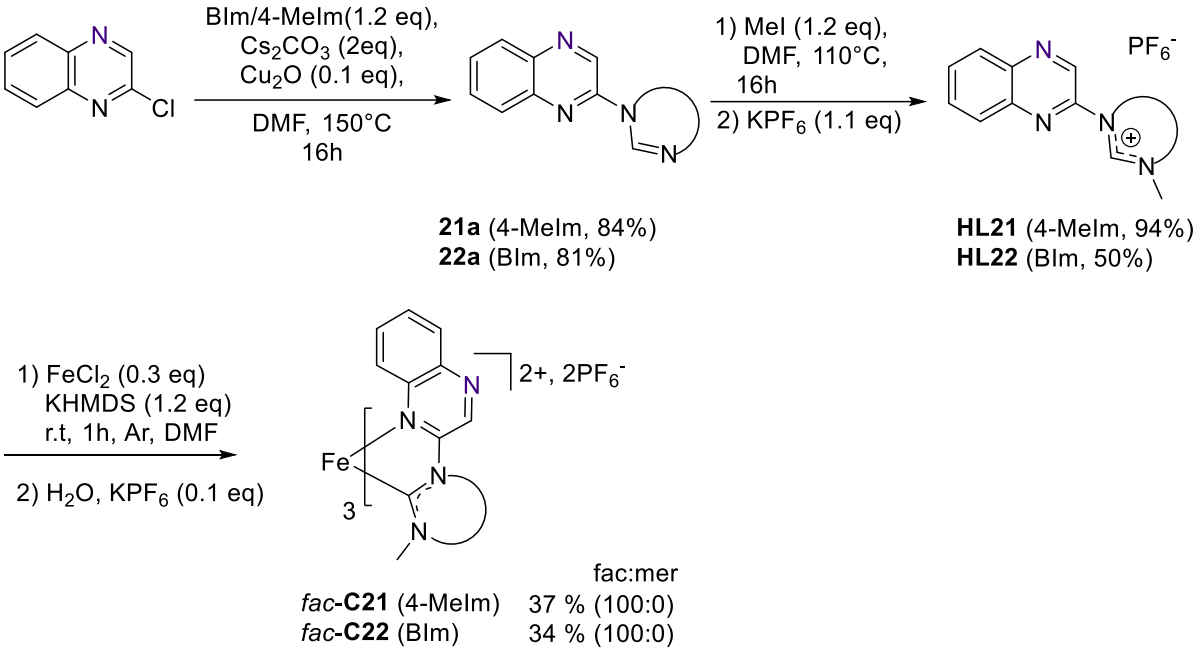

Scheme 14. Synthesis of ligand precursors **HL21** and **HL22** and synthesis of complexes *fac*-**C21** and *fac*-**C22**.

III. 4.4 X-Ray analysis

Complexes *fac*-**C5**, *mer*-**C7** and *fac*-**C18** were characterized by X-Ray analysis confirming the structural information given by ^{1}H-NMR. Suitable crystals were obtained grown by slow evaporation of the corresponding solvent; methanol for *fac*-**C5** and acetonitrile for *mer*-**C7** and *fac*-**C18** complexes. Figure 42 shows the structures for the three complexes displaying a distorted octahedral geometry and confirming the anticipated configurations. Some selected structural parameters are collected in Table 7.

Facial complexes *fac*-**C5** and *fac*-**C18** show three bidentate ligands with the same orientation, confirming the facial arrangement with each Fe–C bond trans to a Fe–N bond. In comparison to the computationally-optimized structure of *fac*-**C0**,[134] average Fe–C bond distances (1.904 Å for *fac*-**C5** and 1.899 Å for *fac*-**C19** *vs* 1.948 Å for *fac*-**C0**) are significantly shorter, while average Fe–N bond distances are only slightly shorter (2.141 Å for *fac*-**C5** and 2.138 Å for *fac*-**C18** *vs* 2.072 Å for *fac*-**C0**). The steric hindrance exerted by the imine unit is more evident when analyzing the conformation of the bidentate units, which exhibit marked tilting angles of 4.4–13.1° and 5.1–10.4° for *fac*-**C5** for *fac*-**C18**, respectively. Thus, it would

be tempting to correlate the enhanced structural trans-effect in *fac*-**C5** and *fac*-**C18** respect to *fac*-**C0** with a higher kinetic trans-effect, which would explain the obtained selectivity, but analysis into the complexation mechanism is required.[126]

We can clearly observe the presence of several short contacts in these facial complexes. These interactions involve mostly the coordinated atoms ($C_{carbene}$ or N_{azine}) to the iron center with a neighboring CH_3 group (d + 0.2 Å < sum of the Van der Waals radii) for both *fac*-**C5** for *fac*-**C18,** or $N_{quinoline}\cdots H–C^{8}_{quinoline}$ (d + 0.4 Å < sum of the Van der Waals radii) in the case of *fac*-**C18**. Since $C_{carbene}\cdots Cl$ intramolecular interactions have been reported,[146] this type of short contacts might be also envisaged for *fac*-**C18**. Therefore, it is therefore possible that these interactions contribute significantly to the here-obtained facial selectivity.

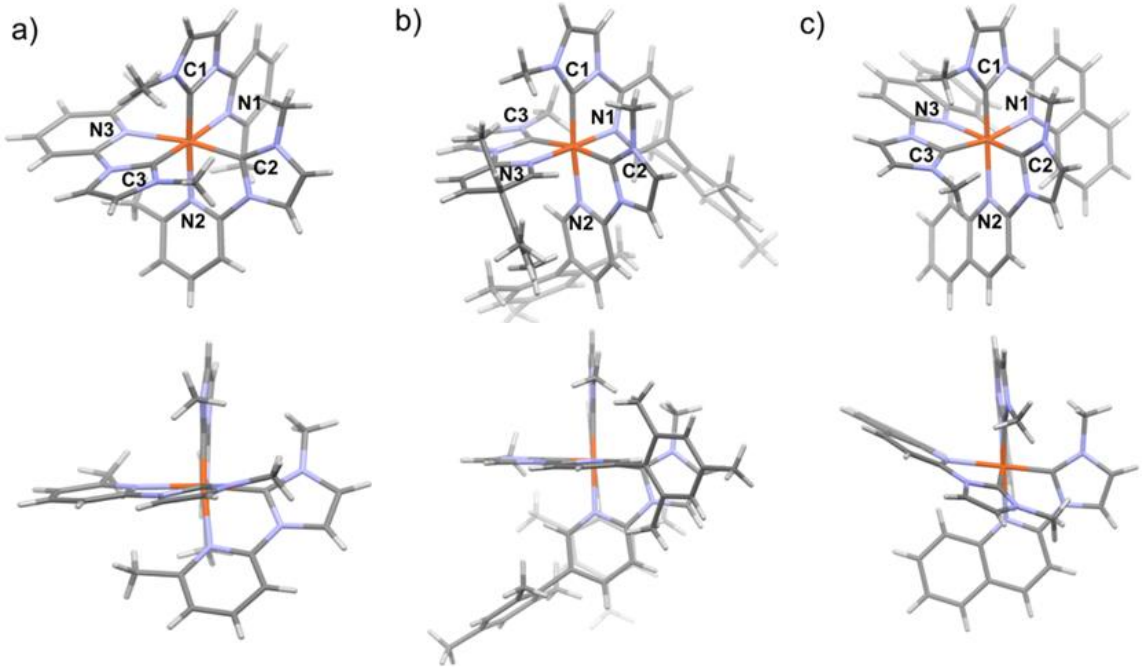

Figure 42. (left) View from the (pseudo)-C_3 axis and (right) side view of the X-ray crystal structures of complexes (a) *fac*-**C5**, (b) *mer*-**C7** and (c) *fac*-**C18** with a partial labelling. Periphery atoms on the ligands are omitted for more clarity. CCDC for *fac*-**C5**: 2126499; *mer*-**C7**: 2126506; *fac*-**C18**: 2126500.

The structure of *mer*-**C7** shows a C_1 symmetry, corresponding the meridional arrangement where only two ligands are oriented in the same direction. While the mutually trans Fe–C and Fe–N bonds are rather comparable to those in the facial complexes, more

remarkable differences are observed for the other four metal-ligand bonds. In fact, being consistent with the stronger trans-effect of the carbene ligand relative to an azine, the mutually trans Fe–C bonds are longer (~1.945 Å) than the mutually trans Fe–N bonds that are shorter (~1.981 Å) than those in *fac*-**C5** and *fac*-**C18**. Moreover, the less crowded coordination sphere allows the ligands to adopt almost coplanar conformations (tilting angles = 0.20–2.38°), resulting in fewer intramolecular short contacts mainly consisting in L···H–$C^6_{pyridine}$ (L = $C_{carbene}$ or N_{azine}).

Calculation of the stretching (ζ), angular (Σ) and trigonal (Θ) distortions from the ideal octahedral structure (Table 7)[147] allows us to have a more global comparison. Taking as reference the calculated structures of *fac*-**C0**, it is evident that the deformation induced by the sterically-demanding azine unit, with an increased asymmetry in bond lengths (ζvalues) and worse M–L interaction (Σ and Θ values, with Σ=0° and Θ=0° for a perfect octahedron). Interestingly, complex *mer*-**C7** displays the most regular coordination sphere even when compared with parent *mer*-**C0**.

Table 7. Selected structural and deformation parameters for complexes *fac*-**C5**, *fac*-**C18** and *mer*-**C7**. The deformation parameters were calculated with OctaDist.[147] For the sake of comparison, data for DFT optimized *fac*-C0 and *mer*-C0 are provided as well, with partial labelling analogous *fac*-**C5** and *mer*-**C7**, respectively.[135]

	fac-**C0**	*fac*-**C5**	*fac*-**C18**	*mer*-**C0**	*mer*-**C7**
Fe-N1 (Å)	2.073	2.105(3)	2.137(2)	2.038	1.975(3)
Fe-N2 (Å)	2.072	2.131(2)	2.135(2)	2.082	2.015(2)
Fe-N3 (Å)	2.070	2.188(2)	2.142(2)	2.042	1.988(3)
Fe-C1 (Å)	1.949	1.893(3)	1.907(2)	1.942	1.903(3)
Fe-C2 (Å)	1.950	1.910(3)	1.899(2)	1.992	1.934(3)
Fe-C3 (Å)	1.947	1.910(3)	1.892(2)	1.983	1.956(3)
C1-Fe-N2 (°)	172.6	174.1(1)	168.6(9)	173.2	173.4(1)
C2-Fe-N3 (°)	172.8	169.9(1)	173.6(9)	–	–
C3-Fe-N1 (°)	172.7	176.6(1)	176.1(9)	–	–
C2-Fe-C3 (°)	–	–	–	170.0	169.9(1)
N1-Fe-N3 (°)	–	–	–	177.0	177.8(1)
$\overline{\langle Fe-X \rangle}$ **(Å)**[a]	2.010	2.023	2.019	2.013	1.962
ζ **(Å)**[b]	0.368	0.710	0.717	0.245	0.185
Σ **(°)**[c]	64.9	81.4	85.9	67.7	61.2
Θ **(°)**[d]	205.1	241.2	257.0	213.3	196.4

[a]Average metal-ligand bond. [b]Length distortion calculated as $\zeta = \sum_{i=1}^{6}(d_i - \langle Fe-X \rangle$, with d_i being a metal-ligand bond length. [c]Angle distortion calculated as $\sum_{i=1}^{12}|90 - \Phi_i|$ with Φ_i being a cis ligand-metal-ligand angle.

Trigonal distortion calculated as$\Theta = \sum_{i=1}^{24}|60 - \theta_i|$, with θ_i being a torsional angle between the ligand atoms on opposite triangular faces of the octahedron viewed along the pseudo-threefold axis.

III. 4.5 Theoretical calculations

In order to gain more insights into the selectivity of the facial coordination, the structural and energetic differences between the *fac* and *mer* isomers for the most relevant complexes of this work have been studied using quantum chemistry calculations (collaboration with Dr. Antonio Francés-Monerris, Valencia). The *fac* vs *mer* thermodynamic stabilities are shown in Figure 43. The most stable configuration for most of the Fe^{II}-NHC family apparently is the *fac* arrangement. A trend that globally agrees with the *fac* preference observed experimentally. However, more specific analyses reveal that the thermodynamic stabilities of the isomers are not the only factor ruling the *fac*/*mer* preferences, suggesting that other factors also play an important role. These factors would include complexation kinetics and/or intramolecular interactions as previously suggested.

The Gibbs energy differences between the two isomers are not equal for all complexes (Figure 43). Whereas **C5**, **C7**, **C9**, and **C13** clearly favor the *fac* disposition (ΔG ~3 kcal/mol), complexes **C0**, **C10**, and **C18** show almost degenerated energies for both *fac* and *mer* arrangements (ΔG ~±1 kcal/mol). This is coherent with the *fac*/*mer* isomer distribution (6:94) observed for **C0**[135] and the *fac* preference (>98:2) exhibited by **C5**, **C9** and **C13**. An eye-chasing case is **C7**, which exists mostly as a *mer* isomer, although the *fac* disposition is thermodynamically more stable. This evidences that the complexation mechanism penalizes the *fac* isomer. Meanwhile, the ΔG values for **C10** and **C18** also do not explain the *fac*/*mer* ratio higher than 94:6 as observed experimentally in terms of thermodynamic stabilities, again pointing to extrinsic factors in the complexation process. Comparing complexes **C0** and **C5** is particularly interesting. The only difference in both complexes is the methyl group at the 6 position of the pyridine ring in **C5**, which is key to induce opposite isomer preferences: **C0** is mostly *mer* whereas **C5** is *fac*.

A detailed analysis of the Fe–N and Fe–C connections as well as the non-covalent interactions between the methyl groups and the C and N dative atoms coordinated to iron is presented in Figure 44 and Table 8. The fact of having a methyl in position 6 of the pyridine in *fac*-**C5** clearly indicates an elongation of the three Fe-N distances by 0.134 Å (on average), due

to steric congestion of the three methyl groups. This effect is illustrated in Figure 44b. As a result, on the opposite side of the molecule, the Fe–C and the Im-CH_3···C distances decrease by -0.005 and -0.051 Å, respectively (Table 8).

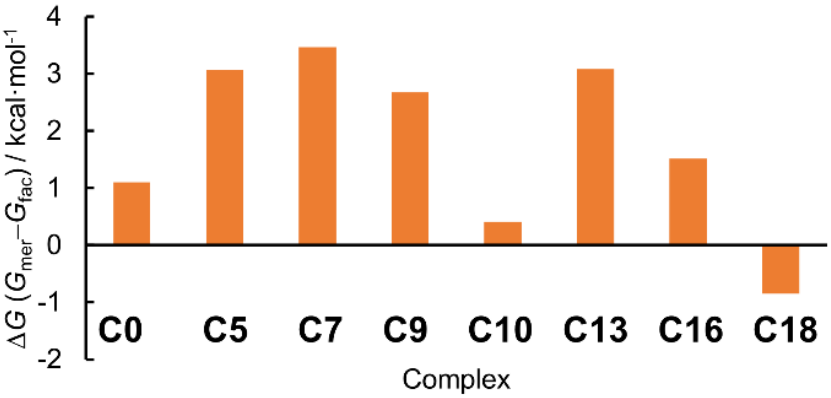

Figure 43. Gibbs energy difference (ΔG) between the *fac* and *mer* isomers for some selected complexes synthesized in this work. Optimized geometries and vibrational frequencies computed at the DFT/B3LYP-D3 level of theory. Energies refined with the DLPNO-CCSD(T) method.

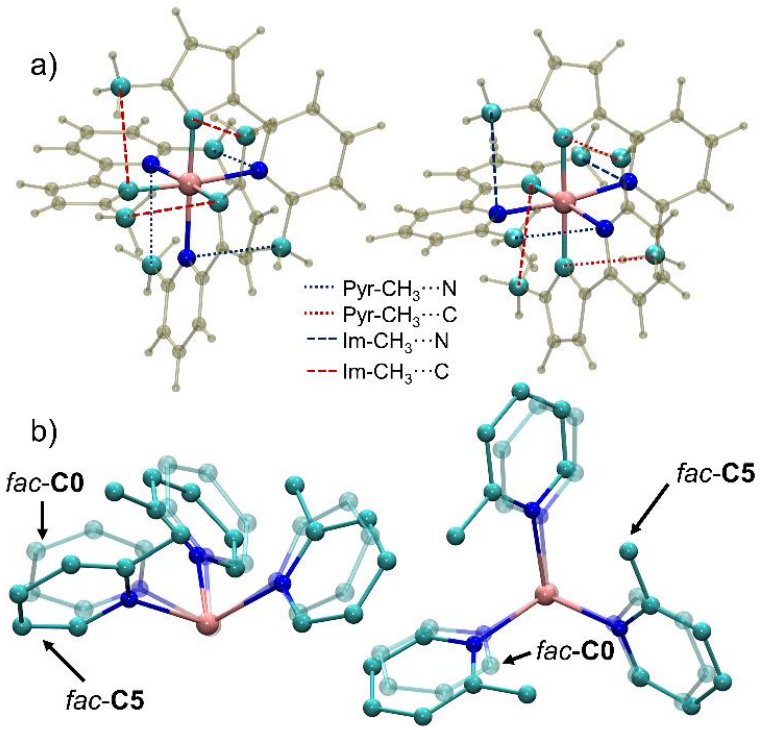

Figure 44. a) DFT/B3LYP-D3 optimized structures of the *fac* (left) and *mer* (right) isomers for **C7** and nomenclature of the intramolecular non-covalent interactions. b) Side (left) and top

(right) views of the *fac* isomer of **C0** (transparent texture) and **C5** (solid texture). For the sake of clarity, only the Fe centers and the pyridine rings are shown.

Regarding *mer*-**C7**, the structural deformation is similar. On average, the Fe-N increases by 0.114 Å and the Fe-C distances decreases by -0.004 Å, respectively. The largest difference between the *mer* isomers of **C0** and **C5** is found for the Im-CH_3···C and Im-CH_3···N distances, which decrease -0.072 Å.

In general, the net structural deformations upon methylation from **C0** to **C5** are almost equal for both isomers. These subtle —yet important— differences impact the relative stability of both isomers. As a matter of fact, the thermodynamic stability for *fac*-**C5** is about ~2 kcal/mol larger than that of *fac*-**C0** with respect to their respective *mer* counterparts (Figure 43). This difference can be attributed to the combination of diverse attractive and repulsive interactions. In this regard, the more pronounced stretching of the more labile Fe–N bonds (as compared to Fe–C) in *fac*-**C5**, as well as the more favorable Pyr-CH_3···N non-covalent interactions (as compared to the Pyr-CH_3···C), in which the methyl group can act as a Lewis base[148] and the N as a Lewis acid, may explain the slight energetic differences.

Table 8. Relevant interatomic distances (in Å) for the *fac* and *mer* isomers of **C0** and **C5** as defined in Figure 44.

Bond/interaction	*fac*-**C0**	*fac*-**C5**	*mer*-**C0**	*mer*-**C7**
Fe-N	2.057	2.195	2.065	2.126
	2.057	2.190	2.030	2.200
	2.057	2.189	2.025	2.135
Fe-C	1.931	1.926	1.927	1.977
	1.930	1.926	1.968	1.917
	1.931	1.926	1.974	1.963
Im-CH3···C	3.175	3.117	3.205	3.166
	3.174	3.135		
	3.172	3.117		
Im-CH3···N			3.224	3.136
			3.209	3.121
Pyr-CH3···C				3.047
				3.005

Pyr-CH3···N	3.045	3.023
	3.043	
	3.039	

In the facial conformation exists a series of non-covalent interactions exists, which are not present in the *mer* arrangement that can also explain the stability of the *fac*-**C7** (Figure 45) over the meridional isomer. The *fac* arrangement clearly shows triple T-stacking interactions between the methyl groups of the mesityl substituent and the aromatic rings (Figure 45), whereas in the *mer* disposition only two 5-Mes groups interact due intrinsic reasons.

Thus, can be hypothesized that principal reason to obtain mainly *mer*-**C7** instead *fac*-**C7** isomer (Table 5) is likely due to the concomitant steric congestion induced by the Mes groups in the complexation mechanism. This analysis evidences again the need to consider mechanistic and other extrinsic factors besides the intrinsic stability of the isomers to fully understand the *fac*/*mer* isomerism in this kind of Fe^{II}-NHC complexes.

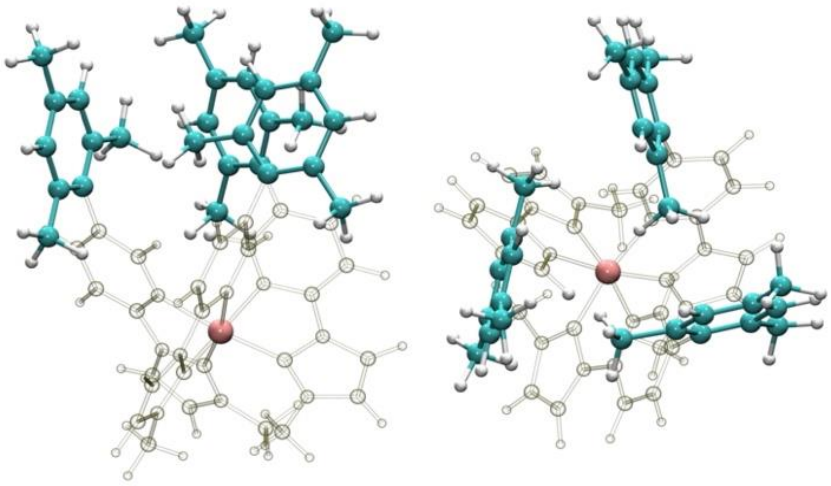

Figure 45. Side (left) and top (right) views of the *fac*-**C7** structure. 5-Mes groups are highlighted as cyan (carbon) and white (hydrogen) spheres.

III. 4.6 Ground-state characterization

Optical and electrochemical properties of all facial and meridional complexes were investigated by UV-Vis spectroscopy (Figure 46) and cyclic voltammetry, and the main results are collected in Table 9. As previously reported compounds,[149] the UV-Vis spectra of all complexes present three main absorption bands. The intense bands below 300 nm correspond to $^1(\pi\rightarrow\pi^*)$ transitions centered on the ligands. At longer wavelengths, two distinct broader and less intense MLCT bands are found at longer wavelengths corresponding to Fe–carbene $^1(d\rightarrow \pi^*_{NHC})$ transitions (320–420 nm) and Fe–azine $^1(d\rightarrow \pi^*_{azine})$ transitions, which extend well into the visible region (380–650 nm).[149] However, several differences can be distinguished arising from the ligand configuration:

- Less intense absorptions are observed for facial complexes due to their higher symmetry.[135]
- Modification of the NHC unit results in a different $^1(d\rightarrow\pi^*_{azine})$ band energy variation in mer and fac series. In fact, an inverse correlation between NHC donation and energy is nicely observed in facial complexes, with MLCT energies varying as *fac*-**C10** (BIm) > *fac*-**C5** (Im) > *fac*-**C9** (4MeIm) (Figure 43, left) and *fac*-**C22** (BIm) > *fac*-**C18** (Im) > *fac*-**C21** (4MeIm) (Figure 46, left). In contrast, no correlation between the MLCT band energy and the NHC donation is identified in the meridional series, with MLCT band energy varying as *mer*-**C7** (Im) > *mer*-**C11** (4MeIm) > *mer*-**C12** (BIm)) (Figure 46, right) (*vide infra*). As a result, while a MLCT blue-shift is obtained with the BIm carbene in a facial coordination (*fac*-**C10** vs *fac*-**C5** or *fac*-**C22** vs *fac*-**C19**), the same carbene induces a MLCT red-shift in meridional coordination (*mer*-**C12** vs *mer*-**C7**).

The effect of the 6-substitution on the pyridine unit appears to be related to the relatively elongated 6-Me-pyridine-Fe (Figure 43, left). As a matter of fact, *fac*-**C5** (6R=Me) and *fac*-**C16** (6R=Cl) present an almost identical spectra no matter the distinct electronic nature of their substituents. The increased steric hindrance of the ^{i}Pr in complex *fac*-**C13**, can be the reason of the less intense UV-vis spectrum. As for the benzannulation of the azine unit, a noticeable shift to lower energies is clearly noticed in the absorbance spectrum as a result of the more stabilized π^* orbitals in comparison to the pyridine-based complexes. For instance, bands appeared red-shifted *ca.* 3200 cm^{-1} for *fac*-**C20** (quinolyl) and *ca.* 5000 cm^{-1} for *fac*-**C21**

(quinoxalyl) respect to *fac*-**C7** (pyridyl), also reflecting the higher accepting character of the quinoxaline moiety (Figure 46). When comparing *fac*-**C20** (quinolyl) and **C22** (isoquinolyl), a slight blue-shift is observed for the latter (Figure 47).

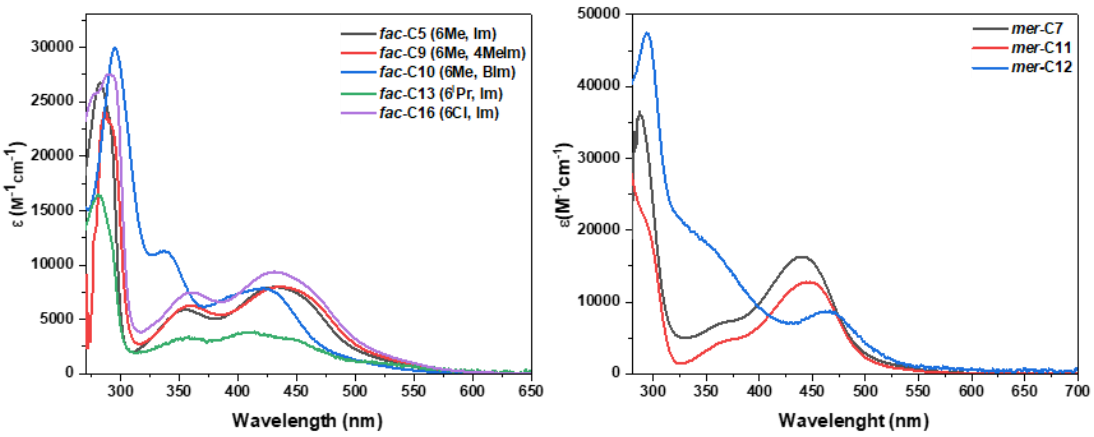

Figure 46. UV-Vis spectra in air-equilibrated acetonitrile solution at room temperature to show: (left) NHC influence and azine variation through substitution in facial series; (right) NHC influence in meridional series.

Concerning the redox properties, cyclic voltammetry of the complexes was carried out with SCE as standard electrode and ferrocene as internal reference (Fc^{+}/Fc = 0.39V/SCE in acetonitrile) (see experimental part for further details). At positive potentials, these bidentate *fac*/*mer* complexes display reversible Fe^{II} to Fe^{III} oxidations in most cases with potentials ranging between 0.62–1.30 V (Table 8). These values can be nicely correlated to the π-back donation of Fe^{II} to both NHC and azine moieties, which results in higher reduction potentials due to the stabilization of the t_{2g}-like orbital (HOMO). Thus, the increasing electron withdrawing character on going from 4MeIm to Im to bIm nicely correlates with an anodic shift of the oxidation potential in both facial (*fac*-**C9** < *fac*-**C5**< *fac*-**C10** < *fac*-**C21**< *fac*-**C19**< *fac*-**C21)** and meridional series (*mer*-**C11** < *mer*-**C7**< *mer*-**C12**). The same effect is observed when only the azine unit is modified; *e.g.* 0.69 V for *fac*-**C5** (pyridyl-Im), 0.79 V for *fac*-**C18** (quinolyl-Im) and 1.08 V for *fac*-**C19** (quinoxalyl-Im).

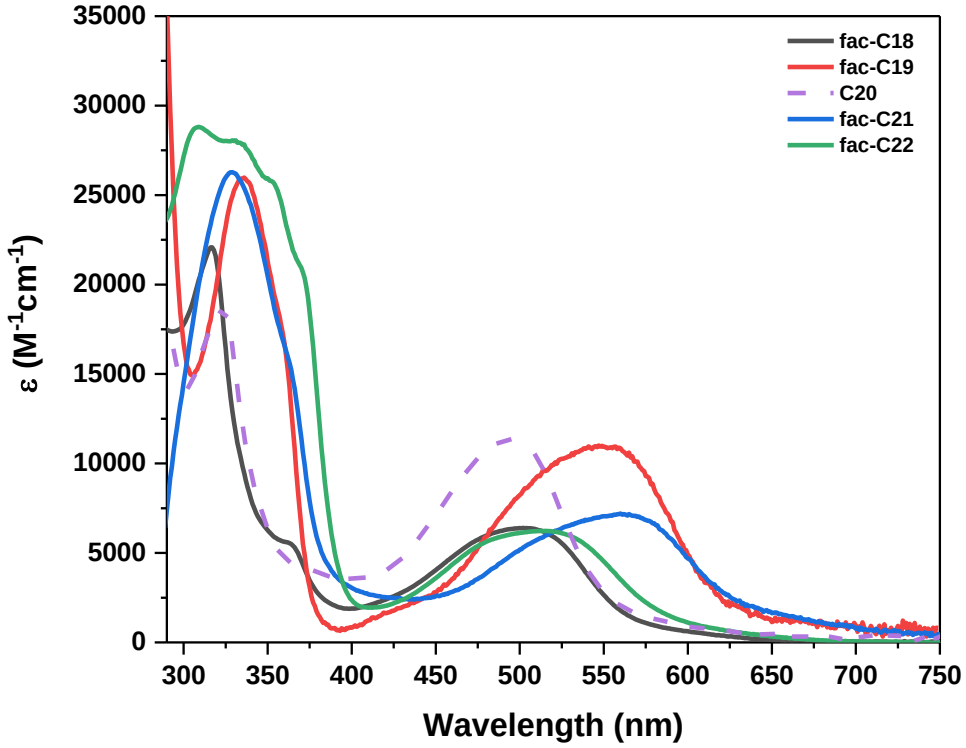

Figure 47. UV-Vis spectra in air-equilibrated acetonitrile solution at room temperature to show azine variation through substitution or π-conjugation extension and NHC influence in facial series.

On the cathodic range, remarkable differences are obtained as well (-1.91 to -0.82 V). As for parent **C0** (-1.94V, -1.97V), reduction is believed to take place at the azine unit for *mer*-**C7** (-1.86 V) and *mer*-**C11** (-1.90 V), together with those bearing π-extended azines (*fac*-**C18**, *fac*-**C19**, **C20**, *fac*-**C21,** *fac*-**C22**), which show drastic cathodic shifts that correspond well with their increased acceptor character and thus, lower π* orbitals. Moreover, the introduction of more π-conjugated NHC units (BIm) seems to contribute to more delocalized LUMO, resulting in lower potentials as well (*fac*-**C10** vs *fac*-**C5** and fac-**C9**; *fac*-**C22** vs *fac*-**C19** and *fac*-**C21**; and *mer*-**C12** vs *mer*-**C7** and *mer*-**C11**).[116] However, the interpretation is less straightforward for *fac*-**C14** and *fac*-**C16**, exhibiting different 6R substituents. It is reasonable to think that the steric hindrance exerted by the azine unit in these facial complexes will partially hinder their coordination to the metallic center and therefore, the exact nature of the Fe-L interactions.

Table 9. Photophysical and electrochemical data for the facial or meridional Fe^{II} complexes.

Complex	$\lambda_{abs\text{-}max}$ (nm) [$\varepsilon(M^{-1}.cm^{-1})$][a]	E_{ox}[b] [V vs SCE]	E_{red} [V vs SCE]	ΔE [V][c]
fac-**C5**	285 [26795] 355 [5891] 435 [7957]	0.69 (rev)	-1.59 (qr) -1.87 (rev)	2.28
fac-**C9**	286 [24398] 357 [6237] 436 [7928]	0.62 (rev)	-1.59 (rev) -1.90 (qr)	2.21
fac-**C10**	293 [29471] 340 [11185] 419 [7839]	0.95 (rev)	-1.19 (rev) -1.60 (rev)	2.14
fac-**C13**	283 [16359] 351 [3274] 416 [3810]	0.81 (rev)	-1.42 (rev) -1.91 (irr)	2.23
fac-**C16**	278 [25731] 293 [27383] 362 [7470] 428 [9332]	0.86 (rev)	-1.59 (irr)	2.45
fac-**C18**	317 [22077] 367 [5157] 508 [6354]	0.79 (rev)	-1.41 (irr) -1.63 (irr) -1.75 (irr)	2.20
fac-**C19**	338 [25764] 428 [1916] 555 [10856]	1.08 (qr)	-0.82 (irr) -1.16 (irr) -1.51 (irr)	1.90
C20	323 [18675] 371 [4202] 503 [6443]	0.86 (rev)	-1.59 (rev) -1.79 (irr)	2.45
fac-**C21**	328 [26324] 363 [16001] 564 [7139]	1.01 (rev)	-1.00 (irr) -1.17 (irr) -1.69 (irr)	2.01
fac-**C22**	308 [28777] 334 [27996] 354 [25738] 372 [20212] 511 [6281]	1.30 (qr)	-1.62 (irr)	2.92
mer-**C7**	289 [35856] 362 [6987] 444 [16187]	0.73 (rev)	-1.86 (rev)	2.59
mer-**C11**	296 [19460] 368 [4589] 451 [12640]	0.66 (rev)	-1.90 (rev)	2.56
mer-**C12**	293 [47267] 360 [16852] 464 [8562]	1.06 (rev)	-1.37 (rev) -1.84 (irr)	2.43

[a]Measured in CH_3CN at 25°C; [b]First oxidation potential. Potentials are quoted *vs* SCE. Recorded in CH_3CN using NBu_4PF_6 (0.1M) as supporting electrolyte at 100 mVs^{-1}; under these conditions, $E_{1/2\ (Fc+/Fc)}$ = 0.39V/SCE; rev = reversible ; qr = quasi-reversible; irr = irreversible. [c]Electrochemical band gap ($\Delta E=E_{ox}-E_{red1}$).

In consequence, these results highlight the subtle relationship between molecular structure and the corresponding electronic effects. For facial pyridyl-based complexes, and evident dependence of the MLCT energies on the carbene donor strength was identified (Figure 46, left and right). However, meridional complexes are more sensitive to the π-conjugation of

the carbene unit, whit opposing effects for BIm-based complexes *fac*-**C10** (Figure 46, rigth) and *fac*-**C22** (Figure 47) with respect to *mer*-**C12** (Figure 46, right). This result could be attributed to a different localization of the LUMO, *i.e.* on the NHC moiety rather than on the azine, as it has previously reported for related complexes,[150] precluding any direct comparison. The unexpected redshift of the MLCT band in *mer*-**C12** could thus be consistent with the higher stabilization of the t_{2g}-like orbital as a result of the π-accepting character of the BIm moiety that is largely offset by a noticeable stabilization of the π* orbital.

Moreover, selection of π-extended azines (*fac*-**C18**, *fac*-**C19**, **C20**, *fac*-**C21,** *fac*-**C22**) leads to a sizeable stabilization of the ligand π* orbital. In consequence, their UV-vis spectra are systematically shifted towards lower energies, with their MLCT band extending over a good part of the visible range. More interesting, considering that these complexes may have high-lying MC states due to their greatly stabilized t_{2g}-like orbitals, an inversion of their relative order of their MLCT and MC excited states could be readily conceivable. The dynamics of the excited state relaxation is currently been investigated by transient absorption spectroscopy in a partnership with Prof. Dr. Stefan Haacke in the University of Strasbourg.

III. 5 Conclusions and perspectives

In this chapter we have described the ligand design guidelines to selectively access both facial and meridional isomers in azine-NHC Fe(II) complexes by means of a room-temperature protocol. As we have demonstrated, the origin of this outstanding selectivity stems from the bulkiness of the azine unit in nearby positions to the N coordinating atom. Interestingly, increase of the steric hindrance at the alpha position (6-substituted derivatives) with relatively small substituents such as a methyl group or a chlorine atom resulted in a surprising *fac* configuration. In fact, considering the common orientation of these substituents, similar substitution patterns of bidentate ligands have been typically reported to lead to the *mer* isomer. In the case of the highly sterically demanding mesitylene group, target complexes were only achieved upon moving away the steric hindrance to position 5 of the azine unit, where *mer* isomers were mostly obtained instead. In spite of some preliminary computational calculations, explanation of the *fac*/*mer* selectivity requires a deeper investigation on the complexation mechanism, which is currently ongoing in collaboration with Dr. Antonio Francés Monerris.

Structural characterization of these complexes has revealed that *fac* isomers possess more distorted coordination spheres than the *mer* isomers, which could be deleterious for their EE dynamics. Nevertheless, it is also reasonable to think that the presence of more interligand interactions in *fac* derivates could prevent Fe-N bond elongation, which has been shown to be the main coordinate driving the MLCT excited states decay.[133] On the other hand, the nature of both the NHC unit and the extension of π-conjugation appeared to be the key parameters controlling their optical and redox properties, with both isomers exhibiting distinct behaviors. The use of π-extended azines is of particular relevance due to their low-lying MLCT manifold, which results in an improved absorbance in the visible range. In addition, the possible reduction of the electronic coupling with the MC states could contribute to longer-lived MLCT. A proper analysis of *fac*/*mer* influence on the EE kinetics will be the object of a following contribution to be taken in Strasbourg by Prof. Dr. Stefan Haacke.

Thus, this chapter highlights the great potential of this type of complexes that capitalize on the synergetic effect of combining a certain substitution pattern at the azine unit together with NHC. As a result, not only non-labile iron(II) complexes with a ligand-encoded stereochemistry can be prepared, but also with opto-electronic properties that can be easily fine-tuned as a function of both the azine and the NHC moieties. Moreover, π-extended quinoline and quinoxaline moieties exerted a similar preference for facial isomerism.

IV. Fe(III) complexes bearing tridentate anionic ligands

IV. Fe(III) complexes bearing tridentate anionic ligands

IV. 1 Introduction

As already mentioned in the introduction, the destabilization of the MC states is crucial for the development of photoactive iron complexes. Thus, the use of ligands inducing a sufficiently strong ligand field is a common feature of the different reported synthetic strategies (see §I.2.3). In this regard, the nature of the donor units plays a pivotal role on the energy splitting of the metal d orbitals. As theoretically shown by the group of Jakubikova, C-donor ligands induce the strongest ligand fields, followed by N-donors and O-donors, being the latter the weakest ligands (Figure 48).[42]

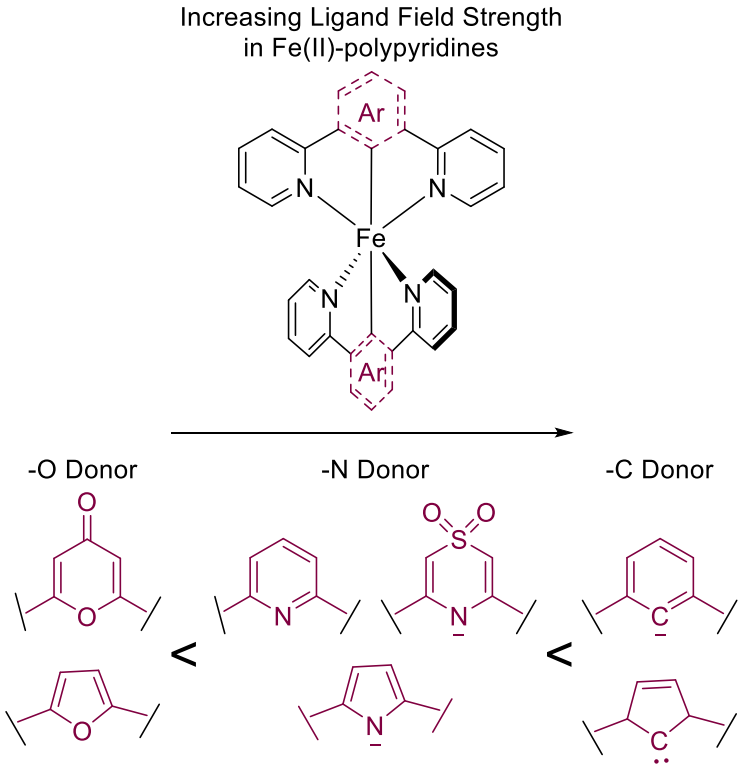

Figure 48. Fe(II)-polypyridines with different ligand donor strength investigated by Jakubikova and co-workers inspired from reference 42.

According to the angular orbital model, these distinct properties can be interpreted in terms of the different orbital overlap between C-, N- and O-based orbitals with the d metal orbitals (Figure 49).[151]

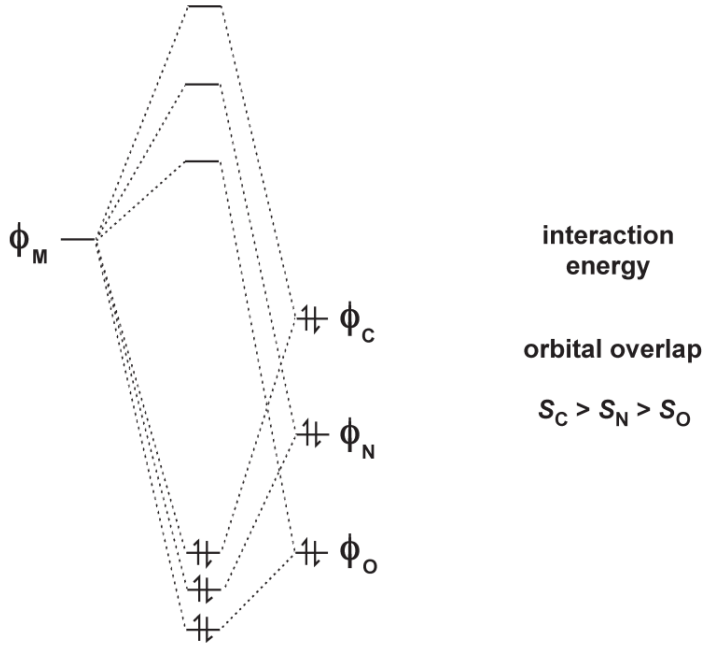

Figure 49. Angular overlap diagram to illustrate the higher interaction energy of C-based respect to N- and O- based ligands, thus justifying a stronger field strength. Taken from reference 151.

In the case of C-donors, Jakubikova also showed that cyclometalating units outperform NHC ligands. These results can be nicely illustrated by the experimental works of Che[152] and Berkefeld[69] dealing with photoactive iron complexes (Figure 50). The work of Che reported a MLCT excited state with a 21.4 ps lifetime for complex **[Fe(bpy^C)(bpy^NHC)]**$^{+}$ containing one cyclometalating unit plus one NCH unit. In comparison, Berkefeld reported a two-fold cyclomettalated **[(**^{phen}**N,N^C)**$_2$**Fe]** complex showing a MLCT excited state as well with a substantially increased ESL of 1 ns (2.4 ns in the solid state), thus proving their stronger capability to induce high ligand fields (Figure 50).

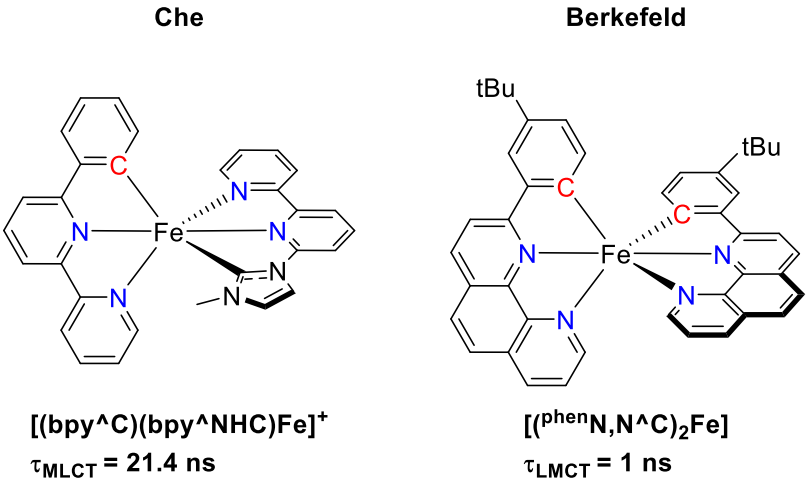

Figure 50. Structure and ESL of **[Fe(bpy^C)(bpy^NHC)]**$^{+}$ and **[Fe(**^{phen}**N,N^C)**$_2$**]** complexes.

However, imposing a strong electron-donating coordinating sphere results in a concomitant destabilization of Fe(II) respect to higher oxidation states, making the complexes easier to oxidize into Fe(III), as observed for neutral NHC[79] or (formally) anionic ligands such as cyclometallating rings,[153] amides,[72] or phenoxides.[154] For instance, Figure 51 depicts some Fe(IV) exemplars. Interestingly, while **[Fe**^{IV}**(**^{benzNHC}**OCO)**$_2$**]** has been described to be stable only in solid state (Figure 51a),[154] anionic **[Fe**^{IV}**(L-6H)]**$^{2-}$ is exceptionally stable under aqueous, acidic or basic media due to the shielding effect provided by the macropolycyclic cage on around the iron center.[155] Nevertheless, it is possible to counteract the overall metal orbital destabilization by means of the introduction of electron withdrawing groups. In fact, Jakubikova presented a theoretical analysis of Fe-pyridylcyclometallated complexes, in which the introduction of nitro (-NO_2) and carboxylic acids (-COOH) onto the ligand scaffold stabilized the orbital energies *via* electrostatic effects, conferring them oxidative stability in the Fe(II) oxidation state. But more importantly, the ligand field was maintained or even improved, constituting a very useful design strategy when using very strong ligands.[153]

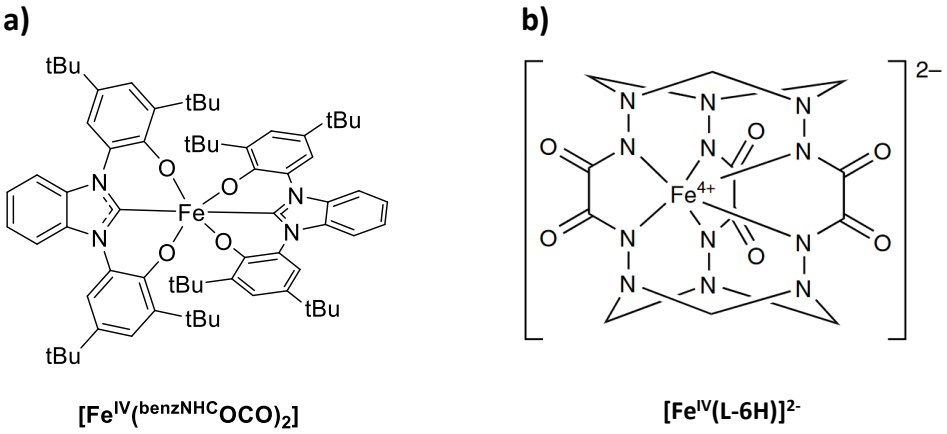

Figure 51. Structures of a) **[Fe^{IV}(^{benzNHC}OCO)$_2$]** and b) **[Fe^{IV}(L-6H)]$^{2-}$** complexes. Taken from references 154 and 155.

Another appealing feature of this type of complex bearing anionic ligands are the presence of rather low-energy absorptions. Furuyama described a set of Fe(II)-complexes **[Fe(PyrNH)$_2$]** and **[Fe(BzPyrNH)$_2$]** with two amido and four imino bonds (Figure 52b) in which the IR absorptions are assigned to MLCT transitions. On the other hand, Wenger reported the use of a tridentate bisNHC-carbazolate ligand (**L^{CNC}**), yielding the Fe(III)-based **[Fe(L^{CNC})$_2$]$^+$** complex (Figure 52).[156] The IR absorption was attributed to a ^{2}LMCT transition instead. Unfortunately, the authors characterized the excited state, revealing a ^{2}LMCT ESL of only 1.3 ps. However, they did not study in detail such a fast decay.

Thus, the objective of this chapter was to develop iron complexes bearing tridentate anionic ligands that could stabilize Fe(II). To modulate the electron-donation character of the coordination sphere, several strategies will be investigated including the substitution of NHC by imine donors or the introduction of electron-withdrawing moieties within the ligand scaffold.

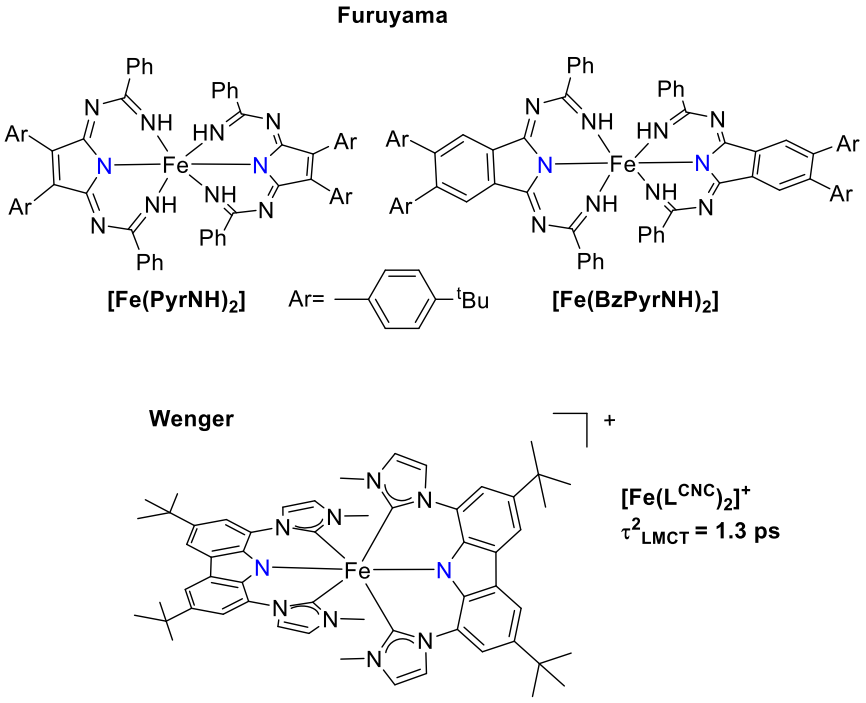

Figure 52. (Top) Complexes aminamide-Fe(II) **[Fe(PyrNH)$_2$]** and **[Fe(BzPyrNH)$_2$]**. (bottom) Structures and ESL of **[Fe(L^{CNC})$_2$]$^+$** complexes.

IV. 2 Amido tridentate anionic ligands

Motivated by the outstanding panchromatic absorption and nanosecond ESL of the pincer-like amido complexes reported by Herbert,[72] we decided to explore the effects of other anionic N-donor ligands on the properties of Fe complexes. To this end, we selected the carbazole-based ligands **H$_3$L23, H$_3$L23** and **HL25** shown in scheme 16. These ligands were expected to induce strong ligand-fields as a result of strong donor units (carbazolate together with NHC in **H$_3$L23** and **H$_3$L24**) as well as an improved M–L interaction due to the 6-membered chelate rings (Figure 53). Modulation of the donor properties of the ligands was envisaged at the lateral coordinating units.

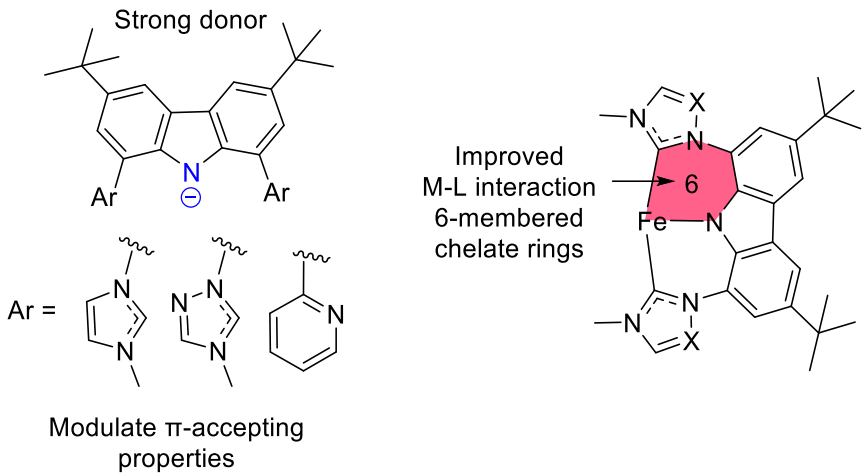

Figure 53. Electronical schematic representation of bisNHC-carbazolate ligand.

It is important to note that two articles from Wenger's group were published while developing the work described in this section: the first one concerning **HL25** (pyridine, See scheme 15),[157] then a second one in early 2022 concerning **H_3L24** (imidazole).[156]

IV. 2.1 Ligand synthesis

The synthesis of the ligands is depicted in Scheme 16. Introduction of two *t*-butyl groups at positions 4 and 7 of the carbazole scaffold was performed via a double Friedel-Craft alkylation with ^{t}BuCl and $AlCl_3$ in DCM, yielding intermediate **23a**. Subsequent bromination of positions 2 and 9 using bromine in acetic acid afforded the dibrominated intermediate **23b**, which allowed the introduction of the lateral coordination unites. The ligands **H_3L23** and **H_3L24** started with the introduction of either imidazole or 1*H*-1,2,4-triazole under Ullmann coupling conditions employing Cu_2O and Cs_2CO_3 in DMF, affording intermediates **23c** and **24c**, followed by the quaternization with MeI in DMF and anion metathesis, resulting in **H_3L23** (imidazolium) and **H_3L24** (1,2,4-triazolium) ligand precursors with 77% and 80% yield, respectively. In the other hand, the pyridyl-based ligand **HL25** was obtained in 80% yield by a Stille coupling reaction of **23b** with 2-(tributyltin)pyridine (Scheme 15).

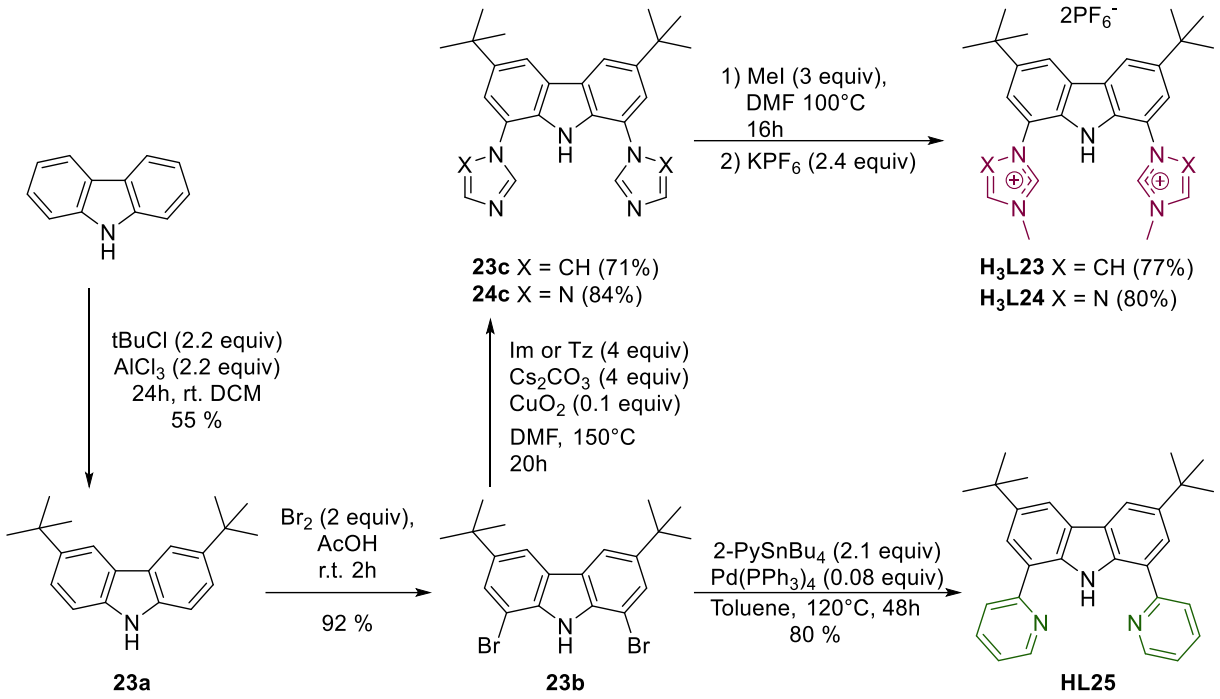

Scheme 15. Synthetic route of ligands **H_3L23, H_3L24** and **HL25**.

IV. 2.2 Complex synthesis: homoleptic series

With the target ligands in hand, we proceeded with the complexation reactions starting with **H_3L23** (imidazolium) (Scheme 16). Capitalizing on our experience, we opted for a step-wise protocol with the formation of the ligand **L23** in THF at low temperature (-40ºC) prior to metal coordination following $FeCl_2$ addition (See §III.2.1).[35] Selection of LiHMDS was motivated to favor LiCl formation as a driving force for the reaction. After purification of the reaction crude, a green solid was obtained. The ^{1}H-NMR analysis was not consistent with the initial target ferrous complex **C23** in Fe(II) oxidation state, with no signals from the ligand being neither observed (Figure 54). Instead, the corresponding paramagnetic Fe(III) species **C23$^+$** was obtained (40% yield) as established by HRMS and X-ray analysis and further confirmed by UV-vis spectroscopy and electrochemistry (see below). The formation of the Fe(III) form resulted from the strong donor character of the ligand. A difference in ^{1}H-NMR between ligand **H_3L23** and complex **C23$^+$** can be observed in Figure 54, attributed to the paramagnetic nature of the complex.[158]

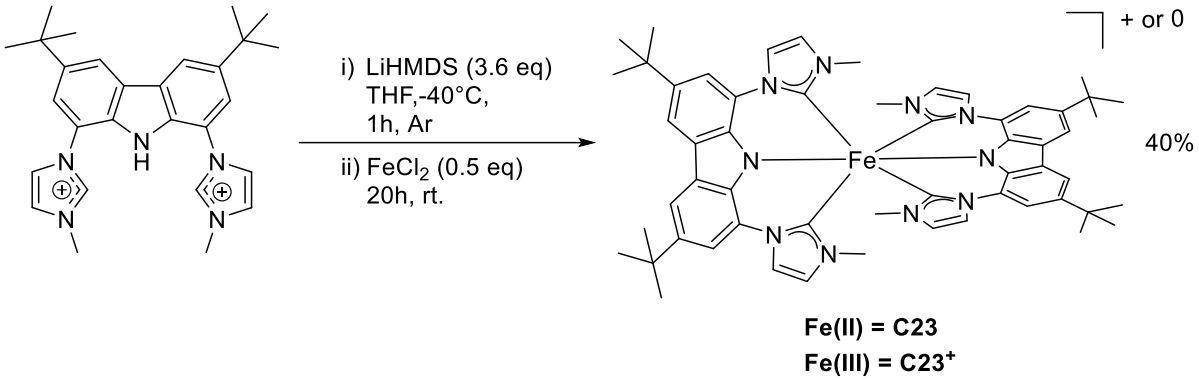

Scheme 16. Synthesis of complex **C23**$^{+}$. Counteranion is PF_6^- for all charged compounds.

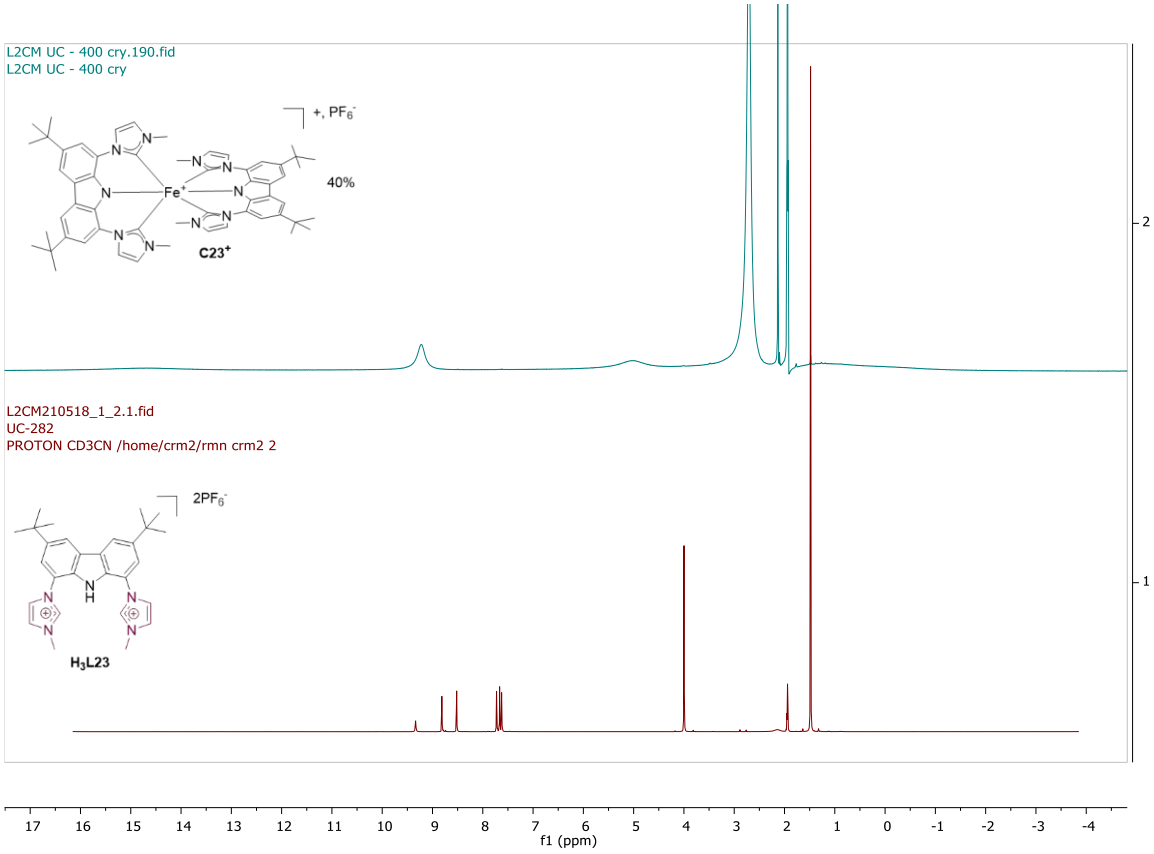

Figure 54. ^{1}H-NMR of complex **C23**$^{+}$ (top, cyan) and ligand **H$_3$L23** (bottom, red) recorded in in ACN-d_3.

Crystals suitable for X-ray diffraction were obtained by slow evaporation of CH_3CN. Nicely, the formation of the homoleptic complex **C23**$^{+}$ was confirmed. The associated X-ray structure is shown in Figure 55 and some selected structural parameters are gathered in Table 10. Interestingly, the octahedral geometry around the central iron atom is close to an ideal octahedron, with an average bite angle of ≈176.4° approaching the ideal 180°. The Fe–N bond

distances are slightly shorter (1.898(2) and 1.900(2) Å) than the Fe–C bonds lengths (1.991(2)–2.014(2) Å). The bond lengths are in the expectable range of values according to previously reports of iron(III) complexes containing Fe-N_{amido} and Fe-C_{NHC} reported by Herbert[72] and Wärnmark.[80] On the other hand, a pronounced torsion of 34.18º is observed for the NHC units respect to the carbazole moiety, resulting in an helical conformation for the tridentate ligand. Thanks to the X-ray structure we could envisage that both isomers exists, for more clarity in Figure 55 only one is shown.

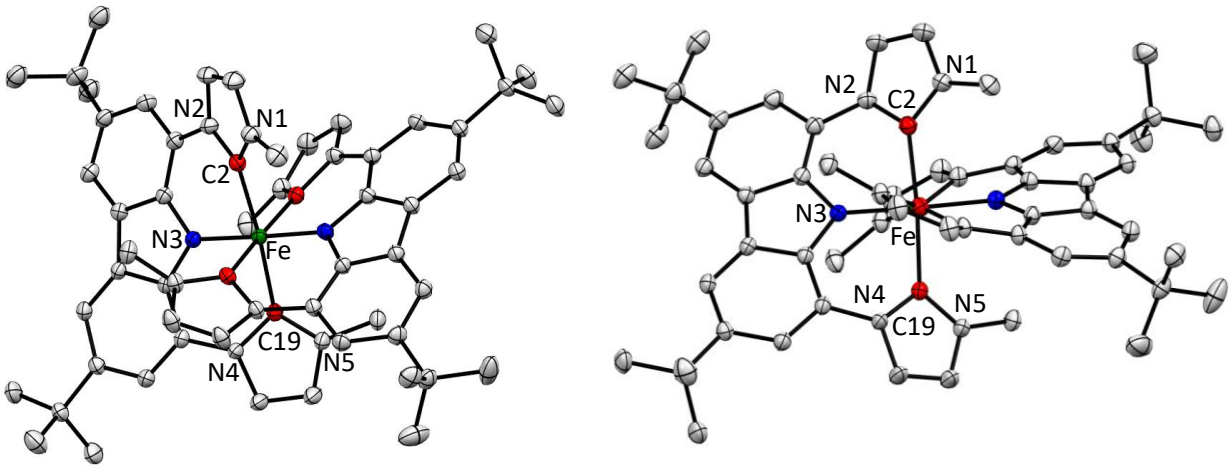

Figure 55. X-Ray crystal structure view of **C23**$^{+}$ complex. Hydrogen atoms and PF_6^- molecules are omitted for clarity.

Table 10. Selected structural and deformation parameters for **C23**$^{+}$ (esd in parenthesis).

Atoms	Bond distance (Å)	Atoms	Angle (°)	Torsion angle (°)
Fe–C2	1.991(2)	**C2-Fe-C19**	175.1(8)	-
Fe–N3	1.900(2)	**N3-Fe-N3'**	178.3(7)	-
Fe–C19	2.010(2)	**C2'-Fe-C19'**	175.8(8)	-
Fe–C2'	1.999(2)	**N2-N5**	-	45.5(2)
Fe–N3'	1.898(2)	**N2'-N5'**	-	38.7(2)
Fe–C19'	2.014(2)	-	-	-

After having validated the complexation conditions, we switched to the other ligands of the series, *i.e.* **H_3L24** (triazolium) and **HL25** (pyridine). To our surprise, these

complexations were unsuccessful. Therefore, a new set of optimization reactions was performed, with the results being collected in Table 11. Since **HL25** (pyridine) was supposed to be a ligand with better coordination ability, we began the new optimization process with this precursor upon adjusting the number of base equivalents to 1.2 per number of acidic-H (three for **H_3L24** and one for **HL25**). In order to favor the coordination to the metal center, a series of reactions were performed on changing the iron source for more labile species: $FeBr_2$ (entry 2) and $FeOTf_2$ (entry 3) respect to $FeCl_2$ (entry 1). However, no complex was obtained, with the initial ligand being recovered after the reaction. Considering the slightly lower bite angle imposed by **L25** (6-membered pyridine) in comparison to **L23** (5-membered imidazole), the metal coordination might be more difficult. As a result, an attempt was done with $FeCl_3$ instead since Wenger contemporarily reported a Cr(III) complex with the same ligand (entry 4).[157] Nevertheless, no complex was neither obtained, so ion size seemed not to play an important role. Following the same train of thought, another test was carried out increasing the temperature of the coordination step up to 50°C, but without success (entry 5).

Table 11. Optimization of the complexation reaction for **H_3L24** (triazolium) and **HL25** (pyridine).

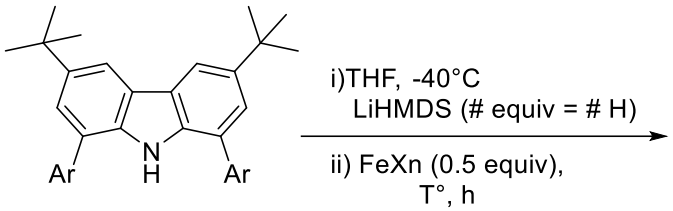

Ar = Ar
HL25 py = py
H_3L24 tz = tz

Entry	Ligand	Base	T (°C)	Time Reaction (h)	FeX_n	Product[a]
1	py	LiHMDS	rt	24	$FeCl_2$	s.m.
2	tz					–
3	py	LiHMDS	rt	48	$FeBr_2$	s.m.
4	tz					–
5	py	LiHMDS	rt	72	$FeOTf_2$	s.m.
6	tz					–
7	py	LiHMDS	rt	72	$FeCl_3$	s.m.
8	tz					–
9	py	LiHMDS	50	48	$FeCl_2$	s.m.
10	tz					–

[a]s.m.=starting material, – = any product recovered.

Similar results were obtained for the complexation reactions of **H_3L24** (triazolium), with 3.6 equivalents of LiHMDS in the case. In comparison to **HL25** (pyridine), no starting ligand was recovered, which indicated that deprotonation of the NHC units was accomplished in spite of the failed coordination. Considering that the complexation reaction was successfully achieved with **L23**, it seems unlikely that a too strong coordination of Li^+ to **L24** and **L25** could explain these results. Due to a lack of time, additional tests with other bases haven't been possible.

IV. 3 Complex synthesis: heteroleptic series

In order to stabilize Fe(II), we opted for the reduction of the number of strong donor ligands by conceiving tpy-based heteroleptic Fe-complexes (Figure 56). We envisaged that the improved M–L interaction afforded by **L23** (imidazole) could result in a sufficiently high field splitting in spite of the tpy ligand, which would provide with low-energy π* orbitals. Furthermore, tpy ligands allow for an easy and controlled access to heteroleptic complexes as it has previously reported in our lab.[159] The presence of the pendant pyridine in 4'-(pyridin-4-yl)-2,2':6',2''-terpyridine (4'-pytpy) would offer additional opportunities for property fine-tuning due to its electron-withdrawing character, along with the possibility of protonation or even additional metal coordination.

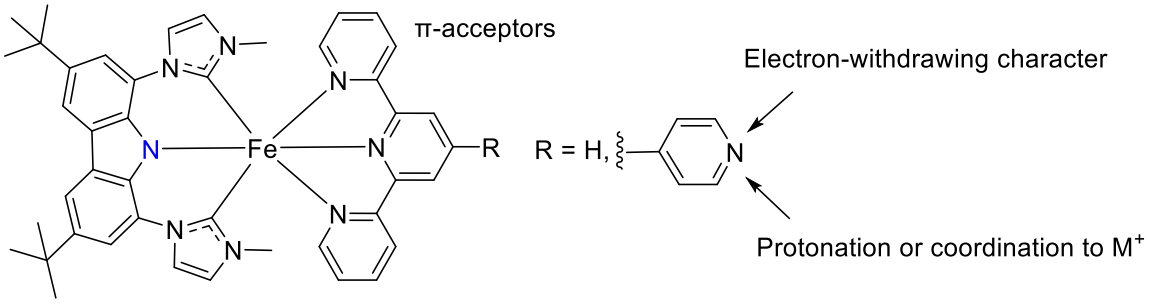

Figure 56. Schematic representation of electronic effects in heteroleptic **[Fe(L23)L]$^{2+}$** complexes. L= tpy and 4-pytpy.

The synthesis of these heteroleptic complexes is shown in Scheme 17. Ligand 4'-pytpy was synthesized following reported protocols,[160] by mixing of 2-acetylpyridine with 4-pyridinecarboxaldehyde in ethanol in the presence of KOH and ammonia solution. Then **[FeCl$_3$(tpy-R)]** compounds were prepared by mixing the corresponding **tpy-R** ligand with one equivalent of $FeCl_3$ in ACN at room temperature for 10 min.[159] As for the synthesis of the heteroleptic complexes, a two-step protocol was followed. After *in-situ* generation of **L23** upon deprotonation of **H$_3$L23** with LiHMDS in THF at -40ºC, the corresponding **[FeCl$_3$(tpy-R)]** was added, affording complexes **[Fe(L23)(tpy)]$^{2+}$** and **[Fe(L23)(4'-pytpy)]$^{2+}$** in 35% and 40% yield respectively.

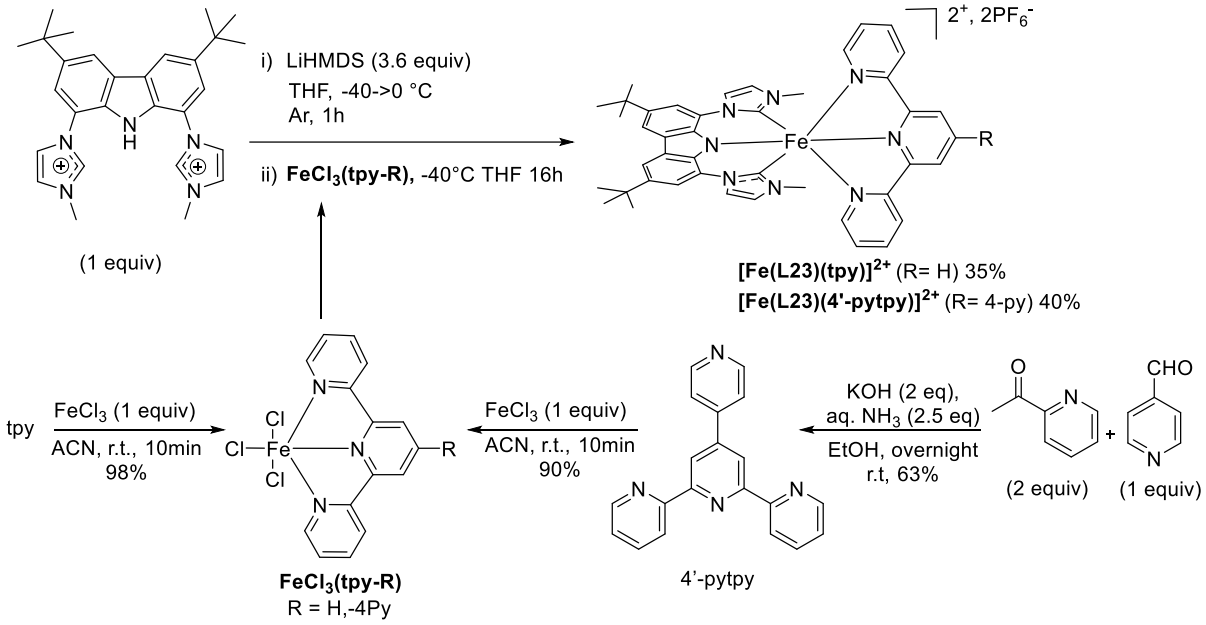

Scheme 17. Synthesis of **[Fe(tpy)]Cl$_3$**, **[Fe(4'pytpy)]Cl$_3$** intermediates and synthesis of heteroleptic **[Fe(L23)(tpy)]$^{2+}$** and **[Fe(L23)(4'-pytpy)]$^{2+}$** complexes.

IV. 3.1 Ground state characterization

The optical and electrochemical properties of complexes **C23$^+$**, **[Fe(L23)(tpy)]$^{2+}$** and **[Fe(L23)(4'-pytpy)]$^{2+}$** were investigated by UV-Vis spectroscopy and cyclic voltammetry and the main results are collected in Table 12 and Figure 57. The UV-vis spectra of the 3 complexes present a set of intense absorption bands in the UV-region (270–400 nm) that are assigned to

$^1(\pi \rightarrow \pi^*)$ transitions. Concerning the visible region, different absorptions are observed. In the case of **C23**$^+$, a series of absorption bands extend up to the green region with relatively high ε values (> $5 \cdot 10^4$ M^{-1} cm^{-1}) that seem to be the result of an admixture of metal 3d and orbital ligands recalling the "HOMO inversion" concept as already described for other similar complexes.[38,72] The lowest-energy band at 700–900 nm is attributed to a LMCT transition.[156] As for the heteroleptic complexes **[Fe(L23)(tpy)]**$^{2+}$and **[Fe(L23)(4'-pytpy)]**$^{2+}$, an absorption band is observed at *ca.* 560 nm, that can be attributed to the MLCT transition $^1(d\pi \rightarrow \pi^*_{tpy})$.[159] The very broad band at the lowest-energy part of the spectrum is tentatively attributed to a LMCT transition, though contributions from LL'CT (ligand-to-ligand charge transfer) transitions are likely as well. Calculations are currently ongoing in collaboration with Dr. Antonio Francés Monerris to gain insight into the exact nature of these electronic transitions.

Cyclic voltammetry of homoleptic and heteroleptic complexes were recorded with SCE as standard electrode and ferrocene as internal reference (Fc^+/Fc = 0.39V/SCE in acetonitrile) (see experimental part for further details). For complex **C23**$^+$, at positive potentials a first reversible anodic peak appears at 0.51 V while for **[Fe(L23)(tpy)]**$^{2+}$ and **[Fe(L23)(4'-pytpy)]**$^{2+}$ complexes at 0.94 V and 0.96 V respectively, which can be attributed to $Fe^{IV/III}$ oxidation. A second anodic event is observed for the three complexes around 1.02–1.17 V that can presumably be attributed to ligand oxidation. Especially in the case of the heteroleptic complexes, these results could support the idea of metal-ligand orbital mixtures as described in the "HOMO inversion" concept.[70,161–163]

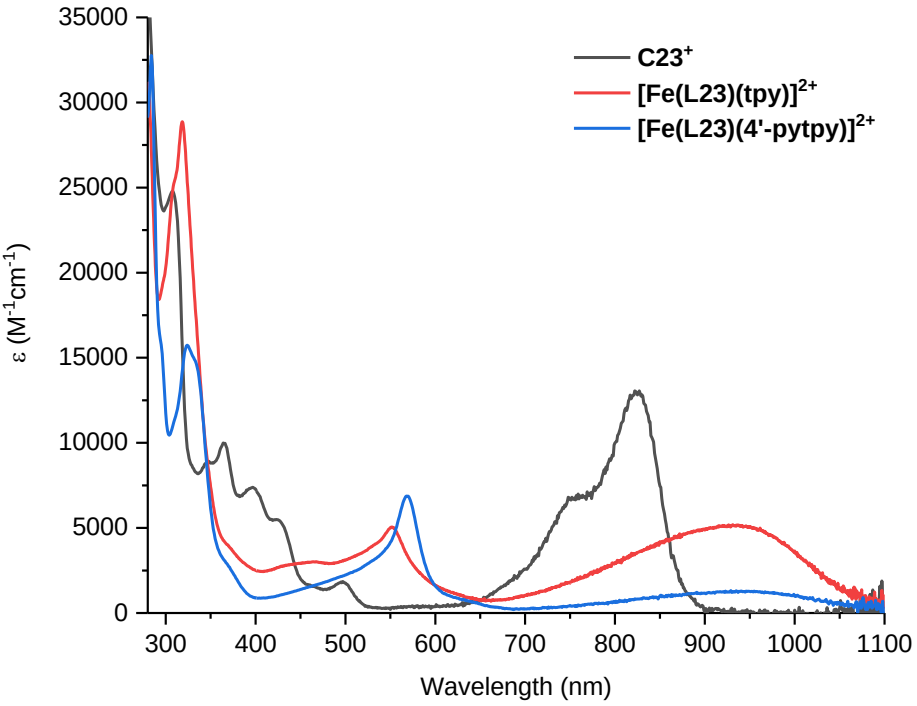

Figure 57. UV-Vis spectra of **C23**$^{+}$, **[Fe(L23)(tpy)]**$^{2+}$ and **[Fe(L23)(4'-pytpy)]**$^{2+}$ complexes in acetonitrile at room temperature.

At negative potentials, **C23**$^{+}$ presents one reversible wave at -0.93 V related to the $Fe^{III/II}$ redox couple. As for **[Fe(L23)(tpy)]**$^{2+}$ and **[Fe(L23)(4'-pytpy)]**$^{2+}$, four reduction waves at negative values appear for each heteroleptic complex: -0.06, -1.26, -1.42 and -1.59 for the former and -0.13 V, -1.43 V, -1.65 V and -1.86 V for the latter. The first reduction potential can be attributed to the redox couple $Fe^{III/II}$ since it is fully reversible and mono-electronic. Moreover, the increase in the reduction value from **C23**$^{+}$ (-0.96V) to **[Fe(L23)(tpy)]**$^{2+}$ (-0.06 V) and **[Fe(L23)(4'-pytpy)]**$^{2+}$ (-0.13V) could reflect well the less enriched metal of the heteroleptic complexes. The other three quasi-reversible cathodic events are confidently assigned to the tpy ligand reduction as for **[Fe(tpy)$_2$]**$^{2+}$.[164]

Table 12. Photophysical and electrochemical data for carbazole-based complexes **C23^{+}**, complex **[Fe(L23)(tpy)]$^{2+}$** and **[Fe(L23)(4'-pytpy)]$^{2+}$.**

Complex	$\lambda_{abs\text{-}max}$ (nm) [εM-1.cm-1)][a]	E_{ox}[b] [V/SCE]	E_{red} [V/SCE]	ΔE [V][c]
C23^{+}	307 [24771] 342 [8559] 364 [9991] 396 [7373] 426 [5450] 496 [1771] 752 [6808] 822 [13050]	0.51 (rev) 1.02 (rev)	-0.93 (rev)	1.44
[Fe(L23)(tpy)]$^{2+}$	319 [28873] 555 |4884] 934 [5178]	0.94 (rev) 1.11 (rev)	- 0.06 (rev) -1.26 (qr) -1.42 (qr) -1.59 (qr)	1.00
[Fe(L23)(4'-pytpy)]$^{2+}$	284 [32784] 323 [15670] 568 [6944] 946 [1240]	0.96 (rev) 1.17 (qr)	-0.13 (rev) -1.43 (qr) -1.65 (qr) -1.86 (qr)	1.09

[a]Measured in CH_3CN at 25°C; [b]First oxidation potential. Potentials are quoted *vs* SCE. Recorded in ACN using NBu_4PF_6 (0.1M) as supporting electrolyte at 100 mVs^{-1}; under these conditions, $E_{1/2\ (Fc+/Fc)}$ = 0.39V/SCE; rev = reversible; qr = quasi-reversible; irr = irreversible. [c]Electrochemical band gap ($\Delta E=E_{ox}-E_{red1}$).

Due to the strong donor character of the amido ligand we obtained three Fe(III) complexes. In the following section we will abord the cyclometalated ligands that are anionic strong donor ligands as well.

IV.4 Cyclometalated tridentate anionic ligands

Bauer's group has recently reported a nice Fe(III) example in which the complex **[Fe(ImP)$_2$]$^{+}$** (HImP=1,1'-(1,3- phenylene)bis(3-methyl-1-imidazol-2-ylidene)) (Figure 58),[163] shows a Janus-type dual emission by combining MLCT and LMCT luminescence. Interesting, the corresponding excited states exhibited a record 4.2 ns ESL for the MLCT state and a 0.2 ns ESL for LMCT state. Furthermore, not only luminescence is very rare for Fe-based compounds,[69,79,80] but a dual emission is a rather uncommon feature even for noble metals.[165] The unusual and unique properties of **[Fe(ImP)$_2$]$^{+}$** complex can be attributed to the ligand design upon combining four NHC units with two cyclometalating phenyl rings with both strong σ-donor and acceptor capabilities (Figure 58).

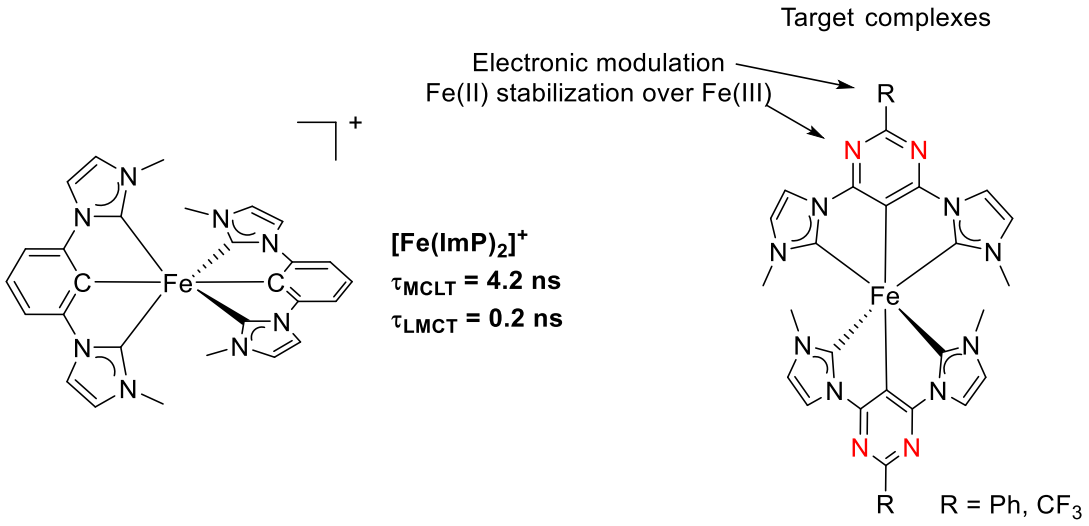

Figure 58. Structure of **[Fe(ImP)$_2$]$^+$** complex and ESL. Target iron bis-cyclometallated complexes.

In the framework of a 2-month internship at Bauer's lab within the DrEAM program, we envisaged new cyclometalated complexes by incorporating electron-accepting cyclometalating azine units while maintaining the strong σ-donor character of the ligands (Figure 58). This modification was driven by our interest in stabilizing the MLCT excited states for subsequent applications such as *n*-type DSSC[53,166] or photocatalysis (see § I.6). Furthermore, the eventual stabilization of cyclometalated Fe(II) species could be also of utmost importance due to their photocatalytic or luminescent properties.[69]

IV.4.1 Synthetic strategies to access cyclometalated iron complexes

In comparison to other metals, in particular those of the platinum group such as Ru, Os, Rh, Ir, Pd or Pt, cyclometallation reactions involving Fe are synthetically very challenging mainly to the low stability of the Fe-C bond, even when stabilized through multidentate chelates.[167] Since 1959 with the work of Hübel and Braye[168] to 2005 with the work of Klein,[169] iron cyclometalated complexes have been relatively rare. One methodology widely used is the one based of iron(0) precursors bearing phosphine ligands as $Fe(PMe_3)_4$[169–171] or carbonyls like $Fe(CO)_5$[170] that, in combination with ortho-directing groups, afford the corresponding

cyclometallated intermediate has been used by Che[152] and Bauer[172] to obtain heteroleptic complexes upon complexation of a second ligand as reported (Scheme 18).[169,170,173]

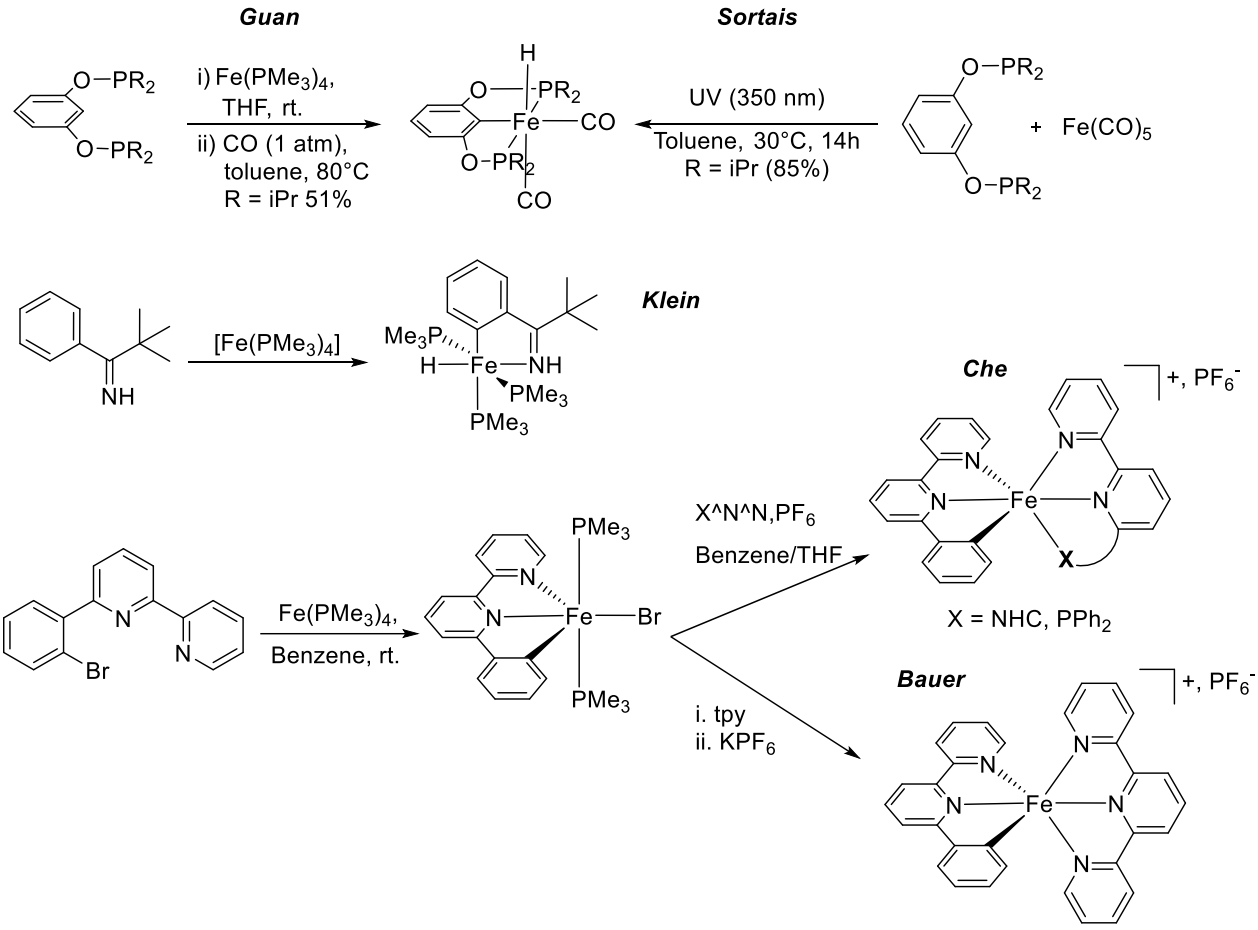

Scheme 18. Assisted synthesis of orthometallation using with $Fe(PMe_3)_4$ and $Fe(CO)_5$ with different ligands.

Methodologies to obtain cyclometalated-iron complexes using transmetalation reagents and bases are scarcer. In regard to transmetalation reactions, metals like zirconium[163] and mercury[174] has been used, but the price of the former and high toxicity of the latter prompt the research for greener alternatives. For instance, Fout reported the use of base as LiHMDS has been employed to form an NCH-Fe(III) bond followed by a further reduction to Fe(0), which allows for a C-H activation to occur, finally affording a cyclometalated C^C^C species (Scheme 19).[175]

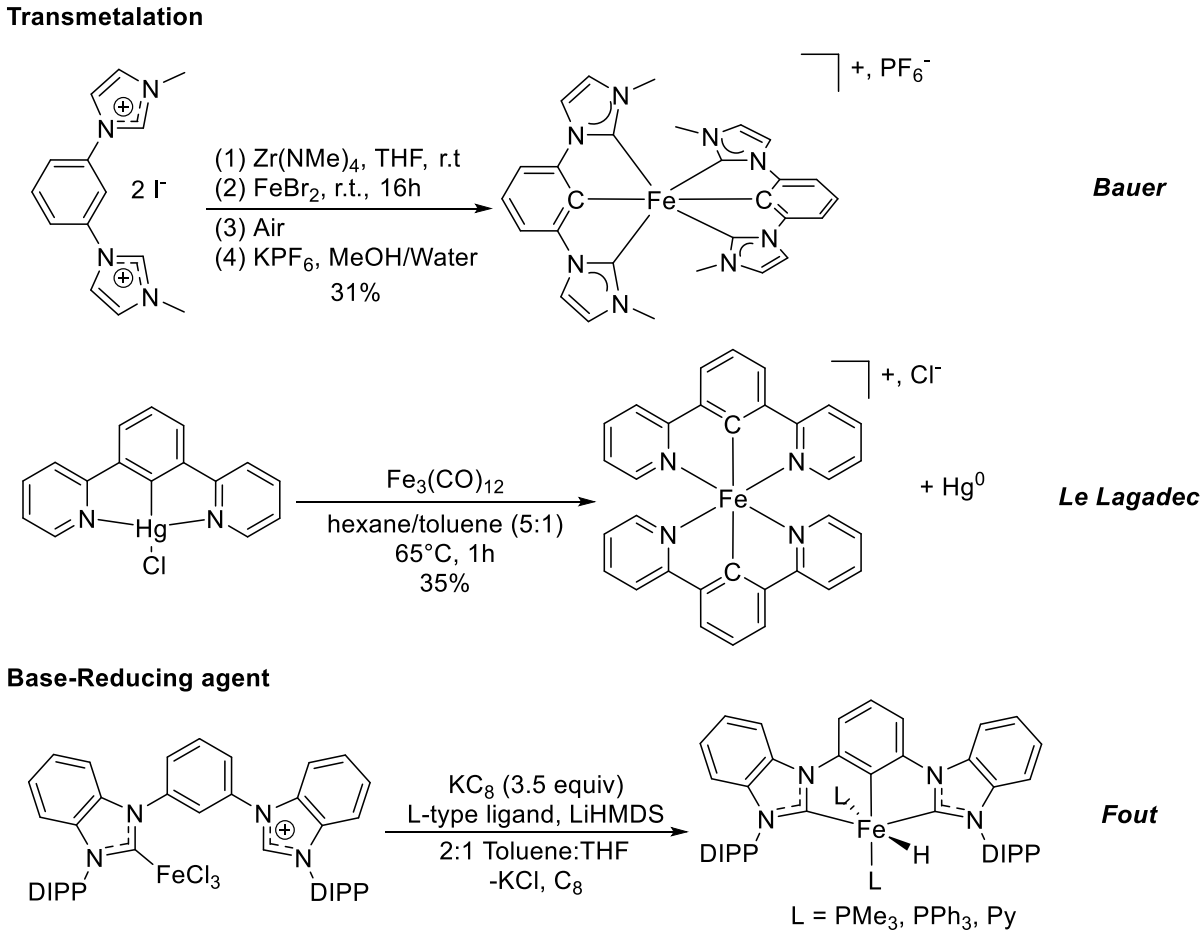

Scheme 19. Stepwise synthesis of heteroleptic Fe(II) complexes with transmetalation and base-reducing approaches.

IV.4.2 Ligand synthesis

The synthesis of the ligand precursors **H3L26** and **H3L27** is shown in Scheme 20. For both syntheses, 3,6-dichloropyrimidines differently functionalized in position 2, *i.e.* a phenyl ring and a trifluoromethyl group were chosen as starting materials. The interest for this heterocyclic unit was multifold: i) it would better stabilize Fe(II) over Fe(III); ii) the cyclometallation could take place in an easier manner; and iii) the pronounced electron acceptor character would stabilize the MLCT excited state. Furthermore, apart from their electronic modulation, the selected substitutions were intended to prevent a possible coordination of the ligand to the iron center in a bidentate fashion upon increasing the steric hindrance (R = Ph) or

reducing the nucleophilicity of the N donor atoms (R = -CF_3) (Scheme 20). Thus, target precursors were prepared by mixing the corresponding 4,6-dichloro-2-phenylpyrimidine with 2.5 equiv of N-methylimidazole in CH_3CN after three hours of stirring at 80°C and a solid corresponding to the target ligand precursors was recovered and used without any further purification.

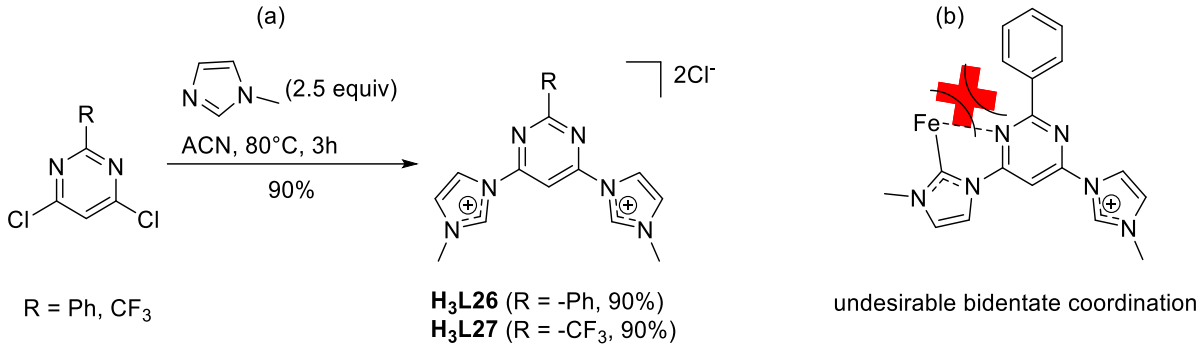

Scheme 20. a) Synthesis of **H_3L26** and **H_3L27** ligands, b) Steric demand in position -2 at the pyrimidine moiety prevents bidentate coordination.

IV.4.3 Synthesis of homoleptic complexes

At first, we followed the Bauer's metalation/transmetalation strategy[163] that starts by reacting the ligand **HL-ImP** with $Zr(NMe)_4$ (Scheme 22). Two possible intermediate organozirconium species could be formed (A or B)[176] from which a transmetalation would happen after the addition of $FeCl_2$. Once the complex is obtained, a presumably air oxidation occurred followed by an anion exchange, affording the final **$[Fe(ImP)_2]^+$** complex with a 31% yield.

Based on the previous results from Bauer, the preparation of complex **$C26^+$** was initially attempted by means of the metalation/transmetalation strategy (Table 13).

Ligand **H_3L26** was first mixed with $Zr(NMe_2)_4$ in THF for 2h, then $FeCl_2$ was added and the reaction mixture was stirred during 16h (Table 13, entry 1). Only byproduct **28** was formed. The high electrophilicity of the position 4 and 6 of the pyrimidine ring in combination with the imidazolium as leaving group clearly favor the double S_NAr reactions of the amides

instead of deprotonating the procarbenic proton. Then we changed the reaction times in order to decrease this undesired side reaction. As in entries 2 and 3, the ligand **H_3L26** was mixed with $Zr(NMe_2)_4$ in THF for 1 h instead, then $FeCl_2$ was added and stirred for 16h and 2h, resulting in the same **28** product. The formation of byproduct **28** as only product regardless the time of metalation/transmetalation prompted us to change of strategy.

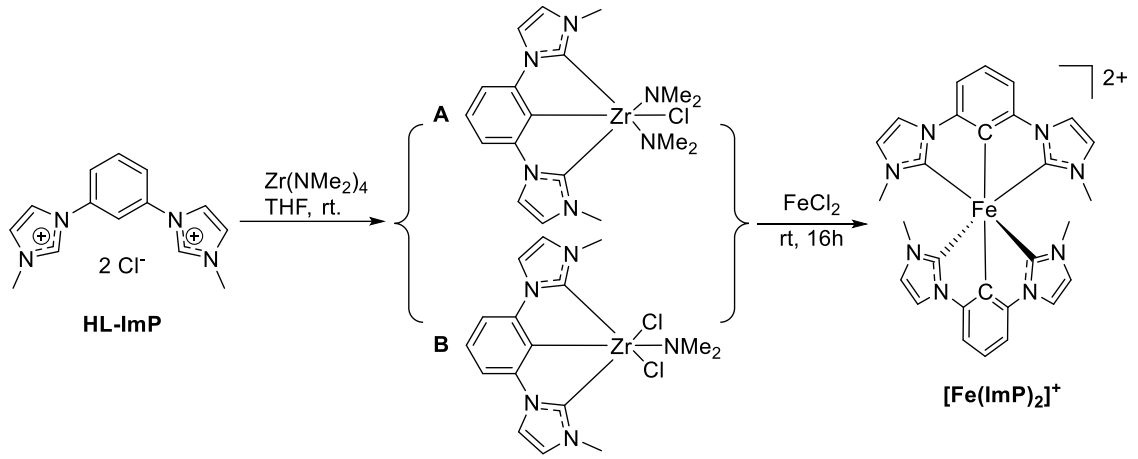

Scheme 21. Schematic representation via a metalation/transmetalation strategy in **$[Fe(ImP)_2]^+$** complex formation.

Aiming to avoid byproduct **28**, we tried to inhibit its formation decreasing the number of NMe_2 surrounding the Zr center by addition of 2 equiv of MeI to form the intermediate $Zr(NMe_2)_2I_2$. So, we mixed $Zr(NMe_2)_4$ with MeI (entry 3) for 1h, then ligand **H_3L26** was added and stirred over 3h, after this time $FeCl_2$ was added and led stirring overnight. Unfortunately, the only product was still byproduct **28**.

Additionally, instead of -NMe_2 we opted for a more sterically hindered base. $ZrCl_4$ was mixed with 4 equiv of TMPMgCl (2,2,6,6-tetramethylpiperidinylmagnesium chloride lithium) in THF with the aim to form $Zr(TMP)_4$ and thus prevent the substitution of the imidazolium (Entry 5). However, the reaction did not proceed either, giving a decomposition of the ligand and no substitution of the TMP over the pyrimidine.

Table 13. Synthesis of complex **C26**$^{+}$ metalation/transmetalation method.

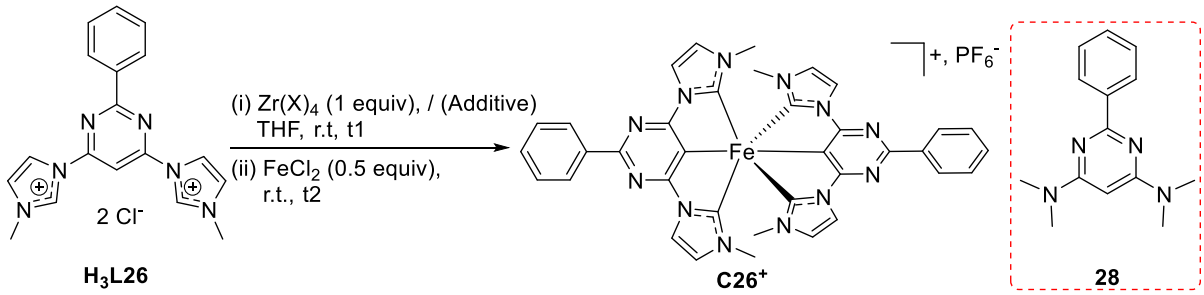

Entry	t1, t2 (h)	Additive (equiv)	Product
1	2, 16	-	**28**
2	1, 16	-	**28**
3	1, 3	-	**28**
4[a]	(Zr + MeI 1 h)	MeI (2)	**28**
5[b]	2, 16	TMPMgCl (4)	ligand degradation

[a]$Zr(NMe_2)_4$ with MeI (2 equiv) with for 1h, then ligand **H_3L26** for 2h, then $FeCl_2$ overnight. [b]$ZrCl_4$ + TMPMgCl (TMPMgCl= 2,2,6,6-Tetramethylpiperidinylmagnesium chloride lithium chloride).

In view of these results, the transmetalation/metalation strategy was abandoned and we decided to change the approach by using [Fe(HMDS)$_2$] (HMDS=hexamethyldisilazane), so as to deprotonate-coordinate as fast as possible to promote the complex formation.[177] Contrary to other reported protocols, we opted by an *in situ* formation of this starting material due to its high reactivity, which makes difficult its proper storage. The [Fe(HMDS)$_2$] was formed under Schlenk conditions by mixing $FeCl_2$ and LiHMDS at low temperature (Scheme 22). In parallel, in another Schlenk the ligand **H_3L26** was deprotonated with LiHMDS to generate the carbenes (Scheme 22, **L26**), then it was transferred into the Schlenk containing the preformed [Fe(HMDS)$_2$] at -40°C. The reaction mixture was stirred overnight allowing it to reach room temperature, and complex **C26**$^{+}$ was obtained in 36% yield after a filtration over Celite.

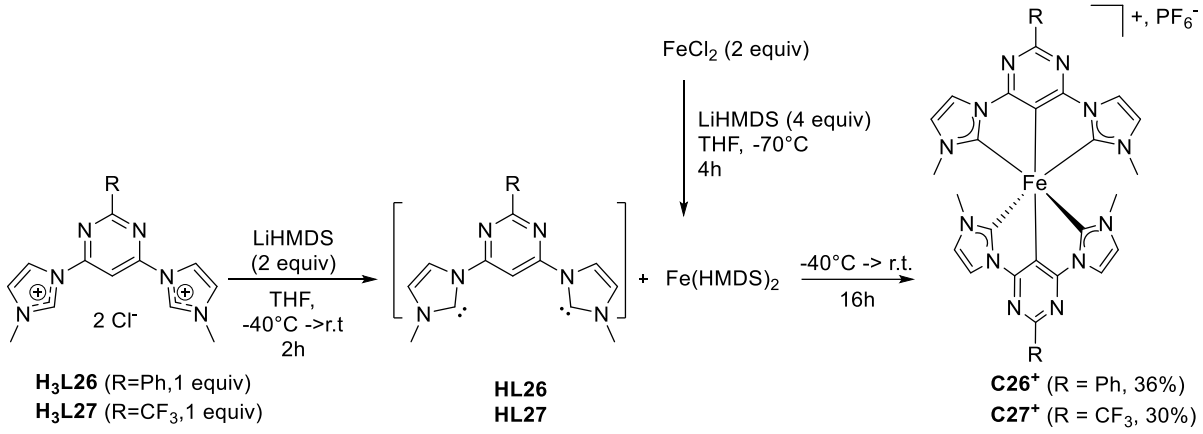

Scheme 22. Synthetic route to **C26**$^{+}$ **and C27**$^{+}$ complexes, base approach.

The complex formation was confirmed by mass spectrometry and ^{1}H-NMR (Figure 59, bottom). The ^{1}H-NMR of **C26**$^{+}$ (Figure 59, bottom) shows a shift in all its signals in comparison to the ligand **H$_3$L27** (Figure 59, top), appearing over a very large chemical shift range (-4 to 13 ppm). Furthermore, the coupling loss and the peak broadening can be clearly attributed to the paramagnetic Fe(III) center. With this stablished protocol, we proceeded to do the same with ligand **H$_3$L27** affording the complex **C27**$^{+}$ with 30% yield. This result is remarkable since at first glance the protocol is similar to the one reported by Fout (Scheme 19),[175] but with this approach we avoid the use of an external reducing reagent to get the cyclometallated complex.

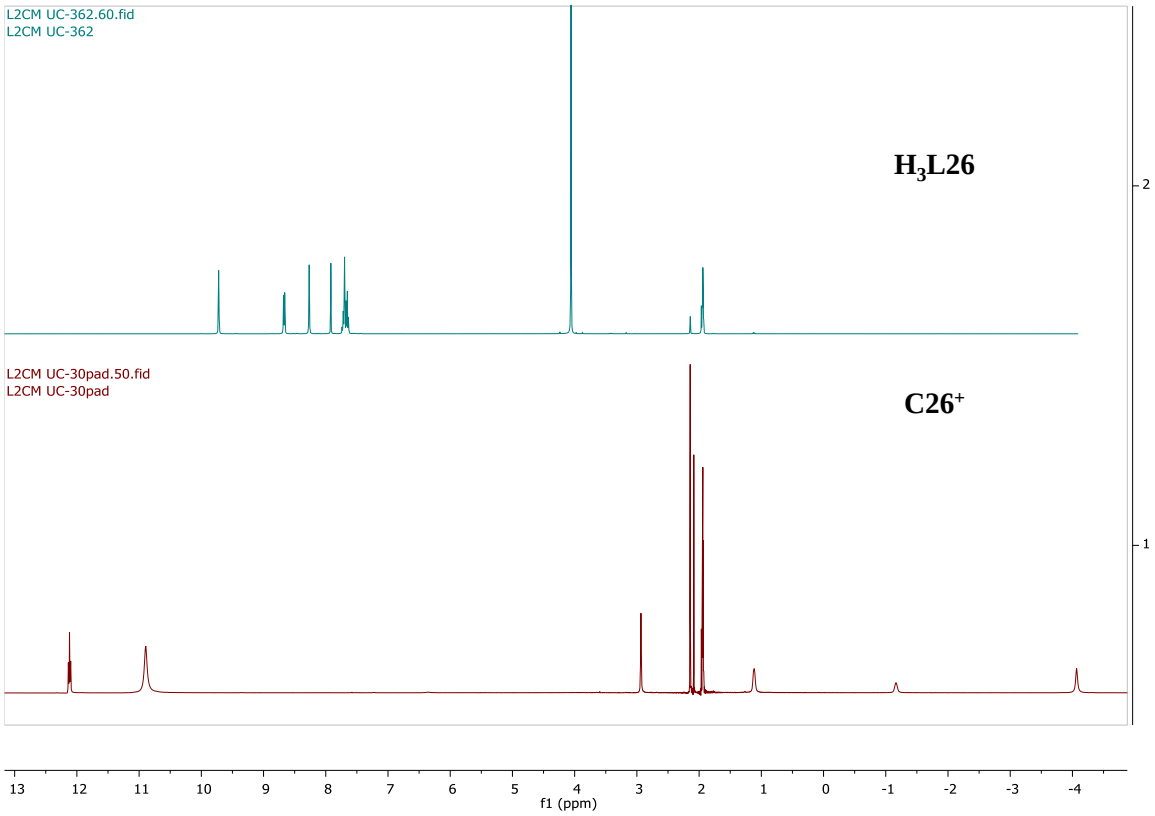

Figure 59. ^{1}H-NMR in ACN-d_3 of ligand **H$_3$L26** (top) and complex **C26$^+$** (bottom).

IV.4.4 Ground state characterization

Optical and electrochemical properties of complexes **C26$^+$** and **C27$^+$** were investigated by UV-Vis spectroscopy and cyclic voltammetry, and the main results are collected in Table 14 and Figure 60. The data of complex **[Fe(ImP)$_2$]$^+$** reported by Bauer is added for comparison reasons. Both complexes display three distinct absorption bands. At the highest energy side of the spectra (200–250 nm), intense absorption bands assigned to π–π* transitions are observed. In the range of 300–450 nm, there are two additional bands that are can be ascribed to MLCT transitions.[163] In fact, the electron accepting character of the pyrimidine backbone results in a bathochromic shift of these MLCT bands respect to that of **[Fe(ImP)$_2$]$^+$**. In addition, a further bathochromic shift is observed for **C27$^+$** in comparison to **C26$^+$**, which agrees well with the lower ligand-based π* orbital of the CF_3 derivative.

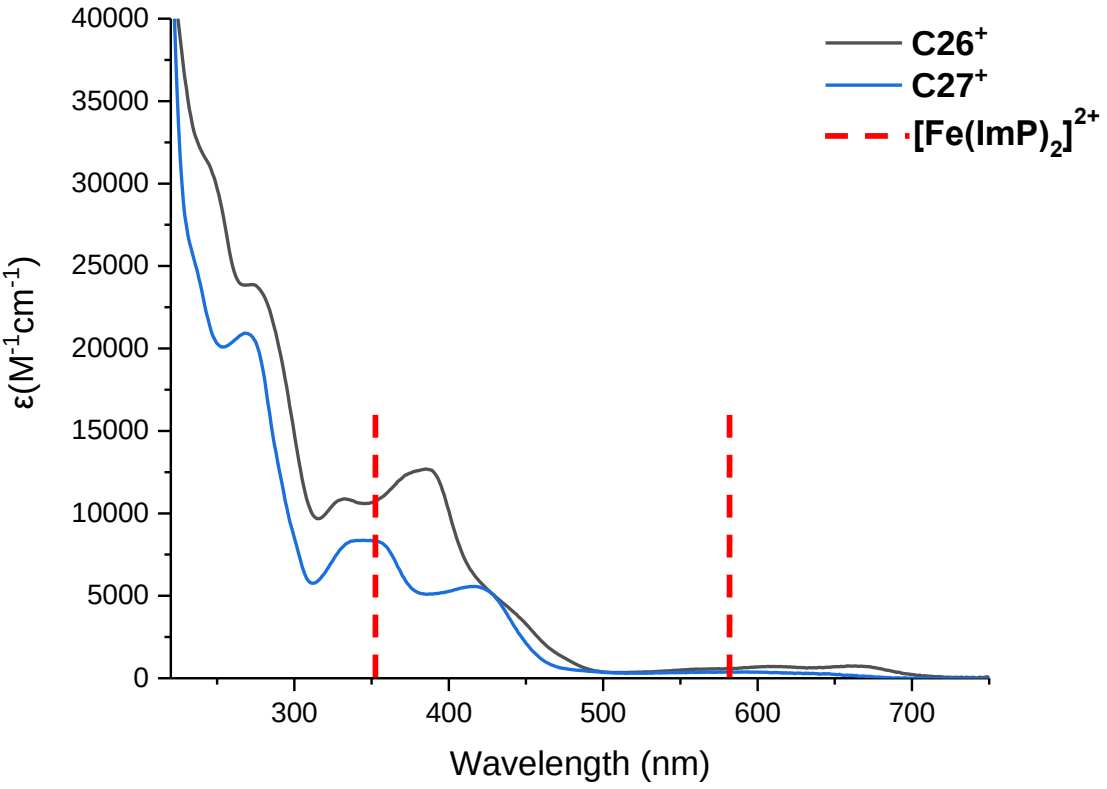

Figure 60. UV-vis spectra in air-equilibrated acetonitrile solution of **C26**$^{+}$ and **C27**$^{+}$ complexes. Corresponding data for **[Fe(ImP)$_2$]**$^{+}$ (dotted lines at 351 nm for MLCT and 585 nm for LMCT transitions) are shown for comparison reasons.

Table 14. Photophysical and electrochemical data for **C26**$^{+}$, **C27**$^{+}$ and **[Fe(ImP)$_2$]**$^{+}$ complexes.

Complex	$\lambda_{abs\text{-}max}$ (nm) [ε($M^{-1}.cm^{-1}$)][a]	E_{ox}[b] [V/SCE]	E_{red} [V/SCE]	ΔE [V][c]
C26^{+}	275 [23735] 329 [10922] 386 [12767] 557 [521] 606 [741] 665 [720]	0.71 (rev)	-0.35 (rev)	1.06
C27^{+}	268 [20973] 346 [8375] 421 [5569] 595 [393]	1.03 (rev)	-0.063 (rev)	1.09
[Fe(ImP)$_2$]$^{+}$	351 [6000] 585 [540]	0.47 (qr) 1.62 (irr)	-0.77 (rev)	1.24

[a]Measured in CH_3CN at 25°C; [b]First oxidation potential. Potentials are quoted *vs* SCE. Recorded in CH_3CN using NBu_4PF_6 (0.1M) as supporting electrolyte at 100 mVs^{-1}; under these conditions, $E_{1/2\ (Fc+/Fc)}$ = 0.39V/SCE; rev = reversible; irr = irreversible; qr = quasi-reversible. [c]Electrochemical band gap ($\Delta E=E_{ox}-E_{red}$). [d]Data taken from reference 204 considering $E_{1/2(Fc+/Fc)}$ = 0.39 V/SCE.

At longer wavelengths (590–670 nm), the broad bands with very low extinction coefficients are tentatively assigned to LMCT transitions, which are again red-shifted in comparison to **[Fe(ImP)$_2$]$^+$**.[163] In the case of **C26$^+$**, the presence of the phenyl substituent leads to an increased absorption, especially in the UV region.

As for the electrochemistry, at positive values, both complexes present one reversible oxidation potential at 0.71 V and 1.03 V for **C26$^+$** and **C27$^+$**, respectively, attributed to the couple redox Fe^{III}/Fe^{IV}, while for **[Fe(ImP)$_2$]$^+$** the much lower value of 0.47 V indicates a clear effect of the electron withdrawing pyrimidine backbone. However, no the ligand-centered oxidation was observed as in parent **[Fe(ImP)$_2$]$^+$** (1.62 V).Concerning the cathodic potentials, one reversible wave reduction is observed at -0.35 V and -0.063 V for **C26$^+$** and **C27$^+$**, respectively, that is attributed to the redox couple Fe^{II}/Fe^{III}. From these results it becomes clear the stabilizing orbital effect of having an electron withdrawing group as $-CF_3$ in comparison to the one with -Ph group, without a remarkable change in the electrochemical band gap. Interestingly, the reduction to the divalent species becomes noticeable easier for the pyrimidine series respect to the phenyl-based **[Fe(ImP)$_2$]$^+$**.

IV.5 Conclusions

In this chapter, we synthesized and characterized a set of strong anionic ligands bearing NHC units, three N-amido (carbazolate series) and two C-anionic (cyclometalated series). In regard to the N-amido series, we successfully afforded three complexes, one homoleptic and two heteroleptic. The metal–ligand interaction was maximized due to the formation of 6-membered chelates. The strength of the coordination sphere was modulated as a function of the number of coordinated N-amido ligands, although in all cases Fe(III) species were obtained. Interestingly, both homoleptic and heteroleptic compounds seemed to have metal-based and ligand-based orbital mixing as evidenced by their oxidation behavior, suggesting that this type of ligands could be useful to achieve a full "HOMO inversion" as defined by Jakubikova. More distinct properties arose from their reduction behavior, with the heteroleptic complexes featuring a remarkably anodically shifted first reduction potential that could reflect the less enrich metal ion respect to the homoleptic complex. In addition, reduction of the tpy moieties

was observed as well due to their strong acceptor character. Interestingly, both series of complexes displayed an enlarged absorbance until the IR region, with the heteroleptic complexes seemingly showing a higher contribution of outwards electronic transfers (from the carbazolate and the metal towards the tpy, MLCT+LL'CT) respect to the inwards LMCT transitions.

As for the C-anionic ligands, a new methodology to get two new bis-cyclometalated Fe-CCC complexes was developed without the use of glove box and avoiding the use of any transmetallating or reducing reagent. These complexes feature a cyclometalating pyrimidine unit that allows for stabilization orbital effects induced by the pyrimidine backbone and the substituents in position 2. This is reflected on the redox potentials between **C26**$^{+}$ and **C27**$^{+}$ and **[Fe(ImP)$_2$]**$^{+}$: as the electron withdrawing character increases, an anodically shift is observed their reduction potential wave. The UV-vis absorption display three distinct absorption bands corresponding to π–π* (200–250 nm), MLCT (300–450 nm) and LMCT (590–670 nm) transitions which are lower energy in comparison to **[Fe(ImP)$_2$]**$^{+}$. Finally, the presence of the phenyl substituent leads to an increased absorption specially in the UV region.

As a perspective, further optimization reactions are required to perform the coordination of the different N-amido ligands. Moreover, the dynamics of the excited state relaxation of all complexes will be investigated (TAS experiments) in collaboration with Prof. Dr. Haacke in Strasbourg and with Dr. Antonio Francés Monerris in Valencia will determine the nature of the electronic transitions corresponding to the UV-vis transitions. These calculations and experiments will allow us to understand better the impact of the ligand nature on the ESL. In order to complete this part of the work.

V. Iron complexes as photosensitizers towards H_2-evolving bimetallic photocatalysts

V. Iron complexes as photosensitizers towards H_2-evolving bimetallic photocatalysts

V.1 Introduction

Hydrogen is the most abundant element in the universe. Consisting only in one proton and one electron, it is the building block for the formation of all other elements in the stars by means of nuclear reactions. It is also one of the most abundant elements in the Earth's crust as well as in living organisms, although it is mostly found combined to other elements as in the case of water (H_2O). Furthermore, hydrogen plays a pivotal role in acid-base reactions, where protons are exchanged between molecules.

Molecular dihydrogen (H_2) is used for numerous industrial purposes such as the production of fertilizers, food processing, pharmaceutics, metallurgy and refining just to name a few. However, H_2 is not abundant in nature and must be produced from hydrogenated compounds (NH_4, MeOH, *i.e.*). Interesting, H_2 is a particularly light energy carrier that can deliver or store enormous amount of energy. For instance, 1 kg of H_2 (energy density = 120 MJ kg^{-1}) generates more than three times energy than 1 kg of gasoline (energy density = 44 MJ kg^{-1}).[178] In addition, H_2 can be used as power generator in fuel cells to produce electricity, power or heat, justifying its growing interest as a key actor for the energy transition. Indeed, the demand of H_2 has grown more than threefold since 1970 and is continuously rising (Figure 61).[179]

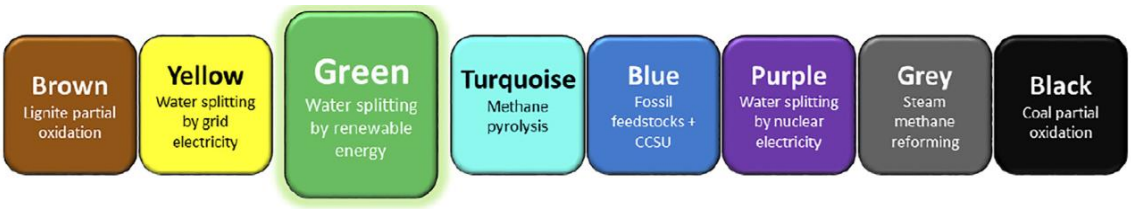

Figure 61. Colors of the hydrogen production processes. Taken from reference 180.

Currently, most of the production of H_2 comes from fossil fuels (*black and grey hydrogen,* Figure 61) and, in a lower scale, water electrolysis and biomass (*yellow and brown*

hydrogen). Unfortunately, the production via fossil fuels generates a massive production of greenhouse gases as by products. Thus, there is an urgent need to find environmentally friendly processes for its sustainable production. In this regard, water splitting (WS) is a very promising alternative (Eq 1). Splitting water evolves in H_2 and oxygen (O_2) as products and can be separated in two half reaction: proton reduction (Eq 2) and water oxidation (Eq 3) with relatively low carbon footprint is associated to this production methodology, ultimately depending on the electricity source (*purple hydrogen* from nuclear power; *green hydrogen* from renewable sources, with sunlight receiving increasingly attention.

$$H_2O \rightleftharpoons H_2 + \frac{1}{2}\,O_2 \qquad \Delta E° = 1.23\,V \qquad \textbf{Eq 1}$$

$$2H^+ + 2e^- \rightleftharpoons H_2 \qquad E^0 = 0\,V\ vs\ RHE \qquad \textbf{Eq 2}$$

$$H_2O \rightleftharpoons \frac{1}{2}O_2 + 2H^+ + 2\,e^- \qquad E^0 = 1.23\,V\ vs\ RHE \qquad \textbf{Eq 3}$$

Nevertheless, WS into H_2 and O_2 is an extremely difficult process both from a thermodynamic and kinetic point of view. In this regard, alternatives are in constant development such as molecular catalysis,[181] photoelectrochemical at solid or semiconductor surfaces,[2] biomass conversion or enzymatic[3–5] as alternatives in the quest for greener hydrogen production. Among these alternatives, the molecular systems provide the tools to obtain atom-efficient catalysts with outstanding intrinsic activities.[181] Indeed, molecular systems can be subjected to high level of design and modification through chemical synthesis. In addition, the mechanisms and kinetics can be probed through spectroscopic measurements, allowing us to have a better understanding of hydrogen evolution systems. Thus the approach here addressed, will be the photocatalytic molecular homogeneous systems. The photocatalytic H_2 production can be classified depending on the origin and nature of the proton and electron. According to literature, four main types can be identified (Scheme 23).[182]

i) **Direct R-H Substrates.** Hydrogen production from R-H substrates produces electron and proton equivalents from homo- or heterolysis of R-H bonds. This process often uses inner sphere mechanisms, with the catalyst directly bounded to the substrate. The common substates are alkanes, primary and secondary alcohols, which after H_2 generation produce alkenes, aldehydes or ketones as by-products.

ii) **Acids.** Hydrogen can come directly from acids, the main drawback here is the degradation of the catalyst by oxidation of the conjugate base.

iii) **Carbon Monoxide.** Reaction between water-gas-shift (WGS) couples the oxidation of CO to CO_2 with the reduction of water to H_2.

iv) **Indirect RH substrates and acids.** This is the most common approach.[6] The first approach was a three-system component that consisted on 1) A redox photosensitizer (PS), which absorbs light and make the electron transfer to 2) An electron relay (ER) that transfer the electrons to the 3) Proton reduction catalyst (Cat).

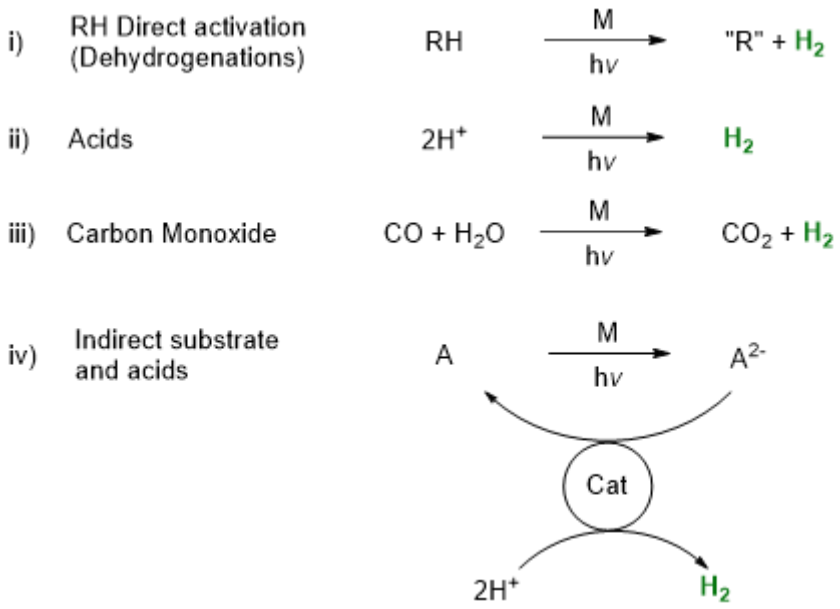

Scheme 23. Schematic representation of H_2 production in a molecular homogeneous catalytic system. Inspired by reference [182].

The first reported systems were the three-component ones, containing a PS, Cat and an electron relay (ER). Afterwards, further research that showed that the electrons could be transferred directly from PS to Cat, without the necessity of the ER,[182] and the three-component system was simplified into a two-component one. In the two-component system the electron transfer is limited by the diffusion (Figure 62a), whereas in the single-component system (dyad), the photosensitizer and the proton reduction catalyst (PRC) are chemically linked and thus, a vectorial electron transfer through a conjugated linker is required (Figure 62b). In both systems, a sacrificial reagent/electron donor (SR) is required to regenerate the photo-oxidized chromophore.

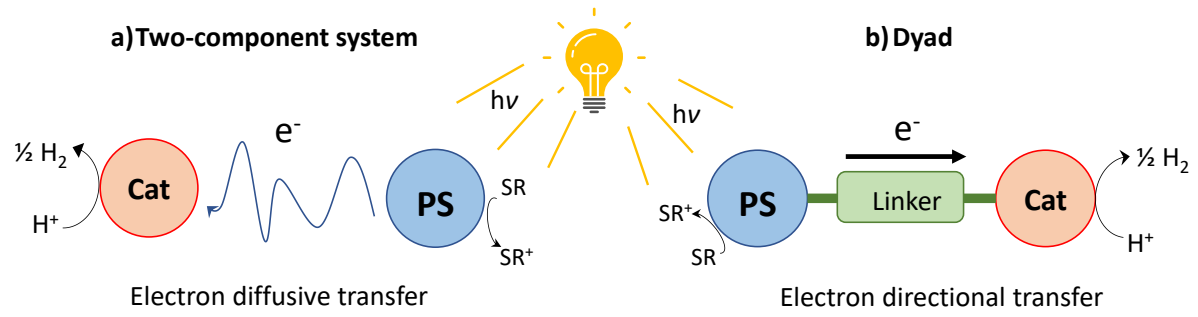

Figure 62. General schemes for light-driven proton reduction catalysts: a) two-component system; b) dyad. PS = Photosensitizer, Cat = Catalyst (PRC), SR = Sacrificial reagent.

For the two-component system, a wide range of PS have been studied and developed in order to allow thermodynamically-favored electron transfer (Figure 63), such as organic molecules (e.g. Eosin Y) [183–185] or metal complexes. The former possess rather intense, though narrow, absorptions and suffer from photostability issues. The latter comprise Co or Zn-porphyrin pigments[180,186,187] or noble metal-based complexes. PS based on Ru[188,189] and Ir[190,191] have been widely used because they combine long-lived charge transfer excited states, broad light absorption (UV-visible-NIR) and favorable ground and excited state redox properties (Figure 63).

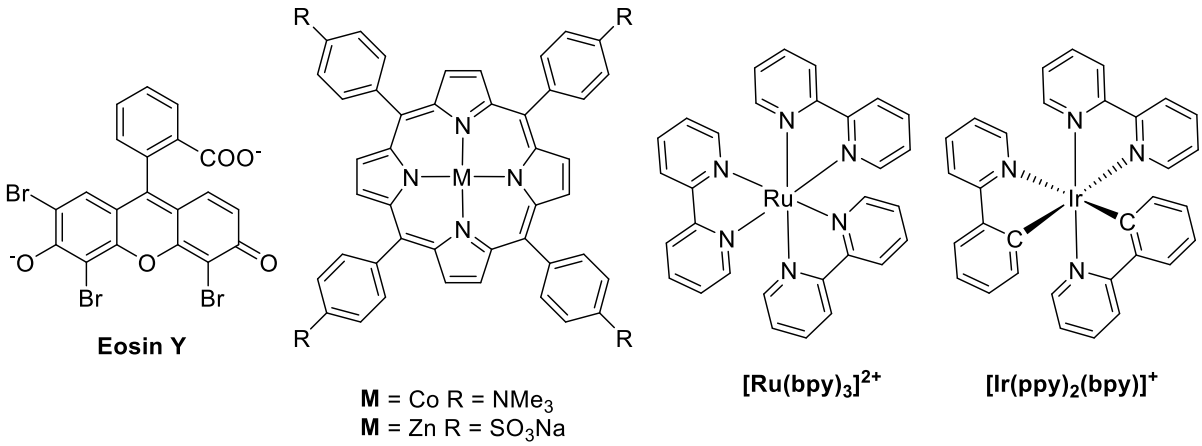

Figure 63. Selected representation of organic, metal-porphyrin and metal-based photosensitizers.

Concerning the proton reduction, numerous noble metal-based PRC have been studied especially Pt, Ru and Rh based due to the low overpotential towards proton reduction requiring less energy to perform the reduction (Figure 64).[181,182,192,193] However, their high cost has stimulated the development of more sustainable and affordable alternatives.[187] Particularly molecular catalysts bioinspired by hydrogenases, have been developed based on their active site which are binuclear complexes with two iron or a combination of nickel and iron centers (Figure 64).[194] Inspired by these enzymes, chemists use first row transition metals like Fe Ni, Co, Mn and Cu for the preparation of noble metal-free hydrogen-evolving catalysts.[196] In particular cobaloximes played a pivotal role in H_2 evolution due to their performance and easy synthesis, but typically with low stability.[180,197,198] In the last decade, Co-polyamines catalysts have received a great deal of attention due to their robustness and better catalytic activities (Figure 64).

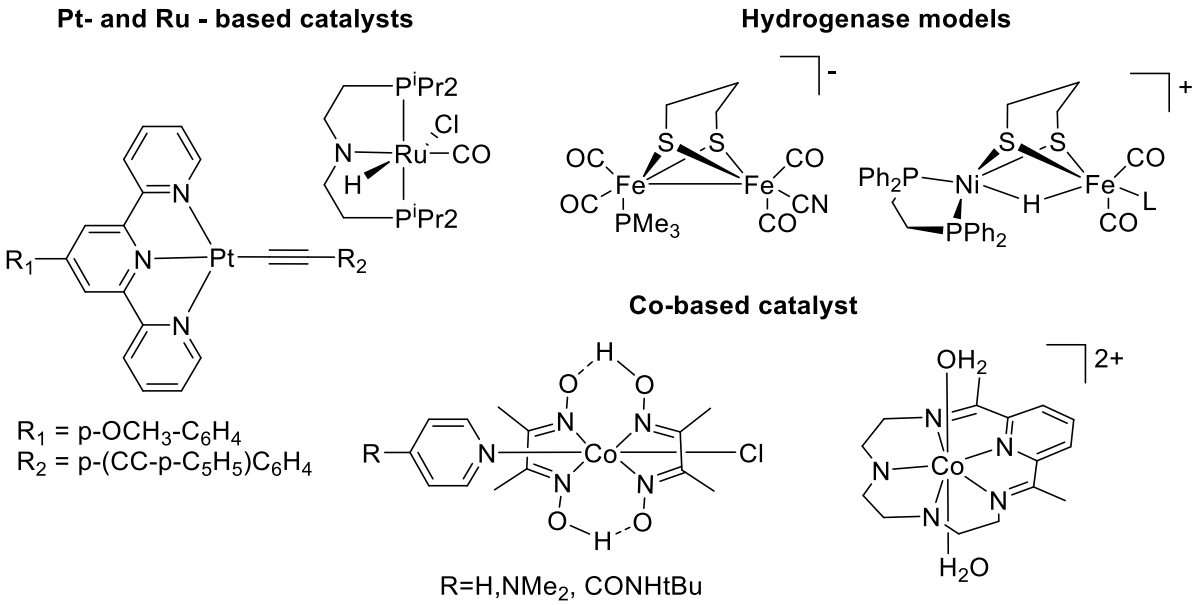

Figure 64. Selected Ru- and Pt-based catalysts, hydrogenase model catalysts and Co-based catalysts for hydrogen production.

A two-component system were both PS and Cat comprising complexes based on non-noble metals was reported by Wärnmark in 2022.[199] The system is composed of **[Fe(phtmeimb)$_2$]$^+$** acting as PS, mixed with the cobaloxime **[CoCl(dmgH)$_2$(py)]** as PRC. As sacrificial electron donor they reported triethanolamine (TEOA) and a mixture of [HNEt$_3$][BF$_4$]

as source of protons (Figure 65). The reported TON is remarkable for an Earth abundant photosensitizer, enabling TON over >1000 without degradation. The H_2 evolution proceeds through reductive quenching of the ^{2}LMCT state of the iron complex instead of via the MLCT states. The fact that Fe(III)–NHC complex has an efficient energy transfer from the reactive ^{2}LMCT state opens even more the door to possible applications in solar energy conversion processes for catalyst based on Earth abundant metals.

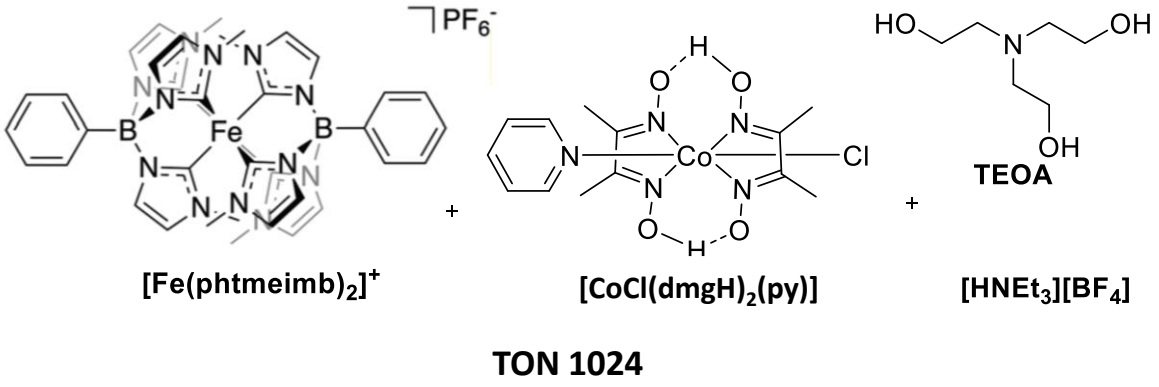

Figure 65. Structures of **[Fe(phtmeimb)$_2$]$^+$** complex and cobaloxime **[Co(dmgH)$_2$pyCl]** in two-system component for hydrogen production, inspired from reference 199.

In regard to dyads for hydrogen evolution, different models have been synthesized so far.[181,188,194] In late 1980s, one of the first dyads was reported by Rillema and coworkers in a system composed by a polypyridyl Ru(II)-Pt(II) complex (Figure 66),[200] although they did not report any H_2 production, these dinuclear complex drew attention due to their potential application as photo-hydrogen-evolving molecular device. To date, various binuclear systems have been synthesized, for example in 2003 Sun's group reported a supramolecular complex with an hydrogenase Fe_2S_2 tethered to a $[Ru(tpy)_2]^{2+}$ (Figure 66),[201] although they did not exhibit desirable H_2 production. An example of a dyad with H_2 production was reported by Sakai's group in 2006.[202] The molecular device was constituted of $[Ru(bpy)_3]^{2+}$ derivative and a Pt(II) catalyst that afforded a TON of 4.8 with EDTA as the SR (Figure 66). It is important to note that they demonstrated that the covalent bond connecting the Ru(II) sensitizer to the Pt(II) catalyst is essential for the photocatalytic H_2 production since mixing $[Ru(bpy)_3]^{2+}$ and K_2PtCl_4 under the same conditions instead of the dyad did not lead to H_2 formation. Artero *et al.* coupled cobaloximes with Ru(II) tris(diimine) moieties to synthesize supramolecular

photocatalyst for photochemical H_2 production (Figure 66).[203] The production of H_2 in this system showed a TON of 85 with TEA as SR. The connection between the PS and the Cat is assured by a fully conjugated bridge, which facilitates electron transfer both through conjugated bonds or by outer-sphere electron transfer pathways.

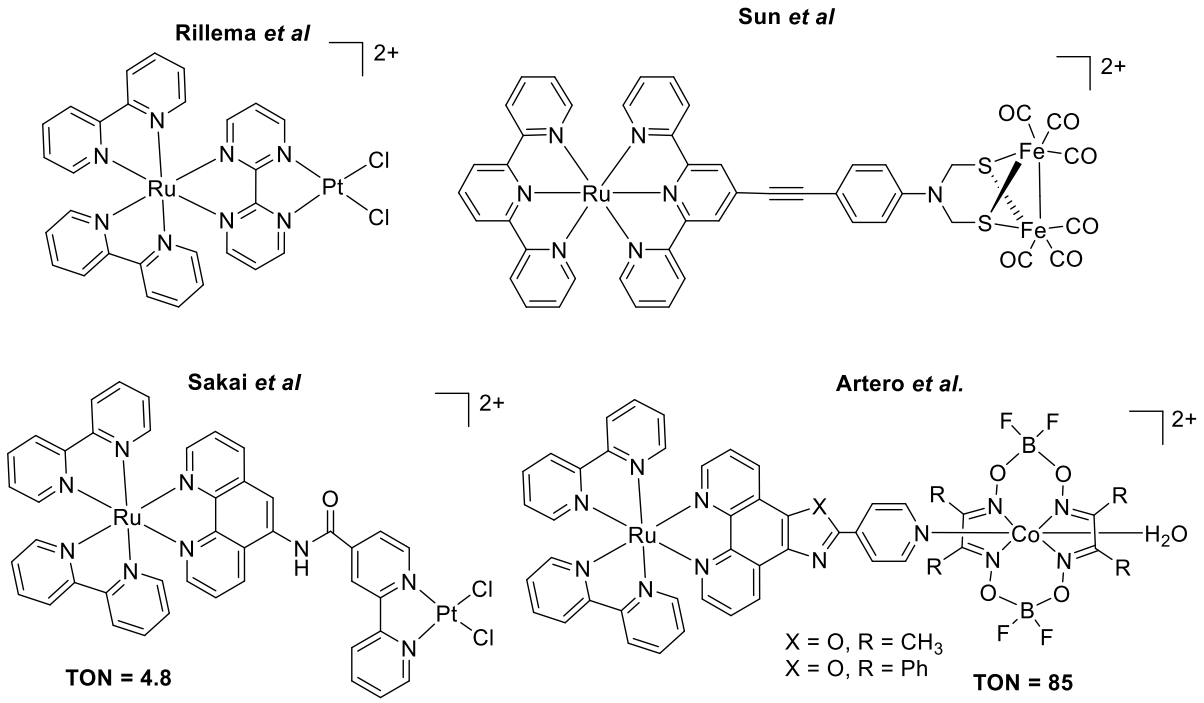

Figure 66. Selected examples of Ru(II)-Pt(II), Ru(II)-Fe(I), Ru(II)-Pt(II) and Ru(II)-Co(II) dyads for H_2 evolution.

One-component system where both PS and Cat units are based on Earth abundant metals are very rare. In this regard, the only example so far for photocatalytic dyad comprising Fe-based PS has been described by Bauer and co-workers in the course of this doctoral work. In particular, these authors reported a Fe(II)-Co(III) dyad where the reduction proceeds with TEOA as sacrificial reductant and the proton source comes from a solution ACN/Water. The photocatalytic performance of the dyad is increased by a factor of two in respect to the equivalent two-component system. This increase was directly assigned to the directional charge effect of the linker between the Fe(II) and Co(III) metal centers (Figure 67).[204] According to their measurements of dyad **[Fe-BL-Co]**, the electron transfer occurred from ^{3}MLCT state of **[Fe-BL-Co]** to the cobalt moiety.

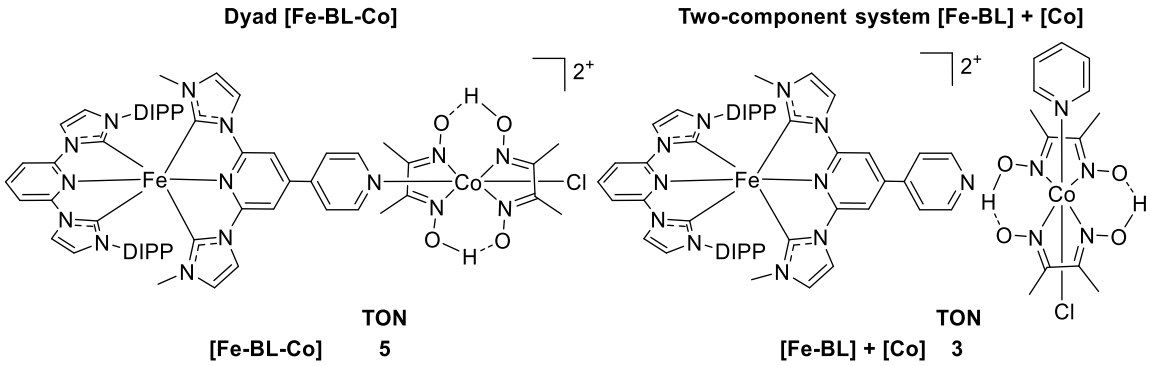

Figure 67. Structures of single-component system (**[Fe-BL-Co]**) in hydrogen evolution and two-component system (**[Fe-BL]+[Co]**). DIPP=2,6-diisopropylphenyl.

Considering the advantages of dyads over multi-component system, specially towards the preparation of photoelectrodes for device fabrication, the development of highly efficient and sustainable dyads is of great importance for the progress of this technology. Capitalizing on its abundance and low price, rationally-designed Fe(II)-based complexes with long-lived ESL are serious candidates for the development of robust PS for effective Cat activation by means of photoinduced electronic transfers. To this end, a consortium comprising Prof. Dr. S. Haacke (Univ. Strasbourg, France), Prof. Dr. M. Bauer (Univ. Paderborn, Germany), Prof. Dr. K. Heyne (Free Univ. Berlin, Germany) and our group was created aiming at developing noble metal-free Fe-Co multi-metallic assemblies for H^+ reduction. The general scheme for the assemblies as well as the initial molecular targets is depicted in Figure 68.

At a first stage, and capitalizing on our group's expertise, we decided to start our investigation with tridentate Fe(II) complexes bearing C_{NHC}^N_{py}^C_{NHC} ligands with different linker units to tune the π-conjugation (Figure 68, green). Concerning the Co PRC, the most straightforward approach would consist on a cobaloxime at which the Fe(II)-PS would be axially coordinated via a pyridine moiety (Figure 68, orange). As an alternative, a more stable polyimine Co PRC could be obtained upon coordination of the Fe(II)-PS through a bipyridine unit (Figure 68). Interestingly, this approach may simplify the 2-electron transfer required for the H^+ reduction by having two PS next to the Co center.

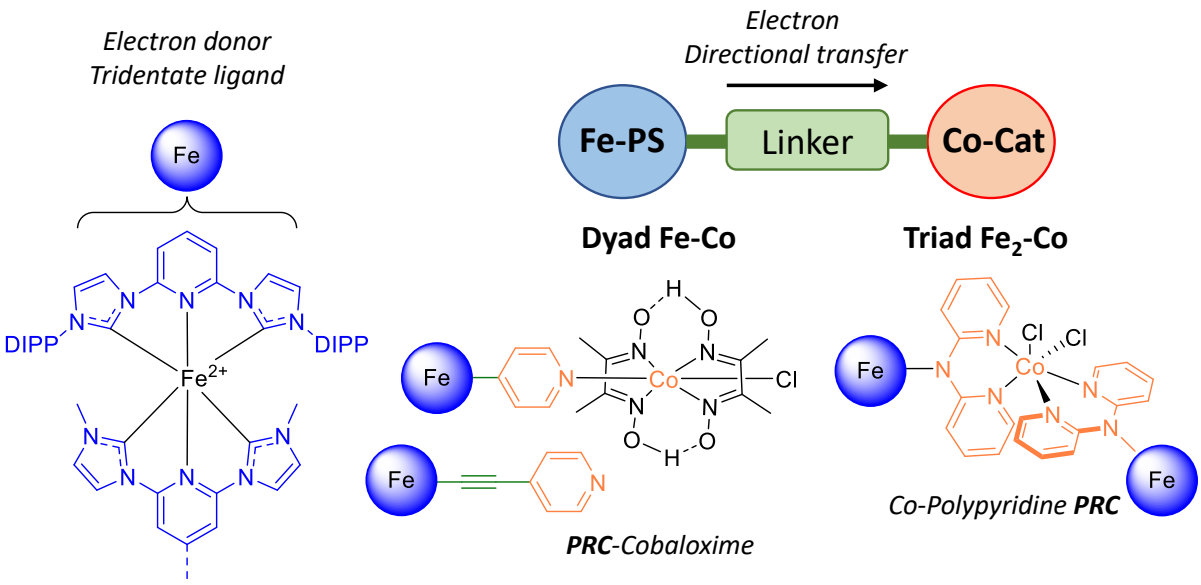

Figure 68. Schematic representation of Fe(II)-Co(II) dyad. Iron-based photosensitizer in blue, linkers in green, (orange) different coordinative ways to Co, dyad Fe-Co or triad Fe_2-Co.

Thus, with the long-term target of developing noble metal-free Fe-Co dyads in mind, this chapter will deal with the synthesis of some ditopic ligands and the corresponding ferrous complexes as a starting point for this international project.

V.2 Ditopic ligand synthesis

It is relevant to mention that this part of the thesis started almost at the same time than the bidentate azine-NHC Fe(II) complexes (Section §III), and the works of Bauer and Wärnmark group's had not been reported at that time (Sections §IV.1 and IV.4). Within the framework of the project, we focused our attention to the ligand synthesis and preparation of heteroleptic complexes. We conceived three different carbene-based ligands, of which the imidazolium precursors (pre-ligands) **H_2L28**, **H_2L29** and **H_2L30** are shown in Figure 69.

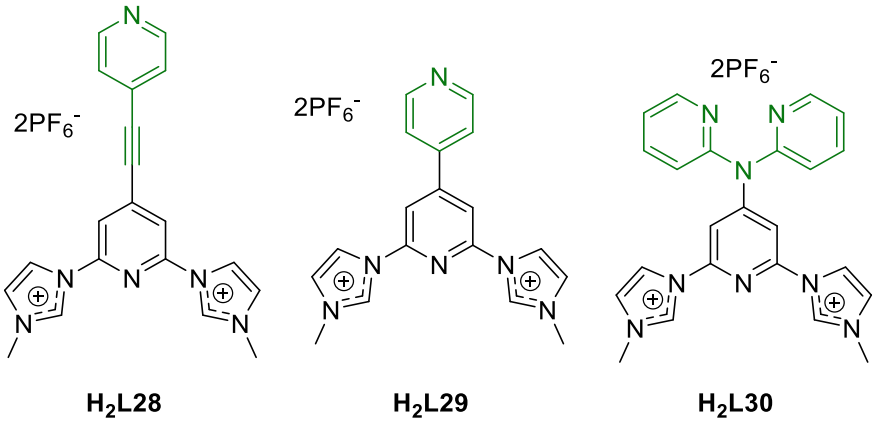

Figure 69. Structures of ligands precursors **H2L28**, **H2L29** and **H2L30**.

The synthesis to get access to the ditopic ligands for monodentate Co coordination ligands **H2L28** and **H2L29** was envisaged starting from commercially available 2,6-dichloropyridine to from intermediate **A** with Suzuki and Sonogashira coupling reactions, respectively (Scheme 24), and further imidazolidine introduction and quaternization will afford the corresponding ligands.

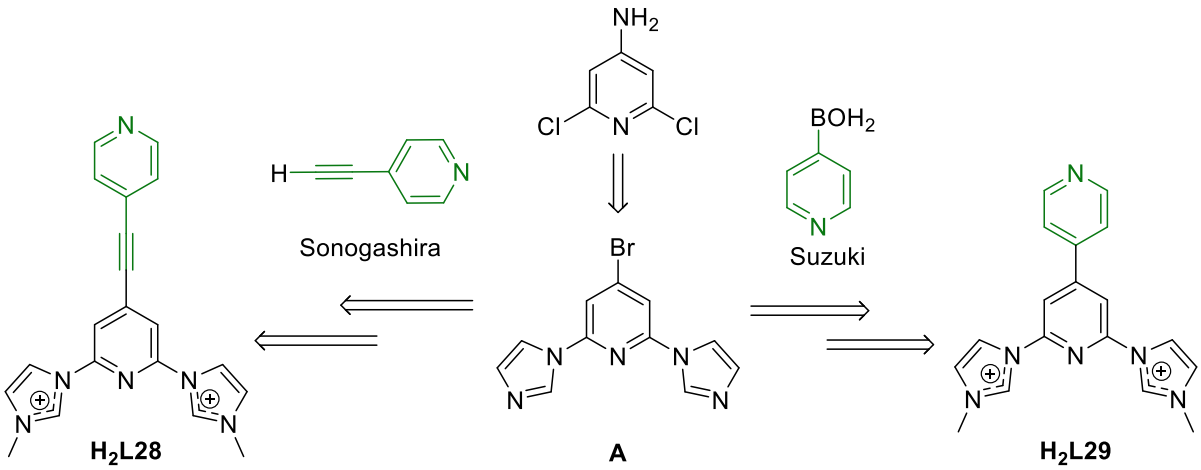

Scheme 24. Retrosynthetic analysis of **H2L28**, and **H2L29**, starting from compound **A**.

Concerning the synthesis of **H2L30**, we initially envisaged the introduction of the dipyridylamino moiety by means of a nucleophilic aromatic substitution (S_NAr). However, intermediate **A** would not be sufficiently reactive in this regard, so we sought for an alternative synthetic pathway. The 2,4,6-trifluoropyridine, instead, would favor this reactivity, with

position 4 being the most activated to favor the monosubstitution (Scheme 25). Then the introduction of two units of methylimidazole would afford the final ligand **H_2L30**.

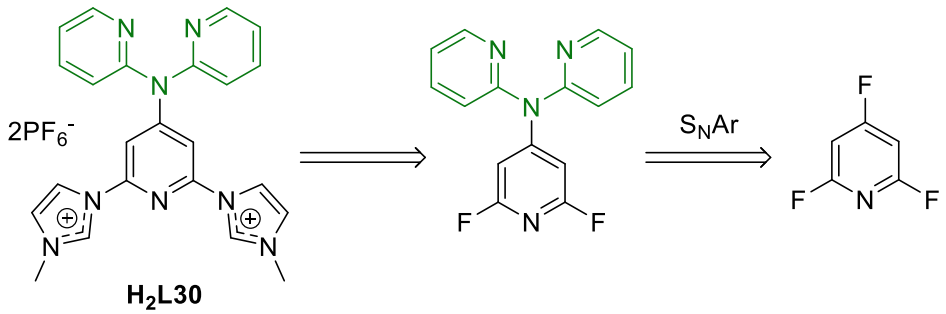

Scheme 25. Retrosynthetic analysis of **H_2L30** ligand.

V.2.1 Iron complexes for monodentate coordination of Cobalt

The synthesis started with the reaction of 2,6-dichloro-4-aminopyridine with *in-situ* generated potassium imidazolate in diglyme at 150ºC overnight afforded the substitution product **1A** in 84% yield. Then a Sandmeyer reaction on intermediate **1A** was made to introduce a bromine atom in position -4 affording intermediate **A** in 54% yield. In parallel, **B** was synthetized starting with the reaction of 4-chloropyridium chloride salt and NaI in ACN at 80 °C obtaining the 4-iodopyridine 55 % yield (Scheme 26). Afterwards, a Sonogashira coupling between 4-iodopyridine with ethynyltrimethylsilane (TMSA) was warried out by mixing these two reactants in degassed Et_3N with $PdCl_2(PPh_3)_2$ and PPh_3 at 80°C overnight affording intermediate **B-TMSA** with 79% yield, which after a fast deprotection **B** was obtained. **B** was then involved in another Sonogashira coupling with **A** in order to get **B1** under several conditions that are collected in Table 15.

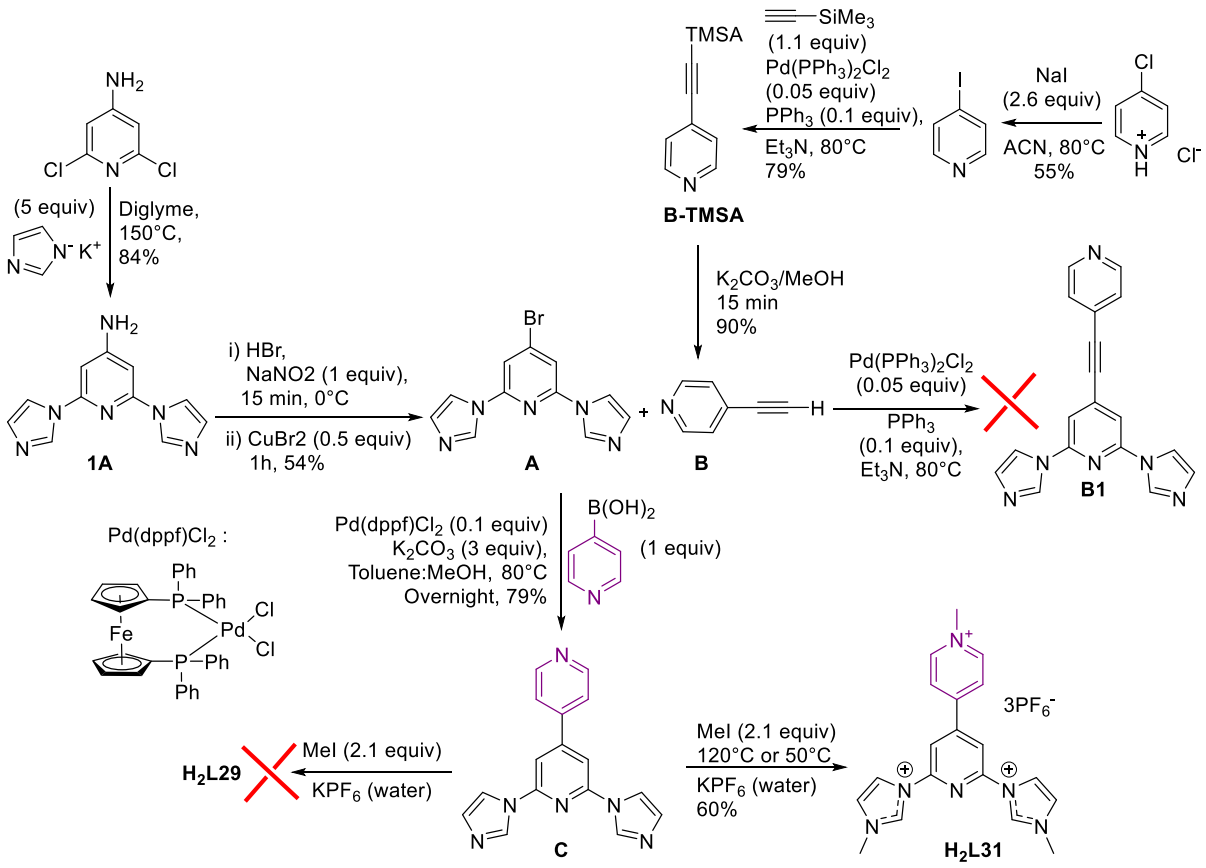

Scheme 26. Schematic synthesis of intermediates **1A-C** and ligand **H_2L31**.

When the same Sonogashira conditions described for **B** were used, no product was obtained (entry 1). We decided to increase the reaction temperature to force the reaction, selecting then a mixture of solvents DMF+Et_3N (1:2) (both degassed) but no product was observed (entry 2). Moreover, a change on the catalyst for the more reactive $Pd(PPh_3)_4$ and the solvents-base mixture to THF:DIPA:MeOH (5:3:3) (DIPA=diisopropylamine) under reflux conditions did not lead to product formation either (entry 3). At this point, we changed the strategy and instead of reacting **A** with **B**, we decided to react **A** with TMSA (entries 4 and 5). Whether by using the first conditions of entries 2 or 3 the reaction did not proceed. Since we did not observe any indication of Sonogashira coupling product, we decided to start working on the ligand **H_2L29**.

Table 15. Sonogashira reactions between intermediate **A** with **B**.

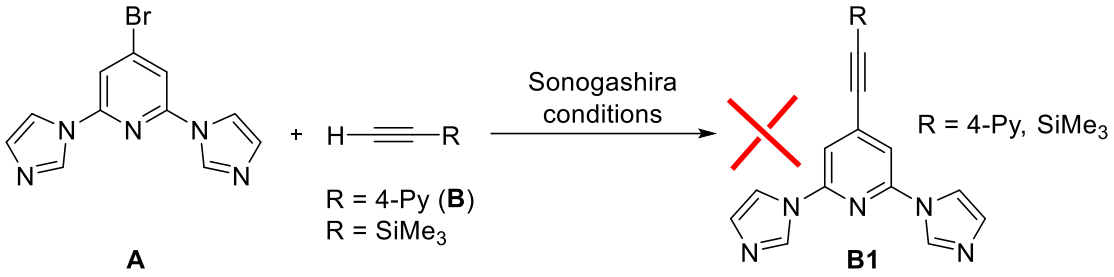

Entry	Pd catalyst (0.05 equiv)	Solvent	T (°C)	Base	R	Product
1[a]	$PdCl_2(PPh_3)_2$	Et_3N	80	Et_3N	4-Py	n.r.
2[a]	$PdCl_2(PPh_3)_2$	DMF: Et_3N (1:2)	150	Et_3N	4-Py	n.r.
3	$Pd(PPh_3)_4$	THF:DIPA:MeOH (5:3:3)	Reflux	DIPA	4-Py	n.r.
4[a]	$PdCl_2(PPh_3)_2$	DMF: Et_3N (1:2)	150	Et_3N	$SiMe_3$	n.r.
5	$Pd(PPh_3)_4$	THF:DIPA:MeOH (5:3:3)	Reflux	DIPA	$SiMe_3$	n.r.

a=Addition of 0.1 eq of PPh_3; n.r. = no reaction.

Since the introduction of the alkyne linker was unsuccessful, we then examined the direct introduction of pyridine at the 4-position of **A** and we moved to the synthesis of **H_2L29**. A Suzuki coupling between **A** and 4-pyridinylbroronic acid afforded **C** in 79% yield (Scheme 26). The quaternization of the imidazole units was performed reacting **C** with 2.1 equivalents of MeI. After anion exchange with aqueous solution of KPF_6, the tris-methylated product **H_2L31** was isolated as a single product instead of **H_2L29** (Figure 70, top). Efforts to avoid the quaternization of the pyridine were made. First addition of only 1 equiv of MeI followed by NMR showed a competition between the pyridine and the imidazole moieties, then a decrease on the temperature reaction from 120°C to 50°C yet the result was the ligand **H_2L31** (Scheme 26). In order to study the relative reactivity of both imidazole and 4-pyridine units, we carried out a new reaction by adding only one equivalent of MeI at room temperature and following the reaction by ^{1}H-NMR. After the addition we could observe the apparition of two signals corresponding to the quaternized imidazole and pyridine (Figure 70, bottom), and the signals of the starting material intermediate **C**. The integrals between the imidazolate and methylpyridium were 3:2, indicating that the pendant pyridine is competing with the imidazole in the nucleophilic substitution over MeI.

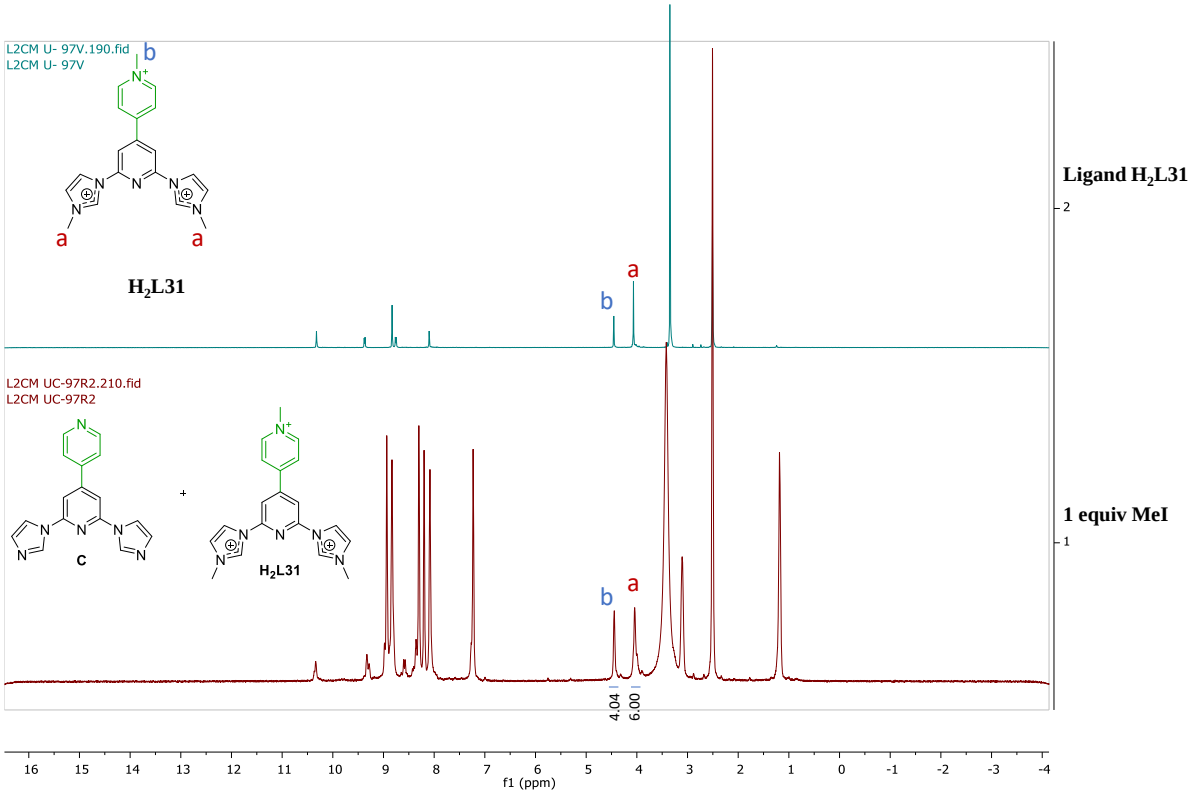

Figure 70. ^{1}H-NMR of ligand **H$_2$L31** (green) and mixture of intermediate **C** and ligand **H$_2$L31** with 1 equiv of MeI (red).

An alternative synthetic strategy to prepare the ligand precursors **H$_3$L28** and **H$_3$L29**, where the quaternization step is avoided, is depicted in Scheme 27. In order to overcome this selectivity issue, we started from 2,6-dichloropyridine instead of 4-amino-2,6-dichloropyridine that can be selectively iodinated in position -4 affording a reactive intermediate susceptible to react in coupling reactions and nucleophilic substitutions (Scheme 27). In addition, 2,6-dichloropyridine is much cheaper (14 times cheaper than 4-amino-2,6-dichloropyridine).[205,206] We started introducing an iodine atom in position 4 on the 2,6-dichloropyridine by using *n*-BuLi and I_2 at -78°C in THF, affording the intermediate **D** with 60% yield. **D** was then reacted with 4-pyridinylboronic acid under Suzuki coupling conditions affording the intermediate **E** with 78% yield. Afterwards, intermediate **E** was mixed with 2.1 equiv of N-methylimidazole at 150°C giving the desired ligand **H$_2$L29** after anion exchange with saturated aqueous solution of KPF_6. The fact that we used N-methylimidazole to introduce the imidazolium unit avoided the aforementioned problem of the quaternization selectivity as in ligand **H$_2$L31**.

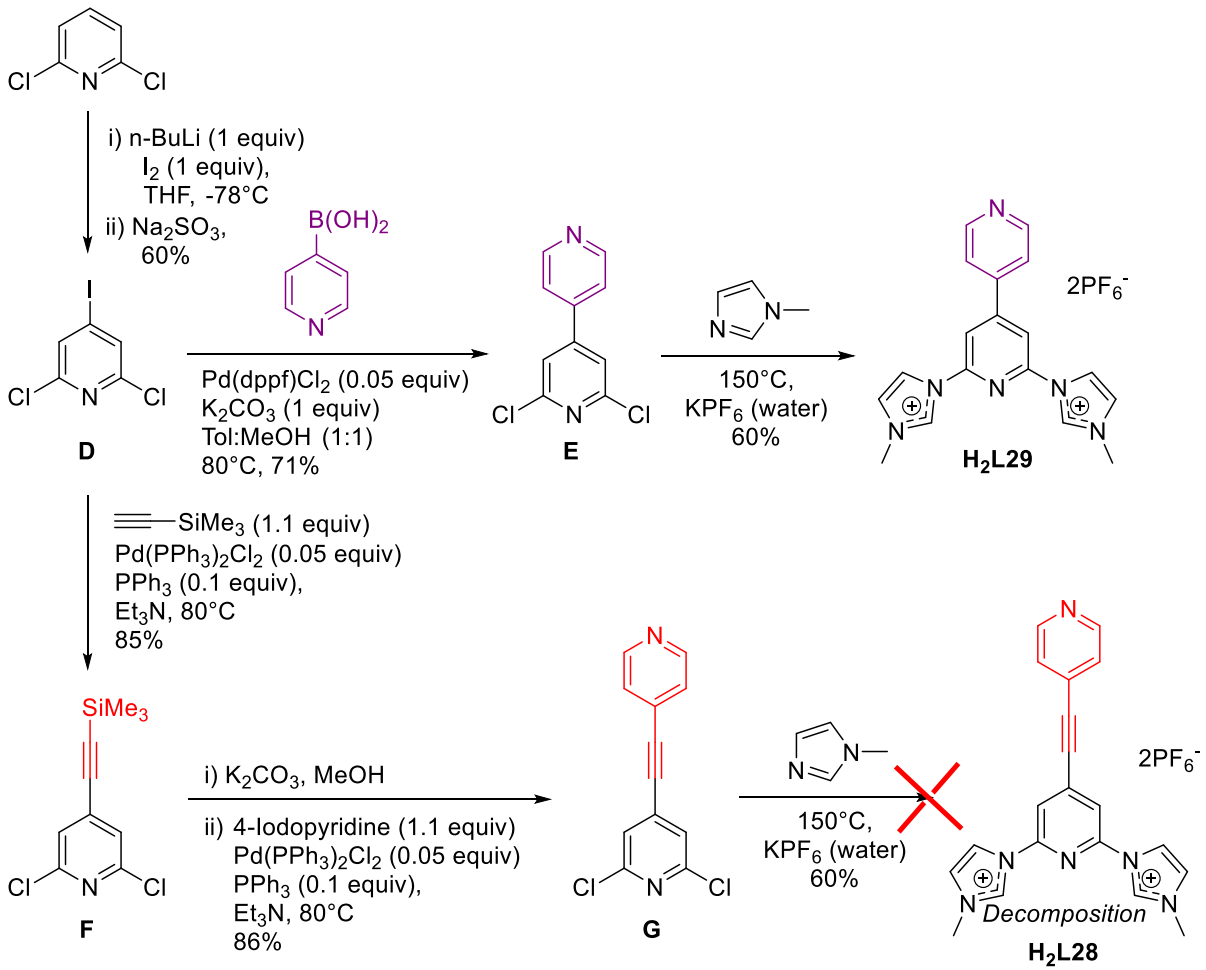

Scheme 27. Schematic representation of synthesis to get **H_2L28** and **H_2L29** with intermediates **D-F**.

In order to access **H_2L28**, **D** was subjected to a Sonogashira coupling with TMSA, giving the intermediate **F** in 86% yield. After a fast deprotection of the -$SiMe_3$ group with K_2CO_3 in MeOH at room temperature, the subsequent terminal alkyne was reacted without further purification with 4-iodopyridine under Sonogashira conditions giving the intermediate **G** with 36% yield. Unfortunately, attempts to react intermediate **G** with N-methylimidazole under the same conditions as previously described for **H_2L29** did not lead to **H_2L28**. Compound **G** decomposed into intractable mixture of side products; the triple bond probably suffered from nucleophilic attacks.

The numerous issues faced with the chemistry of the alkyne-containing intermediates, drew us to interrupt our investigations on these types of ligands.

V.2.2 Iron complexes for bidentate coordination of Cobalt

The proposed synthetic route for **H_2L30** is shown in Scheme 28. First a nucleophilic substitution of the reactant 2,2'-dipyridylamine over position -4 of the 2,4,6-trifluoropyridine would afford intermediate I, then a double nucleophilic substitution of previously formed imidazolate on positions -2 and -6 giving intermediate **J** to finally perform a quaternization over the imidazoles to get the final ligand **H_2L30**.

Scheme 28. Schematic representation of synthesis

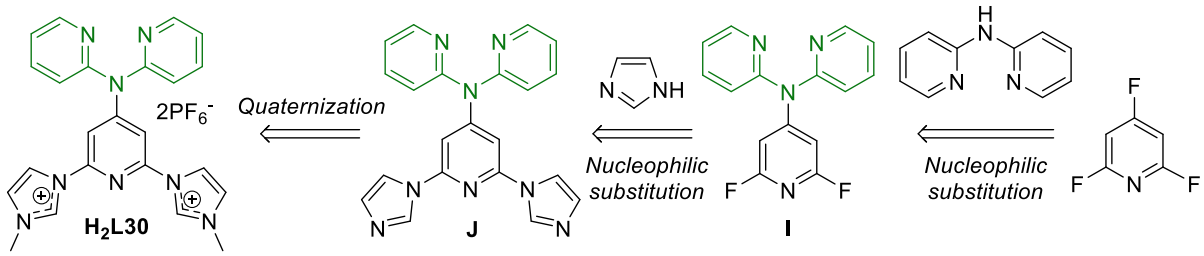

for ligand **H_2L30**.

Attempts to deal with S_NAr of 2,2'-dipyridylamine over 2,4,6-trifluoropyridine are collected in Table B. The first attempt was following a reported protocol,[207] in which they form the nucleophile under Schlenk conditions, in our case mixing 2,2'-dipyridylamine with NaH in DMF at 0°C (Entry 1), followed by the addition of 2,4,6-trifluoropyridine and heating up at 90°C overnight. However, the reaction did not lead to the target compound. It is important to note that neither the desired product or the starting 2,4,6-trifluoropyridine were observed. Another try was carried out upon changing the base to K_2CO_3 in DMF at 0°C as reported for another similar protocol (Entry 2).[208] The reaction mixture was slowly warmed to room temperature and followed by TLC, but there were no signs of product and starting material, suggesting that the starting material was lost from the reacting mixture.

Table 16. Optimization of the reactions conditions of the S_NAr.

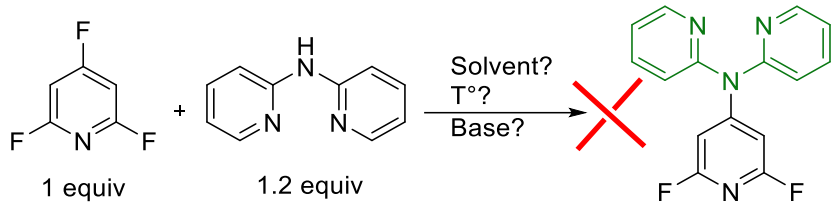

Entry	Solvent	Temperature (°C)	Base (n equiv)	Yield (%)
1	DMF	0 - 90	NaH (1.2)	n.r.
2	DMF	0 - r.t.	K_2CO_3	n.r.
3	EtOH	0 - r.t.	-	n.r.
4	DMF	r.t.-90	-	n.r.
5	THF	0 - reflux	LiHMDS (1.2)	n.r.
6[a]	ACN	90°C	-	n.r.

a=Microwave, power 60W, T°=90°C, 1h, ACN; n.r. = no reaction.

After bibliographic research we found a couple of methodologies for the same reactant (2,4,6-trifluoropyridine) in which they use a base in an protic media (MeOH and EtOH)[209,210] or aprotic media (THF, DMSO)[211,212] mixed with an amine as nucleophile, in anhydrous conditions deprotonating the nucleophile,[213,214] or even without a base just taking advance of the nucleophilicity of the reactants.[210,215,216]. With this in mind, reactions without a base in EtOH and DMF at r.t. and heating at 90°C were tried, but the reaction did not proceed as expected obtaining only the starting nucleophile 2,2'-dipyridylamine (entries 3-4). Another attempt was done by deprotonating the amine prior to the addition of the 2,4,6-trifluoropyridine seeking to increase the amine nucleophilicity (Entry 3) but without success. As a last attempt in order to promote a S_NAr we followed a microwave-assisted protocol. The two reactants were mixed in a mw tube in ACN and heated to 90°C for 1h (60w). Unfortunately, the result was the same without any trace of trifluoropyridne or product. A possible explanation for this lack of reactivity could be due to the nature of the 2,4,6-trifluoropyridine, which has a flash point of 17°C at 1 atm.[217] The flash point is related to vapor pressure, which is dependent on the temperature, meaning that at T°>17°C there is the lowest necessary concentration of vapor to ignite. Thus, even when the system was closed it is possible that 2,4,6-trifluoropyridine was out of the reaction mixture and did not react, which agrees well with the fact that we did not observe any trace of 2,4,6-trifluoropyridine after reaction time.

Based on these results, a new synthetic approach was investigated (Scheme 29). Compound **D** obtained in scheme 27, was reacted under Ullmann conditions with 2,2'-dipyridylamine in DMF at 150°C affording **K** in 76% yield. Introduction of the imidazole units in **K** was performed using the potassium imidazolate salt in diglyme yielding **L** in 91% yield. The quaternization of the imidazole moieties was selectively achieved, leading to the expected ligand precursor **H_2L30** in 70% yield

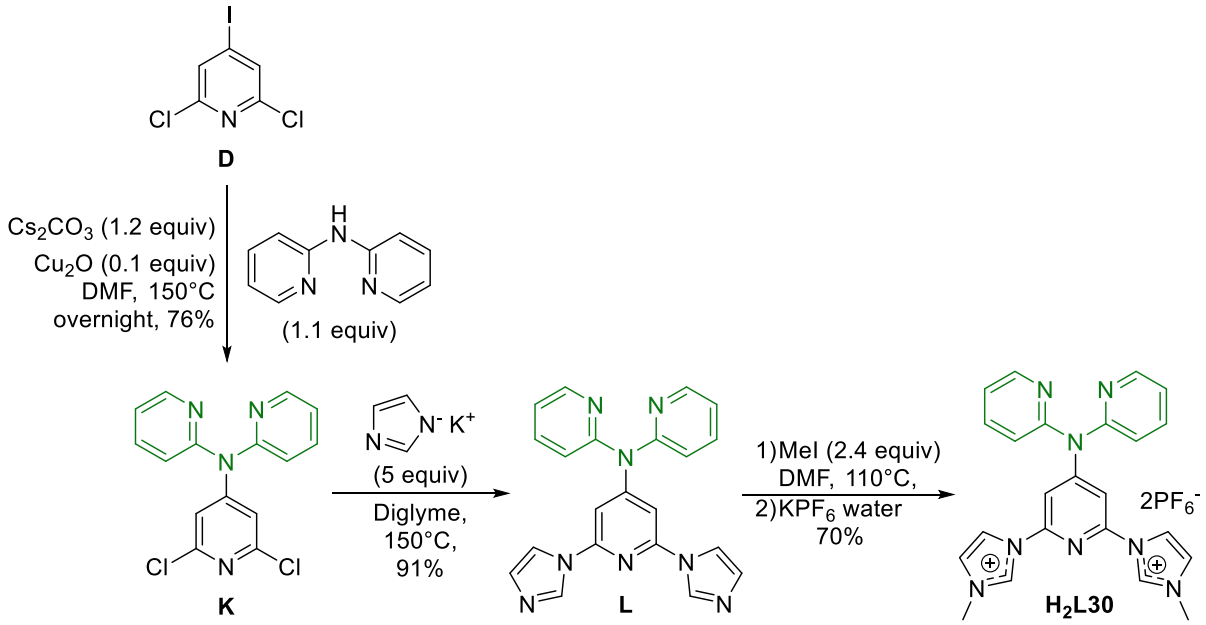

Scheme 29. Alternative synthetic approach to obtain **H_2L30**.

Approximately, at this moment of the thesis, Bauer reported the synthesis and complexation of the heteroleptic version and dyad of our ligand **L29**.[204] As a result, we continued our investigation focusing only on the ligand **H_2L30**.

V.3 Synthesis of homoleptic and heteroleptic complexes bearing ditopic ligands toward H_2 evolution

The work described in this part was carried out during an internship in the laboratory of Prof. Dr. Bauer at the University of Paderborn in the framework of the international DrEAM program of Lorraine Université d'Excellence (LUE).

Although the final goal is to prepare a heteroleptic complex with the ligand **H_2L30** and the so called Bulky Ligand (**BuL)** reported by Bauer,[204] we first synthesized the homoleptic version in order to optimize the complexation conditions as well as for comparison reasons. The different reaction conditions used for the synthesis of **$[FeL30_2]^{2+}$** are collected in Table 17. We first chose some already reported conditions for the complexation of this tridentate ligands[71,218,219] preconizing $FeBr_2$ as iron source (0.5 equiv) and ^{t}BuOK as the base in DMF, but after 5-10 min of stirring no complex formation was detected (entry 1). A plausible explanation could be the coordination of the iron center by dipyridine side thus competing with the C^N^C ligand (Figure 71a).

Table 17. Complexation reactions of ligand precursor **H_2L30** to obtain **$[Fe(L30)_2]^{2+}$**.

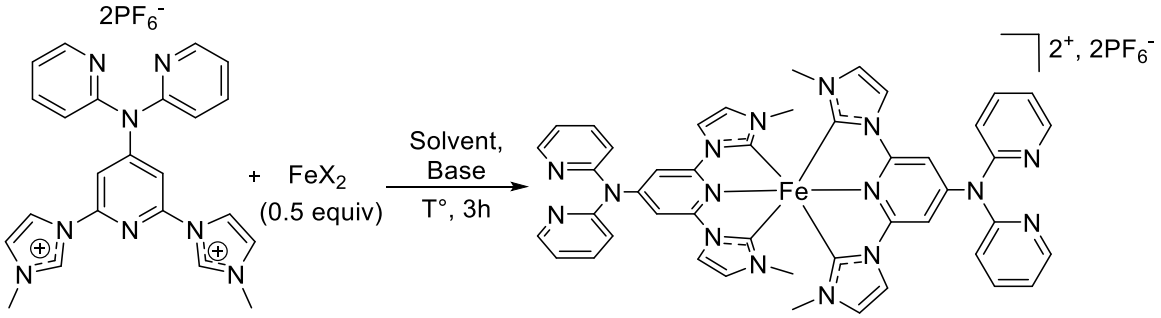

H_2L30 **$[Fe(L30)_2]^{2+}$**

Entry	FeX_2	Solvent	Base (equiv)	T (°C)	$[Fe(L30)_2]^{2+}$ (%)
1	$FeBr_2$	DMF	^{t}BuOK (2.1)	r.t.	n.p.
2	$FeBr_2$	THF	LiHMDS (2.1)	-20 – rt	n.p.
3	$FeCl_2$	DMF	^{t}BuOK (2.1)	r.t	40

n.p. = no product.

To avoid the competitive coordination, we decided to first form the carbene by deprotonation with LiHMDS in THF before iron addition. One could expect that once the carbenes would be formed and available to complex the metal, the probability to obtain the complex **[Fe(L30)$_2$]$^{2+}$** would be higher. The deprotonation was carried out at -20°C and let it arrive to r.t. (later we realized that temperature is key for this ligand, beyond 0°C it starts to decompose, see Heteroleptic complex). Unfortunately, after iron addition no complex was observed (entry 2). A plausible explanation is the formation of an unstable intermediate that compete with Fe-center (Figure 71b). In order to reduce the competitive coordination between the iron center and the bipyridine, we changed the iron source to $FeCl_2$. The lower lability of the chlorine ligands respect to the bromo ones might have an impact. The ligand **H$_2$L30** and $FeCl_2$ were mixed in DMF for 5 min at r.t., then ^{t}BuOK was added at r.t. and stirred for 3h (entry 3). Gratifyingly, the complex **[Fe(30)$_2$]$^{2+}$** was obtained with 40% yield. With the conditions for the coordination of **L30** in hands, we proceeded to synthesize the heteroleptic version.

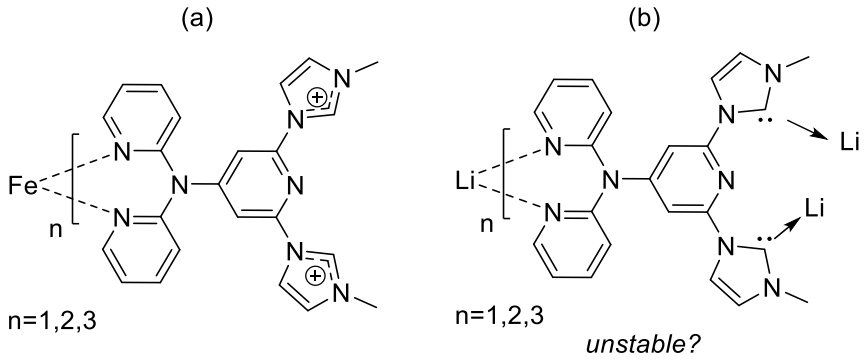

Figure 71. Possible intermediates in the **[Fe(L30)$_2$]$^{2+}$** complex formation.

The synthesis of heteroleptic Fe(II)-NHC complexes described by Bauer and co-workers[204] was based on the use of a tridentate bulky ligand (**BuL**) to kinetically inhibit the formation of the homoleptic complex. Thus, we followed the same protocol starting with the formation of an iron-base Fe(HMDS)$_2$. This latter is obtained by mixing $FeCl_2$ and LiHMDS in dry THF at -70°C and, after a couple of hours, the reactant Fe(HMDS)$_2$ is obtained. It can be stored under inert conditions or used immediately after its preparation (Scheme 30, A).[204] The synthesis continues with addition of a stoichiometric quantity of Fe(HMDS)$_2$ to **BuL** in THF. Monosubstituted **M** is formed after 7h, which is stabilized due to the steric hindrance

exerted by the diisopropylphenyl groups. In parallel, in another schlenk the ligand **H_2L30** was suspended in THF and deprotonated with 2 equiv of LiHMDS at -40° allowing it to reach 0°C during 7h. A particular mention for **H_2L30** is that temperature should not go beyond 0°C or it decomposes. After this time the deprotonated **L30** was transfer into the schlenk with **M** and it was stirred overnight reaching room temperature. Nicely, the heteroleptic complex **[Fe(BuL)(L30)]$^{2+}$** was obtained with a 33% yield.

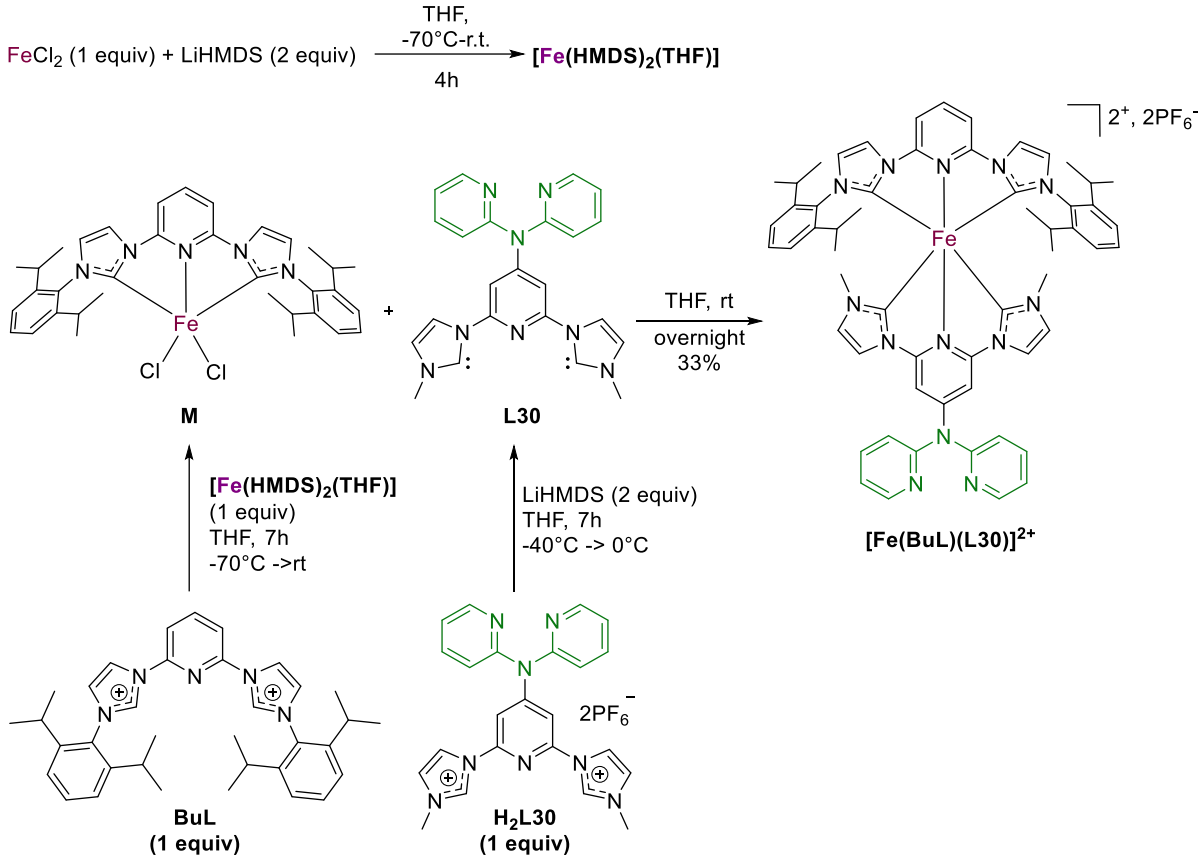

Scheme 30. Schematic synthetic representation of **[Fe(BuL)(L30)]$^{2+}$** complex.

Following this procedure we were able to synthesize an heteroleptic and ditopic complex that can be used to further coordinate a cobalt ion at the dipyridyl site.[204] The main goal will be to have a dyad and/or a triad that can be tested in photocatalytic H_2 evolution reaction, which won't be addressed in this thesis due to lack of time.

V.4 Ground state characterization

Optical and electrochemical properties of both complexes were investigated by UV-Vis spectroscopy (Figure 72) and cyclic voltammetry, and the main results are collected in Table 18. Results for **[Fe(BuL)(L29)]**$^{2+}$[204] and **[Fe(pbmi)$_2$]**$^{2+}$ (See §I.2.3)[31] are included as well for comparison reasons.

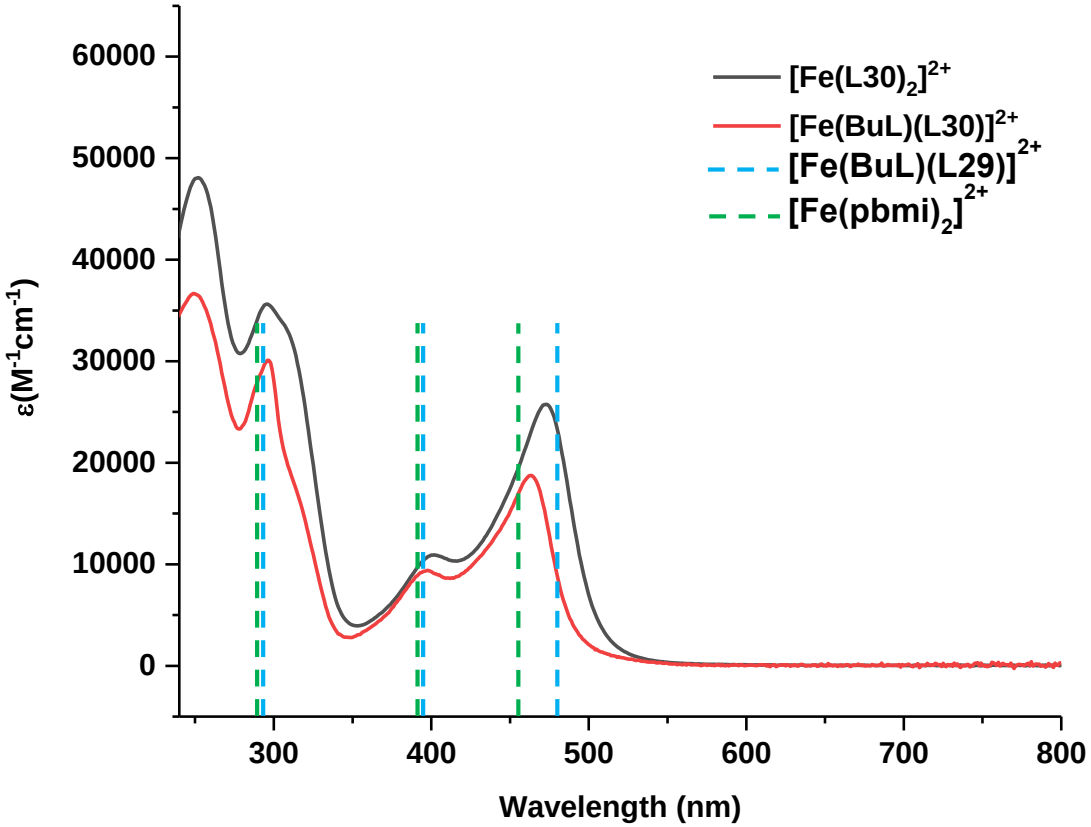

Figure 72. UV-Vis spectra of **[Fe(L30)$_2$]**$^{2+}$ and **[Fe(BuL)(L30)]**$^{2+}$ complexes in air-equilibrated acetonitrile solution at room temperature. Corresponding data for **[Fe(BuL)(L29)]**$^{2+}$ (blue-dotted lines) and **[Fe(pbmi)$_2$]**$^{2+}$ (green-dotted lines) are shown for comparison reasons.

Table 18. Photophysical and electrochemical data for **[Fe(L30)$_2$]$^{2+}$** and **[Fe(BL)(L30)]$^{2+}$** complexes.

Complex	$\lambda_{abs\text{-}max}$ (nm) [ε($M^{-1}.cm^{-1}$)][a]	E_{ox}[b] [V/SCE]	E_{red} [V/SCE]	ΔE [V][c]
[Fe(L30)$_2$]$^{2+}$	295 [35614] 401 [10901] 472 [25724]	0.59 (rev)	n.d.	
Fe(BuL)(L30)]$^{2+}$	297 [35550] 399 [9349] 464 [18723]	0.76 (rev)	-1.97 (irr)	2.73
[Fe(BuL)(L29)]$^{2+}$ [d]	294 [16800] 398 [8900] 486 [11200]	0.86 (rev)	-1.58 (rev)	2.44
[Fe(pbmi)$_2$]$^{2+}$ [e]	287 [31400] 393 [9000] 460 [15900]	0.80 (rev)	-1.95 (irr)	2.75

[a]Measured in CH_3CN at 25°C. [b]First oxidation potential. Potentials are quoted vs SCE. Recorded in CH_3CN using NBu_4PF_6 (0.1M) as supporting electrolyte at 100 mV^{s-1}; under these conditions, $E_{1/2\ (Fc+/Fc)}$ = 0.39V/SCE; rev = reversible; qr = quasi-reversible; irr = irreversible; n.d.= no detected. [c]Electrochemical band gap ($\Delta E=E_{ox}-E_{red}$[1]).[d]Data taken from the paper from reference 204 considering $E_{1/2(Fc+/Fc)}$ = 0.39 V/SCE. [e]Data taken from the paper from reference 159.

The UV-Vis spectra of **[Fe(L30)$_2$]$^{2+}$** and **[Fe(BuL)(L30)]$^{2+}$** complexes present three main absorption bands. The intense bands below 300 nm correspond to $^1(\pi–\pi^*)$ transitions centered on the ligands. At longer wavelengths, two different broader and less intense MLCT bands are found corresponding to Fe–carbene $^1(d–\pi^*_{NHC})$ (320–420 nm) and Fe–azine $^1(d–\pi^*_{azine})$ (380–550 nm) transitions. A less intense absorption is observed for the heteroleptic **[Fe(BuL)(L30)]$^{2+}$** complex, which could be explained by the slightly elongated Fe–C_{NHC} bond distances due to the bulky substituents (DIPP) on the imidazole part.[204] It is noteworthy that a similar effect was observed for complex *fac*-**C13** (See section III.4.2). On the other hand, a redshift is observed for the Fe-azine MLCT transition in the homoleptic complex **[Fe(L30)$_2$]$^{2+}$** respect to the heteroleptic complexes **[Fe(BuL)(L30)]$^{2+}$**.

Cyclic voltammetry of homoleptic **[Fe(L30)$_2$]$^{2+}$** and heteroleptic **[Fe(BuL)(L30)]$^{2+}$** complexes was recorded with SCE as standard electrode and ferrocene as internal reference (Fc^+/Fc = 0.39V/SCE in acetonitrile) (cyclic voltammograms are depicted in Experimental part, Section §5). In both cases, the oxidation can be attributed to the couple redox $Fe^{III/}Fe^{II}$. For complex **[Fe(L30)$_2$]$^{2+}$**, its oxidation potential is found at 0.59 V while that of the heteroleptic complex **[Fe(BuL)(L30)]$^{2+}$** is shifted to more anodic values (0.76V). The more stabilized pseudo-t_{2g} level of the latter is attributed to the coordination of the **BuL** ligand which compares well that of **[Fe(pbmi)$_2$]$^{2+}$**, thus suggesting the less acceptor character of **L30**.

In the negative potentials' region, one irreversible reduction at -1.97 V wave was observed for **[Fe(BuL)(L30)]$^{2+}$** that is almost identical to that of **[Fe(pbmi)$_2$]$^{2+}$**. However, no reduction was recorded for **[Fe(L30)$_2$]$^{2+}$** within the electrochemical window, which is in line with a more destabilized π* level.

Therefore, these results seem to indicate that the photoinduced charge transfer in heteroleptic **[Fe(BuL)(L30)]$^{2+}$** takes place in the opposite direction to what was initially intended (d–π*$_{azine\text{-}BuL}$ instead of d–π*$_{azine\text{-}L30}$), though the coordination of the cobalt ion could well invert this behavior. Moreover, it is important to note that comparison with the heteroleptic complex **[Fe(BuL)(L29)]$^{2+}$** reported by Bauer may be misleading. In fact, the same trends, *i.e.* more positive potentials for both anodic and cathodic events, are found for both heteroleptic complexes respect to **[Fe(L30)$_2$]$^{2+}$**. Nevertheless, the reduction must take place on **L29** instead of **BuL** due to the presence of the 4,4'-bipyridyl moiety as suggested by the noticeable more positive reduction potential.[159]

V.5 Conclusions and perspectives.

In this chapter we described different synthetic routes to obtain ligands **H$_2$L28**–**H$_2$L30**. We have explored diverse synthetic approaches that have led us to finally succeeded in obtaining two ligands, namely **H$_2$L29** and **H$_2$L30**. The complex with the ligand **H$_2$L29** was reported during this doctoral work, so we focused on ligand **H$_2$L30** from which we obtained two complexes, the homoleptic **[Fe(C30)$_2$]$^{2+}$** and the heteroleptic version **[Fe(BuL)(L30)]$^{2+}$**. It is remarkably that in both cases, from the two possible coordinative sites (C^N^C and N^N) it was possible to selectively coordinate the iron center to the tridentate one. On the other hand, the heteroleptic complex was obtained through a stepwise protocol, in which a sterically demanding tridentate ligand (**BuL**) kinetically inhibited the formation of the homoleptic complex allowing us to introduce a subsequent step.

For both complexes the ground state characterization was made. We could observe from UV-Vis spectra of **[Fe(L30)$_2$]$^{2+}$** and **[Fe(BuL)(L30)]$^{2+}$** that the complexes present three main absorption bands corresponding to ^{1}(π–π*) transitions centered on the ligands, two different broader and less intense bands corresponding to Fe–carbene ^{1}(d–π*$_{NHC}$) MLCT transitions, and

transitions corresponding to Fe–azine $^1(d–\pi^*_{azine})$. It is worth to note the slight reduction of the absorbance intensity of **[Fe(BuL)(L30)]$^{2+}$** attributed to the slightly elongated Fe–C_{NHC} bond distances due to the bulky substituents (DIPP) on the imidazole part. Further, a redshift is observed for the Fe-azine MLCT transition in the homoleptic complex **[Fe(L30)$_2$]$^{2+}$** respect to the heteroleptic complexes **[Fe(BuL)(L30)]$^{2+}$**.

A more distinct behavior was revealed by the electrochemical investigation. Indeed, both homoleptic **[Fe(L30)2]$^{2+}$** and heteroleptic **[Fe(BuL)(L30)]$^{2+}$** present a metal-based oxidation. However, reduction was only observed for the heteroleptic species under the conditions of our experiments. The electron-rich character of the dipyridyl units in **L30** must cathodically shift the reduction potential out of the electrochemical window. A more critical result comes from the comparison of **[Fe(BuL)(L30)]$^{2+}$** with **[Fe(BuL)(L29)]$^{2+}$**. In fact, the electron-rich character of **L30** seems to favour the MLCT implicating **BuL** ligand instead of **L29**, thus precluding the target electronic transfer towards the Co coordinating site. Therefore, although actual Co coordination may exert a sufficient pull effect, these results clearly show the necessity to increase the electronic differences between the terminal (push) and ditopic (pull) ligands. For instance, the use of an anionic terminal ligand and/or the introduction of electron reservoir units within the ditopic ligand could be envisaged.

VI. General conclusion and perspectives

VI. General conclusion and perspectives

In this doctoral work we had a fundamental approach developing a stereoselective synthesis of Fe(II)-complexes bearing bidentate azine-NHC asymmetric ligands and the synthesis of Fe(III)-complexes bearing two different types of anionic ligands (N-amido, C-anionic). Moreover, we dabbled into more applied chemistry as for the synthesis heteroleptic Fe(II) complexes towards H_2 production in water splitting reactions.

In regard to the stereoselective synthesis of bidentate azine-NHC Fe(II) complexes, we developed a room-temperature methodology to selectively access complexes with facial or meridional geometry. To achieve this selective *fac/mer* control we designed several ligands with modified substitution of the azine with groups of various degrees of bulkiness such as Mes and CH_3 (See §III.4, Scheme 9). We discovered that the selectivity is closely related to the bulkiness in the proximity to the azine's N coordinating atom. The *fac* selectivity was achieved when the CH_3 (smaller steric hindrance) was at the alpha position of the nitrogen coordinated to the iron center (See §III.4, Table 4). Interestingly, increasing the steric hindrance in this position (6-substituted derivative series) with substituents like isopropyl or chlorine groups afforded the same selectivity (See §III.4.3, Table 6). In fact, comparable substitution sequences of bidentate ligands have often been observed to lead to the *mer* isomer, considering the common orientation of these substituents. In case of a more sterically demanding group (Mes), a *mer* selectivity was afforded only with Mes in position 5 of the azine (See §III.4, Table 4). To evaluate the scope of our *fac/mer* selective methodology, we used carbenes of varied electronic nature from more accepting (bIm) to more donating (4MeIm) moieties. We observed that regardless the NHC electronic nature, the selectivity was maintained, affording a set of facial and meridional complexes with different carbenes (See §III.4.1, Table 5). To improve the optical properties of the pyridine-based complexes, quinoline and quinoxaline-based ligands were prepared. Interestingly, complexation with both ligands afforded the facial stereoselectivity exclusively (See §III.4.3, Schemes 12 and 13). As in the pyridine-substituted series, we further investigated the effect of the NHC. The synthesis of two additional quinoxaline-based ligands with bIm and 4MeIm as NHC was performed. Interestingly, the complexation proceeded with *fac* stereoselectivity, being consistent with previous results (See §III.4.3, Scheme 14).

In spite of preliminary computational calculations performed by Dr. Antonio Francés Monerris (Valencia), understanding the *fac/mer* selectivity requires a deeper investigation on the complexation mechanism, which is currently on going. So far structural characterization has shown that the *fac* isomers display more distorted coordination spheres (See §III.4.4, Figure 42, Table 7), than the *mer* ones, which could be deleterious to their EE dynamics. However, it is also conceivable that the facial configurations results in interligand interactions that are no present in the meridional one (See §III.4.5, Figure 44, Table 8). These interactions in the facial conformation might prevent the Fe-N bond elongation, which has been demonstrated to be the primary factor causing the MLCT excited states decay. On the other hand, the nature of both NHC and π-conjugation appeared to be the key parameters controlling their optical and redox properties, with both isomers exhibiting distinct behaviors (See §III.4.6). The use of π-extended azines is of particular relevance due to their low-lying MLCT manifold, resulting in an improved absorbance in the UV-vis spectrum (See §III.4.6, Figures 46 and 47, Table 9). Furthermore, the possible reduction of the electronic coupling with the MC states could contribute to longer-lived MLCT. In this regard, a collaboration with Prof. Dr. Stefan Haacke in Strasbourg is being carried out to study the influence on the EE kinetics. This part of the thesis highlights the great potential of these complexes, which can take advantage of the synergistic effect of coupling a specific substitution pattern at the azine unit with the NHC, is thus highlighted. As a result a synthesis of non-labile iron(II) complexes with stereoselectivity presumably given by inter-ligand interactions. Additionally, the opto-electronic characteristics that can be easily modified as a function of both the azine and the NHC moieties.

In regard to the Fe(III) complexes bearing tridentate anionic ligands, we aimed at obtaining iron complexes with increased long-lived excited state lifetimes. The strategy was the use of strong donor ligands such as amides and cyclometallating units in order to induce strong ligand field and destabilize the MC states (See §IV). Hence, we synthesized and characterized different anionic ligands that bear NHC units together with N-amido donors (carbazolate series) (See §IV.2.1, Scheme 15) or with C-anionic donors (cyclometallated series) (See §IV.4.2, Scheme 20). Concerning the N-amido series, we reported the synthesis of three complexes, one homoleptic (See §IV.2.2, Scheme 16) and two heteroleptic (See §IV.3, Scheme 17) with maximized metal-ligand interactions due to the formation of 6-membered chelates. The strength of the coordination sphere was modulated as a function of the number of coordinated N-amido ligands, although in all cases Fe(III) species were obtained.

Interestingly, both homoleptic and heteroleptic compounds seemed to have metal-based and ligand-based orbital mixing as evidenced by their oxidation behavior (See §IV.4.4, Figure 57 and Table 12), suggesting that this type of ligands could be useful to achieve a full "HOMO inversion" as defined by Jakubikova. More distinct properties arose from their reduction behavior, with the heteroleptic complexes featuring a remarkably anodically shifted first reduction potential that could reflect the less enrich metal ion respect to the homoleptic complex. In addition, reduction of the tpy moieties was observed as well due to their strong acceptor character. Interestingly, both series of complexes displayed charged transfer bands of different nature almost over the whole visible range and extending until the IR region.

As for the C-anionic series, during a 2-month internship with Prof. Dr. Bauer in Paderborn in the framework of the DrEAM program of Lorraine University of Excellence (LUE), we developed a methodology that allowed us to get new bis-cyclometalated Fe-CCC complexes (See §IV.4.3, Scheme 22), highlighting that the use of glove box, a transmetallating or reducing reagent was avoided. The ground state properties of the obtained homoleptic complexes were investigated. These complexes feature a cyclometalating pyrimidine unit that allow for an orbital stabilization induced by the pyrimidine backbone and the substituents in position 2 (-Ph, -CF_3), as the electron withdrawing character increases, an anodically shift is observed in their reduction potential waves. Both complexes display three distinct absorption bands corresponding to π–π*, MLCT and LMCT transitions that are found at lower energy by comparison with the one reported by Bauer with a phenyl backbone instead of a pyrimidine. The presence of the phenyl substituent on the pyrimidine leads to an increase of absorption intensity (See §IV.4.4, Figure 60, Table 14). Calculations are ongoing in collaboration with Dr. Antonio Francés Monerris to get insights into the nature of the observed UV-vis absorptions for both the N-amido and cyclometallated iron complexes. As complementary measurements in collaboration with Prof. Dr. Haacke in Strasbourg are conducted to measure the dynamics of the excited state relaxation (TAS experiments). Next in order, a series of reductions test will be conducted to the cyclometallated complexes in order to obtain Fe(II)-CCC complexes, then the ground state and excited state properties of the complexes will be investigated. Finally, the synthesis of heteroleptic complexes with push-pull ligands will be attempted aiming to obtain Fe(II)-CCC complexes with vectorial electron flux.

Finally, yet important in this doctoral work, we get into the skyrocketing trend of green H_2 production, due to its huge energy density (120 MJ kg^{-1}) and its large industrial application (pharmaceutical, refining, agriculture, etc), pursuing the production of green H_2 with zero

carbon print. In order to fulfil this goal, we planned the synthesis of a set ligands in order to design a bimetallic heteroleptic ditopic Fe-Co dyads that will be tested as photosensitizers in water splitting reaction in the reduction of protons ($2H^+ + 2e^- \rightleftharpoons H_2\ E^0 = 0\ V\ vs\ RHE$). This part of the synthesis of the ligands was carried out in our laboratory (L2CM) while the heteroleptic synthesis of the complex was made in the framework of the DrEAM programme in Germany with Prof. Dr. Bauer.

After having explored different approaches to obtain the targeted ligands (See §V.2.1, Schemes 26, 27, and 29), we succeeded in having two out of three ligands: one for a monodentate Co coordination to give a dyad (See §.V.2, Figure 68), and one for a bidentate cobalt coordination, possibly allowing the access to both a dyad and a triad (See §V.2, Figure 68). At this time, Bauer and co-workers reported the heteroleptic complex with one of the ligands for monodentate Co coordination (See §V.2.1, Scheme 27, ligand **H_2L29**). So we focused in the synthesis of the homoleptic and heteroleptic (See §V.3, Scheme 30) complexes with our ligand. The homoleptic complex **[Fe(L30)$_2$]$^{2+}$** was afforded in 40% yield (See §V.3 Table 17). Then, the heteroleptic complex was achieved by following a procedure reported by Bauer in which they use a tridentate bulky ligand (**BuL**) to kinetically inhibit the formation of the heteroleptic complex. [Fe(HMDS)$_2$(THF)] in solution was used as a combined source of iron and base to coordinate **BuL**, then ligand **H_2L30** was in parallel deprotonated and added into the solution of **[FeBuL]**$^{2+}$ affording the heteroleptic complex **[Fe(BuL)(L30)]$^{2+}$** (See §V.3, Scheme 30).

It is worth noting that in both cases, we selectively coordinate the iron center to the tridentate one from the two possible coordinative sites (C^N^C and N^N). Moreover, we were able to synthesize a heteroleptic ditopic complex that may coordinate a cobalt ion using Bauer's protocol. The ground state characterization revealed that the electron-rich nature of the dipyridyl units appears to favor the MLCT implying the **BuL** ligand rather than **L30**, preventing the target electronic transfer towards the Co coordinating site. As a result, while actual Co coordination may exert a sufficient pull effect, these findings clearly demonstrate the need to increase the electronic differences between terminal (push) and ditopic (pull) ligands. For example, using an anionic terminal ligand and/or the introduction of electron reservoir units within the ditopic ligand could be envisaged.

The project is currently ongoing, targeting the differences in electron character between the terminal and ditopic ligand so as to favor a vectorial electron transfer towards the

Co coordination site. As for our complex, it will be coordinated to cobalt in order to obtain a triad (Figure 78) and thus evaluate:

- Stability of the triad, ground state characterization and ESL.
- Their performance in photocatalytic H_2 evolution and compare activities between dyad and triads.

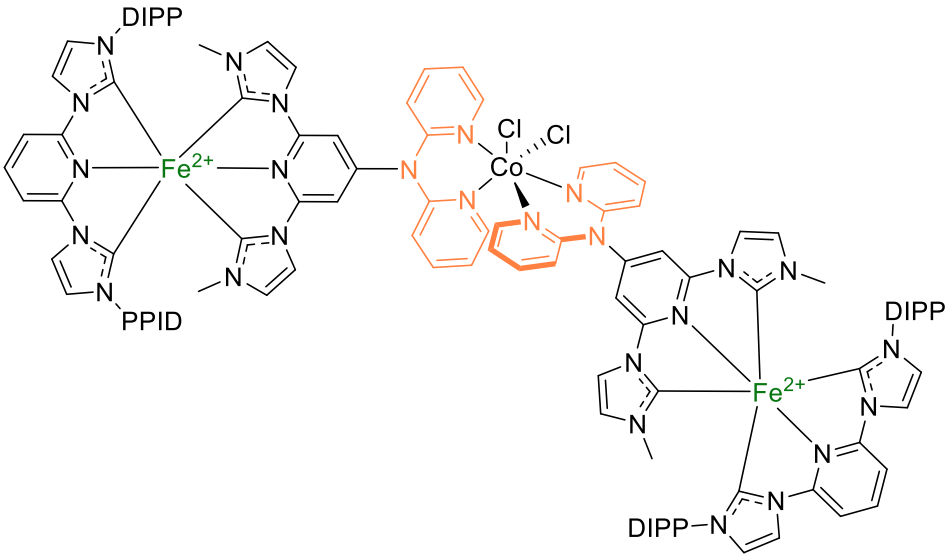

Figure 73. Structure of triad **[(Fe(BuL)(L30))$_2$CoCl$_2$]**.

VII. Experimental part

VIII. Experimental part

VII.1 Materials and methods

Solvents and commercially available reagents were used as received without further purification. All complexation reactions were performed under argon atmosphere using standard Schlenk techniques. Solvents were dried using standard protocols when necessary. All reactions were monitored by thin layer chromatography using TLC 60 F-254 (Merk) plates. Purifications by chromatography were performed with silica gel 60 (0.063-0.2 mm/70-230 mesh). The NMR spectra were recorded at 25°C on a DRX400 Bruker spectrometer. The chemical shifts are reported in ppm and calibrated by using tetramethylsilane (TMS) or signals from the residual protons of the deuterated solvents. High resolution mass spectra were recorded on a Bruker micro TOF-Q spectrometer. UV-vis spectra were recorded in a 1 cm path length quartz on a Evolution 201 (Thermo Scientific). Cyclic voltammetry was performed on a Ratiometer PST006 potentiostat using a conventional three-electrode cell. Saturated calomel electrode (SCE) was separated from the test compartment using a bridge tube. The solutions of studied complexes (0.2 mM) were purged with argon before each measurement. The test solution was acetonitrile containing 0.1 M Bu_4NPF_6 as supporting electrolyte. The working electrode was vitreous carbon rod (1 cm^2) wire and the counter electrode was a 1 cm^2 Pt disc. After measurement, ferrocene was added as the internal reference for calibration. All potentials were quoted versus SCE. In these conditions, the redox potential of the couple Fc^+/Fc was found at 0.39 V. In all the experiments, the scan rate was 100 mV/s.

VII.2 General schemes for HL1-HL22 synthesis (III. Bidentate azine NHC Fe(II))

Compounds **HL3-HL8** (§III.4)

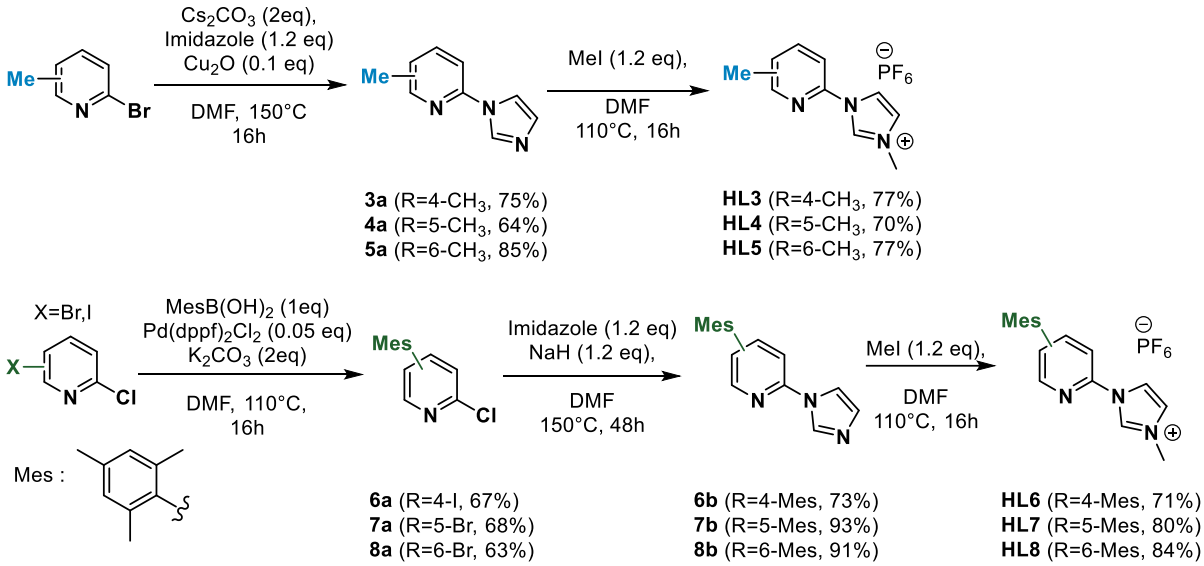

3a (R=4-CH_3, 75%)
4a (R=5-CH_3, 64%)
5a (R=6-CH_3, 85%)

HL3 (R=4-CH_3, 77%)
HL4 (R=5-CH_3, 70%)
HL5 (R=6-CH_3, 77%)

6a (R=4-I, 67%)
7a (R=5-Br, 68%)
8a (R=6-Br, 63%)

6b (R=4-Mes, 73%)
7b (R=5-Mes, 93%)
8b (R=6-Mes, 91%)

HL6 (R=4-Mes, 71%)
HL7 (R=5-Mes, 80%)
HL8 (R=6-Mes, 84%)

Compounds **HL9-HL12** (§III.4.1)

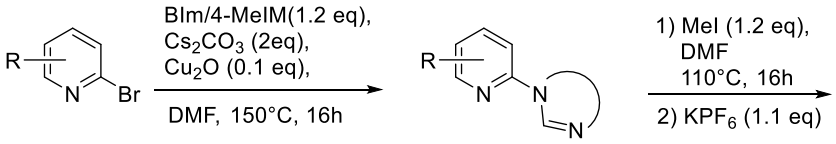

R = 6-Me
R = 5-Mes

9a, R = 6-Me (4-methylimidazole, 85%)
10a, R = 6-Me (Benzimidazole, 74%)
11a, R = 5-Mes (4-methylimidazole, 75%)
12a, R = 5-Mes (Benzimidazole, 76%)

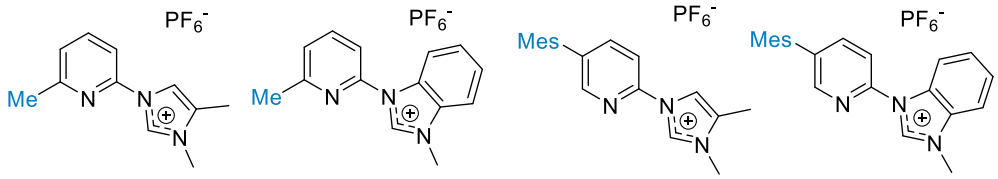

HL9, 87%
HL10, 75%
HL11, 80%
HL12, 75%

Compounds **HL13-HL17** (§III.4.2)

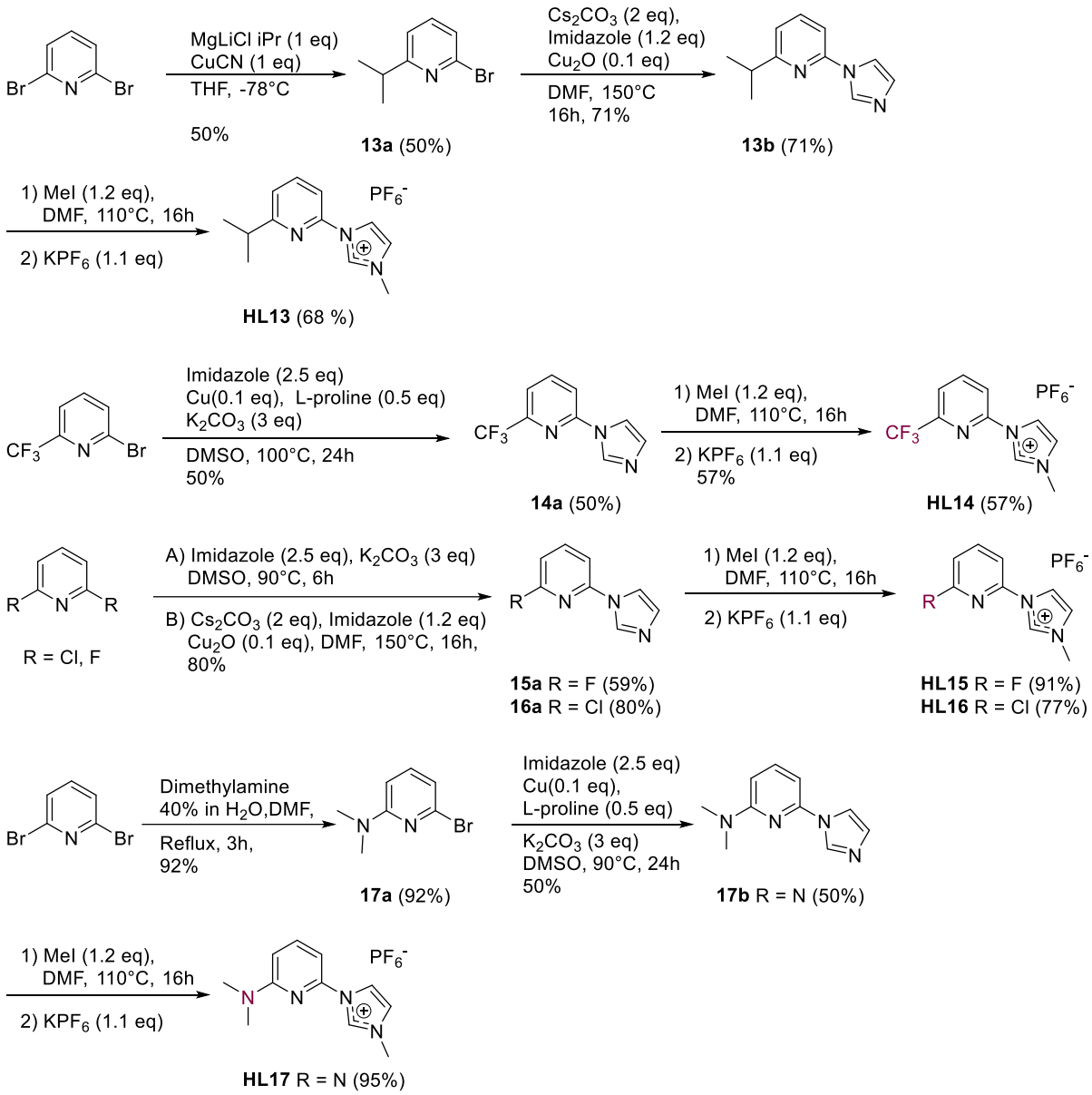

Compounds **HL18-HL22** (§III.4.3)

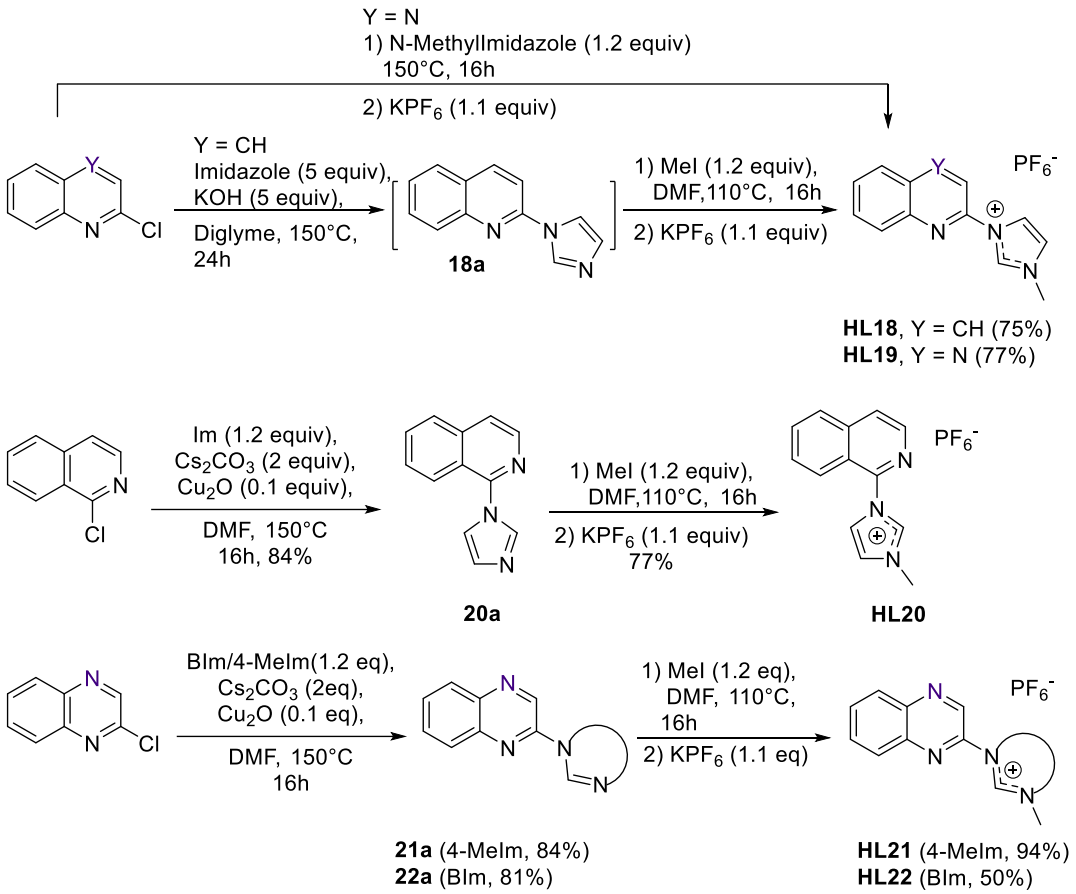

VII.3 Synthesis of ligands HL1-HL22 (III. Bidentate azine NHC Fe(II))

General imidazole introduction

Method A

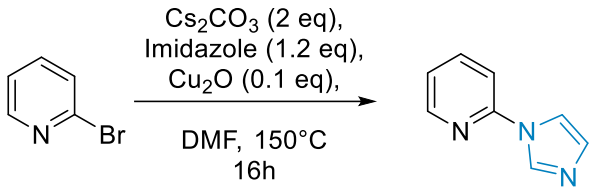

In a round flask charged with bromopyridine (1 g, 5.81 mmol, 1 equiv), Cs_2CO_3 (3.7 g, 11.62 mmol, 2 equiv), Cu_2O (83.17 mg, 0.58 mmol, 0.1 equiv) and imidazole derivative (0.45 g, 6.97 mmol, 1.2 equiv), was added DMF (12 mL) and the mixture was stirred at 150°C with a sand bath overnight. The reaction was monitored by TLC until no starting bromopyridine was observed. The reaction was quenched by addition of H_2O (15 mL) and ammonia (5mL 10% v/v) and extracted with CH_2Cl_2 (3 x 15 mL). The organic phases were dried over Mg_2SO_4 and purified over silica column (3:1 Hex:EtOAc + 1% Et_3N).

Method B

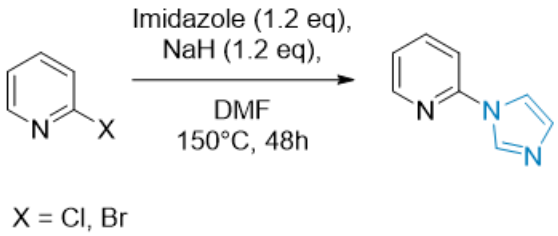

X = Cl, Br

In a Schlenk containing imidazole (0.29 g, 4.31 mmol, 1.2 equiv) was submitted to three Argon-vacuum cycles, then DMF (7 mL) was added, and the temperature was lowered to 0°C. Afterwards, NaH (0.151 g of a suspension in mineral oil, 4.31 mmol, 1.2 equiv) was added portion wise and the mixture was stirred until no H_2 evolution was observed. Then the corresponding 2-halopyridine (3.6 mmol, 1 equiv) was added. The reaction was stirred at 150 °C in a sand bath for 48 h and monitored by TLC until total consumption of the halopyridine. The reaction was then quenched by addition of H_2O (15 mL) and extracted with CH_2Cl_2 (3 x

10 mL). The organic phases were dried over Mg_2SO_4 and purified over silica column (3:1 Hex: EtOAc + 1% Et_3N).

Method C: General Suzuki cross-coupling reaction for mesitylene introduction

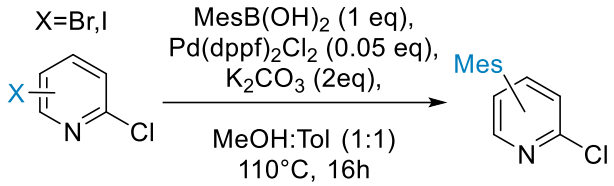

A round flask charged with 20 mL of MeOH:Toluene (1:1) was degassed by bubbling with Ar for 20 min, then bromo/iodo-2-chloropyridine (0.73/0.86 g, 2.59 mmol, 1 equiv), 2,4,6-trimethyboronic acid (0.42 g, 2.59 mmol, 1 equiv), K_2CO_3 (1.07 g, 7.79 mmol, 3 equiv), $Pd(dppf)Cl_2$ (0.19 g, 0.25 mmol, 0.01 equiv) were added and stirred at 80°C using a sand bath overnight. The reaction was monitored by TLC until no starting halopyridine was observed, then CH_2Cl_2 (15 mL) was added ant the reaction was filtered over celite and purified over silica column.

VII.3.1 Compounds 3a-17b

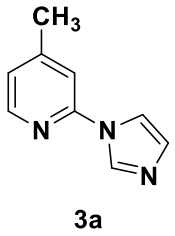

3a

2-(imidazole-1-yl)-4-methyl pyridine (**3a**).[220] According to aforementioned method B: 0.3 g (75%) of a white solid. Elution mixture for flash chromatography 3:1 Hex: EtOAc + 1% Et_3N. **^{1}H NMR** (400 MHz, $CDCl_3$) δ 8.35 (s, 1H), 8.31 (d, *J* = 5.1 Hz, 1H), 7.62 (s, 1H), 7.17 (d, *J* = 3.9 Hz, 2H), 7.04 (d, *J* = 5.0 Hz, 1H), 2.42 (s, 3H) ppm.

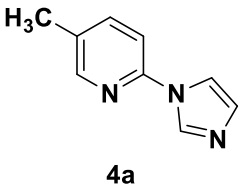

4a

2-(imidazole-1-yl)-5-methyl pyridine (**4a**).[220] According to aforementioned method B.: 0.4 g (64%) of a yellowish solid. Elution mixture for flash chromatography 3:1 Hex: EtOAc + 1% Et_3N. **^{1}H NMR** (400 MHz, $CDCl_3$) δ 8.28 (s, 2H), 7.60 (d, *J* = 7.7 Hz, 2H), 7.23 (d, *J* = 8.3 Hz, 1H), 7.16 (s, 1H), 2.35 (s, 3H) ppm.

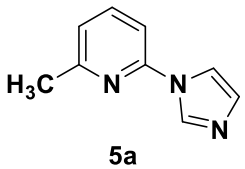

5a

2-(imidazole-1-yl)-6-methyl pyridine (**5a**).[221] According to aforementioned method A: 0.86 g (85%) of a yellowish solid. Elution mixture for flash chromatography 1:1 Hex: EtOAc + 1% Et_3N. **^{1}H NMR** (400 MHz, $CDCl_3$) δ 8.36 (s, 1H), 7.68 (t, *J* = 7.8 Hz, 1H), 7.63 (s, 1H), 7.18 (s, 1H), 7.14 (d, *J* = 8.1 Hz, 1H), 7.07 (d, *J* = 7.6 Hz, 1H), 2.55 (s, 3H) ppm.

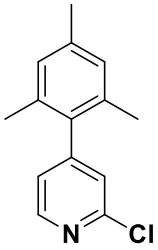

6a

2-chloro-4-mesitylpyridine (**6a**).[221] According to the general mesitylene introduction C: 0.38 g (67) of a yellow solid. Elution mixture for flash chromatography 9:1 Hex: EtOAc. **^{1}H NMR** (400 MHz, $CDCl_3$) δ 8.44 (dd, *J* = 5.0, 0.7 Hz, 1H), 7.15 (dd, *J* = 1.4, 0.7 Hz, 1H), 7.04 (dd, *J* = 5.0, 1.4 Hz, 1H), 6.95 (s, 2H), 2.33 (s, 3H), 2.00 (s, 6H).

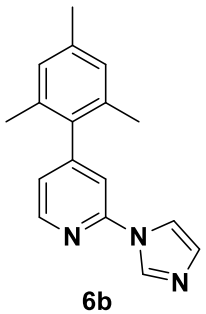

6b

2-(imidazole-1-yl)-4-mesitylpyridine (**6b**). According to aforementioned method A: 0.32 g (73%) of a yellowish solid. Elution mixture for flash chromatography 3:1 Hex: EtOAc + 1% Et_3N. **^{1}H NMR** (400 MHz, $CDCl_3$) δ 8.53 (dd, *J* = 5.0, 0.8 Hz, 1H), 8.37 (t, *J* = 1.1 Hz, 1H), 7.65 (t, *J* = 1.4 Hz, 1H), 7.19 (dt, *J* = 14.1, 1.1 Hz, 2H), 7.06 (dd, *J* = 5.0, 1.3 Hz, 1H), 6.98 (s, 2H), 2.35 (s, 3H), 2.04 (s, 6H). **^{13}C{^{1}H} NMR** (100 MHz, $CDCl_3$) δ 153.2, 149.6, 149.3, 138.2, 135.5, 135.1, 135.0, 130.8, 128.6, 123.2, 116.1, 113.1, 21.1, 20.6. **HRMS** (ESI-TOF) m/z: $[M + H]^+$ Calcd for $C_{17}H_{18}N_3$ 264.1495; Found: 264.1478.

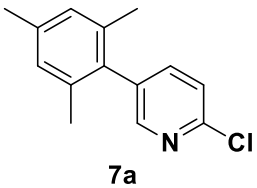

7a

2-chloro-5-mesitylpyridine (**7a**).[222] According to the general mesitylene introduction C: 0.77g (68%) of a yellow powder. Elution mixture for flash chromatography 20:1 Hex: EtOAc. **^{1}H NMR** (400 MHz, $CDCl_3$) δ 8.20 (pd, *J* = 2.5, 0.6 Hz, 1H), 7.47 (dd, *J* = 8.1, 2.4 Hz, 1H), 7.40 (dd, *J* = 8.1, 0.7 Hz, 1H), 6.97 (s, 2H), 2.33 (s,3H), 2.00 (s, 6H).

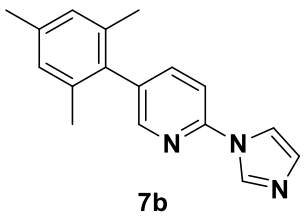

7b

2-(imidazole-1-yl)-5-mesitylpyridine (**7b**). According to aforementioned method **A**: 0.28 g, (93%) of a pale-yellow solid. Elution mixture for flash chromatography 3:1 Hex: EtOAc + 1% Et_3N. **^{1}H NMR** (400 MHz, $CDCl_3$) δ 8.39 (s, 1H), 8.26 (d, *J* = 1.7 Hz, 1H), 7.68 (s, 1H), 7.62 (dd, *J* = 8.3, 2.2 Hz, 1H), 7.43 (d, *J* = 8.3 Hz, 1H), 7.20 (s, 1H), 6.97 (s, 2H), 2.33 (s, 3H), 2.03 (s, 6H). **^{13}C{^{1}H} NMR** (100 MHz, $CDCl_3$) δ 149.7, 147.9, 140.2, 138.1, 136.4, 135.3, 135.1, 134.0, 130.9, 128.6, 116.3, 112.2, 21.2. **HRMS** (ESI-TOF) m/z: $[M + H]^+$ Calcd for $C_{17}H_{18}N_3$: 264.1495; Found: 264.1500.

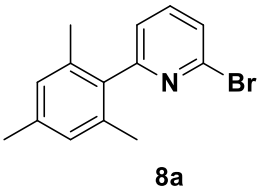

8a

2-chloro-6-mesitylpyridine (**8a**)[223]. According to the general mesitylene introduction method C: 0.73 g (63%) of a pale-yellow solid. Elution mixture for flash chromatography 30:1 Hex: EtOAc. **^{1}H NMR** (400 MHz, $CDCl_3$) δ 7.63 (dd, *J* = 15.3, 7.8 Hz, 1H), 7.47 (dd, *J* = 7.9, 0.9 Hz, 1H), 7.21 (dd, *J* = 7.5, 0.9 Hz, 1H), 6.97 (s, 2H), 2.33 (s, 3H), 2.06 (s, 6H).

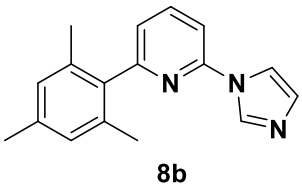

8b

2-(imidazole-1-yl)-6-mesitylpyridine (**8b**)[224]. According to aforementioned method A: 0.34 g (91%) of a white solid. Elution mixture for flash chromatography 2:1 Hex: EtOAc + 1% Et_3N. **^{1}H NMR** (400 MHz, $CDCl_3$) δ 8.38 (t, *J* = 1.1 Hz, 1H), 7.88 (dd, *J* = 8.2, 7.6 Hz, 1H), 7.68 (t, *J* = 1.4 Hz, 1H), 7.31 (dd, *J* = 8.2, 0.8 Hz, 1H), 7.19 (dd, *J* = 1.5, 1.0 Hz, 1H), 7.17 (dd, *J* = 7.6, 0.8 Hz, 1H), 7.00 – 6.95 (m, 2H), 2.35 (s, 3H), 2.08 (s, 6H).

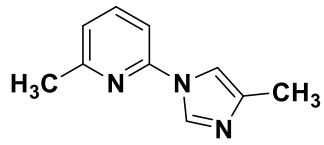

9a

2-(4-methylimidazol-1-yl)-6-methyl pyridine (**9a**). According to aforementioned method A: 0.61 g (85%) of a white solid. Elution mixture for flash chromatography 1:1 Hex: EtOAc + 1% Et_3N. **^{1}H NMR** (400 MHz, $CDCl_3$) δ 8.22 (d, *J* = 1.3 Hz, 1H), 7.65 (t, *J* = 7.8 Hz, 1H), 7.33 (s, 1H), 7.07 (d, *J* = 8.1 Hz, 1H), 7.04 (d, *J* = 7.6 Hz, 1H), 2.54 (s, 3H), 2.28 (s, 3H). **^{13}C{^{1}H} NMR** (100 MHz, $CDCl_3$) δ 158.7, 148.6, 139.7, 139.1, 134.3, 121.2, 112.6, 109.0, 24.4, 13.8. **HRMS** (ESI-TOF) m/z: $[M + H]^+$ Calcd for $C_{10}H_{12}N_3$: 174.1026; Found: 174.1033.

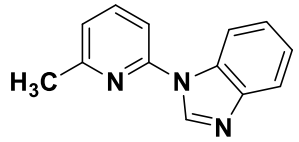

10a

2-(benzimidazol-1-yl)-6-methyl pyridine (**10a**)[225]. According to aforementioned method A: 0.42 g (74%) of a yellow solid. Elution mixture for flash chromatography 3:1 Hex: EtOAc + 1% Et_3N. **^{1}H NMR** (400 MHz, $CDCl_3$) δ 8.57 (d, *J* = 1.2 Hz, 1H), 8.07 (ddt, *J* = 7.4, 2.3, 1.0 Hz, 1H), 7.86 (dt, *J* = 8.4, 1.0 Hz, 1H), 7.82 – 7.73 (m, 1H), 7.42 – 7.29 (m, 3H), 7.15 (dd, *J* = 7.7, 2.8 Hz, 1H), 2.64 (s, 3H).

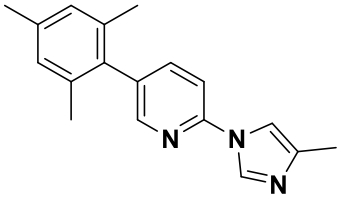

11a

5-mesityl-2-(4-methyl-1H-imidazol-1-yl)pyridine (**11a**). According to aforementioned method A: 0.6 g (75%) of a yellow solid. Elution mixture for flash chromatography 1:1 Hex: EtOAc + 1% Et_3N. **^{1}H NMR** (400 MHz, $CDCl_3$) δ 8.29 (d, *J* = 1.4 Hz, 1H), 8.26 (dd, *J* = 2.2, 0.8 Hz, 1H), 7.61 (dd, *J* = 8.3, 2.3 Hz, 1H), 7.41 – 7.35 (m, 2H), 7.01 – 6.96 (m, 2H), 2.35 (s, 3H), 2.32 (s, 3H), 2.04 (s, 6H). **^{13}C{^{1}H} NMR** (100 MHz, $CDCl_3$) δ 149.6, 148.0, 140.1, 140.1, 138.0, 136.5, 134.9, 134.3, 134.1, 128.6, 112.6, 111.8, 21.2, 21.0, 14.0. **HRMS** (ESI-TOF) m/z: $[M+H]^+$ Calcd for $C_{18}H_{20}N_3$ 278.1652; Found: 278.1645.

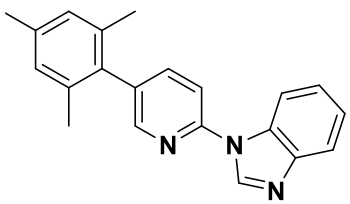

12a

1-(5-mesitylpyridin-2-yl)-1H-benzo[d]imidazole (**12a**). According to aforementioned method A: 0.41 g (76%) of a yellowish solid. Elution mixture for flash chromatography 3:1 Hex: EtOAc + 1% Et_3N. **^{1}H NMR** (400 MHz, $CDCl_3$) δ 8.66 (s, 1H), 8.42 (dd, *J* = 2.3, 0.8 Hz, 1H), 8.15 (dd, *J* = 8.3, 1.0 Hz, 1H), 7.90 (dd, *J* = 6.9, 1.6 Hz, 1H), 7.73 (dd, *J* = 8.2, 2.2 Hz, 1H), 7.67 (dd, *J* = 8.3, 0.9 Hz, 1H), 7.45 – 7.35 (m, 2H), 7.02 (s, 2H), 2.37 (s, 3H), 2.09 (s, 6H). **^{13}C{^{1}H} NMR** (100 MHz, $CDCl_3$) δ 150.0, 148.6, 144.9, 141.5, 140.1, 138.1, 136.4, 135.1, 134.0, 132.3, 128.6, 124.3, 123.4, 120.9, 114.0, 112.9, 21.2, 21.0. **HRMS** (ESI-TOF) m/z: $[M+H]^+$ Calcd for $C_{21}H_{20}N_3$ 314.1655; Found: 314.1686.

Synthesis of 2-chloro-6-isopropylpyridine (**13a**)[226].

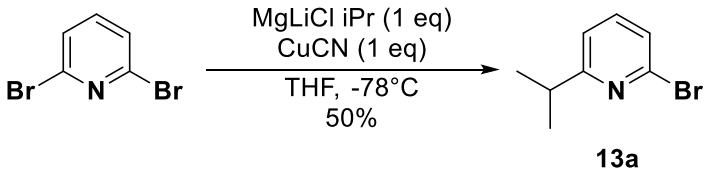

13a

In a Schlenk cupper cyanide (0.227 g, 2.53 mmol, 1 equiv) was suspended in 8 mL of THF, the mixture was cooled to -78°C, then Isopropyl magnesium chloride (1.95 mL of a 1.3M solution in THF, 2.53 mmol, 1 equiv) was added dropwise and the medium was stirred for 30 min, afterwards 2,6-dibromopyridine (0.600 g, 2.53 mmol, 1 equiv) was added and the mixture was warmed to room temperature and stirred overnight. The resulting mixture was diluted with diethyl ether (15 mL), washed with aqueous ammonia (2 x 10 mL) and brine (2 x 10 mL). The organic layer was dried over $MgSO_4$ and the solvent was removed under vacuum. The crude product was purified over silica column using n-Hexane:EtOAc (12:1) affording 0.41g of the desired product (80%). **^{1}H NMR** (400 MHz, $CDCl_3$) δ 7.45 (t, *J* = 7.7 Hz, 1H), 7.28 (dd, *J* = 7.8, 0.7 Hz, 1H), 7.11 (d, *J* = 7.9 Hz, 1H), 3.03 (hept, *J* = 6.9 Hz, 1H), 1.28 (d, *J* = 6.9 Hz, 6H) ppm.

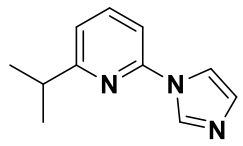

13b

2-(imidazole-1-yl)-6-isopropylpyridine (**13b**). According to aforementioned method A: 0.28g (71%) of a yellowish solid. Elution mixture for flash chromatography 1:1 Hex: EtOAc + 1% Et_3N. **^{1}H NMR** (400 MHz, $CDCl_3$) δ 8.38 (s, 1H), 7.71 (t, *J* = 7.9 Hz, 1H), 7.66 (s, 1H), 7.18 (s, 1H), 7.14 (d, *J* = 7.8 Hz, 1H), 7.09 (d, *J* = 7.7 Hz, 1H), 3.06 (hept, *J* = 6.9 Hz, 1H), 1.32 (d, *J* = 6.9 Hz, 6H). **^{13}C{^{1}H} NMR** (100 MHz, CD_3CN) δ 162.2, 143.0, 133.8, 129.7, 125.1, 113.7, 110.8, 103.9, 30.7, 24.4, 17.0. **HRMS** (ESI-TOF) m/z: $[M+H]^+$ Calcd for $C_{11}H_{14}N_3$ 188.1182; Found: 188.1175.

Synthesis of 2-(1H-imidazol-1-yl)-6-(trifluoromethyl)pyridine (**14a**)

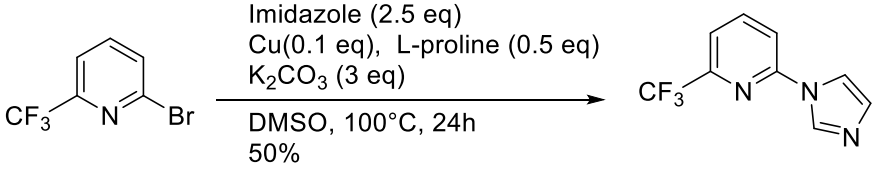

14a (50%)

2-(1H-imidazol-1-yl)-6-(trifluoromethyl)pyridine (**14a**). A 50 mL round bottomed flask was charged with 2-bromo-6(trifluoromethyl)pyridine (0.4 g, 1.77 mmol, 1 equiv), imidazole (0.241 g, 3.54 mmol, 2 equiv), CuI (0.034 g, 0.177 mmol, 0.1 equiv), L-proline (0.041 g, 0.354 mmol, 0.5 equiv), K_2CO_3 (0.489 g, 3.54 mmol, 3 equiv) and dry DMSO (10 mL). Then the reaction mixture was heated at 90°C for 24 h. The reaction medium was poured into ice cold water. The cooled mixture was partitioned between ethyl acetate and saturated NH_4Cl, the organic layer was washed with brine, dried over $MgSO_4$ and concentrated in vacuo to afford

desired compound (0.280 g, 74 % yield). **^{1}H NMR** (400 MHz, $CDCl_3$) δ 8.36 (s, 1H), 7.97-7.93 (m, 1H), 7.64-7.63 (m, 1H), 7.54 (d, *J*= 7.59 Hz, 1H), 7.5 (d, *J*= 8.28 Hz, 1H), 7.16 (s, 1H). **^{13}C{^{1}H} NMR** (100 MHz, $CDCl_3$) δ 149.2, 148.0 (q, J = 35.8 Hz), 140.8, 135.2, 131.3, 121.0 (d, J = 274.3 Hz), 118.4 (q, J = 2.8 Hz), 116.3, 115.1.**^{19}F NMR** (400 MHz, $CDCl_3$) δ -68.39. **HRMS** (ESI-TOF) m/z: $[M+H]^+$ Calcd for $C_9H_7F_3N_3$ 214.0592; Found: 214.0597.

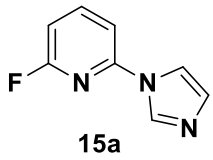

15a

2-fluoro-6-(1H-imidazol-1-yl)pyridine (**15a)** was synthesized according to a literature procedure[227]. **^{1}H NMR** (400 MHz, $CDCl_3$) δ 8.31 (s, 1H), 7.90 (q, *J* = 7.9 Hz, 1H), 7.59 (s, 1H), 7.22 (dd, *J* = 7.8, 1.8 Hz, 1H), 7.17 (s, 1H), 6.85 (dd, *J* = 8.1, 2.7 Hz, 1H).

Synthesis of 2-chloro-6-(1-imidazol-1-yl)pyridine (**16a**).[228]

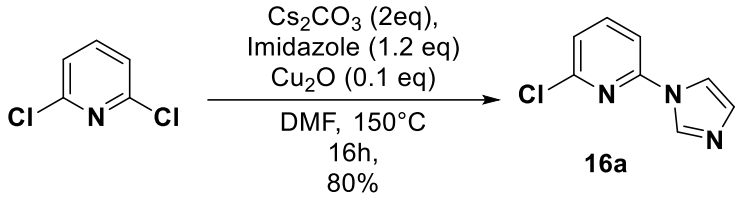

16a

In a round flask charged with 2,6-dibromopyridine (0.5 g, 3.38 mmol, 1equiv), imidazole (0.276 g, 4.05 mmol, 1.2 equiv) and Cs_2CO_3 (2.2 g, 6.76 mmol, 2equiv) and Cu_2O (0.032 g, 0.338 mmol, 0.1 eq) were mixed and stirred at 150°C overnight. After this time the reaction was quenched by addition of H_2O (10 mL) and extracted with CH_2Cl_2 (5mL x 3), the organic phase was washed with $NaHCO_{3aq}$ (5 mL x 2), dried over $MgSO_4$ and the solvent was removed under vacuum, affording **16a** (0.48 g, 80%) as a white powder. Elution mixture for flash chromatography 1:1 Hex: EtOAc + 1% Et3N. **^{1}H NMR** (400 MHz, $CDCl_3$) δ 8.32 (s, 1H), 7.72 (t, *J* = 7.9 Hz, 1H), 7.57 (s, 1H), 7.22 (dd, *J* = 15.8, 7.9 Hz, 2H), 7.13 (s, 1H).

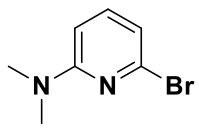

17a

6-bromo-N,N-dimethylpyridin-2-amine (**17a**) was synthesized using following literature procedure[229]. **^{1}H NMR** (400 MHz, $CDCl_3$) δ 7.18 (dd, *J* = 7.6, 0.6 Hz, 1H), 6.60 (d, *J* = 7.4 Hz, 1H), 6.31 (d, *J* = 8.4 Hz, 1H), 2.99 (s, 6H).

Synthesis of 6-(1*H*-imidazol-1-yl)-*N*,*N*-dimethylpyridin-2-amine (**17b**).

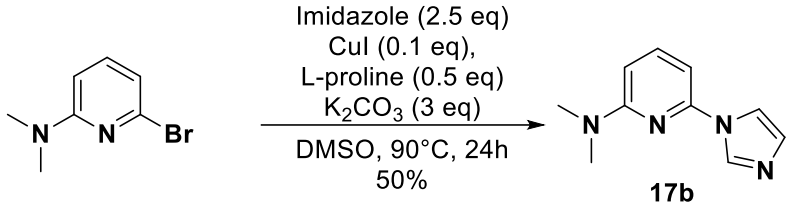

In a 50 mL round bottomed flask was charged with **17a** (0.3 g, 1.49 mmol, 1eq), imidazole (0.254 g, 3.73 mmol, 2.5 eq), CuI (0.029 g, 0.149 mmol, 0.1 eq), L-proline (0.086 g, 0.746 mmol, 0.5 eq), K_2CO_3 (0.618 g, 4.48 mmol, 3 eq) and dry DMSO (10 mL). Then the reaction mixture was heated at 90 °C for 24 h. After completion of reaction, the mixture was poured into ice cold water. The cooled mixture was partitioned between ethyl acetate and saturated NH_4Cl, the organic layer was washed with brine, dried over $MgSO_4$ and concentrated in vacuo to get desired compound **17b** (0.2 g, 50% yield) and used for next step without purification. **^{1}H NMR** (400 MHz, $CDCl_3$) δ 8.24 (s, 1H), 7.51 (s, 1H), 7.46-7.42 (m, 1H), 7.06 (s, 1H), 6.46 (d, J= 7.59 Hz, 1H), 6.32 (d, J= 8.44 Hz, 1H), 3.03 (s, 6H). **^{13}C{^{1}H} NMR** (100 MHz, $CDCl_3$) δ 158.5, 147.4, 139.6, 135.0, 129.9, 116.1, 103.6, 98.3, 37.9.
HRMS (ESI-TOF) m/z: $[M+H]^+$ Calcd for $C_{10}H_{13}N_4$ 189.1140; Found: 189.1157.

VII.3.2 Synthesis if compounds HL3-HL22

Method D: <u>General quaternization method</u> at the imidazole moiety

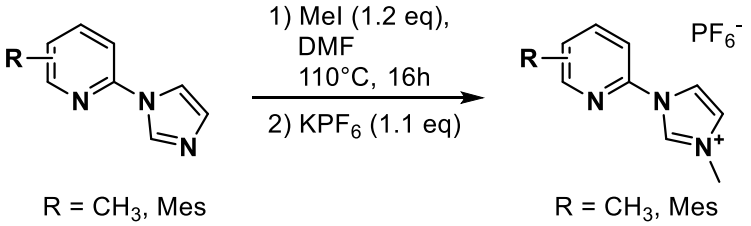

2-imidazole-6-methylpyridine (3.69 mmol, 0.54 g, 1 equiv) and MeI (4.43 mmol, 0.63 g, 1.2 equiv) in DMF (10 mL) were mixed in a 25 mL round flask and heated at 80 °C in a sand bath overnight with constant stirring. After this time, the solvent was almost removed in vacuum, then H_2O (7 mL) was added, followed for KPF_6 (4.06 mmol, 0.75 g, 1.1 equiv). The solution was stirred for 30 min and the precipitate was filtered through a glass funnel filter #3, washed with diethyl ether (3 x 10mL) and the solid was recovered.

Compounds HL3-HL19

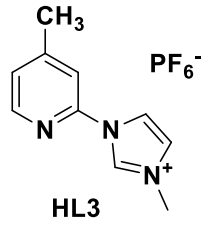

3-methyl-1-(4-methylpyridin)-imidazolium hexafluorophosphate (**HL3 PF_6^-**). General quaternization method D afforded 0.47 g, (77%) of a yellowish powder. **^{1}H NMR** (400 MHz, CD_3CN) δ 9.24 (d, *J* = 1.8 Hz, 1H), 8.42 (d, *J* = 5.1 Hz, 1H), 8.03 (t, *J* = 2.0 Hz, 1H), 7.60 (s, 1H), 7.54 (t, *J* = 1.9 Hz, 1H), 7.40 (d, *J* = 5.0 Hz, 1H), 3.96 (s, 3H), 2.49 (s, 3H). **^{13}C{^{1}H}NMR** (100 MHz, CD_3CN) δ 153.3, 149.6, 147.1, 135.1, 126.7, 125.3, 119.7, 115.1, 37.1, 20.8. **HRMS** (ESI-TOF) m/z: $[M - PF_6^-]^+$ Calcd for $C_{10}H_{12}N_3$ 174.1031; Found: 174.1048.

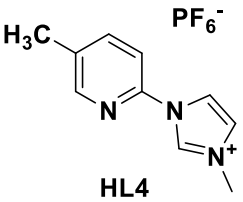

3-methyl-1-(5-methylpyridin)-imidazolium hexafluorophosphate (**HL4 PF_6^-**). General quaternization method D afforded 0.5 g, (70 %) of a white-yellowish powder. **^{1}H NMR** (400 MHz, CD_3CN) δ 9.22 (d, *J* = 1.7 Hz, 1H), 8.42 – 8.39 (m, 1H), 8.02 (t, *J* = 2.0 Hz, 1H), 7.90 (ddd, *J* = 8.3, 2.3, 0.9 Hz, 1H), 7.61 (d, *J* = 8.3 Hz, 1H), 7.53 (t, *J* = 1.9 Hz, 1H), 3.95 (s, 3H), 2.42 (s, 3H). **^{13}C{^{1}H} NMR** (100 MHz, CD_3CN) δ 150.1, 144.9, 141.2, 136.5, 134.9, 125.2, 119.8, 114.0, 37.0, 17.6. **HRMS** (ESI-TOF) m/z: $[M - PF_6^-]^+$ Calcd for $C_{10}H_{12}N_3$ 174.1026;. Found: 174.1019.

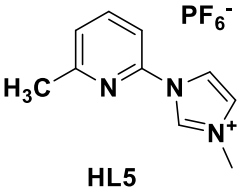

3-methyl-1-(6-methylpyridin)-imidazolium hexafluorophosphate (**HL5 PF_6^-**). General quaternization method D afforded 0.8 g, (77%) of a yellowish powder. **^{1}H NMR** (400 MHz, CD_3CN) δ 9.25 (td, *J* = 1.7, 0.8 Hz, 1H), 8.05 (t, *J* = 1.9 Hz, 1H), 7.96 (t, *J* = 7.9 Hz, 1H), 7.53 (t, *J* = 2.0 Hz, 1H), 7.52 – 7.50 (m, 1H), 7.43 (d, *J* = 7.7 Hz, 1H), 3.96 (d, *J* = 0.6 Hz, 3H), 2.58 (s, 3H). **^{13}C{^{1}H} NMR** (100 MHz, CD_3CN) δ 159.3, 145.4, 140.2, 134.3, 124.5, 124.4, 118.9, 110.4, 36.2, 22.9. **HRMS** (ESI-TOF) m/z: $[M - PF_6^-]^+$ Calcd for $C_{10}H_{12}N_3$ 174.1031; Found: 174.1046.

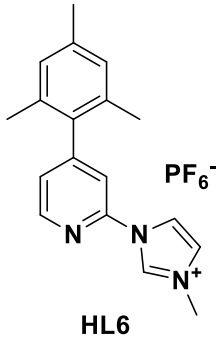

HL6

1-(4-mesitylpyridin)-3-mehtylimidazolium hexafluorophosphate (**HL6 PF_6^-**). General quaternization method D afforded 0.48 g (71%), of a yellowish powder. **^{1}H NMR** (400 MHz, CD_3CN) δ 9.63 (s, 1H), 8.62 (dd, *J* = 4.9, 0.8 Hz, 1H), 8.13 (t, *J* = 1.9 Hz, 1H), 7.67 (t, *J* = 1.0 Hz, 1H), 7.59 (t, *J* = 1.9 Hz, 1H), 7.37 (dd, *J* = 5.0, 1.3 Hz, 1H), 7.02 (s, 2H), 4.00 (s, 3H), 2.32 (s, 3H), 2.02 (s, 6H). **^{13}C{^{1}H} NMR** (100 MHz, CD_3CN) δ 154.9, 150.5, 147.8, 139.3, 135.9, 135.8, 135.8, 129.4, 127.4, 125.6, 120.2, 116.0, 37.5, 21.1, 20.6. **HRMS** (ESI-TOF) m/z: $[M - PF_6^-]^+$ Calcd for $C_{18}H_{20}N_3$ 278.1657; Found: 278.1662.

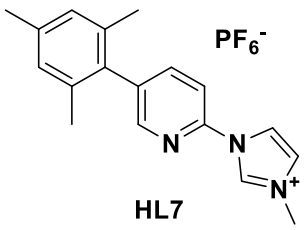

HL7

1-(5-mesitylpyridin)-3-mehtylimidazolium hexafluorophosphate (**HL7 PF_6^-**). General quaternization method D afforded 0.56 g, (80%) of a yellowish powder. **^{1}H NMR** (400 MHz, CD_3CN) δ 9.30 (s, 1H), 8.38 (d, *J* = 2.2 Hz, 1H), 8.11 (t, *J* = 1.9 Hz, 1H), 7.91 (dd, *J* = 8.4, 2.2 Hz, 1H), 7.80 (d, *J* = 8.3 Hz, 1H), 7.58 (s, 1H), 7.02 (s, 2H), 3.98 (s, 3H), 2.32 (s, 3H), 2.01 (s, 6H). **^{13}C{^{1}H} NMR** (100 MHz, CD_3CN) δ 149.4, 144.9, 141.1, 138.1, 137.9, 135.8, 134.3, 133.0, 128.1, 124.5, 119.0, 113.5, 36.2, 19.6. **HRMS** (ESI-TOF) m/z: $[M - PF_6^-]^+$ Calcd for $C_{18}H_{20}N_3$ m/z: 278.1657; Found: 278.1668.

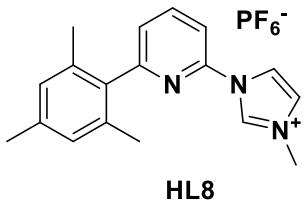

HL8

1-(6-mesitylpyridin)-3-mehtylimidazolium hexafluorophosphate (**HL8 PF_6^-**). General quaternization method D afforded 0.39 g, (84%) of a pale yellow powder. **^{1}H NMR** (400 MHz, CD_3CN) δ 9.35 (q, *J* = 0.9 Hz, 1H), 8.15 (t, *J* = 7.9 Hz, 1H), 8.08 (t, *J* = 1.9 Hz, 1H), 7.73 (dd, *J* = 8.2, 0.7 Hz, 1H), 7.55 (t, *J* = 1.9 Hz, 1H), 7.49 (dd, *J* = 7.7, 0.7 Hz, 1H), 7.00 (s, 2H), 3.94 (s, 3H), 2.32 (s, 3H), 2.03 (s, 6H). **^{13}C{^{1}H} NMR** (100 MHz, CD_3CN) δ 159.6, 145.9, 140.4, 138.1, 135.7, 135.4, 134.4, 128.0, 126.2, 124.4, 118.9, 111.6, 36.2, 19.8, 19.0. **HRMS** (ESI-TOF) m/z: $[M - PF_6^-]^+$ Calcd for $C_{18}H_{20}N_3$ m/z: 278.1652; Found: 278.1652.

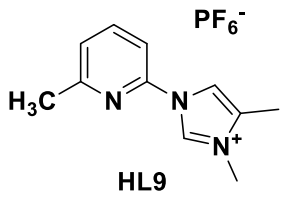

HL9

3,4-dimethyl-1-(6-methylpyridin-2-yl)-imidazolium hexafluorophosphate (**HL9 PF_6^-**). General quaternization method D afforded 0.61 g, (87 %) of a white powder. **^{1}H NMR** (400 MHz, CD_3CN) δ 9.19 (s, 1H), 7.94 (tt, *J* = 7.9, 1.7 Hz, 1H), 7.83 (s, 1H), 7.45 (d, *J* = 8.1 Hz, 1H), 7.40 (d, *J* = 7.8 Hz, 1H), 3.82 (s, 3H), 2.57 (s, 3H), 2.36 (s, 3H). **^{13}C{^{1}H} NMR** (100

MHz, CD_3CN) δ 159.2, 145.4, 140.1, 133.4, 133.2, 124.3, 115.5, 110.0, 33.5, 22.9, 8.0. **HRMS** (ESI-TOF) m/z: $[M - PF_6^-]^+$ Calcd for $C_{11}H_{14}N_3$ m/z: 188.1182; Found: 188.1178.

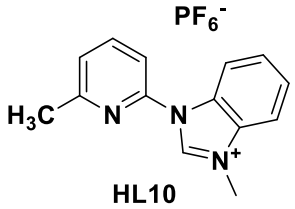

3-methyl-1-(6-methylpyridin-2-yl)-benzimidazolium hexafluorophosphate (**HL10 PF_6^-**). General quaternization method D afforded 1.1 g, (75 %) of a yellowish powder. **^{1}H NMR** (400 MHz, CD_3CN) δ 9.52 (s, 1H), 8.44 – 8.36 (m, 1H), 8.05 (t, *J* = 7.9 Hz, 1H), 7.99 – 7.91 (m, 1H), 7.78 (td, *J* = 6.4, 3.6 Hz, 2H), 7.63 (d, *J* = 8.0 Hz, 1H), 7.51 (d, *J* = 7.7 Hz, 1H), 4.17 (s, 3H), 2.66 (s, 3H). **^{13}C{^{1}H} NMR** (100 MHz, CD_3CN) δ 159.6, 146.1, 140.5, 140.3, 132.4, 129.7, 127.7, 127.3, 124.5, 115.5, 113.3, 113.3, 33.4, 23.0. **HRMS** (ESI-TOF) m/z: $[M - PF_6^-]^+$ Calcd for $C_{14}H_{14}N_3$ m/z: 224.1188; Found: 224.1175.

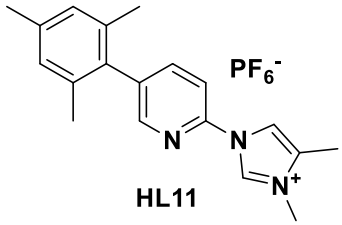

1-(5-mesitylpyridin-2-yl)-3,4-dimethyl-1H-imidazol-3-ium hexafluorophosphate (**HL11 PF_6^-**). General quaternization method D afforded 0.38 g, (80 %) of a yellowish powder. **^{1}H NMR** (400 MHz, CD_3CN) δ 9.23 (d, *J* = 1.8 Hz, 1H), 8.36 (d, *J* = 2.2 Hz, 1H), 7.89 (dd, *J* = 8.3, 2.2 Hz, 2H), 7.74 (d, *J* = 8.3 Hz, 1H), 7.02 (s, 2H), 3.86 (s, 3H), 2.39 (s, 3H), 2.32 (s, 3H), 2.01 (s, 6H). **^{13}C{^{1}H} NMR** (100 MHz, CD_3CN) δ 150.6, 146.1, 142.3, 139.1, 137.0, 134.7, 134.5, 134.3, 129.3, 116.8, 114.4, 34.8, 21.0, 20.8, 9.2. **HRMS** (ESI-TOF) m/z: $[M - PF_6^-]^+$ Calcd for $C_{19}H_{22}N_3$ m/z: 292.1814; Found: 292.1828.

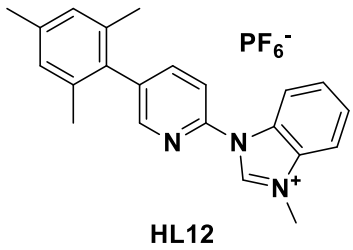

1-(5-mesitylpyridin-2-yl)-3-methyl-1H-benzoimidazol-3-ium hexafluorophosphate (**HL12 PF_6^-**). General quaternization method D afforded 0.44 g, (75 %) of a yellowish powder. **^{1}H NMR** (400 MHz, CD_3CN) δ 9.70 (d, *J* = 3.4 Hz, 1H), 8.51 (d, *J* = 2.2 Hz, 1H), 8.42 (dt, *J* = 7.4, 3.3 Hz, 1H), 7.98 (dd, *J* = 6.0, 3.8 Hz, 3H), 7.85 – 7.76 (m, 2H), 7.05 (s, 2H), 4.21 (s, 3H), 2.34 (s, 3H), 2.06 (s, 6H). **^{13}C{^{1}H} NMR** (100 MHz, CD_3CN) δ 151.1, 146.8, 142.4, 141.9, 139.3, 139.2, 137.0, 134.4, 133.7, 131.0, 129.4, 129.1, 128.6, 117.6, 116.6, 114.6, 34.8, 21.1, 20.9. **HRMS** (ESI-TOF) m/z: $[M - PF_6^-]^+$ Calcd for $C_{22}H_{22}N_3$ m/z: 328.1805; Found: 328.1773.

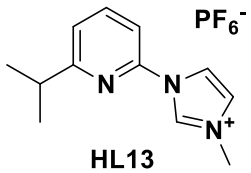

1-(6-isopropylpyridinyl)-3-methyl-1-imidazolium hexafluorophosphate (**HL13 PF_6^-**). General quaternization method D afforded 0.32 g, (68 %) of a yellowish powder. **^{1}H NMR** (400 MHz, CD_3CN) δ 9.32 (s, 1H), 8.07 (t, *J* = 2.0 Hz, 1H), 7.99 (t, *J* = 7.9 Hz, 1H), 7.52 (d, *J* = 8.2 Hz, 2H), 7.45 (d, *J* = 7.7 Hz, 1H), 3.96 (s, 3H), 3.14 (hept, *J* = 6.9 Hz, 1H), 1.33 (d, *J* = 6.9 Hz, 6H). **^{13}C{^{1}H} NMR** (100 MHz, CD_3CN) δ 169.0, 146.6, 141.7, 135.5, 125.6, 123.6, 120.0, 111.7, 37.4, 36.6, 22.4. **HRMS** (ESI-TOF) m/z: $[M - PF_6^-]^+$ Calcd for $C_{12}H_{16}N_3$ 202.1344; Found: 202.1329.

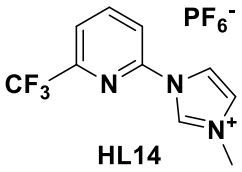

3 - methyl - 1 - (6 - (trifluoromethyl) pyridinyl) imidazolium hexafluorophosphate (**HL14 PF_6^-**). General quaternization method D afforded 0.22 g, (84 %) of off-white powder. **^{1}H NMR** (400 MHz, CD_3CN) δ 9.36 (s, 1H), 8.40-8.36 (m, 1H), 8.13-8.12 (m, 1H), 8.03-7.99 (m, 2H), 7.61-7.60 (m, 1H), 4.00 (s, 3H). **^{13}C{^{1}H} NMR** (100 MHz, CD_3CN) δ 147.8 (q, *J* = 36.0 Hz), 147.5, 144.0, 136.1, 126.1, 123.0 (q, *J* = 2.8 Hz), 121.9 (q, *J* = 273.1 Hz), 120.4, 118.7, 37.6. **^{19}F NMR** (376 MHz, CD_3CN) δ -68.80 (s, 3F), -72.89 (d, *J*= 1.9 Hz, 6F). **HRMS** (ESI-TOF) m/z: $[M - PF_6^-]^+$ Calcd for $C_{10}H_9F_3N_3$ 228.0743; Found: 228.0743.

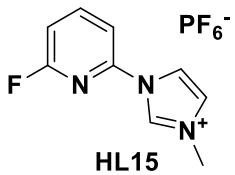

1-(6-fluoropyridinyl)-3-methyl-imidazolium hexafluorophosphate (**HL15 PF_6^-**). General quaternization method D afforded 0.22 g, (84%) of a yellowish powder. **^{1}H NMR** (400 MHz, CD_3CN) δ 9.25 (s, 1H), 8.26 (qt, *J*= 7.88 Hz, 1H), 8.06-8.05 (m, 1H), 7.68 (dd, *J*= 1.60 Hz, 1H), 7.59-7.58 (m, 1H), 7.28 (dd, *J*= 2.26 Hz, 1H), 3.99 (s, 3H). **^{13}C{^{1}H} NMR** (100 MHz, CD_3CN,) δ 163.2 (d, *J* = 244.7 Hz), 146.8 (d, *J* = 8.3 Hz), 145.3 (d, *J* = 14.1 Hz), 135.9, 125.9, 120.3, 112.3 (d, J = 4.4 Hz), 111.9 (d, *J* = 35.0 Hz), 37.5. **^{19}F NMR** (376 MHz, CD_3CN) δ -67.94 (s, 1F), -72.81 (d, *J*= 1.9 Hz, 6F). **HRMS** (ESI-TOF) m/z: $[M - PF_6^-]^+$ Calcd for $C_9H_9FN_3$ 178.0781; Found: 178.0784.

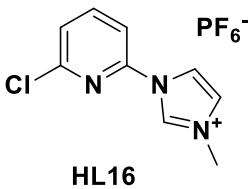

1-(6-chloropyridinyl)-3-methyl-imidazolium hexafluorophosphate (**HL16 PF_6^-**). General quaternization method D afforded 0.55 g, (77%) of a yellowish powder. **^{1}H NMR** (400 MHz, CD_3CN) δ 9.26 (s, 1H), 8.10 (t, *J* = 8.0 Hz, 1H), 8.03 (t, *J* = 2.0 Hz, 1H), 7.70 (d, *J* = 8.0 Hz, 1H), 7.62 (d, *J* = 7.9 Hz, 1H), 7.56 (s, 1H), 3.96 (s, 3H). **^{13}C{^{1}H} NMR** (100 MHz, CD_3CN) δ 152.0,

147.6, 145.0, 136.6, 127.5, 126.6, 121.0, 114.5, 38.2. **HRMS** (ESI-TOF) m/z: $[M - PF_6^-]^+$ Calcd for $C_9H_9N_3$ 194.0480; Found: 194.0504.

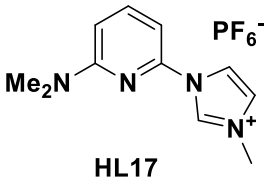

HL17

1-(6-(dimethylamino))-3-methyl-imidazolium hexafluorophosphate (**HL17 PF_6^-**). General quaternization method D afforded 0.16 g, (95 %) of a white powder. **^{1}H NMR** (400 MHz, CD_3CN) δ 9.28 (s, 1H), 8.02-8.01 (m, 1H), 7.75-7.71 (m, 1H), 7.52-7.51 (m, 1H), 6.84 (d, J= 7.56 Hz, 1H), 6.75 (d, J= 8.61 Hz, 1H), 3.96 (s, 3H), 3.14 (s, 6H). **^{13}C{^{1}H} NMR** (100 MHz, CD_3CN) δ 159.2, 145.2, 140.9, 134.9, 124.9, 119.5, 107.7, 99.3, 37.8, 36.9. **HRMS** (ESI-TOF) m/z: $[M - PF_6^-]^+$ Calcd for $C_{11}H_{15}N_4$ 203.1297; Found: 203.1297.

Synthesis of 3-methyl-1-(quinolinyl)imidazolium hexafluoro phosphate (**HL18 PF_6^-**).[230]

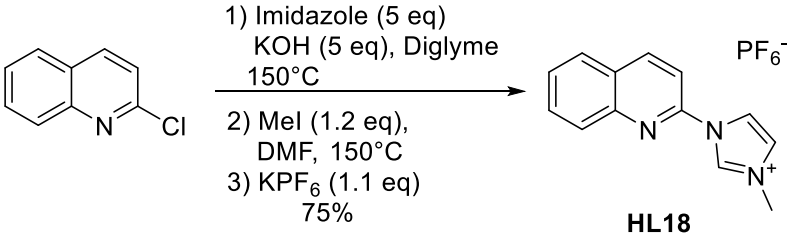

HL18

In a Schlenk charged with imidazole (15.27 mmol, 1.04 g, 5 equiv) and KOH (15.27 mmol, 0.85 g, 5 equiv) was heated up to 250 °C until everything is melted, and a salt is formed via elimination of H_2O. In other Schlenk 2-chloroquinoline (3.05 mmol, 0.5 g, 1 equiv) was dissolved in diglyme (10 mL) and is transferred via canula into the Schlenk with the mixture of imidazole and KOH. The reaction was stirred at 150 °C in a heating mantle for 18h. The mixture was quenched with water (15 mL) and extracted with CH_2Cl_2 (3 X 10 mL), the organic layer was washed with NaCl solution (2 x 5mL) and dried over $MgSO_4$. The solvent was evaporated and used in the next step without other purification. Then, 6 mL of ACN were added followed by MeI (3.66 mmol, 0.52 g, 1.2 equiv), the mixture was heated to 50 °C overnight in a sand bath. After this time, ACN was almost removed, H_2O (10 mL) was added, followed for KPF_6 (3.35 mmol, 0.62 g, 1.1 equiv). The solution was stirred for 30 min and the precipitated was filtered through a glass funnel filter #3, washed with diethyl ether (3 x 10mL) and the solid was recovered affording **HL19 PF_6^-** in 0.8 g, (75%) of an intense yellowish powder. **^{1}H NMR** (400 MHz, DMSO) δ 10.19 (s, 1H), 8.83 (d, *J* = 8.8 Hz, 1H), 8.65 (t, *J* = 2.0 Hz, 1H), 8.18 – 8.11 (m, 1H), 8.07 (d, *J* = 7.4 Hz, 0H), 8.01 (t, *J* = 1.8 Hz, 1H), 7.94 (ddd, *J* = 8.6, 6.9, 1.5 Hz, 1H), 7.76 (ddd, *J* = 8.2, 6.9, 1.3 Hz, 1H), 4.02 (s, 3H).

Synthesis of 3-methyl-1-(quinoxalinyl)imidazolium hexafluoro phosphate (**HL19 PF_6^-**).[230]

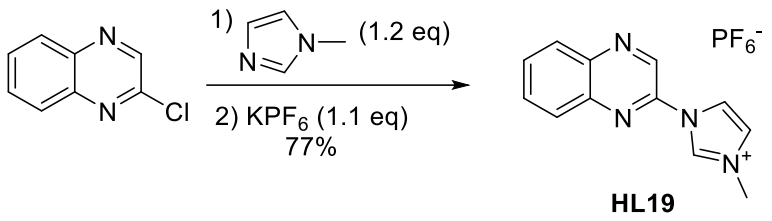

In a sealed tube 2 with 2-chloroquinoxaline (1.82 mmol, 0.3 g, 1 equiv) and N-methylimidazole (2.18 mmol, 0.19 g, 1.2 equiv) were stirred in a sand bath at 150 °C overnight. Then a small portion of MeOH was added (minimum for solubilizing) followed by H_2O (5 mL) and KPF_6 (2 mmol, 0.37 g, 1.1 equiv). The solution was stirred for 30 min and the precipitated was filtered through a glass funnel filter #3, washed with diethyl ether (3x10mL) and the solid was recovered affording **HL19 PF_6^-** in 0.5 g, (77%) of an orange powder. **^{1}H NMR** (400 MHz, CD_3CN) δ 9.47 (td, *J* = 1.6, 0.8 Hz, 1H), 9.29 (s, 1H), 8.29 (t, *J* = 2.0 Hz, 1H), 8.29 – 8.21 (m, 1H), 8.13 (ddt, *J* = 6.9, 3.6, 1.8 Hz, 1H), 8.05 – 7.94 (m, 2H), 7.65 (t, *J* = 1.9 Hz, 1H), 4.03 (d, *J* = 0.6 Hz, 3H).

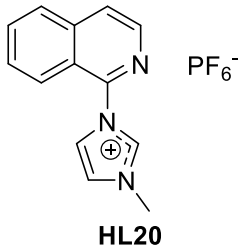

1-(isoquinoline-1-yl)-3-methyl-1H-imidazolium hexafluoro phosphate (**HL20 PF_6^-**). According to aforementioned method to ligand **HL18.** 0.3 g (77%) of a yellowish solid. **^{1}H NMR** (400 MHz, CD_3CN) δ 9.00 (s, 1H), 8.51 (d, J = 5.7 Hz, 1H), 8.20 – 8.15 (m, 1H), 8.09 (d, J = 5.6 Hz, 1H), 7.98 – 7.93 (m, 2H), 7.91 (t, J = 1.8 Hz, 1H), 7.86 – 7.80 (m, 1H), 7.64 (t, J = 1.8 Hz, 1H), 4.02 (s, 3H). **13C{^{1}H} NMR** (100 MHz, CD_3CN) δ 146.25, 141.90, 139.54, 137.92, 133.02, 130.79, 128.55, 125.11, 125.05, 124.11, 124.01, 123.09, 37.45.**HRMS** (ESI-TOF) m/z: $[M - PF_6^-]^+$ Calcd for $C_{13}H_{12}N_3$ 210.1026; Found: 210.1043.

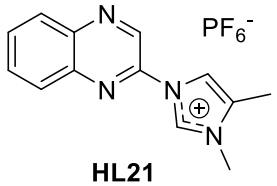

3,4-dimethyl-1-(quinoxalin-2-yl)-1H-imidazol-3-ium hexafluoro phosphate (**HL21 PF_6^-**). $^-$). According to aforementioned method to ligand **HL18.** 0.5 g (94%). **^{1}H NMR** (400 MHz, CD_3CN) δ 9.45 (s, 1H), 9.28 (s, 1H), 8.30 – 8.25 (m, 1H), 8.17 – 8.14 (m, 1H), 8.11 (t, J = 3.0, 1.3 Hz, 1H), 8.05 – 7.97 (m, 2H), 3.93 (s, 3H), 2.46 (s, 3H). **13C{^{1}H} NMR** (100 MHz, CD_3CN) ^{13}C NMR (101 MHz, Acetonitrile-d_3) δ 143.55, 141.88, 140.60, 138.16, 135.56, 135.10, 133.46, 132.52, 130.35, 129.72, 117.05, 35.12, 9.31. **HRMS** (ESI-TOF) m/z: $[M - PF_6^-]^+$ Calcd for $C_{13}H_{13}N_4$ 225.1135; Found: 225.1094.

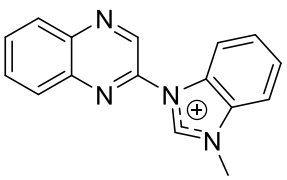

HL22

PF_6^- Synthesis of 3-methyl-1-(quinoxalin-2-yl)-1H-benzo[d]imidazol-3-ium hexafluoro phosphate (**HL22 PF_6^-**). According to aforementioned method to ligand **HL18.** 0.38 g (50%). **^{1}H NMR** (400 MHz, CD_3CN) δ 9.78 (s, 1H), 9.37 (s, 1H), 8.71 – 8.64 (m, 1H), 8.34 – 8.22 (m, 3H), 8.08 – 7.99 (m, 3H), 7.87 (t, J = 4.3 Hz, 1H), 7.85 (t, J = 3.6 Hz, 1H), 4.25 (s, 3H). **13C{^{1}H} NMR** (100 MHz, CD_3CN) δ 143.25, 143.19, 142.12, 140.92, 139.89, 133.59, 133.42, 132.77, 130.96, 130.37, 129.92, 129.58, 129.06, 117.21, 114.77, 35.07. **HRMS** (ESI-TOF) m/z: $[M - PF_6^-]^+$ Calcd for $C_{16}H_{13}N_4$ 261.1135; Found: 261.1156.

VII.4 General schemes for H_3L23-H_3L27 synthesis (IV. Fe(III) complexes bearing tridentate anionic ligands)

Compounds **H_3L23-H_3L25** (§IV.2.1)

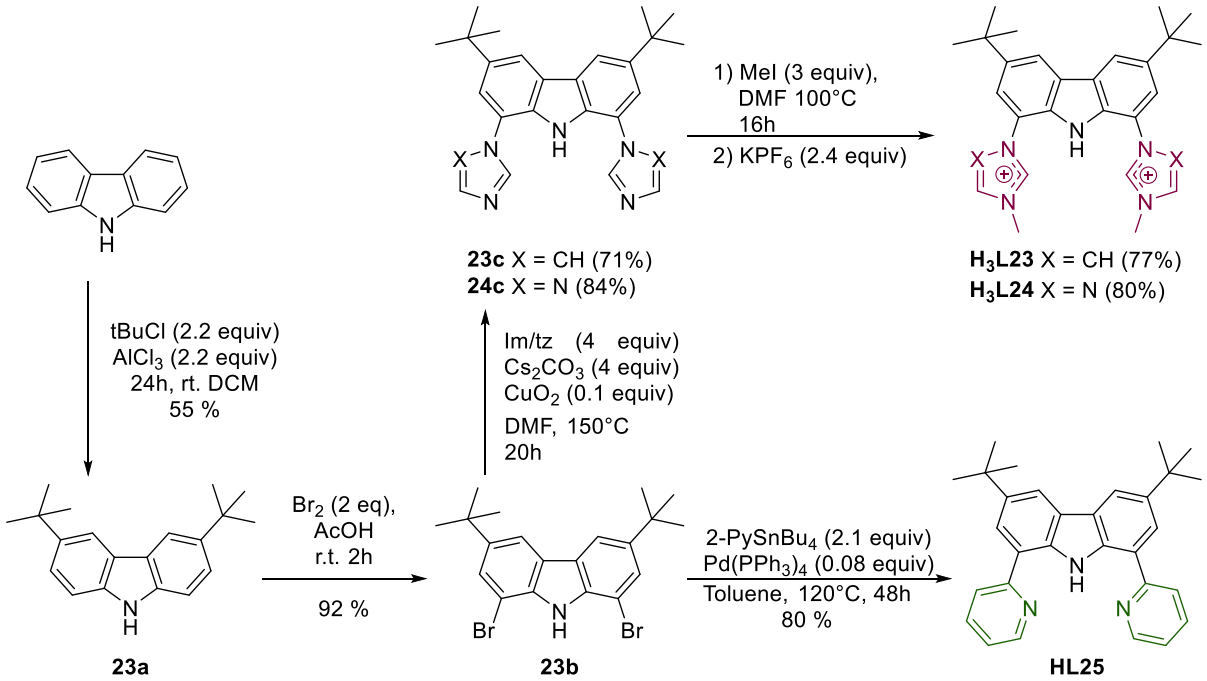

Compounds **FeCl3(tpy), 4'-pytpy** (§IV.3)

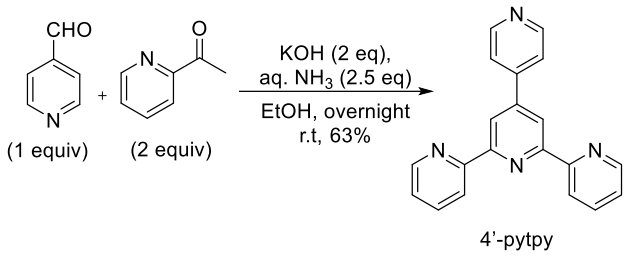

Compounds **H_3L26** and **H_3L27** (§IV.4)

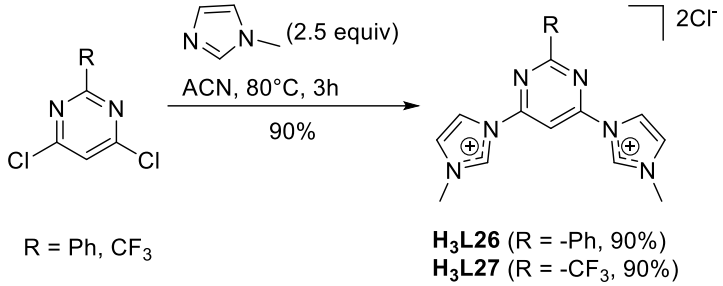

VII.4.1 Synthesis of ligands H_3L23-H_3L27 (IV. Fe(III) complexes bearing tridentate anionic ligands

VII.4.1.1 Compounds 23a-24c

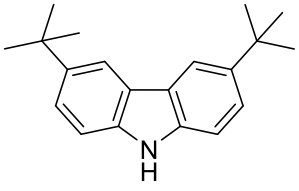

23a

3,6-di-tert-butyl-9H-carbazole (**23a**) was synthesized according to a literature procedure.[231] 2.2 g (55%). **^{1}H NMR** (400 MHz, $CDCl_3$) δ 8.08 (d, J = 2.0 Hz, 2H), 7.84 (s, 1H), 7.47 (dd, J = 8.5, 1.9 Hz, 2H), 7.33 (dd, J = 8.5, 0.7 Hz, 2H), 1.46 (s, 18H).

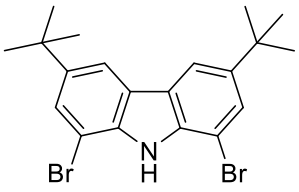

23b

1,8-dibromo-3,6-di-tert-butyl-9H-carbazole (**23b**) was synthesized according to a literature procedure.[227] 2.4 g (92%). **^{1}H NMR** (400 MHz, $CDCl_3$) δ 8.13 (s, 1H), 7.98 (d, J = 1.3 Hz, 3H), 7.64 (d, J = 1.7 Hz, 2H), 1.44 (s, 18H).

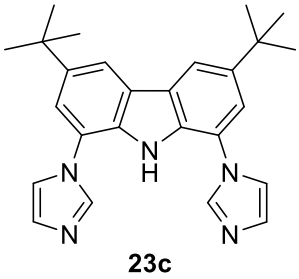

23c

3,6-di-tert-butyl-1,8-di(1H-imidazol-1-yl)-9H-carbazole (**23c**) was synthesized according to a literature procedure.[156] 0.34 g (71%). **^{1}H NMR** (400 MHz, $CDCl_3$) δ 10.34 (s, 1H), 8.16 (d, J = 1.7 Hz, 2H), 7.74 (s, 2H), 7.40 (d, J = 1.7 Hz, 2H), 7.24 (s, 2H), 7.06 (s, 2H), 1.48 (s, 18H).

Synthesis of 3,6-di-tert-butyl-1,8-di(1H-1,2,4-triazol-1-yl)-9H-carbazole (**24c**).

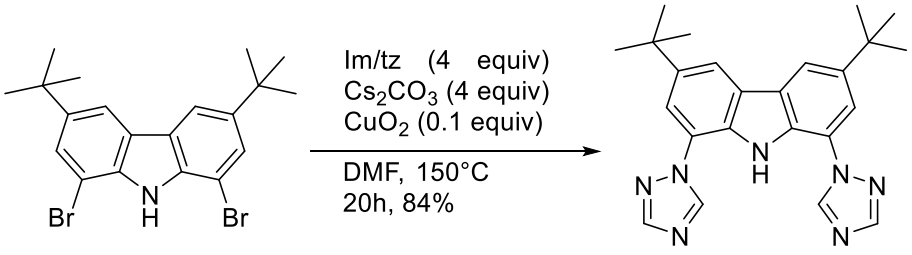

24c

In a round flask with **23b** (0.35 g, 0.8 mmol), 1,2,4-triazole (0.22 g, 3.2 mmol), CuI (0.015 g, 0.08 mmol), K_2CO_3 (0.44 g, 3.2 mmol), 3.5 mL of DMF were added. The reaction was heated at 150 °C in a sand bath for 48h. After this time the mixture was filtered through celite and washed with CH_2Cl_2 (3 x 10 mL) and the solvents were removed under vacuum. The crude was purified by silica chromatographic column using a mixture Hexane:EtOAc + 1%Et_3N ((2:1)+1%). The fractions were collected affording **24c** in 0.28 g (84%). **^{1}H NMR** (400 MHz, $CDCl_3$) δ 10.85 (s, 1H), 8.79 (s, 2H), 8.32 (s, 2H), 8.15 (s, 2H), 7.65 (d, J = 1.5 Hz, 2H), 1.52 (s, 18H). **13C{^{1}H} NMR** (100 MHz, $CDCl_3$) δ 152.69, 143.46, 141.23, 130.01, 125.89, 121.21, 116.66, 113.83, 35.11, 32.11.

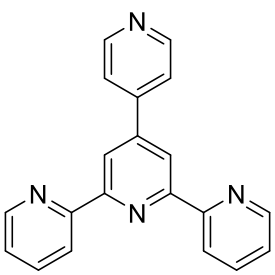

4'-pytpy

4'-(pyridin-4-yl)-2,2':6',2''-terpyridine (**4'-pytpy**) was synthesized according to a literature procedure[232] in 1.51 g (63 %). **^{1}H NMR** (400 MHz, $CDCl_3$) δ 8.77 (dttt, J = 6.1, 4.5, 4.4, 3.1, 2.8, 1.7, 1.4 Hz, 1H), 8.74 (ddd, J = 4.8, 1.8, 0.9 Hz, 1H), 8.68 (dt, J = 7.9, 1.1 Hz, 1H), 7.90 (ddd, J = 7.9, 7.5, 1.8 Hz, 1H), 7.80 (dd, J = 6.2, 4.5 Hz, 1H), 7.38 (ddd, J = 7.5, 4.8, 1.2 Hz, 1H).

VII.4.1.2 Compounds H_3L23-H_3L27

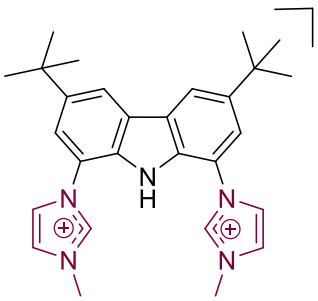

H_3L23

3,3'-(3,6-di-tert-butyl-9H-carbazole-1,8-diyl)bis(1-methyl-1H-3'l4-imidazol-1-ium) (**H_3L23**) was synthesized according to a literature procedure in 0.9 g (77%).[156] **^{1}H NMR** (400 MHz, CD_3CN) δ 9.34 (s, 2H), 8.81 (s, 2H), 8.52 (d, *J* = 1.3 Hz, 2H), 7.73 (t, *J* = 1.8 Hz, 1H), 7.66 (d, *J* = 1.6 Hz, 2H), 7.63 (t, *J* = 1.6 Hz, 5H), 4.00 (s, 6H).

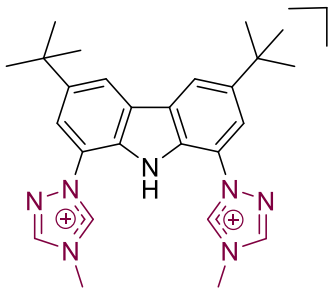

H_3L24

1,1'-(3,6-di-tert-butyl-9H-carbazole-1,8-diyl)bis(4-methyl-4H-1l4,2,4-triazol-4-ium) (**H_3L24**) followed the general quaternization method D in 0.27 g (80 %). **^{1}H NMR** (400 MHz, CD_3CN) δ 10.65 (s, 1H), 10.18 (s, 2H), 8.89 (s, 2H), 8.58 (d, J = 1.7 Hz, 2H), 7.87 (d, J = 1.7 Hz, 2H), 4.09 (s, 6H), 2.13 (s, 28H). **13C{^{1}H} NMR** (100 MHz, CD_3CN) δ 146.61, 145.69, 143.30, 131.79, 126.91, 121.45, 119.78, 119.49, 35.88, 35.81, 31.92. . **HRMS** (ESI-TOF) m/z: $[M - 2\ PF_6^-]^+$ Calcd for $C_{26}H_{33}N_7$ 221.6393; Found: 221.6394.

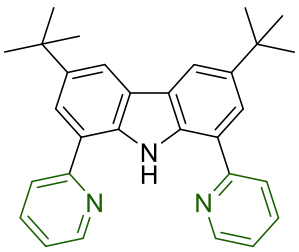

HL25

3,6-di-tert-butyl-1,8-di(pyridin-2-yl)-9H-carbazole (**HL25**) was synthesized according to a literature procedure. 0.42 g (80%).[157] **^{1}H NMR** (400 MHz, CD_3CN) δ 12.86 (s, 1H), 8.91 (dt, *J* = 4.7, 1.5 Hz, 2H), 8.24 (d, *J* = 1.7 Hz, 2H), 8.09 – 8.01 (m, 4H), 7.86 (t, *J* = 7.5 Hz, 2H), 7.28 (t, *J* = 5.6 Hz, 3H), 1.55 (s, 17H).

Synthesis of 1,1'-(2-phenylpyrimidine-4,6-diyl)bis(3-methyl-1H-imidazol-3-ium) bis chloride (**H_3L26**)

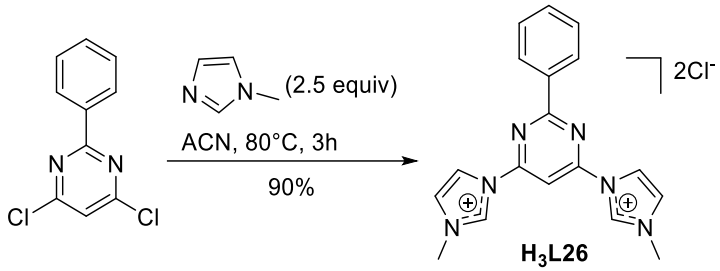

In a round flask charged with 4,6-dichloro-2-phenylpyrimidine (2.28 mmol, 0.51 g, 1 equiv) was dissolved in 25 mL of ACN and N-methylimidazole (5.7 mmol, 0.45 mL, 2.5 equiv) were stirred in a sand bath at 90 °C in a sand bath for 5h, after this time a precipitate was formed. The solvent was removed under vacuum and the solid was recovered and washed with acetone (3 x 10 mL) and diethylether (3 x 10 mL). The was recovered affording **H_3L26 2Cl$^-$** in 0.79 g, (90%) of an withe powder. %). **^{1}H NMR** (400 MHz, DMSO-*d*6) δ 9.72 (s, 1H), 8.67 (td, J = 2.2, 0.9 Hz, 1H), 8.27 (t, J = 1.9 Hz, 1H), 7.92 (s, 0H), 7.75 – 7.62 (m, 3H), 4.06 (s, 2H). **13C{^{1}H} NMR** (100 MHz, DMSO-*d*6) δ 166.29, 156.77, 136.72, 134.71, 134.03, 129.78, 129.59, 126.55, 119.77, 98.01, 37.63. **HRMS** (ESI-TOF) m/z: [M –2 Cl$^-$]$^+$ Calcd for $C_{18}H_{18}N_6$ 159.0791; Found: 159.0797.

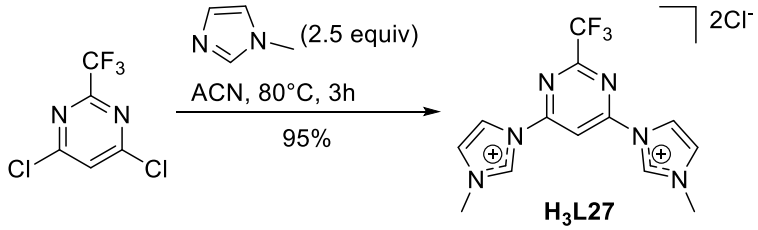

1,1'-(2-trifluoropyrimidine-4,6-diyl)bis(3-methyl-1H-imidazol-3-ium) bis chloride (**H_3L27**) was obtained according to aforementioned method to ligand **H_3L26.** 0.48 g (95%). **^{1}H NMR** 1H NMR (400 MHz, $MeOD_4$) δ 10.40 (s, 1H), 9.32 (d, J = 3.3 Hz, 2H), 8.85 (t, J = 4.5, 2.4 Hz, 2H), 8.06 (t, J = 2.7, 2.5, 2.0 Hz, 0H), 4.24 (s, 10H). (400 MHz, DMSO-*d*6) δ 10.68 (s, 2H), 10.16 (s, 1H), 9.36 (t, J = 2.1 Hz, 2H), 8.16 (t, J = 1.9 Hz, 2H), 4.06 (s, 6H). **13C{^{1}H} NMR** (100 MHz, DMSO-d6) δ 157.60, 155.28 (q, *J* = 681.1, 78.3, 39.4 Hz), 137.93, 126.36, 120.21, 116.33 (q, *J* = 688.7, 474.1, 229.7 Hz), 104.12, 37.31. **^{19}F NMR** (376 MHz, DMSO-*d*6) δ -69.38. **HRMS** (ESI-TOF) m/z: [M –2 Cl$^-$]$^+$ Calcd for $C_{13}H_{13}F_3N_6$ 155.0572; Found: 155.0787.

VII.5 General schemes for H_2L28-H_2L31 synthesis (IV. Iron complexes as photosensitizers towards H2-evolition)

Compounds **1A-C** and **H_2L31** (§V.2)

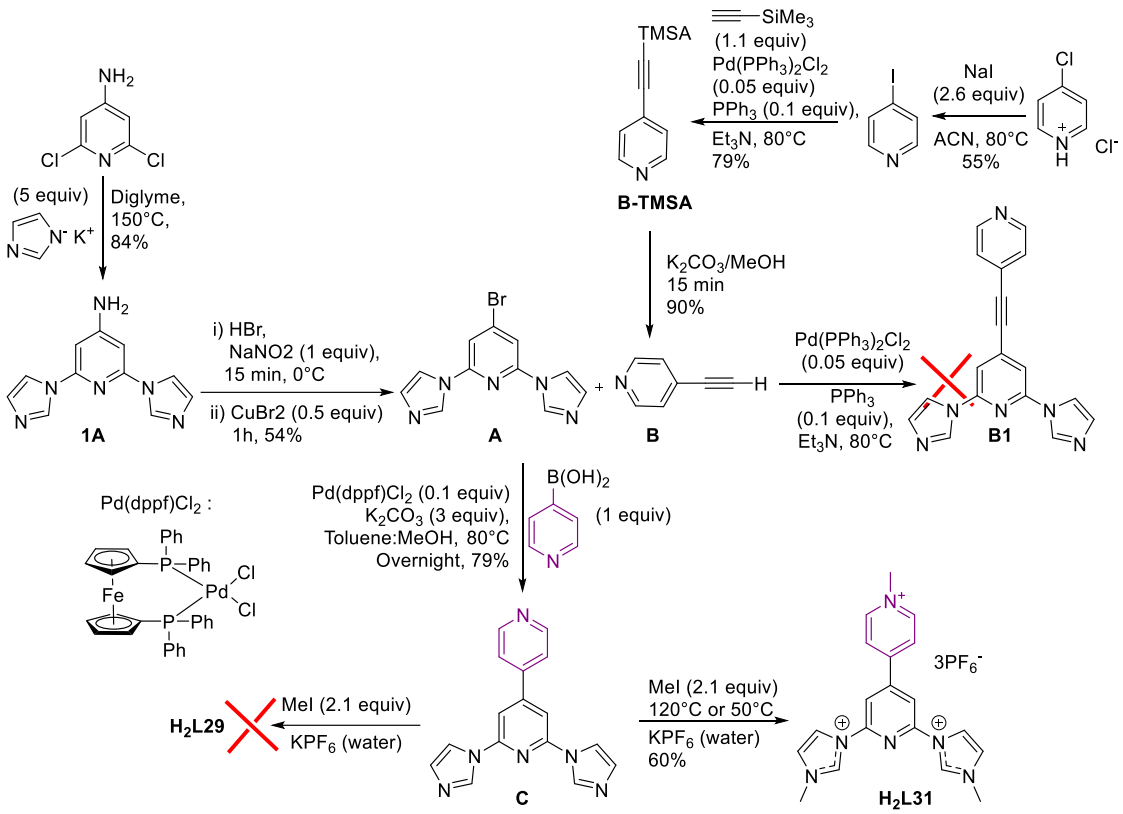

Compounds **D-G** and **H_2L29** (§V.2)

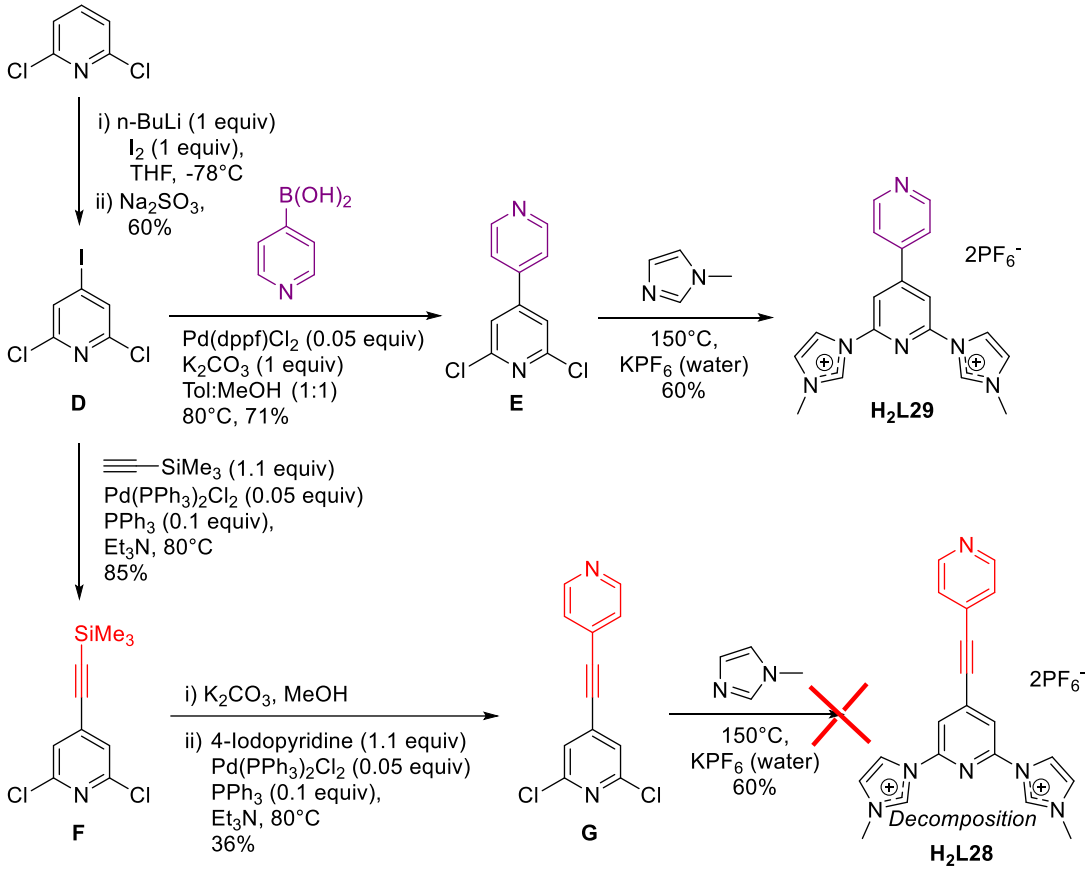

Compounds **K,L** and **H_2L30** (§V.2)

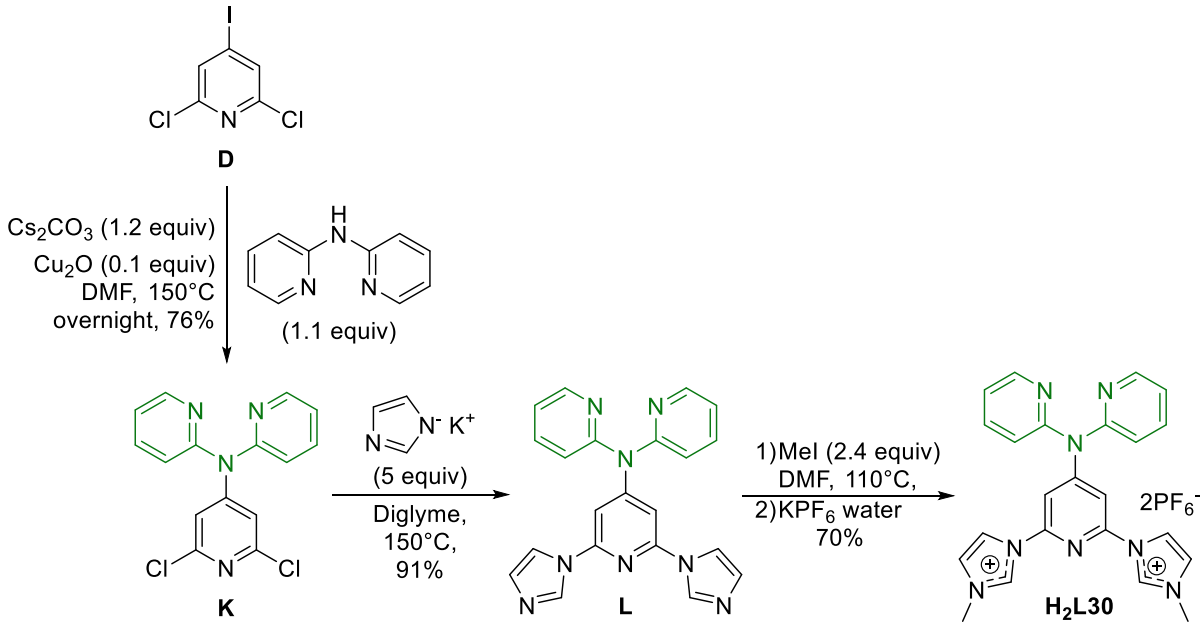

VII.5.1 Synthesis of ligands H_2L28-H_2L31 (IV. Iron complexes as photosensitizers towards H_2-evolution)

VII.5.1.1 Compounds 1A-L, H_2L28-H_2L31

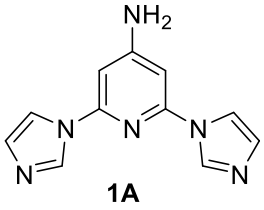

1A

Synthesis of 2,6-di(1H-imidazol-1-yl)pyridin-4-amine (**1A**) was according to a literature procedure.[166] 0.69 g (84 %) **^{1}H NMR** (400 MHz, DMSO-*d*6) δ 8.50 (t, J = 1.1 Hz, 2H), 7.85 (t, J = 1.4 Hz, 2H), 7.09 (t, J = 1.2 Hz, 2H), 6.70 (s, 2H), 6.68 (s, 2H).

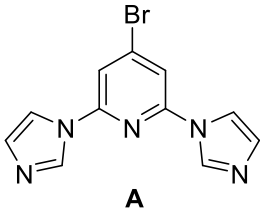

A

Synthesis of 4-bromo-2,6-di(1H-imidazol-1-yl)pyridine (**A**) according to a literature procedure.[166] 0.78 g (54 %) **^{1}H NMR** (400 MHz, DMSO-*d*6) δ 8.36 (t, J = 1.1 Hz, 2H), 7.62 (t, J = 1.4 Hz, 2H), 7.44 (s, 2H), 7.24 (dd, J = 1.6, 0.9 Hz, 2H).

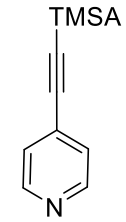

B-TMSA

Synthesis of 4-((trimethylsilyl)ethynyl)pyridine (**B-TMSA**) was according to a literature procedure.[233] **^{1}H NMR** (400 MHz,, $CDCl_3$) δ 8.55 (dd, J = 4.7, 1.4 Hz, 2H), 7.29 (d, J = 6.1 Hz, 2H), 0.25 (s, 6H).

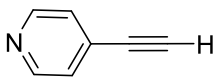

B

Synthesis of 4-(ethynylpyridine) (**B**) was according to a literature procedure 0.17 g (90%).[233] **^{1}H-NMR** (400 MHz,, $CDCl_3$) δ 8.58 (dd, *J* = 4.5, 1.6 Hz, 1H), 7.34 (dd, *J* = 5.9, 1.4 Hz, 1H).

Synthesis of 4-(3,5-di(1H-imidazol-1-yl)phenyl)pyridine (**C**).[234]

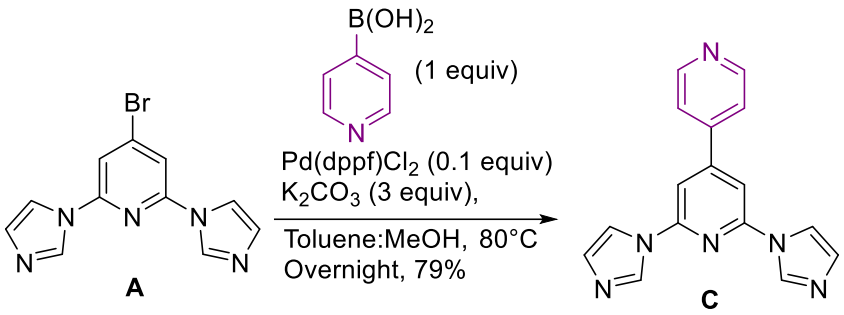

In a round flask with a degassed mixture of 25 mL toluene:MeOH (1:1), 4-bromo-2,6-di(1H-imidazol-1-yl)pyridine (**A**) (0.5 g, 1.72 mmol), 4-pyridinylbroronic acid (0.21 g, 1.72 mmol), K_2CO_3 (5.17 g, 3 mmol), Pd(dppf)Cl_2 (0.12 mg, 0.17 mmol) were added. The mixture was heated at 80°C in a sand bath for 24h. The solid was used without purification in the subsequent reaction.

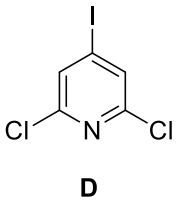

2,6-dichloro-4-iodopyridine (**D**) was synthesized according to a literature procedure 0.51 g (60%).[235] **^{1}H-NMR** (400 MHz,, $CDCl_3$) δ 7.68 (s, 1H).

Synthesis of 2,6-dichloro-4,4'-bipyridine (**E**).

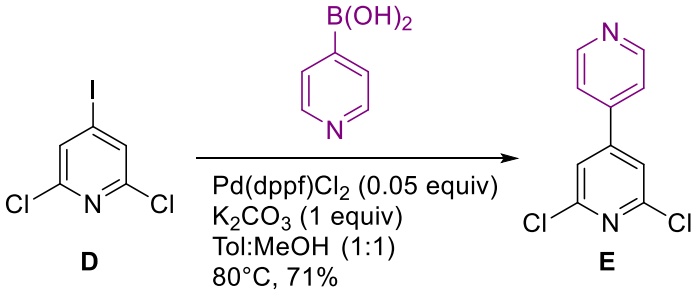

In a round flask with a degassed mixture of 8 mL toluene:MeOH (1:1), 2,6-dichloro-4-iodopyridine (**D**) (0.26 g, 0.96 mmol), 4-pyridinylbroronic acid (0.12 g, 0.96 mmol), K_2CO_3 (0.39 g, 2.8 mmol), Pd(dppf)Cl_2 (0.07 mg, 0.0.09 mmol) were added. The mixture was heated at 80°C in a sand bath for 24h. After this time the mixture was filtered through celite and washed with CH_2Cl_2 (3 x 10 mL) and the solvents were removed under vacuum. The crude was purified by silica chromatographic column using a mixture Hexane:EtOAc + 1%Et_3N

((4:1)+1%). The fractions were collected affording **E** in 0.40 g (71%). **^{1}H-NMR** (400 MHz,, $CDCl_3$) δ 8.78 (dd, J = 5.9, 1.6 Hz, 2H), 7.49 (s, 2H), 7.48 (dd, J = 6.4, 1.7 Hz, 2H).

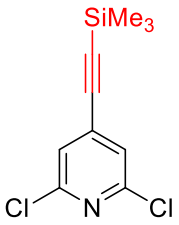

F

Synthesis of 2,6-dichloro-4-((trimethylsilyl)ethynyl)pyridine (**F**) was according to a literature procedure 0.0.22 g (86 %).[236] **^{1}H-NMR** (400 MHz,, $CDCl_3$) δ 7.28 (s, 1H).

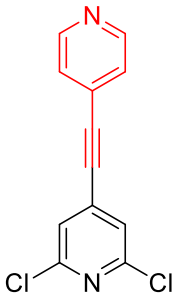

G

Synthesis of 2,6-dichloro-4-(pyridin-4-ylethynyl)pyridine (**G**) was according to a literature procedure 0.0.22 g (86 %).[236] **^{1}H-NMR** (400 MHz,, $CDCl_3$) 8.61 (dd, J = 4.3, 1.5 Hz, 2H), 7.33 (dd, J = 5.6, 1.5 Hz, 2H), 7.32 (s, 2H).

Synthesis of N-(2,6-dichloropyridin-4-yl)-N-(pyridin-2-yl)pyridin-2-amine (**K**).

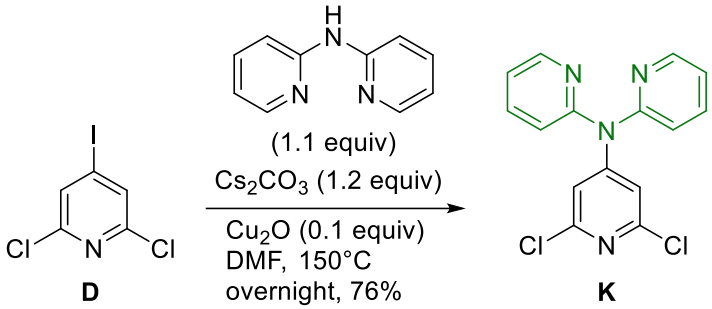

D **K**

In a schlenk with 2,6-dichloro-4-iodopyridine (**D**) (0.2 g, 0.73 mmol), 2,2-dipyridylamine (0.17 g, 0.9 mmol), Cs_2CO_3 (0.45 g, 1.4 mmol) and Cu2O (0.01 g, 0.07 mmol) three vacuum-Argon were made, then 3 mL of DMF were added. The reaction was stirred at 150 °C in a sand bath by 20 h. After this time the mixture was filtered through celite and washed with CH_2Cl_2 (3 x 10 mL) and the solvents were removed under vacuum. The crude was purified by silica chromatographic column using a mixture Hexane:EtOAc + 1%Et_3N ((3:1)+1%). The fractions were collected affording **K** in 0.18 g (76%). **^{1}H-NMR** (400 MHz,, $CDCl_3$) δ 8.47 (ddd, J = 4.9, 2.0, 0.9 Hz, 1H), 7.73 (ddd, J = 8.2, 7.4, 2.0 Hz, 1H), 7.18 (ddd, J = 7.4, 4.9, 1.0

Hz, 1H), 7.03 (dt, J = 8.2, 0.9 Hz, 1H), 6.84 (s, 1H). **13C{^{1}H} NMR** (100 MHz, $CDCl_3$) δ 156.09, 155.25, 150.96, 149.74, 138.99, 121.52, 119.70, 114.79. **HRMS** (ESI-TOF) m/z: Calcd for $C_{15}H_{11}N_5Cl_2$ 318.1908; Found: 318.1918.

Synthesis of N-(2,6-di(1H-imidazol-1-yl)pyridin-4-yl)-N-(pyridin-2-yl)pyridin-2-amine (**L**).

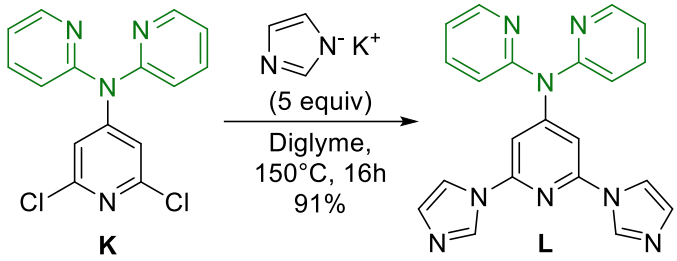

In a Schlenk charged with imidazole (0.85g, 12.5 mmol) and KOH (0.71 g, 12.5 mmol) was heated up to 250 °C until everything is melted, and a salt is formed via elimination of H_2O. In other Schlenk **K** (0.4 g, 1.25 mmol) was dissolved in diglyme (5 mL) and is transferred via canula into the Schlenk with the mixture of imidazole and KOH. The reaction was stirred at 150 °C in a sand bath for 18h. After this time the mixture was poured in water (10 mL) and filtered. The solid was washed with water (2 x 5 mL) and diethylether (3 x 10 mL) and cold THF (2 x 10 mL) affording compound **L** in 0.91 g (91 %). **^{1}H-NMR** (400 MHz, DMSO-*d*6) δ 8.63 (s, 2H), 8.39 (dd, J = 4.9, 1.9 Hz, 2H), 8.00 (t, J = 1.9, 1.4 Hz, 2H), 7.83 (td, J = 7.8, 2.0 Hz, 2H), 7.28 (s, 2H), 7.25 (dd, J = 7.4, 4.9 Hz, 2H), 7.18 (d, J = 8.2 Hz, 2H), 7.08 (s, 2H). **13C{^{1}H} NMR** (100 MHz, DMSO-d_6) δ 157.21, 156.08, 148.83, 148.59, 138.80, 135.58, 130.06, 120.76, 118.90, 116.91, 104.05. . **HRMS** (ESI-TOF) m/z: Calcd for $C_{21}H_{17}N_8$ 381.1571; Found: 381.1561.

VII.5.1.2 Compounds H_2L28-H_2L31

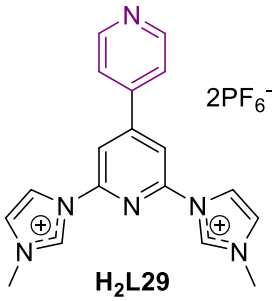

Ligand 1,1'-([4,4'-bipyridine]-2,6-diyl)bis(3-methyl-1H-imidazol-3-ium) bis hexafluoro phosphate (**H_2L29**).[204] General quaternization method D (§VI.2.2) afforded 0.4 g (60%). **^{1}H-NMR** (400 MHz, CD_3CN) δ 9.50 (s, 2H), 8.87 (dd, J = 4.6, 1.5 Hz, 2H), 8.28 (t, J = 2.0 Hz, 2H), 8.19 (s, 2H), 7.86 (dd, J = 4.5, 1.7 Hz, 2H), 7.65 (t, J = 1.9 Hz, 2H), 4.03 (s, 6H).

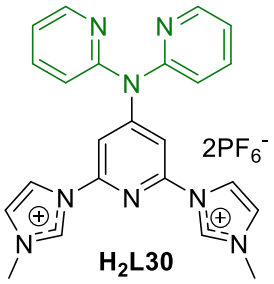

Ligand 1,1'-(4-(di(pyridin-2-yl)amino)pyridine-2,6-diyl)bis(3-methyl-1H-imidazol-3-ium) bis hexafluoro phosphate (**H_2L30**). General quaternization method D (§VI.2.2) afforded 0.55 g (70%). **^{1}H-NMR** (400 MHz, DMSO-*d6*) δ 10.11 (s, 2H), 8.65 (t, J = 1.9 Hz, 2H), 8.46 (dd, J = 5.1, 1.8 Hz, 2H), 7.97 (t, J = 1.8 Hz, 2H), 7.92 (td, J = 7.8, 2.0 Hz, 2H), 7.66 (s, 2H), 7.37 (dd, J = 7.4, 4.9 Hz, 2H), 7.19 (d, J = 8.2 Hz, 2H), 3.95 (s, 6H). **HRMS** (ESI-TOF) m/z [M –2 PF_6^-]$^+$: Calcd for $C_{23}H_{22}N_{58}$ 205.0978; Found: 205.0971.

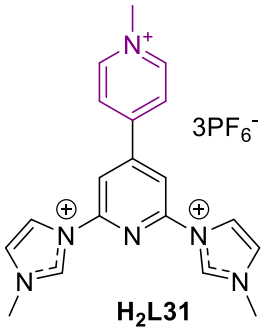

Ligand 1-methyl-2'-(3-methyl-1H-imidazol-3-ium-1-yl)-6'-(1-methyl-1H-imidazol-3-ium-3-yl)-[4,4'-bipyridin]-1-ium bis hexafluoro phosphate (**H_2L31**). General quaternization method D (§VI.2.2) afforded 0.13 g (60%). **^{1}H-NMR** (400 MHz, DMSO-*d6*) δ 10.29 (s, 1H), 9.33 (d, J = 6.3 Hz, 1H), 8.81 (d, J = 1.6 Hz, 2H), 8.74 (d, J = 6.4 Hz, 1H), 8.07 (t, J = 1.9 Hz, 1H), 4.44 (s, 1H), 4.05 (s, 3H). **13C{^{1}H} NMR** (100 MHz, DMSO-d_6) δ 148.88, 148.60, 146.81, 146.36, 136.42, 125.26, 125.18, 119.32, 112.74, 48.04, 36.78. **HRMS** (ESI-TOF) m/z [M –3 PF_6^-]$^+$: Calcd for $C_{23}H_{22}N_{58}$ 205.0978; Found: 205.0971.

VII.5.2 Synthesis of complexes

General complexation method.

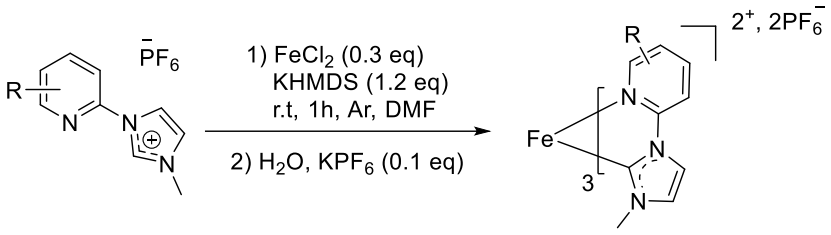

Ligand **HLx** (1 equiv, 0.27 mmol) and $FeCl_2$ (0.3 equiv, 0.09 mmol) were submitted to three vacuum/Ar cycles, after that 1.5 mL of dry and degassed DMF were added, the mixture was stirred under Ar at r.t for 5 min then KHMDS (1.2 equiv, 0.325 mmol) were added. The reaction mixture was stirred at r.t. for 1 h. Afterwards, H_2O (10 mL) was added and 1 mL of KPF_6 (saturated solution) the reaction was vigorously stirred and the precipitated formed was filtered in a glass funnel filter #4 or #3 (depending on particle aggregation: #4 for small, #3 for bigger). The solid was washed with H_2O (10 mL) and diethyl ether (3 x 15 mL) until the solid was a fine powder. The solid was recovered by adding acetonitrile and purified by column chromatography [for 100 mg of ligand 20 cm of high and around 4cm of diameter] using a mixture 10:2:1 (Acetone:water:$KNO_{3(\text{Saturated solution})}$). Recovering of the phases: All the desired phases were mixed in a balloon and an extra amount of H_2O was added. Acetone was subsequently removed under vacuum and a small quantity of NH_4PF_6 was added until a precipitated appeared. The solid was filtered in a glass funnel filter #4, washed with diethyl ether (3 x 10 mL) and recovered with acetonitrile in a round flask.

VII.5.2.1 Complexes C3-C22 (III. Bidentate azine NHC Fe(II))

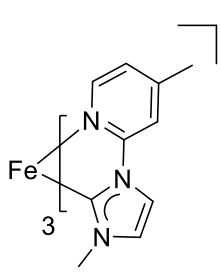

C3

Fac- and *mer*-**C3** in 25:75 ratio. General complexation method afforded 40 mg, (44 % yield) of an orange solid. **^{1}H NMR** (400 MHz, CD_3CN) δ 8.15 (d, *J* = 2.2 Hz, 1H), 8.08 (d, *J* = 2.2 Hz, 1H), 7.99 (dd, *J* = 9.9, 2.3 Hz, 2H), 7.85 (dt, *J* = 1.6, 0.8 Hz, 1H), 7.77 (dt, *J* = 1.5, 0.7 Hz, 1H), 7.66 (d, *J* = 5.6 Hz, 1H), 7.54 (ddt, *J* = 14.8, 1.7, 0.8 Hz, 2H), 7.36 (dd, *J* = 13.7, 2.2 Hz, 2H), 7.14 (dd, *J* = 6.4, 2.3 Hz, 2H), 7.13 – 7.10 (m, 2H), 7.04 (ddd, *J* = 5.9, 1.7, 0.8 Hz, 1H), 6.86 (d, *J* = 5.8 Hz, 1H), 6.73 (dtd, *J* = 6.1, 1.7, 0.8 Hz, 2H), 6.61 (d, *J* = 6.0 Hz, 1H), 3.27 (s, 1H), 3.22 (s, 3H), 2.94 (s, 2H), 2.80 (s, 3H), 2.67 (s, 3H), 2.54 – 2.49 (m, 5H), 2.37 (d, *J* = 7.0 Hz, 6H). **^{13}C{^{1}H} NMR** (100 MHz, CD_3CN) δ 210.4, 208.9, 205.7, 205.2, 155.9, 155.9, 155.5, 154.8, 154.6, 154.3, 154.2, 153.4, 153.0, 151.8, 151.2, 149.8, 128.8, 128.7, 128.7, 128.6, 125.7, 124.9, 124.5, 123.8, 118.5, 117.7, 117.4, 113.7, 113.3, 113.0, 112.7, 36.9, 36.5, 35.9, 35.7, 21.3, 21.0. **HRMS** (ESI-TOF) m/z: $[M - 2PF_6^-]^{2+}$ Calcd for $C_{30}H_{33}N_9Fe$ 287.6099; Found: 287.6117.

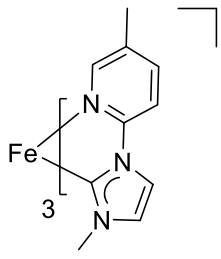

C4

Fac- and *mer*-**C4** in 20:80 ratio. General complexation method afforded 40 mg, (44 %), of an orange solid. **^{1}H NMR** (400 MHz, CD_3CN) δ 8.17 (d, *J* = 2.2 Hz, 1H), 8.09 (d, *J* = 2.2 Hz, 1H), 8.00 (dd, *J* = 10.0, 2.3 Hz, 1H), 7.95 – 7.81 (m, 2H), 7.78 (d, *J* = 8.4 Hz, 1H), 7.65 – 7.49 (m, 5H), 7.35 (dd, *J* = 13.9, 2.1 Hz, 2H), 7.14 (dd, *J* = 8.2, 2.2 Hz, 1H), 7.01 (s, 1H), 6.83 (s, 1H), 6.60 (s, 1H), 3.20 (s, 3H), 2.91 (s, 1H), 2.80 (s, 3H), 2.66 (s, 3H), 2.24 (s, 3H), 2.15 (s, 2H), 2.05 (s, 3H), 1.99 (s, 3H). **^{13}C{^{1}H} NMR** (100 MHz, CD_3CN) δ 211.5, 210.8, 207.8, 206.3, 155.2, 154.7, 154.6, 154.3, 153.4, 153.1, 149.9, 148.3, 144.6, 143.7, 143.3, 142.2, 127.8, 125.0, 124.7, 124.2, 124.1, 124.0, 123.3, 122.7, 121.9, 121.7, 121.2, 120.9, 120.5, 37.0, 36.7, 35.8, 35.8, 21.0, 21.0, 20.7, 20.6. **HRMS** (ESI-TOF) m/z: $[M - 2PF_6^-]^{2+}$ Calcd for $C_{30}H_{33}N_9Fe$ 287.6099; Found: 287.6104.

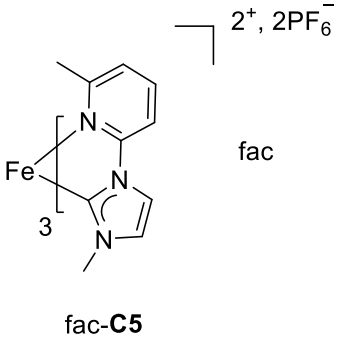

fac-**C5**

Fac-**C5**. General complexation method afforded 45 mg, (45 %), of an orange solid. **^{1}H NMR** (400 MHz, CD_3CN) δ 8.04 (d, *J* = 2.3 Hz, 1H), 7.97 (t, *J* = 7.9 Hz, 1H), 7.72 (d, *J* = 8.1 Hz, 1H), 7.17 – 7.10 (m, 2H), 2.69 (s, 3H), 1.74 (s, 3H). **^{13}C{^{1}H} NMR** (100 MHz, CD_3CN) δ 206.0, 165.0, 153.8, 141.1, 130.2, 125.7, 119.2, 110.7, 36.2, 24.5. **HRMS** (ESI-TOF) m/z: $[M - 2PF_6^-]^{2+}$ Calcd for $C_{30}H_{33}N_9Fe$ 287.6099; Found: 287.6167.

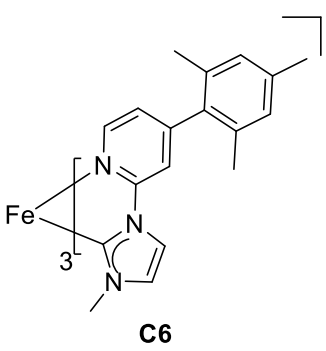

C6

Fac- and *mer*-**C6** in 25:75 ratio. General complexation method afforded 99 mg, (48 %), of an orange solid. **^{1}H NMR** (400 MHz, CD_3CN) δ 8.26 (s, 1H), 8.16 (s, 1H), 8.11 (s, 1H), 8.09 (s, 1H), 7.97 (d, *J* = 5.7 Hz, 2H), 7.90 (s, 2H), 7.83 (s, 1H), 7.61 (s, 3H), 7.49 (s, 1H), 7.42 (s, 1H), 7.37 (d, *J* = 5.9 Hz, 2H), 7.24 (s, 4H), 7.21 – 7.09 (m, 5H), 7.08 – 6.99 (m, 12H), 6.83 (d, *J* = 6.0 Hz, 2H), 6.79 (d, *J* = 5.7 Hz, 2H), 3.38 (s, 3H), 3.09 (s, 2H), 3.01 (s, 3H), 2.89 (s, 3H), 2.35 (s, 11H), 2.32 (d, *J* = 4.2 Hz, 14H), 2.18 (s, 5H), 2.13 (s, 3H), 2.06 (s, 4H), 2.00 (s, 5H), 1.85 (s, 5H), 1.81 (s, 6H). **^{13}C{^{1}H} NMR** (100 MHz, CD_3CN) δ 211.0, 209.6, 208.1, 205.3, 204.7, 156.7, 156.4, 156.1, 155.5, 155.4, 155.0, 154.8, 154.1, 153.6, 152.6, 152.5, 150.6, 139.4, 139.3, 139.3, 136.1, 136.0, 135.9, 135.8, 135.7, 135.7, 135.5, 135.4, 129.3, 129.3, 129.0, 128.9, 128.7, 126.0, 125.3, 124.8, 124.1, 119.2, 118.9, 118.7, 114.3, 114.0, 113.5, 113.3, 37.3, 36.8, 36.0, 35.9, 32.2, 29.7, 21.1, 21.0, 20.9, 20.7, 20.6, 20.4, 20.3. **HRMS** (ESI-TOF) m/z: $[M - 2PF_6^-]^{2+}$ Calcd for $C_{54}H_{57}N_9Fe$ 443.7038; Found: 443.7060.

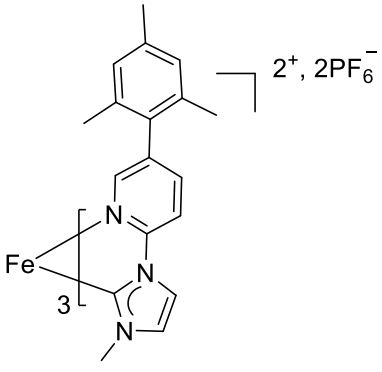

mer-**C7**

Fac and *mer*-**C7** in 4:96 ratio. General complexation method afforded 42 mg, (45 %) of an orange solid. **^{1}H NMR** (400 MHz, CD_3CN) δ 8.18 (d, *J* = 2.1 Hz, 1H), 8.14 (t, *J* = 2.6 Hz, 2H), 8.00 (d, *J* = 8.4 Hz, 1H), 7.84 – 7.74 (m, 3H), 7.67 (dd, *J* = 8.4, 2.0 Hz, 1H), 7.60 (dd, *J* = 8.4, 1.9 Hz, 1H), 7.53 (d, *J* = 1.9 Hz, 1H), 7.31 (dd, *J* = 9.4, 2.0 Hz, 2H), 7.26 (d, *J* = 2.1 Hz, 1H), 7.05 (d, *J* = 1.9 Hz, 1H), 6.96 – 6.83 (m, 7H), 6.72 (d, *J* = 1.8 Hz, 1H), 3.18 (s, 3H), 3.09 (s, 0.4H), 2.91 (s, 3H), 2.87 (s, 3H), 2.26 (s, 6H), 2.23 (s, 4H), 1.90 (s, 3H), 1.85 (s, 3H), 1.62 (s, 3H), 1.56 (s, 3H), 1.50 (s, 3H), 1.42 (s, 3H). **^{13}C{^{1}H} NMR** (100 MHz, CD_3CN) δ 326.0, 321.9, 320.8, 273.1, 271.9,

271.8, 271.4, 271.2, 269.2, 267.1, 260.0, 258.8, 258.68, 257.6, 256.4, 256.3, 256.2, 254.7, 254.0, 253.9, 253.6, 253.6, 253.5, 253.4, 252.5, 250.4, 250.4, 229.8, 229.2, 229.0, 154.1, 153.3, 153.3, 138.1, 138.0, 138.0, 138.0, 137.5, 137.4, 137.4, 137.3. **HRMS** (ESI-TOF) m/z: [M – $2PF_6^-$]$^{2+}$ Calcd for $C_{54}H_{57}N_9Fe$ 443.7038; Found: 443.7057**.**

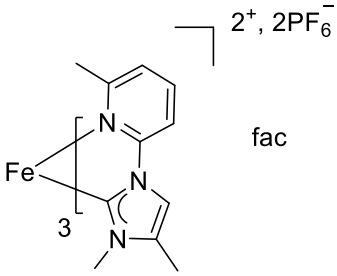

fac-**C9**

Fac-**C9**. General complexation method afforded 44 mg, (48 %) of an orange solid. **^{1}H NMR** (400 MHz, CD_3CN) δ 7.94 (t, *J* = 7.9 Hz, 1H), 7.82 (d, *J* = 1.5 Hz, 1H), 7.61 (d, *J* = 8.1 Hz, 1H), 7.09 (dd, *J* = 7.7, 1.1 Hz, 1H), 2.59 (s, 3H), 1.71 (s, 3H). **^{13}C{^{1}H} NMR** (100 MHz, CD_3CN) δ 206.0, 164.92, 153.9, 140.9, 137.7, 125.0, 116.3, 110.3, 32.5, 24.3, 10.4. **HRMS** (ESI-TOF) m/z: [M – $2PF_6^-$]$^{2+}$ Calcd for $C_{39}H_{39}N_9Fe$ 308.6333; Found: 308.6358.

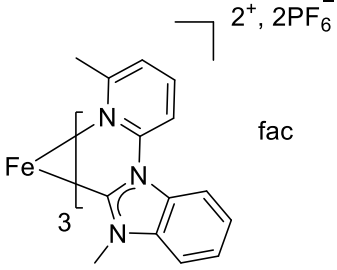

fac-**C10**

Fac-**C10**. General complexation method afforded 35 mg (43 %) of a red-orange solid. ^{1}H NMR (400 MHz, CD_3CN) δ 8.28 (d, *J* = 8.3 Hz, 1H), 8.20 (dd, *J* = 7.6, 1.5 Hz, 1H), 8.05 (t, *J* = 8.0 Hz, 1H), 7.55 – 7.36 (m, 3H), 7.19 – 7.10 (m, 2H), 2.97 (s, 3H), 1.89 (s, 3H). **^{13}C{^{1}H} NMR** (100 MHz, CD_3CN) δ 220.9, 165.3, 154.5, 141.6, 139.5, 132.6, 125.9, 125.8, 125.3, 112.8, 112.2, 111.6, 33.6, 25.0. **HRMS** (ESI-TOF) m/z: [M – $2PF_6^-$]$^{2+}$ Calcd for $C_{42}H_{39}N_9Fe$ 362.6337; Found: 362.6371.

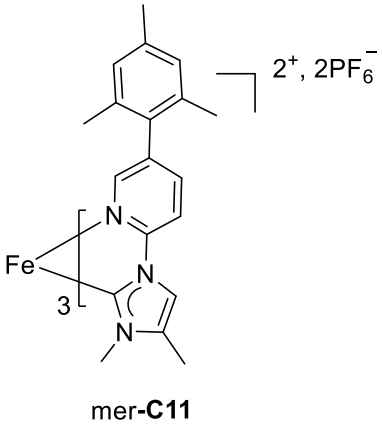

mer-**C11**

Complex *mer*-**C11**. General complexation method afforded 37mg, (49%) of a red-orange solid. **^{1}H NMR** (400 MHz, CD_3CN) δ 7.92 – 7.86 (m, 4H), 7.74 (dd, *J* = 8.4, 2.0 Hz, 1H), 7.67 (s, 1H), 7.65 (t, *J* = 1.8 Hz, 2H), 7.61 (d, *J* = 1.9 Hz, 1H), 7.56 (dd, *J* = 8.4, 1.9 Hz, 1H), 7.17 (d, *J* = 1.9 Hz, 1H), 6.93 (s, 1H), 6.89 (d, *J* = 3.9 Hz, 4H), 6.85 (d, *J* = 7.0 Hz, 3H), 6.67 – 6.62 (m, 1H), 3.06 (d, *J* = 0.8 Hz, 3H), 2.79 – 2.73 (m, 3H), 2.69 (s, 3H), 2.27 – 2.21 (m, 18H), 1.89 (s, 3H), 1.83 (s, 3H), 1.60 (s, 3H), 1.58 (s, 3H), 1.49 (s, 3H), 1.41 (s, 3H). **^{13}C{^{1}H} NMR** (100 MHz, CD_3CN) δ 208.8, 205.4, 203.6, 156.0, 154.8, 154.8, 154.4, 154.2, 152.0, 142.8, 141.4, 140.2, 139.2, 139.1, 139.1, 137.2, 137.0, 137.0, 136.9, 136.8, 136.7, 136.6, 136.6, 136.5, 136.0, 134.9, 133.6, 133.4, 129.3, 129.3, 129.2, 129.2, 129.2, 115.3, 114.7, 114.6, 112.3, 111.7, 111.4, 33.6, 32.8, 32.6,

21.1, 21.0, 21.0, 20.5, 20.4, 20.4, 20.3, 10.3, 10.1. **HRMS** (ESI-TOF) m/z: $[M - 2PF_6^-]^{2+}$ Calcd for $C_{57}H_{63}N_9Fe$ 464.7273; Found: 464.7295.

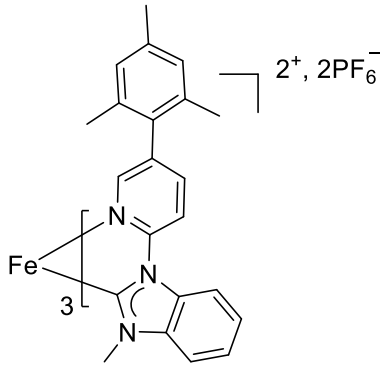

mer-**C12**

Complex *mer*-**C12**. General complexation method afforded 40mg, (40%) of a red-orange solid. **^{1}H NMR** (400 MHz, CD_3CN) δ 8.93 (d, *J* = 2.1 Hz, 1H), 8.25 (dd, *J* = 8.5, 5.1 Hz, 1H), 8.16 – 8.09 (m, 1H), 8.05 – 7.95 (m, 1H), 7.89 – 7.77 (m, 3H), 7.66 (d, *J* = 2.0 Hz, 1H), 7.49 – 7.27 (m, 7H), 7.14 – 6.99 (m, 2H), 6.96 (d, *J* = 8.0 Hz, 2H), 6.88 (s, 1H), 6.82 – 6.65 (m, 3H), 6.61 – 6.55 (m, 2H), 6.37 (dd, *J* = 8.6, 0.9 Hz, 1H), 6.26 (dd, *J* = 7.6, 2.0 Hz, 1H), 3.01 (s, 3H), 2.88 (s, 3H), 2.37 (s, 3H), 2.31 (s, 3H), 2.28 (s, 3H), 2.17 (s, 3H), 2.14 (s, 18H), 2.08 (s, 3H), 2.01 (s, 3H), 1.72 (s, 3H),z 1.65 (s, 3H), 1.56 (s, 3H). **^{13}C{^{1}H} NMR** (100 MHz, CD_3CN) δ 226.6, 224.1, 220.7, 170.7, 164.2, 162.3, 155.7, 155.4, 153.4, 150.7, 150.5, 140.3, 139.8, 139.7, 139.6, 139.2, 139.1, 139.0, 137.7, 137.7, 137.6, 137.5, 137.4, 137.2, 137.0, 136.8, 136.3, 134.8, 134.6, 134.4, 134.0, 132.8, 132.6, 130.5, 129.5, 129.3, 129.1, 128.8, 125.1, 124.7, 124.2, 123.8, 122.6, 112.4, 111.7, 111.6, 111.5, 110.1, 110.1, 110.0, 33.4, 33.4, 32.9, 21.9, 21.2, 21.1, 21.1, 21.0, 21.0, 20.9, 20.8, 20.7. **HRMS** (ESI-TOF) m/z: $[M - 2PF_6^-]^{2+}$ Calcd for $C_{66}H_{63}N_9Fe$ 518.7272; Found: 518.7297.

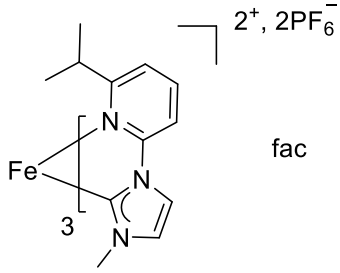

fac-**C13**

Fac-**C13,** General complexation method afforded 34mg, (40%) of an orange solid. **^{1}H NMR** (400 MHz, CD_3CN) δ 8.09 (t, *J* = 8.1 Hz, 1H), 8.06 (d, *J* = 2.3 Hz, 1H), 7.74 (dd, *J* = 8.1, 1.2 Hz, 1H), 7.37 (dd, *J* = 7.9, 1.1 Hz, 1H), 7.14 (d, *J* = 2.3 Hz, 1H), 2.65 (h, *J* = 7.0 Hz, 1H), 2.63 (s, 3H), 1.07 (d, *J* = 6.9 Hz, 3H), 0.41 (d, *J* = 6.7 Hz, 3H). **^{13}C{^{1}H} NMR** (100 MHz, CD_3CN) δ 203.4, 174.0, 152.2, 141.3, 130.8, 121.4, 119.0, 110.8, 36.2, 36.0, 23.4, 23.3. **HRMS** (ESI-TOF) m/z: $[M - 2PF_6^-]^{2+}$ Calcd for $C_{36}H_{45}N_9Fe$ 329.6568; Found: 329.6572 .

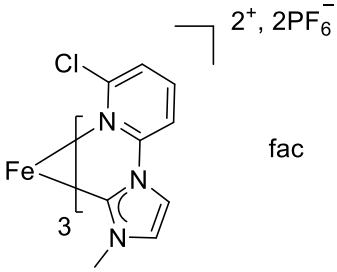

fac-**C16**

Fac-**C16**. General complexation method afforded 15 mg, (18%) of a red solid. **^{1}H NMR** (400 MHz, CD_3CN) δ 8.10 (d, *J* = 2.3 Hz, 1H), 8.04 (t, *J* = 8.0 Hz, 1H), 7.82 (dd, *J* = 8.2, 1.0 Hz, 1H), 7.31 (dd, *J* = 7.9, 1.0 Hz, 1H), 7.19 (d, *J* = 2.3 Hz, 1H), 2.75 (s, 3H). **^{13}C{^{1}H} NMR** (100 MHz, CD_3CN) δ 203.2, 156.8, 154.3, 142.8, 130.5, 125.9, 119.4, 111.2, 36.1. **HRMS** (ESI-TOF) m/z: [M – $2PF_6^-$]$^{2+}$ Calcd for $C_{27}H_{24}Cl_3N_9Fe$ 317.5279 ; Found: 317.5257.

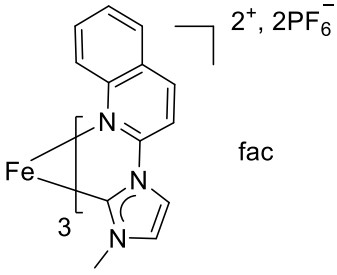

fac-**C18**

Fac-**C18.** General complexation method afforded 67 mg, (37%) of a dark-red solid. **^{1}H NMR** (400 MHz, CD_3CN) δ 8.71 (d, *J* = 8.9 Hz, 1H), 8.10 (d, *J* = 2.1 Hz, 1H), 8.07 (d, *J* = 8.3 Hz, 1H), 7.98 (dd, *J* = 8.8, 1.3 Hz, 1H), 7.48 (t, *J* = 7.6 Hz, 1H), 7.14 (d, *J* = 8.9 Hz, 1H), 7.10 (t, *J* = 1.8 Hz, 1H), 6.95 (ddd, *J* = 8.8, 7.0, 1.6 Hz, 1H), 2.75 (s, 3H). **^{13}C{^{1}H} NMR** (100 MHz, CD_3CN) δ 206.9, 154.1, 149.3, 143.3, 132.5, 130.9, 130.2, 128.8, 128.1, 124.8, 119.8, 112.0. **HRMS** (ESI-TOF) m/z: [M – $2PF_6^-$]$^{2+}$ Calcd for $C_{39}H_{33}N_9Fe$ 341.6099; Found: 341.6099.

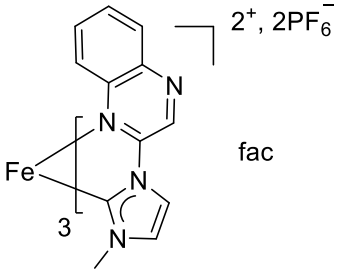

fac-**C19**

Fac-**C19**. General complexation method afforded 76 mg (34%) of a purple solid. **^{1}H NMR** (400 MHz, CD_3CN) δ 9.43 (s, 1H), 8.32 (s, 1H), 8.28 (d, *J* = 8.6 Hz, 1H), 7.73 (t, *J* = 7.7 Hz, 1H), 7.21 (s, 1H), 7.13 (t, *J* = 8.0 Hz, 1H), 6.84 (d, *J* = 8.8 Hz, 1H), 2.79 (s, 3H). **^{13}C{^{1}H} NMR** (100 MHz, CD_3CN) δ 203.2, 149.1, 143.1, 142.8, 136.8, 133.5, 132.5, 131.3, 131.2, 124.0, 120.2, 36.8. **HRMS** (ESI-TOF) m/z: [M – $2PF_6^-$]$^{2+}$ Calcd for $C_{36}H_{30}N_{12}Fe$ 343.1027 ; Found: 343.1031.

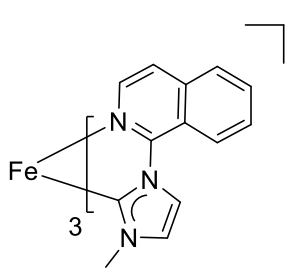

C20

Fac- and *mer*-**C20** in 37:63 ratio. General complexation method afforded 76 mg (34%) of an intense reddish solid. **^{1}H NMR** (400 MHz, CD_3CN) δ 8.81 (d, *J* = 2.4 Hz, 1H), 8.78 (dd, *J* = 6.8, 3.3 Hz, 3H), 8.74 (d, *J* = 2.3 Hz, 1H), 8.71 (d, *J* = 2.3 Hz, 2H), 8.69 – 8.64 (m, 1H), 7.63 (d, *J* = 0.8 Hz, 1H), 7.55 (dd, *J* = 6.4, 0.9 Hz, 2H), 7.50 (d, *J* = 2.3 Hz, 1H), 7.46 (d, *J* = 2.2 Hz, 1H), 7.38 (d, *J* = 2.4 Hz, 1H), 7.33–7.23 (m, 5H), 6.90 (d, *J* = 6.4 Hz, 2H), 6.79 (d, *J* = 6.5 Hz, 1H), 3.24 (s, 3H), 3.03 (s, 5H), 2.76 (s, 3H), 2.72 (s, 3H). **^{13}C{^{1}H} NMR** (100 MHz, CD_3CN) δ 212.15, 211.85, 209.27, 206.82, 155.00, 154.60, 153.92, 153.20, 146.42, 144.87, 142.15, 140.39, 139.15, 138.75, 138.19, 137.74, 133.00, 132.80, 132.56, 132.30, 130.32, 130.24, 130.04, 129.97, 128.69, 128.61, 128.54, 128.47, 128.41, 128.36, 123.64, 123.53, 122.77, 122.74, 122.51, 122.31, 122.04, 121.67, 121.39, 120.95, 120.91, 120.26, 119.86, 119.51, 119.42, 37.01, 36.83, 36.07, 35.85. **HRMS** (ESI-TOF) m/z: $[M - 2PF_6^-]^{2+}$ Calcd for $C_{39}H_{33}N_9Fe$ 341.6099 ; Found: 341.6099.

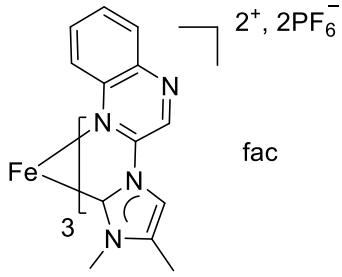

fac-**C21**

Fac-**C21**. General complexation method afforded 45 mg (34%) of a purplish solid. **^{1}H NMR** (400 MHz, CD_3CN) δ 9.35 (s, 1H), 8.26 (dd, J = 8.4, 1.5 Hz, 1H), 8.10 (t, J = 1.2 Hz, 1H), 7.70 (ddd, J = 8.4, 7.0, 1.2 Hz, 1H), 7.11 (ddd, J = 8.6, 7.0, 1.5 Hz, 1H), 6.79 (dd, J = 8.7, 1.2 Hz, 1H), 2.66 (s, 3H), 2.14 (s, 3H). **^{13}C{^{1}H} NMR** (100 MHz, CD_3CN) δ 203.60, 149.14, 143.17, 142.65, 138.87, 136.59, 133.40, 132.43, 131.10, 123.91, 117.07, 33.22, 10.46. **HRMS** (ESI-TOF) m/z: $[M - 2PF_6^-]^{2+}$ Calcd for $C_{39}H_{36}N_{12}Fe$ 364.1262; Found: 364.1291.

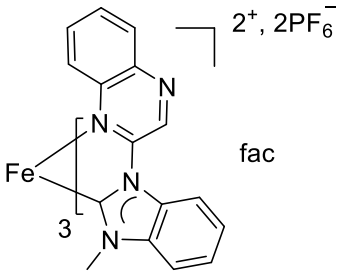

fac-**C22**

Fac-**C22**. General complexation method afforded 35 mg (37%) of an intense reddish solid. **^{1}H NMR HRMS** (400 MHz, CD_3CN)δ 9.92 (s, 1H), 8.29 (dtdd, J = 16.3, 13.3, 11.4, 7.8, 3.9 Hz, 2H), 8.24 (dd, J = 8.4, 1.0 Hz, 2H), 7.72 (ddd, J = 8.3, 6.9, 1.2 Hz, 1H), 7.52 (dtt, J = 19.5, 14.5, 12.3, 10.5, 9.3, 7.3, 5.0 Hz, 3H), 7.48 – 7.43 (m, 1H), 7.22 (ddd, J = 8.7, 7.0, 1.6 Hz, 1H), 7.03 (d, J = 8.5 Hz, 1H), 3.04 (s, 3H). **^{13}C{^{1}H} NMR** (100 MHz, CD_3CN) δ 217.35, 150.64, 142.90, 142.66, 139.18, 137.01, 134.09, 132.37, 132.22, 131.58, 126.83, 126.05, 124.01, 113.72, 112.54, 34.43. **HRMS** (ESI-TOF) m/z: $[M - 2PF_6^-]^{2+}$ Calcd for $C_{48}H_{36}N_{12}Fe$ 418.1262; Found: 418.1268.

VII.5.2.2 Complexes C23^{+} - C27^{+} (IV. Fe(III) complexes bearing tridentate anionic ligands)

Synthesis of complex **C23**$^{+}$

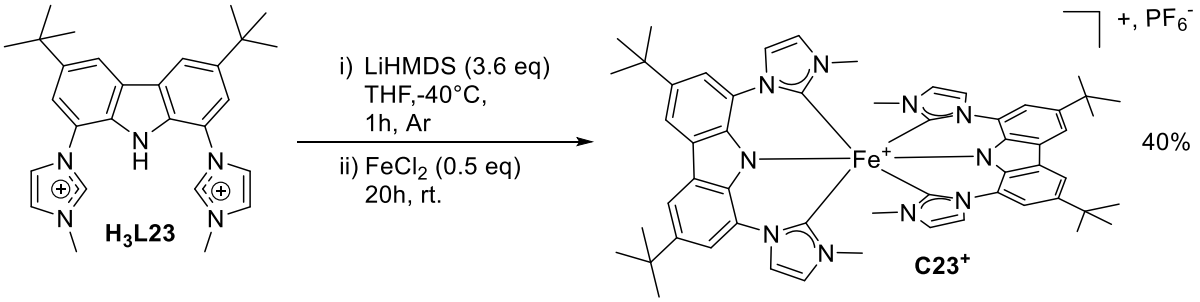

In a Schlenk with ligand **H_3L23** (0.12 mg, 0.16 mmol) three vacuum-argon cycles were made, then 1.5 mL of THF were added. The mixture as cooled to -40 °C and a solution of LiHMDS [1M in THF] (0.58 mL, 0.58 mmol) was added dropwise stirring during 2h reaching room temperature. Then $FeCl_2$ (10.7 mg, 0.082 mmol) was added in solid and the mixture was stirred overnight. Afterwards, H_2O (10 mL) was added and 1 mL of KPF_6 (saturated solution) the reaction was vigorously stirred and the precipitated formed was filtered in a glass funnel filter #4 or #3 (depending on particle aggregation: #4 for small, #3 for bigger). The solid was washed with H_2O (10 mL) and diethyl ether (3 x 15 mL) until the solid was a fine powder. The complex was isolated thorough a neutral alumina column, starting with mixture diethylether:ACN (4:1), gradually increasing to diethylether:ACN (1:1). The fractions were collected

and solvent were removed under vacuum. The green product of the column, was purified by vapor diffusion crystallization with acetone and diethylether as pair of solvents (acetone inside to solubilize the product/diethylether outside the mixture). The crystallization afforded complex **C23**$^{+}$ in 35 mg (40%). **HRMS** (ESI-TOF) m/z: $[M - 2PF_6^-]^{2+}$ Calcd for $C_{56}H_{64}N_{10}Fe$ 932.4659; Found: 932.4670. X-Ray in §VI.6.

Synthesis of Complex **C26**$^{+}$

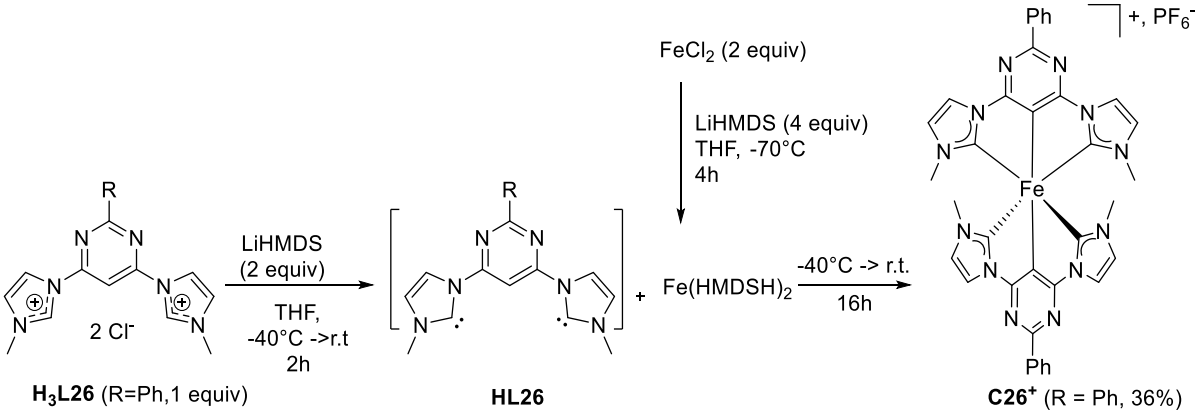

In a schlenk with $FeCl_2$ (8.1 mg, 0.064 mmol) three vacuum-Argon cycles were made, then dry THF (3 mL) was added and the suspension was cooled to -78°C, then LiHMDS [1M in THF] (0.13 mL, 0.128 mmol) was added dropwise, the reaction was allowed to reach r.t. and stirred for 4h forming [Fe(HMDS)2 · THF] . In parallel, in a Schlenk charged with **H$_3$L26** (50 mg, 0.128 mmol) 3 mL of dry THF were added and cooled to -40°C, then a solution of LiHMDS [1M in THF] (0.28 mL, 0.28 mmol) was added dropwise and stirred for 3h reaching r.t. Then the both schlenk's were cooled to -60°C and the mixture of [**HL26**] was transferred via canula into the schlenk with [Fe(HMDS)2 · THF]. The mixture was stirred overnight, after this time, the strong violette reactions was quenched with addition of MeOH (5 mL) and 1 mL of KPF_6 (saturated solution). The solvents were removed under vacuum and supported on neutral alumina. The complex was isolated thorough a neutral alumina column, starting with mixture diethylether: ACN (4:1), gradually increasing to only ACN. The green product of the column, was purified by vapor diffusion crystallization with acetone and diethylether as pair of solvents (acetone inside to solubilize the product/diethylether outside the mixture). The crystallization afforded a green solid **C26**$^{+}$ in 39 mg (36%). **^{1}H NMR** (400 MHz, CD_3CN) δ 12.11 (t, J = 7.5 Hz, 2H), 10.85 (s, 6H), 2.92 (s, 2H), 1.17 (d, J = 7.5 Hz, 2H), -1.11 (t, J = 7.4 Hz, 1H), -4.02 (s, 2H). **HRMS** (ESI-TOF) m/z: $[M - PF_6^-]^{2+}$ Calcd for $C_{36}H_{30}N_{12}Fe$ 686.2060; Found: 686.2054.

Complex **C27**$^{+}$

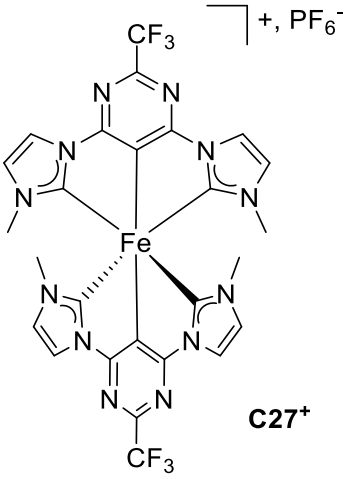

C27^{+}

Complex **C27**$^{+}$. Following the complexation method for **C26**$^{+}$ afforded 32 mg, (30 %) of an green solid. **^{1}H NMR** (400 MHz, CD_3CN) δ 13.92 (s, 6H), 2.57 (s, 2H), -7.01 (s, 2H). **^{19}F NMR** (376 MHz, CD_3CN) δ -23.85, -72.03, -73.90. **HRMS** (ESI-TOF) m/z: $[M - PF_6^-]^{2+}$ Calcd for $C_{26}H_{20}N_{12}F_{12}Fe$ 670.1182; Found: 670.1170.

VII.5.2.3 Complexes $[Fe(L30)_2]^{2+}$ - $[Fe(BL)(L30)]^{2+}$ (IV. Iron complexes as photosensitizers towards H2-evolition)

Complex **$[Fe(L30)_2]^{2+}$**

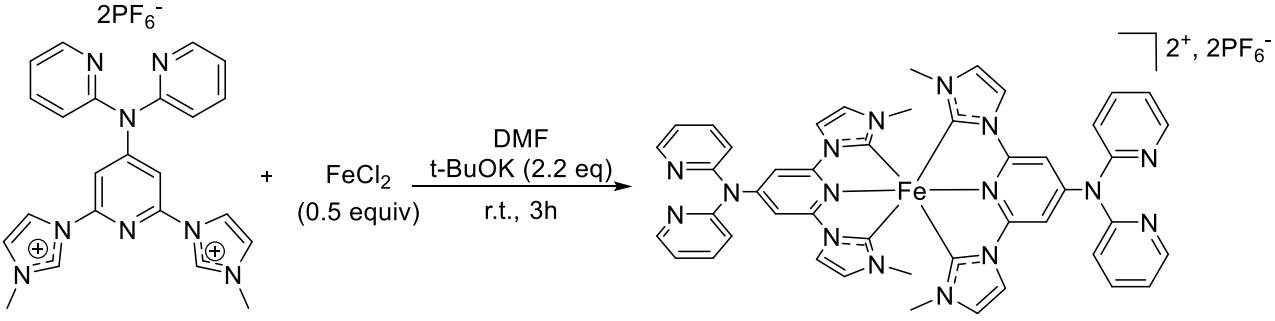

H_2L30 **$[Fe(L30)_2]^{2+}$**

In schlenk with FeCl2 (9.1 mg, 0.07 mmol) and ligand **H_2L30** (100 mg, 0.14 mmol), 2 mL of dry DMF were added. The mixture was stirred for 5 in, then t-BuOK (48 mg, 0.43 mmol). The reaction color turned into dark-reddish. The reaction was stirred for 3h, then solvent was removed under vacuum. The mixture was dissolved in a minimum amount of acetone (0.5 mL) and poured diethylether. The precipitated formed was filtered in a glass funnel filter #4 or #3 (depending on particle aggregation: #4 for small, #3 for bigger). The solid was washed with diethyl ether (3 x 15 mL) until the solid was a fine powder. The crude was purified over

neutral alumina, with mixture diethylether:ACN (2:1), gradually increasing to only ACN. The green product of the column, was purified by vapor diffusion crystallization with CH_2Cl_2 and n-hexane as pair of solvents (CH_2Cl_2 inside to solubilize the product/n-hexane outside the mixture). The crystallization afforded a reddish solid **$[Fe(L30)_2]^{2+}$** in 45 mg (40%). **^{1}H NMR** δ 8.45 (dd, J = 5.1, 1.9 Hz, 4H), 7.87 (ddd, J = 8.1, 7.4, 1.9 Hz, 4H), 7.82 (d, J = 2.2 Hz, 4H), 7.37 (s, 4H), 7.30 (ddd, J = 7.4, 4.9, 1.0 Hz, 4H), 7.25 (dt, J = 8.1, 0.9 Hz, 4H), 6.97 (d, J = 2.2 Hz, 4H), 2.70 (s, 12H). **^{13}C{^{1}H} NMR** (100 MHz, CD_3CN) δ 202.02, 157.13, 154.98, 154.46, 149.99, 139.68, 126.71, 122.07, 120.59, 116.79, 99.29, 35.21. **HRMS** (ESI-TOF) m/z: [M – $2PF_6^-$]$^{2+}$ Calcd for $C_{46}H_{40}FeN_{16}$ 436.1480; Found: 436.1493.

Complex **$[Fe(L30)(BL)]^{2+}$**

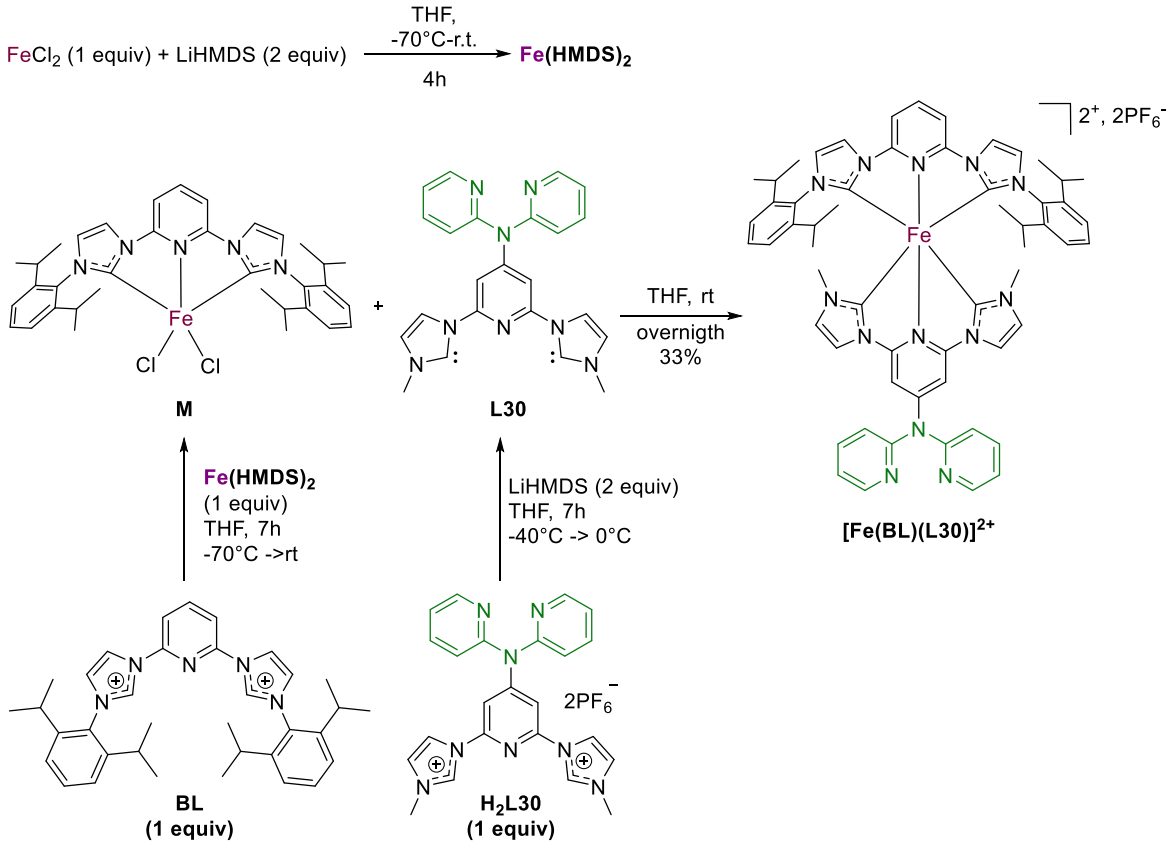

The synthesis of complex **$[Fe(L30)(BL)]^{2+}$** was according to a literature procedure.[204] Reddish solid 41 mg (33%). %). **^{1}H NMR** (400 MHz, CD_3CN) δ 8.52 (ddd, *J* = 4.9, 2.0, 0.8 Hz, 2H), 8.31 – 8.24 (m, 3H), 7.92 (td, *J* = 8.0, 2.5 Hz, 4H), 7.64 (d, *J* = 2.2 Hz, 2H), 7.35 – 7.29 (m, 4H), 7.16 (d, *J* = 2.2 Hz, 2H), 7.08 (d, *J* = 7.8 Hz, 4H), 6.95 (dd, *J* = 9.5, 1.6 Hz, 4H), 6.55 (s, 2H), 2.68 (s, 6H), 1.31 (p, *J* = 6.6 Hz, 4H), 0.85 (d, *J* = 6.7 Hz, 12H), 0.75 (d, *J* = 6.6

Hz, 12H). **$^{13}C\{^{1}H\}$ NMR** (100 MHz, CD_3CN) δ 201.57, 201.39, 157.15, 155.06, 154.94, 153.41, 150.32, 145.90 (d, *J* = 2.1 Hz), 139.78, 138.68, 134.99, 131.38, 131.28, 126.55, 124.68, 122.62, 120.84, 119.53, 116.61, 106.63, 97.67, 35.64, 28.56, 26.70 (d, *J* = 2.0 Hz), 24.14. **HRMS** (ESI-TOF) m/z: $[M - 2PF_6^-]^{2+}$ Calcd for $C_{59}H_{63}FeN_{12}$ 497.7319; Found: 497.7321.

VII.6 XRD Structure determination

Suitable single crystals were selected and XRD data were collected on a Rigaku OD SuperNova dual Source Atlas CCD detector diffractometer for *fac*-**C5** and *mer*-**C7** and on a Bruker D8 Venture diffractometer equipped with a PHOTON III X-ray detector for *fac*-**C18** . The crystals were kept at 100.0(1) K during data collection. Using Olex2[237], the structures were solved with the SHELXT[238] structure solution program using Intrinsic Phasing and refined with the XL[239] refinement package using Least Squares minimization.

Table of Crystal data and structure refinement.

Complex	*fac*-**C5**	*mer*-**C7**	*fac*-**C18**	**C23**$^{+}$
Identification code	UC249	UC254	UC258	UC-400
CCDC number	2126499	2126506	2126500	
Empirical formula	$C_{30}H_{33}F_{12}FeN_9P_2$	$C_{54}H_{63}F_{12}FeN_9O_{2.5}P_2$	$C_{39}H_{33.67}F_{12}FeN_9O_{0.33}P_2$	$C_{56}H_{64}FeN_{10},F_{4.53}P_{,1.52}$
Formula weight	865.44	1223.92	979.52	1077.99
Temperature/K	100.0(1)	100.0(1)	100.0(1)	100(1)
Crystal system	monoclinic	triclinic	monoclinic	monoclinic
Space group	$P2_1/n$	P-1	$P2_1/c$	P $2_1/c$
a/Å	13.5072(4)	13.7392(5)	19.1360(14)	12.4479(13)
b/Å	12.9500(4)	14.5195(5)	8.7370(7)	16.4163(3)
c/Å	20.3565(6)	15.7361(5)	24.799(2)	25.333(15)
α/°	90	88.127(2)	90	90
β/°	103.098(3)	68.396(3)	95.418(3)	91.344
γ/°	90	86.209(3)	90	90
Volume/Å^3	3468.09(18)	2912.11(18)	4127.7(6)	5175.34
Z	4	2	4	4
ρ_{calc}g/cm^3	1.658	1.396	1.576	1.385
μ/mm^{-1}	0.631	0.401	0.541	
F(000)	1760.0	1268.0	1989.0	
Crystal size/mm^3	0.204 × 0.123 × 0.024	0.368 × 0.105 × 0.061	0.55 × 0.15 × 0.08	
Radiation	MoKα (λ = 0.71073)	MoKα (λ = 0.71073)	MoKα (λ = 0.71073)	
2Θ range for data collection/°	3.756 to 61.132	3.938 to 56.652	4.276 to 56.56	
Index ranges	$-19 \le h \le 19$, $-18 \le k \le 18$, $-29 \le l \le 29$	$-17 \le h \le 18$, $-19 \le k \le 19$, $-20 \le l \le 20$	$-25 \le h \le 24$, $-11 \le k \le 11$, $-33 \le l \le 33$	
Reflections collected	83327	48792	142625	
Independent reflections	10620 [R_{int} = 0.0903, R_{sigma} = 0.0641]	14451 [R_{int} = 0.0681, R_{sigma} = 0.0941]	10238 [R_{int} = 0.0704, R_{sigma} = 0.0325]	
Data/restraints/parameters	10620/0/515	14451/3/756	10238/0/618	
Goodness-of-fit on F^2	1.083	1.000	1.087	
Final R indexes [I>=2σ (I)]	R_1 = 0.0599, wR_2 = 0.0979	R_1 = 0.0569, wR_2 = 0.1317	R_1 = 0.0472, wR_2 = 0.1146	
Final R indexes [all data]	R_1 = 0.1035, wR_2 = 0.1123	R_1 = 0.1135, wR_2 = 0.1607	R_1 = 0.0667, wR_2 = 0.1239	
Largest diff. peak/hole / e Å^{-3}	0.69/-0.61	0.77/-0.49	0.55/-0.49	

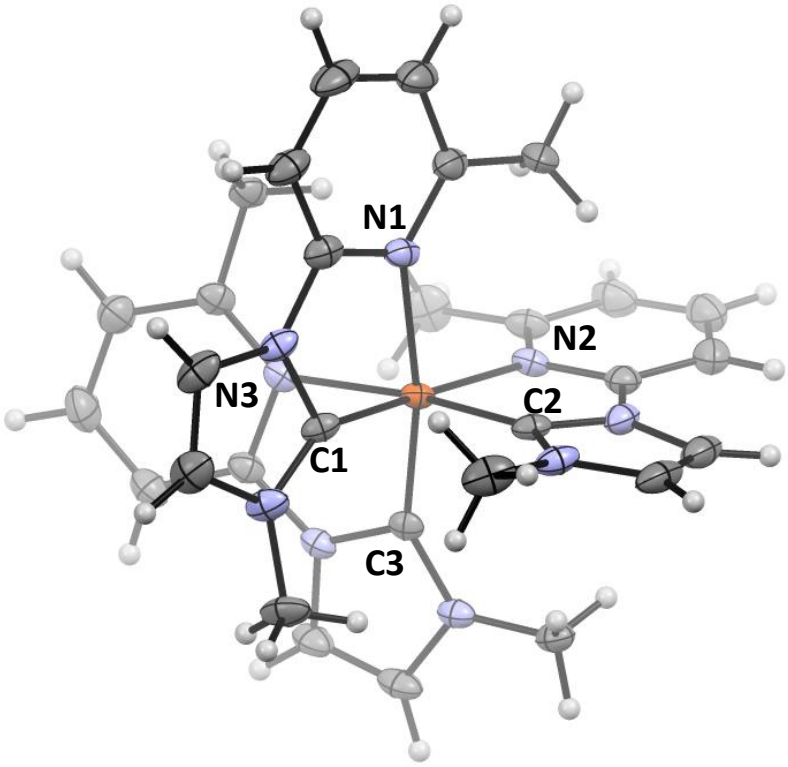

X-ray crystal structure of *fac*-**C5**. Displacement ellipsoids are at the 50% probability level. Counter ions and solvent molecules are omitted for clarity. C: black, H: white; N: blue; Fe: red. Suitable crystals were grown by slow evaporation in methanol.

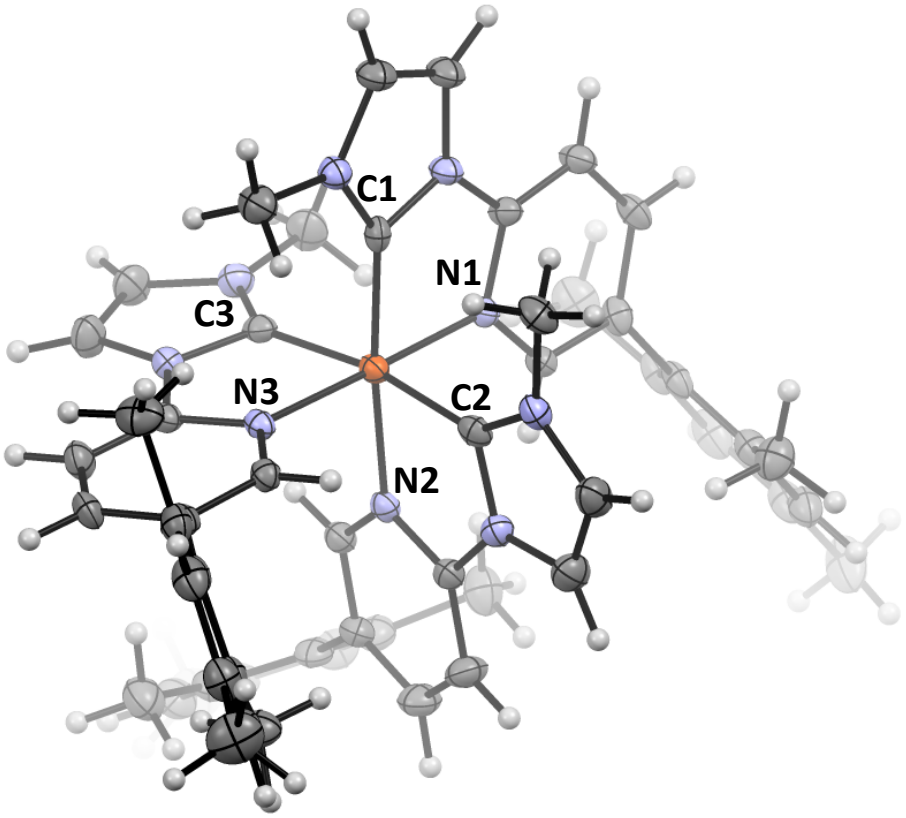

X-ray crystal structure of *mer*-**C7**. Displacement ellipsoids are at the 50% probability level. Counter ions and solvent molecules are omitted for clarity. C: black, H: white; N: blue; Fe: red. Suitable crystals were grown by slow evaporation in acetonitrile.

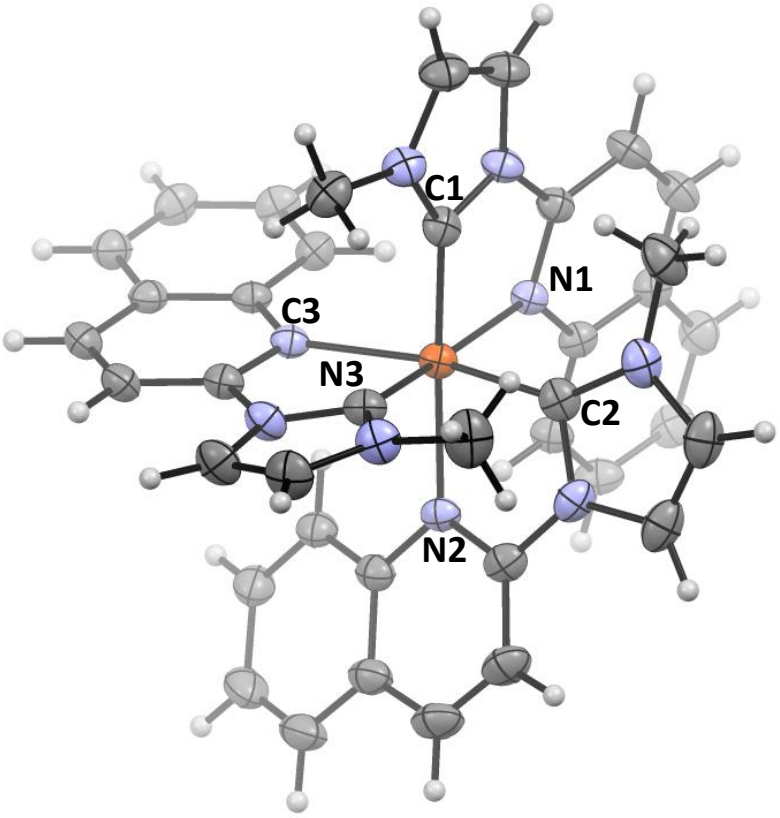

X-ray crystal structure of *fac*-**C18**. Displacement ellipsoids are at the 50% probability level. Counter ions and solvent molecules are omitted for clarity. C: black, H: white; N: blue; Fe: red. Suitable crystals were grown by slow evaporation in acetonitrile.

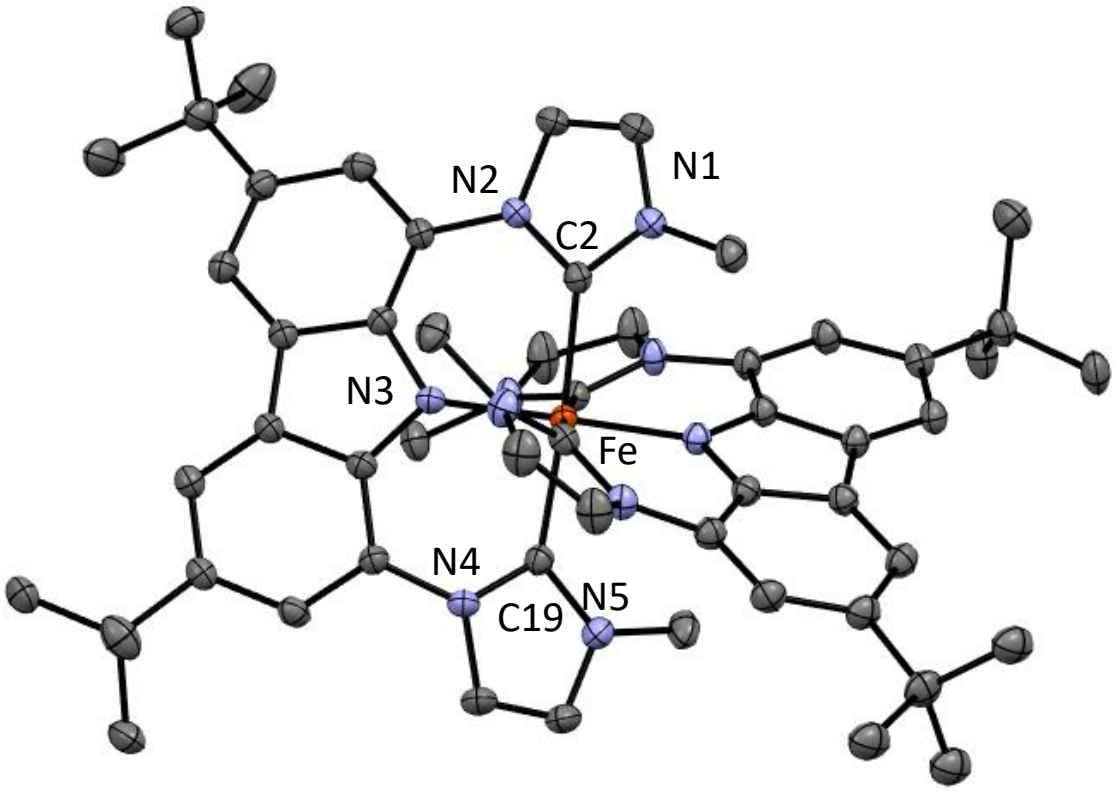

X-ray crystal structure of **C23**$^{+}$. Displacement ellipsoids are at the 50% probability level. Counter ions and solvent molecules are omitted for clarity. C: black; N: blue; Fe: red. Suitable crystals were grown by slow evaporation in acetonitrile. H were omitted for clarity

VII.7 Cyclic voltammetry

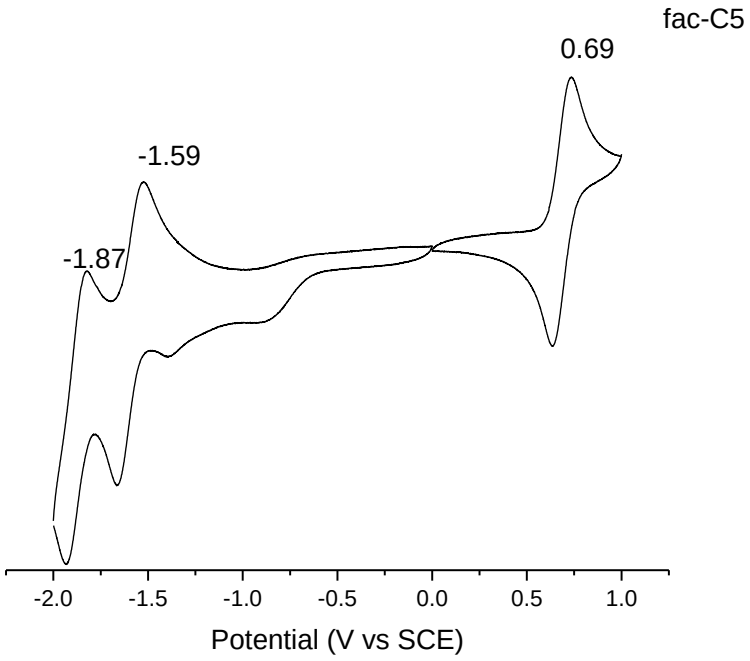

Cyclic voltammetry of complex *fac*-**C5.**

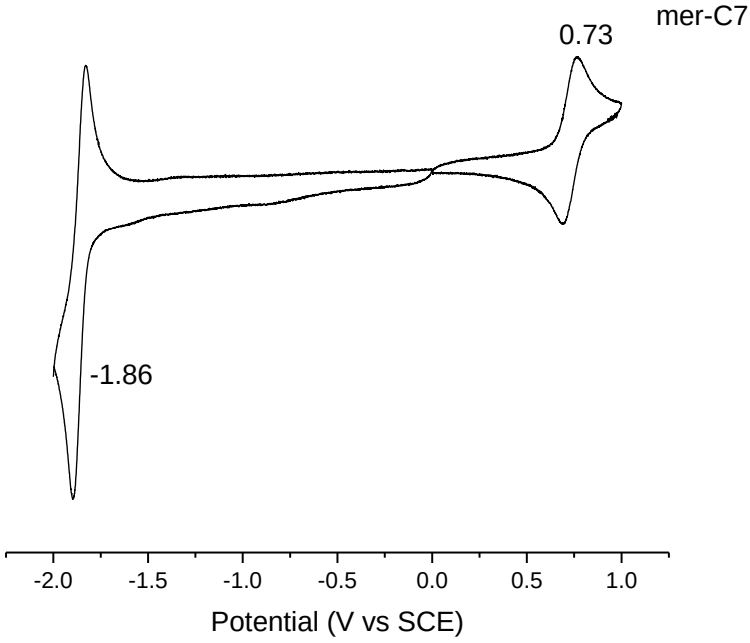

Cyclic voltammetry of complex *mer*-**C7.**

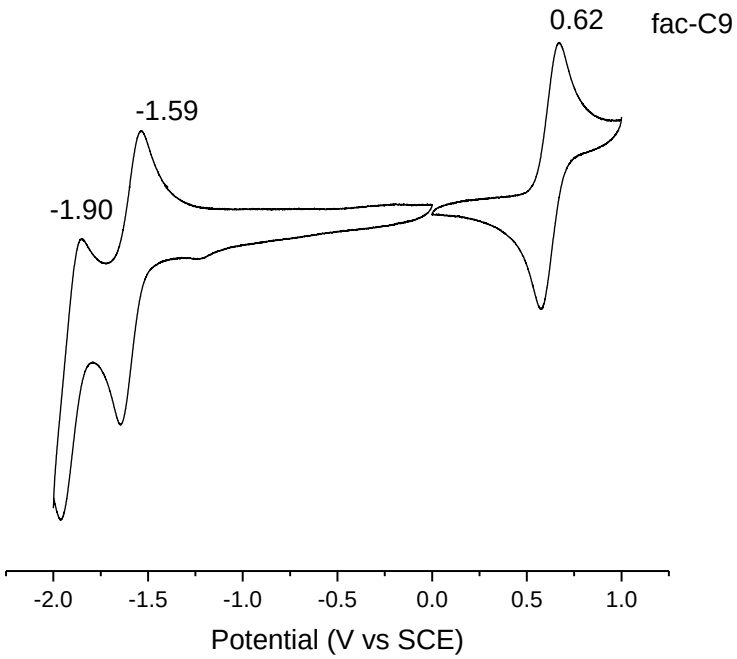

Cyclic voltammetry of complex *fac*-**C9.**

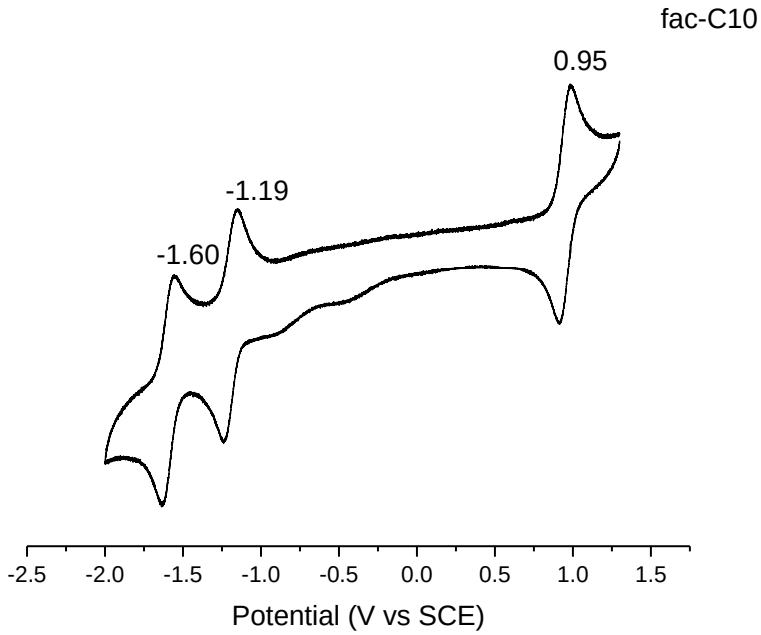

Cyclic voltammetry of complex *fac*-**C10.**

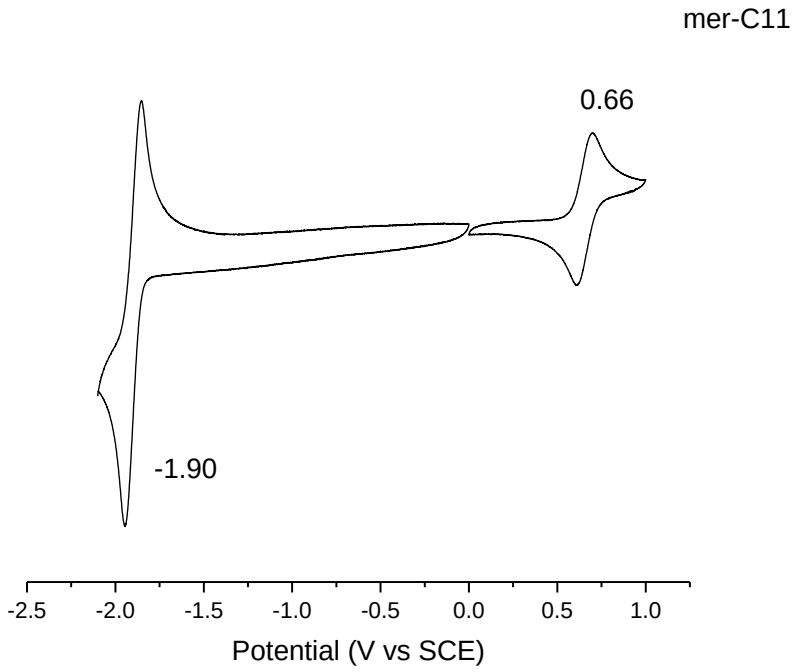

Cyclic voltammetry of complex *mer*-**C11.**

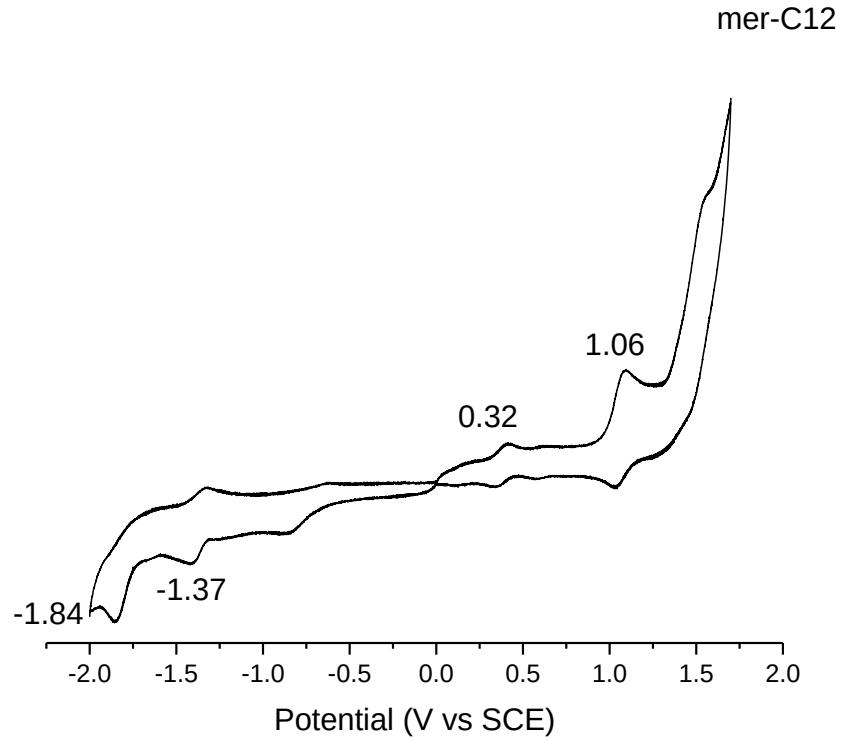

Cyclic voltammetry of complex *mer*-**C12.**

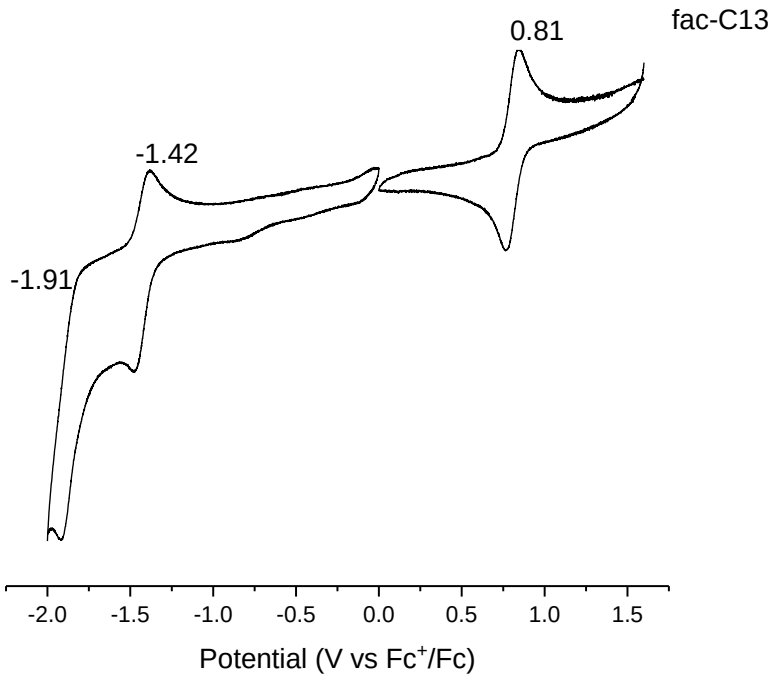

Cyclic voltammetry of complex *fac*-**C13.**

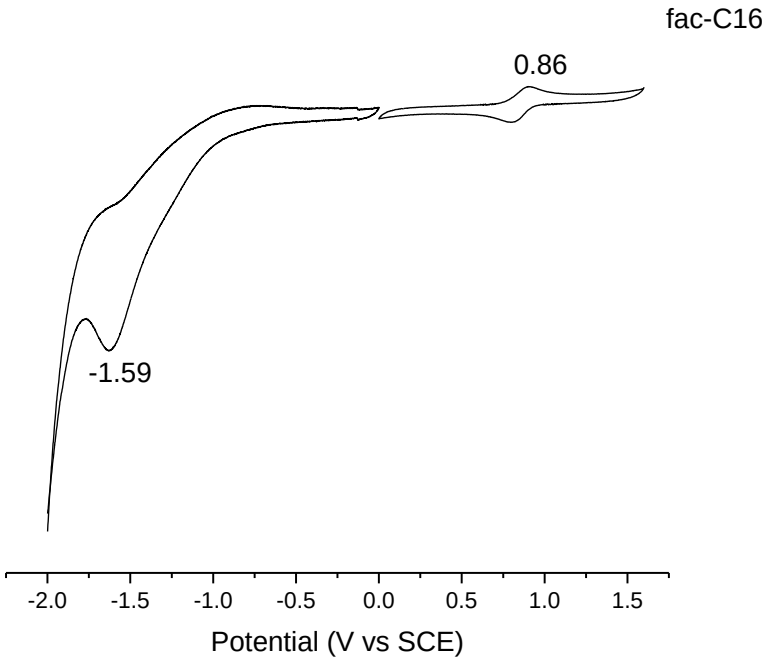

Cyclic voltammetry of complex *fac*-**C16.**

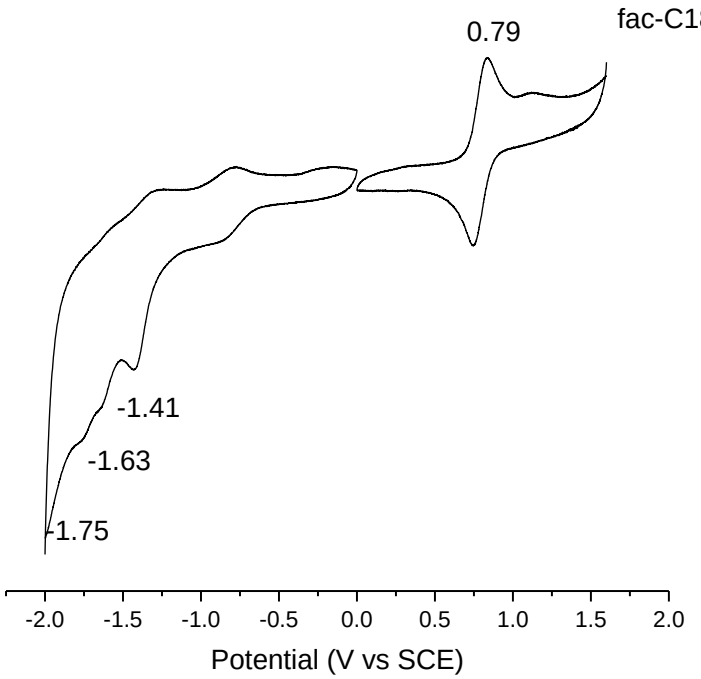

Cyclic voltammetry of complex *fac*-**C18.**

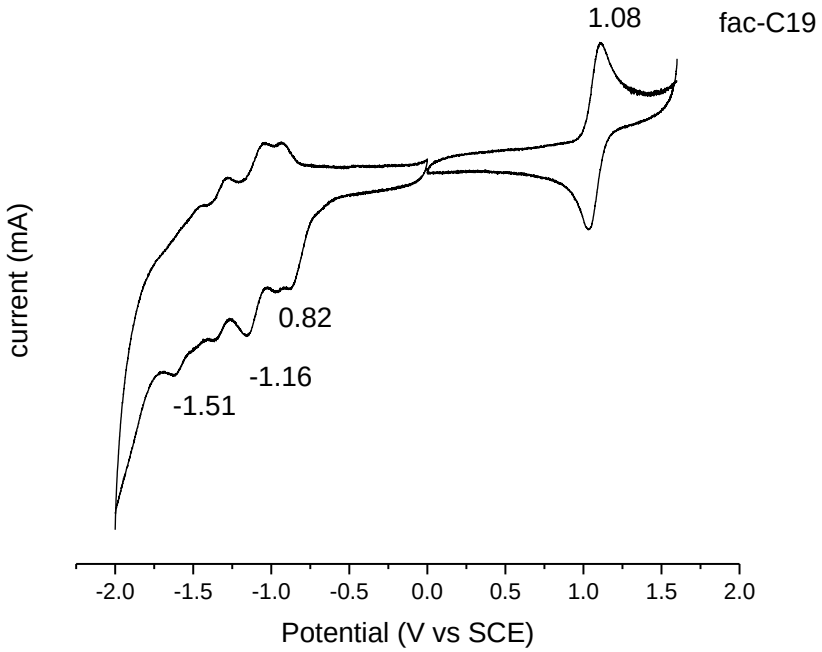

Cyclic voltammetry of complex *fac*-**C19.**

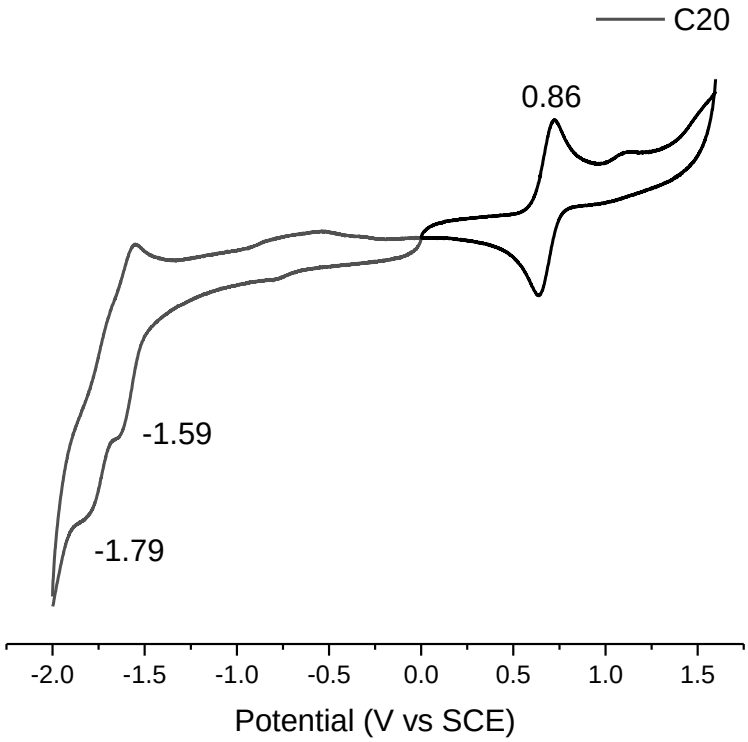

Cyclic voltammetry of complex **C20.**

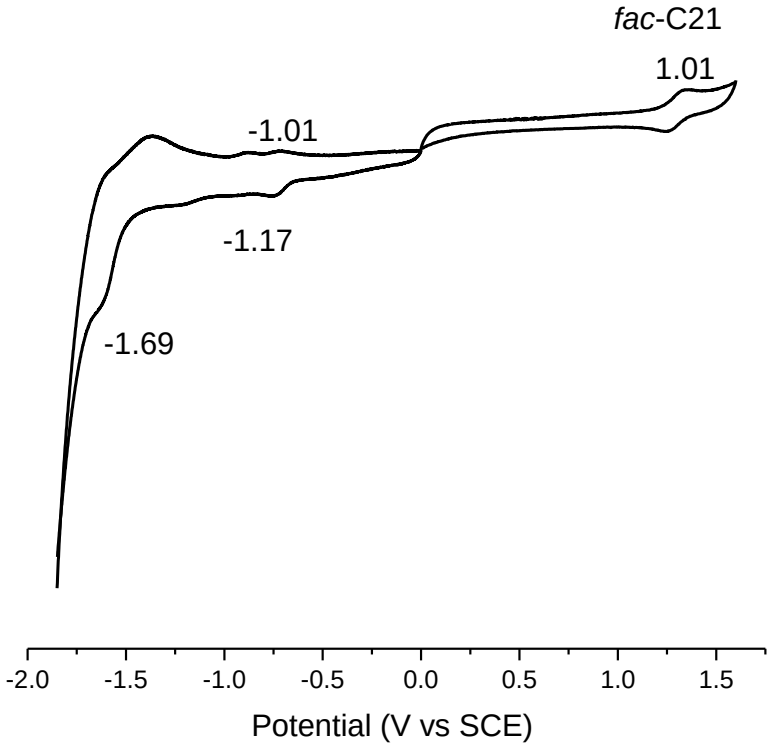

Cyclic voltammetry of complex *fac*-**C21.**

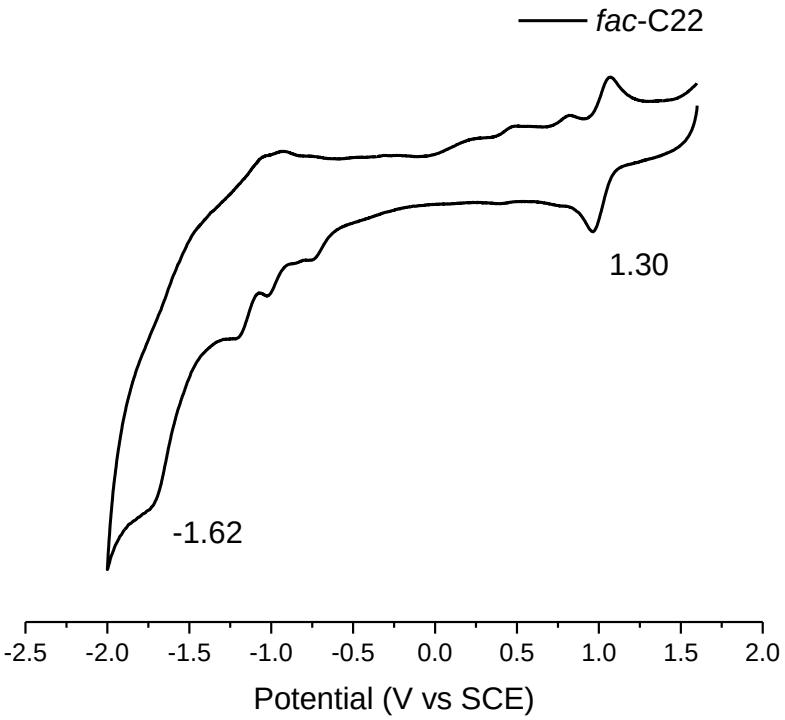

Cyclic voltammetry of complex *fac*-**C22.**

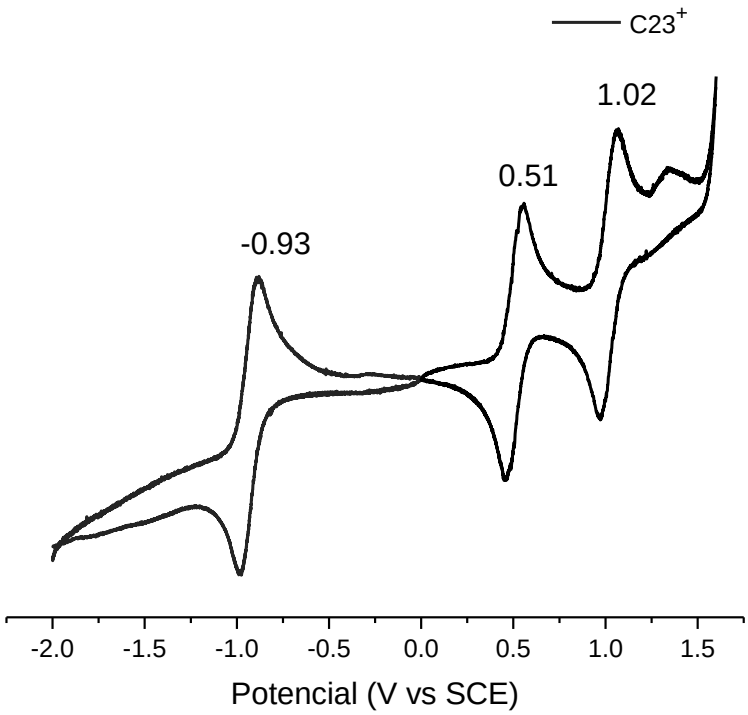

Cyclic voltammetry of complex **C23**$^{+}$

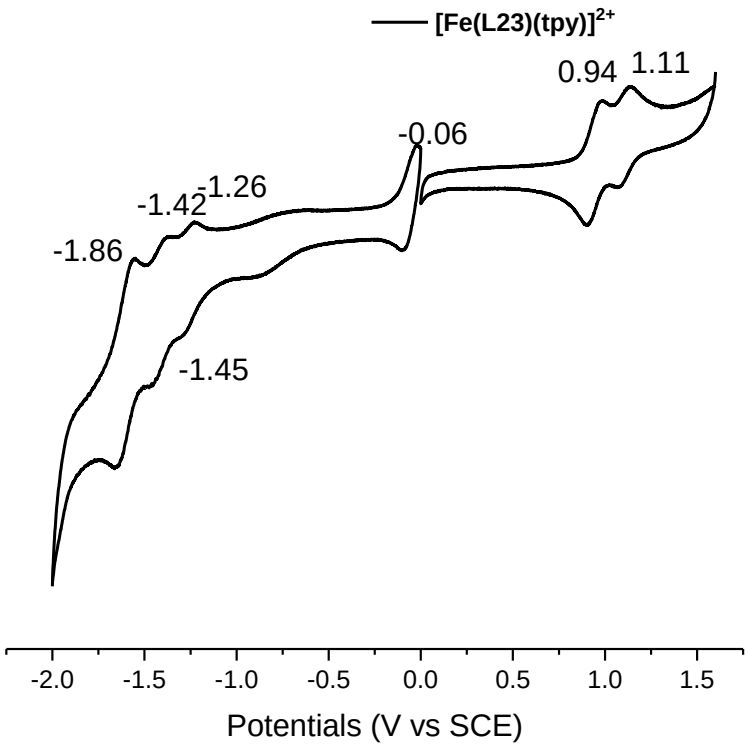

Cyclic voltammetry of complex **[Fe(L23)(tpy)]$^{2+}$**

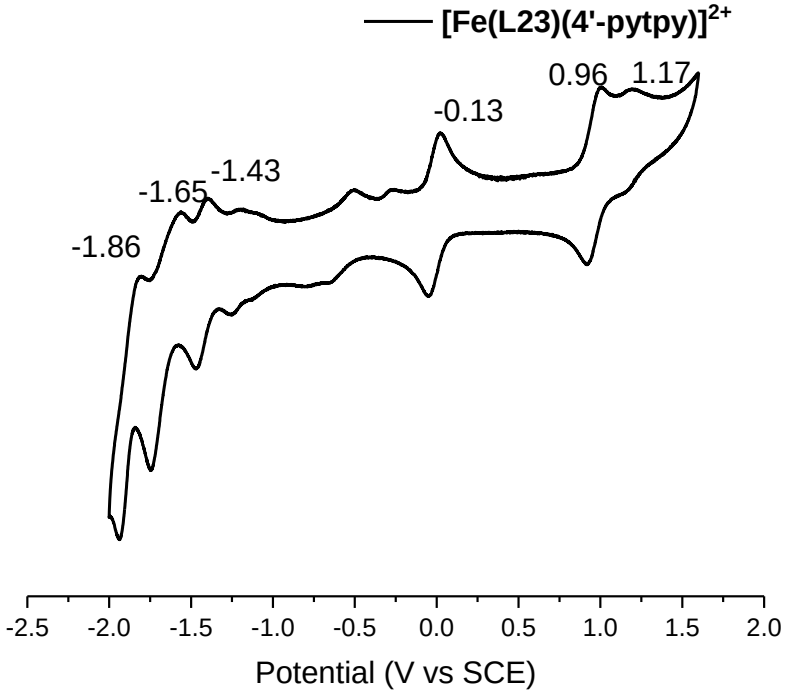

Cyclic voltammetry of complex **[Fe(L23)(4'tpytpy)]$^{2+}$**

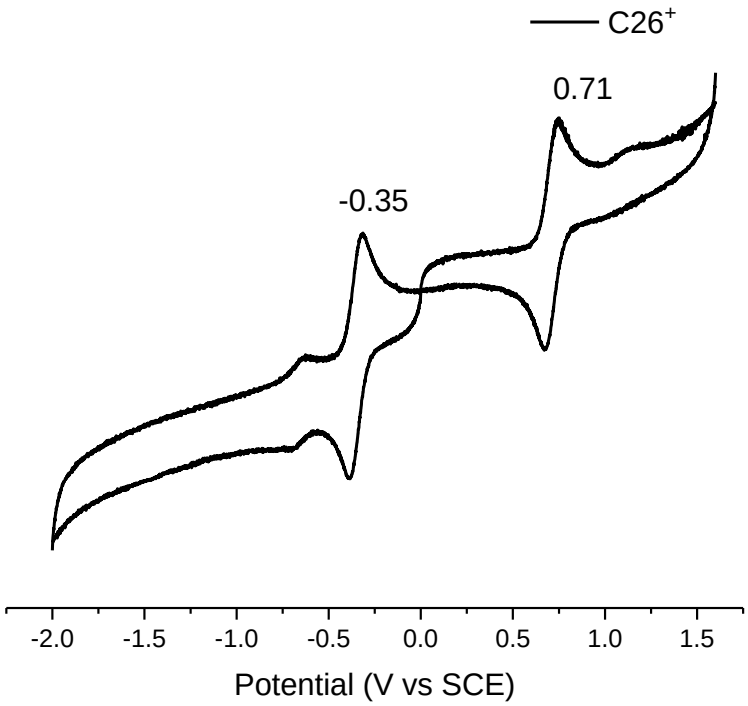

Cyclic voltammetry of complex **C26**$^{+}$

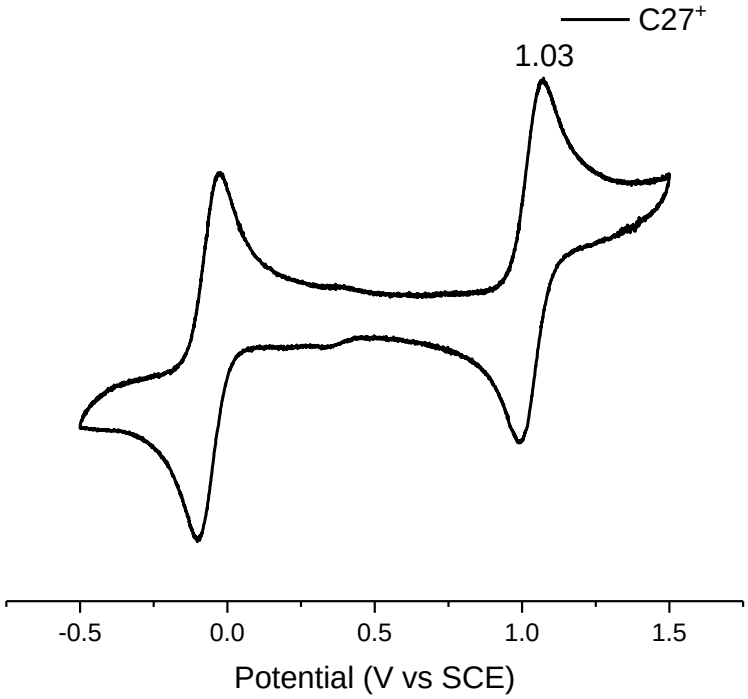

Cyclic voltammetry of complex **C27**$^{+}$

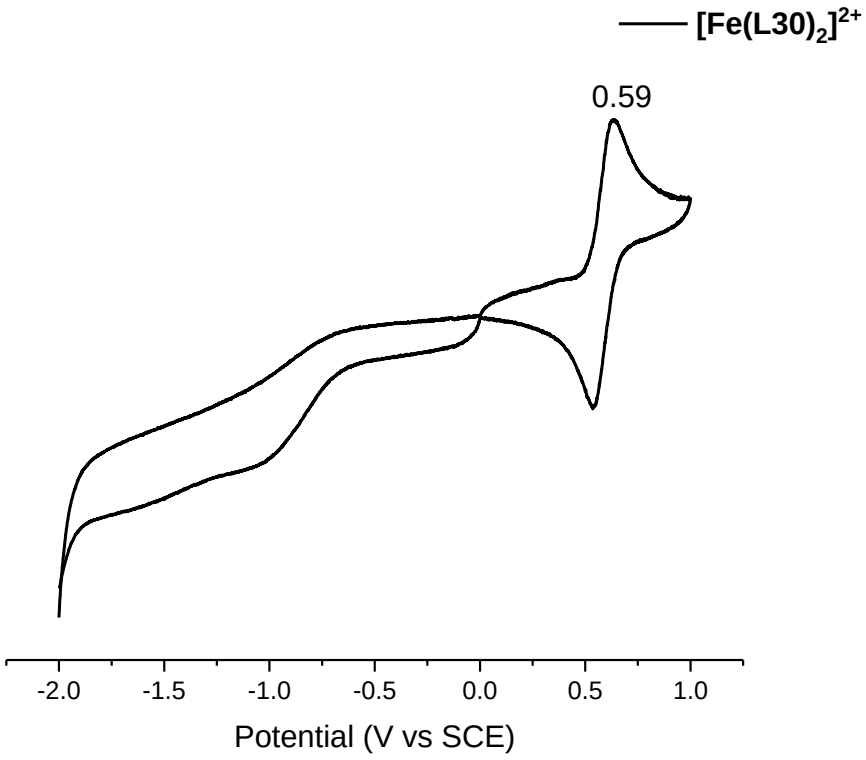

Cyclic voltammetry of complex **[Fe(L30)]$^{2+}$**

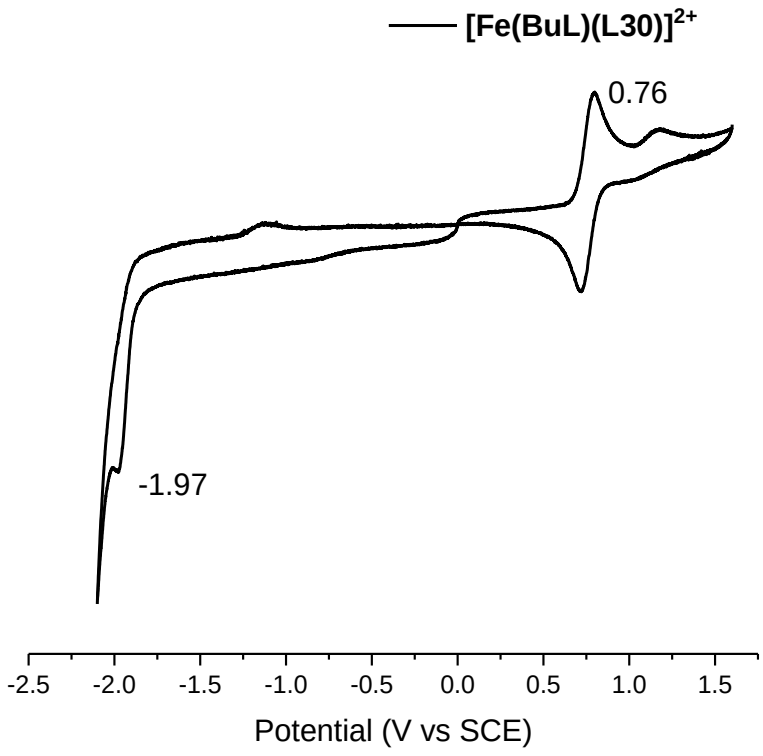

Cyclic voltammetry of complex **[Fe(BuL)(L30)]$^{2+}$**

VIII. References

References

(1) Nkabiti, L. L.; Baker, P. G. L. Earth Abundant Metals as Cost Effective Alternatives in Photocatalytic Applications: A Review. *Adv. Mater. Res.* **2020**, *1158*, 133–146. https://doi.org/10.4028/www.scientific.net/AMR.1158.133.

(2) Armaroli, N.; Balzani, V. The Legacy of Fossil Fuels. *Chem. - Asian J.* **2011**, *6* (3), 768–784. https://doi.org/10.1002/asia.201000797.

(3) Lieth, H.; Whittaker, R. H. *Primary Productivity of the Biosphere*; Ecological studies; Springer-Verlag: New York, 1975.

(4) c=AU; co=Commonwealth of Australia; ou=Department of Sustainability, E. *Space Weather Services website*. https://www.sws.bom.gov.au/Educational/2/1/12 (accessed 2022-09-06).

(5) Nazeeruddin, M. K.; Péchy, P.; Renouard, T.; Zakeeruddin, S. M.; Humphry-Baker, R.; Comte, P.; Liska, P.; Cevey, L.; Costa, E.; Shklover, V.; Spiccia, L.; Deacon, G. B.; Bignozzi, C. A.; Grätzel, M. Engineering of Efficient Panchromatic Sensitizers for Nanocrystalline TiO_2 -Based Solar Cells. *J. Am. Chem. Soc.* **2001**, *123* (8), 1613–1624. https://doi.org/10.1021/ja003299u.

(6) Tay, N. E. S.; Lehnherr, D.; Rovis, T. Photons or Electrons? A Critical Comparison of Electrochemistry and Photoredox Catalysis for Organic Synthesis. *Chem. Rev.* **2022**, *122* (2), 2487–2649. https://doi.org/10.1021/acs.chemrev.1c00384.

(7) Wu, Y.; Li, S.; Chen, Y.; He, W.; Guo, Z. Recent Advances in Noble Metal Complex Based Photodynamic Therapy. *Chem. Sci.* **2022**, *13* (18), 5085–5106. https://doi.org/10.1039/D1SC05478C.

(8) Zou, S.-J.; Shen, Y.; Xie, F.-M.; Chen, J.-D.; Li, Y.-Q.; Tang, J.-X. Recent Advances in Organic Light-Emitting Diodes: Toward Smart Lighting and Displays. *Mater. Chem. Front.* **2020**, *4* (3), 788–820. https://doi.org/10.1039/C9QM00716D.

(9) Mao, H.-T.; Li, G.-F.; Shan, G.-G.; Wang, X.-L.; Su, Z.-M. Recent Progress in Phosphorescent Ir(III) Complexes for Nondoped Organic Light-Emitting Diodes. *Coord. Chem. Rev.* **2020**, *413*, 213283. https://doi.org/10.1016/j.ccr.2020.213283.

(10) Grätzel, M. Solar Energy Conversion by Dye-Sensitized Photovoltaic Cells. *Inorg. Chem.* **2005**, *44* (20), 6841–6851. https://doi.org/10.1021/ic0508371.

(11) Arias-Rotondo, D. M.; McCusker, J. K. The Photophysics of Photoredox Catalysis: A Roadmap for Catalyst Design. *Chem. Soc. Rev.* **2016**, *45* (21), 5803–5820. https://doi.org/10.1039/C6CS00526H.

(12) *Rare Earth Elements—Critical Resources for High Technology | USGS Fact Sheet 087-02*. https://pubs.usgs.gov/fs/2002/fs087-02/ (accessed 2022-09-06).

(13) Izatt, R. M.; Izatt, S. R.; Bruening, R. L.; Izatt, N. E.; Moyer, B. A. Challenges to Achievement of Metal Sustainability in Our High-Tech Society. *Chem Soc Rev* **2014**, *43* (8), 2451–2475. https://doi.org/10.1039/C3CS60440C.

(14) Goldschmidt, V. M. The Principles of Distribution of Chemical Elements in Minerals and Rocks. The Seventh Hugo Müller Lecture, Delivered before the Chemical Society on March 17th, 1937. *J Chem Soc* **1937**, *0* (0), 655–673. https://doi.org/10.1039/JR9370000655.

(15) *Rare Earth Elements—Critical Resources for High Technology | USGS Fact Sheet 087-02*. https://pubs.usgs.gov/fs/2002/fs087-02/ (accessed 2022-09-19).

(16) *Ruthenium today | Precious Metals | SMM - China Metal Market*. https://www.metal.com/Other-Precious-Metals/201102250083 (accessed 2022-09-06).

(17) Graedel, T. E.; Harper, E. M.; Nassar, N. T.; Nuss, P.; Reck, B. K. Criticality of Metals and Metalloids. *Proc. Natl. Acad. Sci.* **2015**, *112* (14), 4257–4262. https://doi.org/10.1073/pnas.1500415112.
(18) Wenger, O. S. Photoactive Complexes with Earth-Abundant Metals. *J. Am. Chem. Soc.* **2018**, *140* (42), 13522–13533. https://doi.org/10.1021/jacs.8b08822.
(19) McCusker, J. K. Electronic Structure in the Transition Metal Block and Its Implications for Light Harvesting. *Science* **2019**, *363* (6426), 484–488. https://doi.org/10.1126/science.aav9104.
(20) Wegeberg, C.; Wenger, O. S. Luminescent First-Row Transition Metal Complexes. *JACS Au* **2021**, *1* (11), 1860–1876. https://doi.org/10.1021/jacsau.1c00353.
(21) Hauser, A.; Reber, C. Spectroscopy and Chemical Bonding in Transition Metal Complexes. In *50 Years of Structure and Bonding – The Anniversary Volume*; Mingos, D. M. P., Ed.; Structure and Bonding; Springer International Publishing: Cham, 2016; Vol. 172, pp 291–312. https://doi.org/10.1007/430_2015_195.
(22) Crosby, G. A. Spectroscopic Investigations of Excited States of Transition-Metal Complexes. *Acc. Chem. Res.* **1975**, *8* (7), 231–238. https://doi.org/10.1021/ar50091a003.
(23) Wagenknecht, P. S.; Ford, P. C. Metal Centered Ligand Field Excited States: Their Roles in the Design and Performance of Transition Metal Based Photochemical Molecular Devices. *Coord. Chem. Rev.* **2011**, *255* (5–6), 591–616. https://doi.org/10.1016/j.ccr.2010.11.016.
(24) Prier, C. K.; Rankic, D. A.; MacMillan, D. W. C. Visible Light Photoredox Catalysis with Transition Metal Complexes: Applications in Organic Synthesis. *Chem. Rev.* **2013**, *113* (7), 5322–5363. https://doi.org/10.1021/cr300503r.
(25) Cannizzo, A.; Milne, C. J.; Consani, C.; Gawelda, W.; Bressler, Ch.; van Mourik, F.; Chergui, M. Light-Induced Spin Crossover in Fe(II)-Based Complexes: The Full Photocycle Unraveled by Ultrafast Optical and X-Ray Spectroscopies. *Coord. Chem. Rev.* **2010**, *254* (21–22), 2677–2686. https://doi.org/10.1016/j.ccr.2009.12.007.
(26) Zhang, W.; Gaffney, K. J. Mechanistic Studies of Photoinduced Spin Crossover and Electron Transfer in Inorganic Complexes. *Acc. Chem. Res.* **2015**, *48* (4), 1140–1148. https://doi.org/10.1021/ar500407p.
(27) Auböck, G.; Chergui, M. Sub-50-Fs Photoinduced Spin Crossover in [Fe(Bpy)3]2+. *Nat. Chem.* **2015**, *7* (8), 629–633. https://doi.org/10.1038/nchem.2305.
(28) Liu, Y.; Harlang, T.; Canton, S. E.; Chábera, P.; Suárez-Alcántara, K.; Fleckhaus, A.; Vithanage, D. A.; Göransson, E.; Corani, A.; Lomoth, R.; Sundström, V.; Wärnmark, K. Towards Longer-Lived Metal-to-Ligand Charge Transfer States of Iron(Ii) Complexes: An N-Heterocyclic Carbene Approach. *Chem. Commun.* **2013**, *49* (57), 6412. https://doi.org/10.1039/c3cc43833c.
(29) Zhang, W.; Kjær, K. S.; Alonso-Mori, R.; Bergmann, U.; Chollet, M.; Fredin, L. A.; Hadt, R. G.; Hartsock, R. W.; Harlang, T.; Kroll, T.; Kubiček, K.; Lemke, H. T.; Liang, H. W.; Liu, Y.; Nielsen, M. M.; Persson, P.; Robinson, J. S.; Solomon, E. I.; Sun, Z.; Sokaras, D.; van Driel, T. B.; Weng, T.-C.; Zhu, D.; Wärnmark, K.; Sundström, V.; Gaffney, K. J. Manipulating Charge Transfer Excited State Relaxation and Spin Crossover in Iron Coordination Complexes with Ligand Substitution. *Chem. Sci.* **2017**, *8* (1), 515–523. https://doi.org/10.1039/C6SC03070J.
(30) Steube, J.; Burkhardt, L.; Päpcke, A.; Moll, J.; Zimmer, P.; Schoch, R.; Wölper, C.; Heinze, K.; Lochbrunner, S.; Bauer, M. Excited-State Kinetics of an Air-Stable Cyclometalated Iron(II) Complex. *Chem. – Eur. J.* **2019**, *25* (51), 11826–11830. https://doi.org/10.1002/chem.201902488.
(31) Liu, L.; Duchanois, T.; Etienne, T.; Monari, A.; Beley, M.; Assfeld, X.; Haacke, S.; Gros, P. C. A New Record Excited State ^{3} MLCT Lifetime for Metalorganic Iron(II) Complexes.

Phys. Chem. Chem. Phys. **2016**, *18* (18), 12550–12556. https://doi.org/10.1039/C6CP01418F.
(32) Carrillo, U.; Francés-Monerris, A.; Marri, A. R.; Cebrián, C.; Gros, P. C. Substituent-Induced Control of *Fac* / *Mer* Isomerism in Azine-NHC Fe(II) Complexes. *ACS Org. Inorg. Au* **2022**, acsorginorgau.2c00038. https://doi.org/10.1021/acsorginorgau.2c00038.
(33) Mengel, A. K. C.; Förster, C.; Breivogel, A.; Mack, K.; Ochsmann, J. R.; Laquai, F.; Ksenofontov, V.; Heinze, K. A Heteroleptic Push-Pull Substituted Iron(II) Bis(Tridentate) Complex with Low-Energy Charge-Transfer States. *Chem. - Eur. J.* **2015**, *21* (2), 704–714. https://doi.org/10.1002/chem.201404955.
(34) Medlycott, E. A.; Hanan, G. S. Designing Tridentate Ligands for Ruthenium(Ii) Complexes with Prolonged Room Temperature Luminescence Lifetimes. *Chem. Soc. Rev.* **2005**, *34* (2), 133. https://doi.org/10.1039/b316486c.
(35) Housecroft, C. E.; Sharpe, A. G. *Inorganic Chemistry: Solutions Manual*, 3. ed.; Pearson Education Limited: Edinburgh Gate Harlow Essex CM20 2JE England, 2008.
(36) Jamula, L. L.; Brown, A. M.; Guo, D.; McCusker, J. K. Synthesis and Characterization of a High-Symmetry Ferrous Polypyridyl Complex: Approaching the $^{5}T_{2}$ / $^{3}T_{1}$ Crossing Point for Fe^{II}. *Inorg. Chem.* **2014**, *53* (1), 15–17. https://doi.org/10.1021/ic402407k.
(37) Britz, A.; Gawelda, W.; Assefa, T. A.; Jamula, L. L.; Yarranton, J. T.; Galler, A.; Khakhulin, D.; Diez, M.; Harder, M.; Doumy, G.; March, A. M.; Bajnóczi, É.; Németh, Z.; Pápai, M.; Rozsályi, E.; Sárosiné Szemes, D.; Cho, H.; Mukherjee, S.; Liu, C.; Kim, T. K.; Schoenlein, R. W.; Southworth, S. H.; Young, L.; Jakubikova, E.; Huse, N.; Vankó, G.; Bressler, C.; McCusker, J. K. Using Ultrafast X-Ray Spectroscopy To Address Questions in Ligand-Field Theory: The Excited State Spin and Structure of $[Fe(Dcpp)_2]^{2+}$. *Inorg. Chem.* **2019**, *58* (14), 9341–9350. https://doi.org/10.1021/acs.inorgchem.9b01063.
(38) Mengel, A. K. C.; Förster, C.; Breivogel, A.; Mack, K.; Ochsmann, J. R.; Laquai, F.; Ksenofontov, V.; Heinze, K. A Heteroleptic Push-Pull Substituted Iron(II) Bis(Tridentate) Complex with Low-Energy Charge-Transfer States. *Chem. - Eur. J.* **2015**, *21* (2), 704–714. https://doi.org/10.1002/chem.201404955.
(39) Förster, C.; Dorn, M.; Reuter, T.; Otto, S.; Davarci, G.; Reich, T.; Carrella, L.; Rentschler, E.; Heinze, K. Ddpd as Expanded Terpyridine: Dramatic Effects of Symmetry and Electronic Properties in First Row Transition Metal Complexes. *Inorganics* **2018**, *6* (3), 86. https://doi.org/10.3390/inorganics6030086.
(40) Darari, M.; Francés-Monerris, A.; Marekha, B.; Doudouh, A.; Wenger, E.; Monari, A.; Haacke, S.; Gros, P. C. Towards Iron(II) Complexes with Octahedral Geometry: Synthesis, Structure and Photophysical Properties. *Molecules* **2020**, *25* (24), 5991. https://doi.org/10.3390/molecules25245991.
(41) Paulus, B. C.; Adelman, S. L.; Jamula, L. L.; McCusker, J. K. Leveraging Excited-State Coherence for Synthetic Control of Ultrafast Dynamics. *Nature* **2020**, *582* (7811), 214–218. https://doi.org/10.1038/s41586-020-2353-2.
(42) Bowman, D. N.; Bondarev, A.; Mukherjee, S.; Jakubikova, E. Tuning the Electronic Structure of Fe(II) Polypyridines via Donor Atom and Ligand Scaffold Modifications: A Computational Study. *Inorg. Chem.* **2015**, *54* (17), 8786–8793. https://doi.org/10.1021/acs.inorgchem.5b01409.
(43) Bourissou, D.; Guerret, O.; Gabbaï, F. P.; Bertrand, G. Stable Carbenes. *Chem. Rev.* **2000**, *100* (1), 39–92. https://doi.org/10.1021/cr940472u.
(44) Arduengo, A. J.; Davidson, F.; Dias, H. V. R.; Goerlich, J. R.; Khasnis, D.; Marshall, W. J.; Prakasha, T. K. An Air Stable Carbene and Mixed Carbene "Dimers." *J. Am. Chem. Soc.* **1997**, *119* (52), 12742–12749. https://doi.org/10.1021/ja973241o.
(45) Housecroft, C. E.; Sharpe, A. G. Inorganic Chemistry. 1297.

(46) Öfele, K. Nucleophilic Cyclic Carbenes as Complex Ligands on Transition Metals. *Angew. Chem. Int. Ed. Engl.* **1969**, *8* (11), 889–930. https://doi.org/10.1002/anie.196908891.
(47) Riener, K.; Haslinger, S.; Raba, A.; Högerl, M. P.; Cokoja, M.; Herrmann, W. A.; Kühn, F. E. Chemistry of Iron *N* -Heterocyclic Carbene Complexes: Syntheses, Structures, Reactivities, and Catalytic Applications. *Chem. Rev.* **2014**, *114* (10), 5215–5272. https://doi.org/10.1021/cr4006439.
(48) Fredin, L. A.; Pápai, M.; Rozsályi, E.; Vankó, G.; Wärnmark, K.; Sundström, V.; Persson, P. Exceptional Excited-State Lifetime of an Iron(II)– *N* -Heterocyclic Carbene Complex Explained. *J. Phys. Chem. Lett.* **2014**, *5* (12), 2066–2071. https://doi.org/10.1021/jz500829w.
(49) Lindh, L.; Chábera, P.; Rosemann, N. W.; Uhlig, J.; Wärnmark, K.; Yartsev, A.; Sundström, V.; Persson, P. Photophysics and Photochemistry of Iron Carbene Complexes for Solar Energy Conversion and Photocatalysis. *Catalysts* **2020**, *10* (3), 315. https://doi.org/10.3390/catal10030315.
(50) Duchanois, T.; Liu, L.; Pastore, M.; Monari, A.; Cebrián, C.; Trolez, Y.; Darari, M.; Magra, K.; Francés-Monerris, A.; Domenichini, E.; Beley, M.; Assfeld, X.; Haacke, S.; Gros, P. NHC-Based Iron Sensitizers for DSSCs. *Inorganics* **2018**, *6* (2), 63. https://doi.org/10.3390/inorganics6020063.
(51) Duchanois, T.; Etienne, T.; Cebrián, C.; Liu, L.; Monari, A.; Beley, M.; Assfeld, X.; Haacke, S.; Gros, P. C. An Iron-Based Photosensitizer with Extended Excited-State Lifetime: Photophysical and Photovoltaic Properties. *Eur. J. Inorg. Chem.* **2015**, *2015* (14), 2469–2477. https://doi.org/10.1002/ejic.201500142.
(52) Harlang, T. C. B.; Liu, Y.; Gordivska, O.; Fredin, L. A.; Ponseca, C. S.; Huang, P.; Chábera, P.; Kjaer, K. S.; Mateos, H.; Uhlig, J.; Lomoth, R.; Wallenberg, R.; Styring, S.; Persson, P.; Sundström, V.; Wärnmark, K. Iron Sensitizer Converts Light to Electrons with 92% Yield. *Nat. Chem.* **2015**, *7* (11), 883–889. https://doi.org/10.1038/nchem.2365.
(53) Marri, A. R.; Marchini, E.; Cabanes, V. D.; Argazzi, R.; Pastore, M.; Caramori, S.; Bignozzi, C. A.; Gros, P. C. A Series of Iron(II)-NHC Sensitizers with Remarkable Power Conversion Efficiency in Photoelectrochemical Cells**. *Chem. – Eur. J.* **2021**, *27* (65), 16260–16269. https://doi.org/10.1002/chem.202103178.
(54) Darari, M.; Domenichini, E.; Francés-Monerris, A.; Cebrián, C.; Magra, K.; Beley, M.; Pastore, M.; Monari, A.; Assfeld, X.; Haacke, S.; Gros, P. C. Iron(II) Complexes with Diazinyl-NHC Ligands: Impact of π-Deficiency of the Azine Core on Photophysical Properties. *Dalton Trans.* **2019**, *48* (29), 10915–10926. https://doi.org/10.1039/C9DT01731C.
(55) Zimmer, P.; Burkhardt, L.; Friedrich, A.; Steube, J.; Neuba, A.; Schepper, R.; Müller, P.; Flörke, U.; Huber, M.; Lochbrunner, S.; Bauer, M. The Connection between NHC Ligand Count and Photophysical Properties in Fe(II) Photosensitizers: An Experimental Study. *Inorg. Chem.* **2018**, *57* (1), 360–373. https://doi.org/10.1021/acs.inorgchem.7b02624.
(56) Reuter, T.; Kruse, A.; Schoch, R.; Lochbrunner, S.; Bauer, M.; Heinze, K. Higher MLCT Lifetime of Carbene Iron(II) Complexes by Chelate Ring Expansion. *Chem. Commun.* **2021**, *57* (61), 7541–7544. https://doi.org/10.1039/D1CC02173G.
(57) Schweinfurth, D.; Hettmanczyk, L.; Suntrup, L.; Sarkar, B. Metal Complexes of Click-Derived Triazoles and Mesoionic Carbenes: Electron Transfer, Photochemistry, Magnetic Bistability, and Catalysis: Metal Complexes of Click-Derived Triazoles and Mesoionic Carbenes: Electron Transfer, Photochemistry, Magnetic Bistability, and Catalysis. *Z. Für Anorg. Allg. Chem.* **2017**, *643* (9), 554–584. https://doi.org/10.1002/zaac.201700030.
(58) Brown, D. G.; Sanguantrakun, N.; Schulze, B.; Schubert, U. S.; Berlinguette, C. P. Bis(Tridentate) Ruthenium–Terpyridine Complexes Featuring Microsecond Excited-

State Lifetimes. *J. Am. Chem. Soc.* **2012**, *134* (30), 12354–12357. https://doi.org/10.1021/ja3039536.
(59) Araki, S.; Wanibe, Y.; Uno, F.; Morikawa, A.; Yamamoto, K.; Chiba, K.; Butsugan, Y. Synthesis and Chemical Transformations of 1,3-Diaryltetrazolium Salts. Preparation of Mercury(II) and Palladium(II) Complexes of 1,3-Diaryltetrazolylene and Reactions of 5-Substituted 1,3-Diphenyltetrazolium Salts with Nucleophiles. *Chem. Ber.* **1993**, *126* (5), 1149–1155. https://doi.org/10.1002/cber.19931260514.
(60) Liu, Y.; Kjaer, K. S.; Fredin, L. A.; Chábera, P.; Harlang, T.; Canton, S. E.; Lidin, S.; Zhang, J.; Lomoth, R.; Bergquist, K.-E.; Persson, P.; Wärnmark, K.; Sundström, V. A Heteroleptic Ferrous Complex with Mesoionic Bis(1,2,3-Triazol-5-Ylidene) Ligands: Taming the MLCT Excited State of Iron(II). *Chem. - Eur. J.* **2015**, *21* (9), 3628–3639. https://doi.org/10.1002/chem.201405184.
(61) Chábera, P.; Kjaer, K. S.; Prakash, O.; Honarfar, A.; Liu, Y.; Fredin, L. A.; Harlang, T. C. B.; Lidin, S.; Uhlig, J.; Sundström, V.; Lomoth, R.; Persson, P.; Wärnmark, K. Fe ^{II} Hexa *N* -Heterocyclic Carbene Complex with a 528 Ps Metal-to-Ligand Charge-Transfer Excited-State Lifetime. *J. Phys. Chem. Lett.* **2018**, *9* (3), 459–463. https://doi.org/10.1021/acs.jpclett.7b02962.
(62) Dierks, P.; Kruse, A.; Bokareva, O. S.; Al-Marri, M. J.; Kalmbach, J.; Baltrun, M.; Neuba, A.; Schoch, R.; Hohloch, S.; Heinze, K.; Seitz, M.; Kühn, O.; Lochbrunner, S.; Bauer, M. Distinct Photodynamics of κ-N and κ-C Pseudoisomeric Iron(II) Complexes. *Chem. Commun.* **2021**, *57* (54), 6640–6643. https://doi.org/10.1039/D1CC01716K.
(63) Wang, X.; Del Guerzo, A.; Schmehl, R. H. Photophysical Behavior of Transition Metal Complexes Having Interacting Ligand Localized and Metal-to-Ligand Charge Transfer States. *J. Photochem. Photobiol. C Photochem. Rev.* **2004**, *5* (1), 55–77. https://doi.org/10.1016/j.jphotochemrev.2004.01.002.
(64) Castellano, F. N. Altering Molecular Photophysics by Merging Organic and Inorganic Chromophores. *Acc. Chem. Res.* **2015**, *48* (3), 828–839. https://doi.org/10.1021/ar500385e.
(65) Leydet, Y.; Bassani, D. M.; Jonusauskas, G.; McClenaghan, N. D. Equilibration between Three Different Excited States in a Bichromophoric Copper(I) Polypyridine Complex. *J. Am. Chem. Soc.* **2007**, *129* (28), 8688–8689. https://doi.org/10.1021/ja072335n.
(66) Francés-Monerris, A.; Gros, P. C.; Pastore, M.; Assfeld, X.; Monari, A. Photophysical Properties of Bichromophoric Fe(II) Complexes Bearing an Aromatic Electron Acceptor. *Theor. Chem. Acc.* **2019**, *138* (7), 86. https://doi.org/10.1007/s00214-019-2471-9.
(67) Dierks, P.; Päpcke, A.; Bokareva, O. S.; Altenburger, B.; Reuter, T.; Heinze, K.; Kühn, O.; Lochbrunner, S.; Bauer, M. Ground- and Excited-State Properties of Iron(II) Complexes Linked to Organic Chromophores. *Inorg. Chem.* **2020**, *59* (20), 14746–14761. https://doi.org/10.1021/acs.inorgchem.0c02039.
(68) Dixon, I. M.; Alary, F.; Boggio-Pasqua, M.; Heully, J.-L. Reversing the Relative ^{3} MLCT– ^{3} MC Order in Fe(II) Complexes Using Cyclometallating Ligands: A Computational Study Aiming at Luminescent Fe(II) Complexes. *Dalton Trans.* **2015**, *44* (30), 13498–13503. https://doi.org/10.1039/C5DT01214G.
(69) Leis, W.; Argüello Cordero, M. A.; Lochbrunner, S.; Schubert, H.; Berkefeld, A. A Photoreactive Iron(II) Complex Luminophore. *J. Am. Chem. Soc.* **2022**, *144* (3), 1169–1173. https://doi.org/10.1021/jacs.1c13083.
(70) Mukherjee, S.; Torres, D. E.; Jakubikova, E. HOMO Inversion as a Strategy for Improving the Light-Absorption Properties of Fe(II) Chromophores. *Chem. Sci.* **2017**, *8* (12), 8115–8126. https://doi.org/10.1039/C7SC02926H.

(71) Marri, A. R.; Marekha, B.; Penfold, T.; Haacke, S.; Gros, P. C. Towards Panchromatic Fe(II) NHC Sensitizers *via* HOMO Inversion. *Inorg. Chem. Front.* **2022**, 10.1039.D2QI01903E. https://doi.org/10.1039/D2QI01903E.
(72) Braun, J. D.; Lozada, I. B.; Kolodziej, C.; Burda, C.; Newman, K. M. E.; van Lierop, J.; Davis, R. L.; Herbert, D. E. Iron(II) Coordination Complexes with Panchromatic Absorption and Nanosecond Charge-Transfer Excited State Lifetimes. *Nat. Chem.* **2019**, *11* (12), 1144–1150. https://doi.org/10.1038/s41557-019-0357-z.
(73) Büldt, L. A.; Guo, X.; Vogel, R.; Prescimone, A.; Wenger, O. S. A Tris(Diisocyanide)Chromium(0) Complex Is a Luminescent Analog of Fe(2,2′-Bipyridine)$_3^{2+}$. *J. Am. Chem. Soc.* **2017**, *139* (2), 985–992. https://doi.org/10.1021/jacs.6b11803.
(74) Büldt, L. A.; Guo, X.; Prescimone, A.; Wenger, O. S. A Molybdenum(0) Isocyanide Analogue of Ru(2,2′-Bipyridine)$_3^{2+}$: A Strong Reductant for Photoredox Catalysis. *Angew. Chem. Int. Ed.* **2016**, *55* (37), 11247–11250. https://doi.org/10.1002/anie.201605571.
(75) Herr, P.; Kerzig, C.; Larsen, C. B.; Häussinger, D.; Wenger, O. S. Manganese(i) Complexes with Metal-to-Ligand Charge Transfer Luminescence and Photoreactivity. *Nat. Chem.* **2021**, *13* (10), 956–962. https://doi.org/10.1038/s41557-021-00744-9.
(76) Pal, A. K.; Li, C.; Hanan, G. S.; Zysman-Colman, E. Blue-Emissive Cobalt(III) Complexes and Their Use in the Photocatalytic Trifluoromethylation of Polycyclic Aromatic Hydrocarbons. *Angew. Chem. Int. Ed.* **2018**, *57* (27), 8027–8031. https://doi.org/10.1002/anie.201802532.
(77) Kaufhold, S.; Rosemann, N. W.; Chábera, P.; Lindh, L.; Bolaño Losada, I.; Uhlig, J.; Pascher, T.; Strand, D.; Wärnmark, K.; Yartsev, A.; Persson, P. Microsecond Photoluminescence and Photoreactivity of a Metal-Centered Excited State in a Hexacarbene–Co(III) Complex. *J. Am. Chem. Soc.* **2021**, *143* (3), 1307–1312. https://doi.org/10.1021/jacs.0c12151.
(78) Chábera, P.; Lindh, L.; Rosemann, N. W.; Prakash, O.; Uhlig, J.; Yartsev, A.; Wärnmark, K.; Sundström, V.; Persson, P. Photofunctionality of Iron(III) N-Heterocyclic Carbenes and Related d Transition Metal Complexes. *Coord. Chem. Rev.* **2021**, *426*, 213517. https://doi.org/10.1016/j.ccr.2020.213517.
(79) Chábera, P.; Liu, Y.; Prakash, O.; Thyrhaug, E.; Nahhas, A. E.; Honarfar, A.; Essén, S.; Fredin, L. A.; Harlang, T. C. B.; Kjær, K. S.; Handrup, K.; Ericson, F.; Tatsuno, H.; Morgan, K.; Schnadt, J.; Häggström, L.; Ericsson, T.; Sobkowiak, A.; Lidin, S.; Huang, P.; Styring, S.; Uhlig, J.; Bendix, J.; Lomoth, R.; Sundström, V.; Persson, P.; Wärnmark, K. A Low-Spin Fe(Iii) Complex with 100-Ps Ligand-to-Metal Charge Transfer Photoluminescence. *Nature* **2017**, *543* (7647), 695–699. https://doi.org/10.1038/nature21430.
(80) Kjær, K. S.; Kaul, N.; Prakash, O.; Chábera, P.; Rosemann, N. W.; Honarfar, A.; Gordivska, O.; Fredin, L. A.; Bergquist, K.-E.; Häggström, L.; Ericsson, T.; Lindh, L.; Yartsev, A.; Styring, S.; Huang, P.; Uhlig, J.; Bendix, J.; Strand, D.; Sundström, V.; Persson, P.; Lomoth, R.; Wärnmark, K. Luminescence and Reactivity of a Charge-Transfer Excited Iron Complex with Nanosecond Lifetime. *Science* **2019**, *363* (6424), 249–253. https://doi.org/10.1126/science.aau7160.
(81) Rosemann, N. W.; Chábera, P.; Prakash, O.; Kaufhold, S.; Wärnmark, K.; Yartsev, A.; Persson, P. Tracing the Full Bimolecular Photocycle of Iron(III)–Carbene Light Harvesters in Electron-Donating Solvents. *J. Am. Chem. Soc.* **2020**, *142* (19), 8565–8569. https://doi.org/10.1021/jacs.0c00755.
(82) Aydogan, A.; Bangle, R. E.; Cadranel, A.; Turlington, M. D.; Conroy, D. T.; Cauët, E.; Singleton, M. L.; Meyer, G. J.; Sampaio, R. N.; Elias, B.; Troian-Gautier, L. Accessing

Photoredox Transformations with an Iron(III) Photosensitizer and Green Light. *J. Am. Chem. Soc.* **2021**, *143* (38), 15661–15673. https://doi.org/10.1021/jacs.1c06081.
(83) Muñoz-García, A. B.; Benesperi, I.; Boschloo, G.; Concepcion, J. J.; Delcamp, J. H.; Gibson, E. A.; Meyer, G. J.; Pavone, M.; Pettersson, H.; Hagfeldt, A.; Freitag, M. Dye-Sensitized Solar Cells Strike Back. *Chem. Soc. Rev.* **2021**, *50* (22), 12450–12550. https://doi.org/10.1039/D0CS01336F.
(84) O'Regan, B.; Gratzelt, M. A Low-Cost, High-Efficiency Solar Cell Based on Dye-Sensitized Colloidal Ti02 Films. *Nat.* **1991**, *353*, 4.
(85) Zhang, D.; Stojanovic, M.; Ren, Y.; Cao, Y.; Eickemeyer, F. T.; Socie, E.; Vlachopoulos, N.; Moser, J.-E.; Zakeeruddin, S. M.; Hagfeldt, A.; Grätzel, M. A Molecular Photosensitizer Achieves a Voc of 1.24 V Enabling Highly Efficient and Stable Dye-Sensitized Solar Cells with Copper(II/I)-Based Electrolyte. *Nat. Commun.* **2021**, *12* (1), 1777. https://doi.org/10.1038/s41467-021-21945-3.
(86) Hagfeldt, A.; Boschloo, G.; Sun, L.; Kloo, L.; Pettersson, H. Dye-Sensitized Solar Cells. *Chem. Rev.* **2010**, *110* (11), 6595–6663. https://doi.org/10.1021/cr900356p.
(87) Nazeeruddin, M. K.; Kay, A.; Rodicio, I.; Humphry-Baker, R.; Mueller, E.; Liska, P.; Vlachopoulos, N.; Graetzel, M. Conversion of Light to Electricity by Cis-X2bis(2,2'-Bipyridyl-4,4'-Dicarboxylate)Ruthenium(II) Charge-Transfer Sensitizers (X = Cl-, Br-, I-, CN-, and SCN-) on Nanocrystalline Titanium Dioxide Electrodes. *J. Am. Chem. Soc.* **1993**, *115* (14), 6382–6390. https://doi.org/10.1021/ja00067a063.
(88) Nazeeruddin, M. K.; De Angelis, F.; Fantacci, S.; Selloni, A.; Viscardi, G.; Liska, P.; Ito, S.; Takeru, B.; Grätzel, M. Combined Experimental and DFT-TDDFT Computational Study of Photoelectrochemical Cell Ruthenium Sensitizers. *J. Am. Chem. Soc.* **2005**, *127* (48), 16835–16847. https://doi.org/10.1021/ja052467l.
(89) Sekar, N.; Gehlot, V. Y. Metal Complex Dyes for Dye-Sensitized Solar Cells: Recent Developments. *Resonance* **2010**, *15* (9), 819–831. https://doi.org/10.1007/s12045-010-0091-8.
(90) Kokkonen, M.; Talebi, P.; Zhou, J.; Asgari, S.; Soomro, S. A.; Elsehrawy, F.; Halme, J.; Ahmad, S.; Hagfeldt, A.; Hashmi, S. G. Advanced Research Trends in Dye-Sensitized Solar Cells. *J. Mater. Chem. A* **2021**, *9* (17), 10527–10545. https://doi.org/10.1039/D1TA00690H.
(91) Park, S.-H.; Lim, J.; Song, I. Y.; Atmakuri, N.; Song, S.; Kwon, Y. S.; Choi, J. M.; Park, T. Stable Dye-Sensitized Solar Cells by Encapsulation of N719-Sensitized TiO2 Electrodes Using Surface-Induced Cross-Linking Polymerization. *Adv. Energy Mater.* **2012**, *2* (2), 219–224. https://doi.org/10.1002/aenm.201100533.
(92) Stengel, I.; Pootrakulchote, N.; Dykeman, R. R.; Mishra, A.; Zakeeruddin, S. M.; Dyson, P. J.; Grätzel, M.; Bäuerle, P. Click-Functionalized Ru(II) Complexes for Dye-Sensitized Solar Cells. *Adv. Energy Mater.* **2012**, *2* (8), 1004–1012. https://doi.org/10.1002/aenm.201100722.
(93) Huang, W.-K.; Wu, H.-P.; Lin, P.-L.; Diau, E. W.-G. Design and Characterization of Heteroleptic Ruthenium Complexes Containing Benzimidazole Ligands for Dye-Sensitized Solar Cells: The Effect of Thiophene and Alkyl Substituents on Photovoltaic Performance. *J. Phys. Chem. C* **2013**, *117* (5), 2059–2065. https://doi.org/10.1021/jp3118693.
(94) Marchini, E.; Darari, M.; Lazzarin, L.; Boaretto, R.; Argazzi, R.; Bignozzi, C. A.; Gros, P. C.; Caramori, S. Recombination and Regeneration Dynamics in FeNHC(II)-Sensitized Solar Cells. *Chem. Commun.* **2020**, *56* (4), 543–546. https://doi.org/10.1039/C9CC07794D.
(95) Pastore, M.; Duchanois, T.; Liu, L.; Monari, A.; Assfeld, X.; Haacke, S.; Gros, P. C. Interfacial Charge Separation and Photovoltaic Efficiency in Fe(II)–Carbene Sensitized

Solar Cells. *Phys. Chem. Chem. Phys.* **2016**, *18* (40), 28069–28081. https://doi.org/10.1039/C6CP05535D.
(96) Lindh, L.; Gordivska, O.; Persson, S.; Michaels, H.; Fan, H.; Chábera, P.; Rosemann, N. W.; Gupta, A. K.; Benesperi, I.; Uhlig, J.; Prakash, O.; Sheibani, E.; Kjaer, K. S.; Boschloo, G.; Yartsev, A.; Freitag, M.; Lomoth, R.; Persson, P.; Wärnmark, K. Dye-Sensitized Solar Cells Based on Fe N-Heterocyclic Carbene Photosensitizers with Improved Rod-like Push-Pull Functionality. *Chem. Sci.* **2021**, *12* (48), 16035–16053. https://doi.org/10.1039/D1SC02963K.
(97) Hockin, B. M.; Li, C.; Robertson, N.; Zysman-Colman, E. Photoredox Catalysts Based on Earth-Abundant Metal Complexes. *Catal. Sci. Technol.* **2019**, *9* (4), 889–915. https://doi.org/10.1039/C8CY02336K.
(98) Kalyanasundaram, K. Photophysics, Photochemistry and Solar Energy Conversion with Tris(Bipyridyl)Ruthenium(II) and Its Analogues. *Coord. Chem. Rev.* **1982**, *46*, 159–244. https://doi.org/10.1016/0010-8545(82)85003-0.
(99) Dixon, I. M.; Collin, J.-P.; Sauvage, J.-P.; Flamigni, L.; Encinas, S.; Barigelletti, F. A Family of Luminescent Coordination Compounds: Iridium(III) Polyimine Complexes. *Chem. Soc. Rev.* **2000**, *29* (6), 385–391. https://doi.org/10.1039/b000704h.
(100) Twilton, J.; Le, C.; Zhang, P.; Shaw, M. H.; Evans, R. W.; MacMillan, D. W. C. The Merger of Transition Metal and Photocatalysis. *Nat. Rev. Chem.* **2017**, *1* (7), 0052. https://doi.org/10.1038/s41570-017-0052.
(101) Pavlishchuk, V. V.; Addison, A. W. Conversion Constants for Redox Potentials Measured versus Different Reference Electrodes in Acetonitrile Solutions at 25°C. *Inorganica Chim. Acta* **2000**, *298* (1), 97–102. https://doi.org/10.1016/S0020-1693(99)00407-7.
(102) Ye, Y.; Sanford, M. S. Merging Visible-Light Photocatalysis and Transition-Metal Catalysis in the Copper-Catalyzed Trifluoromethylation of Boronic Acids with CF_3I. *J. Am. Chem. Soc.* **2012**, *134* (22), 9034–9037. https://doi.org/10.1021/ja301553c.
(103) Ilic, A.; Schwarz, J.; Johnson, C.; de Groot, L. H. M.; Kaufhold, S.; Lomoth, R.; Wärnmark, K. Photoredox Catalysis *via* Consecutive ^{2}LMCT- and ^{3}MLCT-Excitation of an Fe(III / II)–N-Heterocyclic Carbene Complex. *Chem. Sci.* **2022**, *13* (32), 9165–9175. https://doi.org/10.1039/D2SC02122F.
(104) Zhou, W.; Wu, X.; Miao, M.; Wang, Z.; Chen, L.; Shan, S.; Cao, G.; Yu, D. Light Runs Across Iron Catalysts in Organic Transformations. *Chem. – Eur. J.* **2020**, *26* (66), 15052–15064. https://doi.org/10.1002/chem.202000508.
(105) McKenzie, L. K.; Bryant, H. E.; Weinstein, J. A. Transition Metal Complexes as Photosensitisers in One- and Two-Photon Photodynamic Therapy. *Coord. Chem. Rev.* **2019**, *379*, 2–29. https://doi.org/10.1016/j.ccr.2018.03.020.
(106) Baggaley, E.; Weinstein, J. A.; Williams, J. A. G. Lighting the Way to See inside the Live Cell with Luminescent Transition Metal Complexes. *Coord. Chem. Rev.* **2012**, *256* (15–16), 1762–1785. https://doi.org/10.1016/j.ccr.2012.03.018.
(107) Sherlock, B.; Warren, S. C.; Alexandrov, Y.; Yu, F.; Stone, J.; Knight, J.; Neil, M. A. A.; Paterson, C.; French, P. M. W.; Dunsby, C. In Vivo Multiphoton Microscopy Using a Handheld Scanner with Lateral and Axial Motion Compensation. *J. Biophotonics* **2018**, *11* (2), e201700131. https://doi.org/10.1002/jbio.201700131.
(108) Abrahamse, H.; Hamblin, M. R. New Photosensitizers for Photodynamic Therapy. *Biochem. J.* **2016**, *473* (4), 347–364. https://doi.org/10.1042/BJ20150942.
(109) Knoll, J. D.; Turro, C. Control and Utilization of Ruthenium and Rhodium Metal Complex Excited States for Photoactivated Cancer Therapy. *Coord. Chem. Rev.* **2015**, *282–283*, 110–126. https://doi.org/10.1016/j.ccr.2014.05.018.

(110) Mari, C.; Pierroz, V.; Ferrari, S.; Gasser, G. Combination of Ru(II) Complexes and Light: New Frontiers in Cancer Therapy. *Chem. Sci.* **2015**, *6* (5), 2660–2686. https://doi.org/10.1039/C4SC03759F.
(111) Arenas, Y.; Monro, S.; Shi, G.; Mandel, A.; McFarland, S.; Lilge, L. Photodynamic Inactivation of Staphylococcus Aureus and Methicillin-Resistant Staphylococcus Aureus with Ru(II)-Based Type I/Type II Photosensitizers. *Photodiagnosis Photodyn. Ther.* **2013**, *10* (4), 615–625. https://doi.org/10.1016/j.pdpdt.2013.07.001.
(112) Fong, J.; Kasimova, K.; Arenas, Y.; Kaspler, P.; Lazic, S.; Mandel, A.; Lilge, L. A Novel Class of Ruthenium-Based Photosensitizers Effectively Kills in Vitro Cancer Cells and in Vivo Tumors. *Photochem. Photobiol. Sci.* **2015**, *14* (11), 2014–2023. https://doi.org/10.1039/C4PP00438H.
(113) Dabb, S. L.; Fletcher, N. C. Mer and Fac Isomerism in Tris Chelate Diimine Metal Complexes. *Dalton Trans.* **2015**, *44* (10), 4406–4422. https://doi.org/10.1039/C4DT03535F.
(114) Yun, B.-S.; Kim, S.-Y.; Kim, J.-H.; Son, H.-J.; Kang, S. O. Homoleptic Cyclometalated Dibenzothiophene–NHC–Iridium(III) Complexes for Efficient Blue Phosphorescent Organic Light-Emitting Diodes. *J. Mater. Chem. C* **2021**, *9* (11), 4062–4069. https://doi.org/10.1039/D0TC05832G.
(115) Cooke, G.; Ó Máille, G. M.; Quesada, R.; Wang, L.; Varughese, S.; Draper, S. M. Substituted Pyridazines as Ligands in Homoleptic (Fac and Mer) and Heteroleptic Ru(Ii) Complexes. *Dalton Trans.* **2011**, *40* (32), 8206. https://doi.org/10.1039/c1dt10340g.
(116) Magra, K.; Francés-Monerris, A.; Cebrián, C.; Monari, A.; Haacke, S.; Gros, P. C. Bidentate Pyridyl-NHC Ligands: Synthesis, Ground and Excited State Properties of Their Iron(II) Complexes and the Role of the Fac/Mer Isomerism. *Eur J Inorg Chem* **2021**, 1–15. https://doi.org/10.1002/ejic.202100818.
(117) Lathion, T.; Guénée, L.; Besnard, C.; Bousseksou, A.; Piguet, C. Deciphering the Influence of Meridional versus Facial Isomers in Spin Crossover Complexes. *Chem. – Eur. J.* **2018**, *24* (63), 16873–16888. https://doi.org/10.1002/chem.201804161.
(118) Tamayo, A. B.; Alleyne, B. D.; Djurovich, P. I.; Lamansky, S.; Tsyba, I.; Ho, N. N.; Bau, R.; Thompson, M. E. Synthesis and Characterization of Facial and Meridional Tris-Cyclometalated Iridium(III) Complexes. *J. Am. Chem. Soc.* **2003**, *125* (24), 7377–7387. https://doi.org/10.1021/ja034537z.
(119) Lee, J.; Chen, H.-F.; Batagoda, T.; Coburn, C.; Djurovich, P. I.; Thompson, M. E.; Forrest, S. R. Deep Blue Phosphorescent Organic Light-Emitting Diodes with Very High Brightness and Efficiency. *Nat. Mater.* **2016**, *15* (1), 92–98. https://doi.org/10.1038/nmat4446.
(120) Ehnbom, A.; Ghosh, S. K.; Lewis, K. G.; Gladysz, J. A. Octahedral Werner Complexes with Substituted Ethylenediamine Ligands: A Stereochemical Primer for a Historic Series of Compounds Now Emerging as a Modern Family of Catalysts. *Chem. Soc. Rev.* **2016**, *45* (24), 6799–6811. https://doi.org/10.1039/C6CS00604C.
(121) Shopov, D. Y.; Rudshteyn, B.; Campos, J.; Batista, V. S.; Crabtree, R. H.; Brudvig, G. W. Stable Iridium(IV) Complexes of an Oxidation-Resistant Pyridine-Alkoxide Ligand: Highly Divergent Redox Properties Depending on the Isomeric Form Adopted. *J. Am. Chem. Soc.* **2015**, *137* (22), 7243–7250. https://doi.org/10.1021/jacs.5b04185.
(122) Metherell, A. J.; Cullen, W.; Stephenson, A.; Hunter, C. A.; Ward, M. D. Fac and Mer Isomers of Ru(II) Tris(Pyrazolyl-Pyridine) Complexes as Models for the Vertices of Coordination Cages: Structural Characterisation and Hydrogen-Bonding Characteristics. *Dalton Trans* **2014**, *43* (1), 71–84. https://doi.org/10.1039/C3DT52479E.

(123) Morozumi, T.; Matsuoka, R.; Nakamura, T.; Nabeshima, T. Solvent-Dependent *Fac* / *Mer* -Isomerization and Self-Assembly of Triply Helical Complexes Bearing a Pivot Part. *Chem. Sci.* **2021**, *12* (22), 7720–7726. https://doi.org/10.1039/D1SC01529J.
(124) Kieffer, M.; Pilgrim, B. S.; Ronson, T. K.; Roberts, D. A.; Aleksanyan, M.; Nitschke, J. R. Perfluorinated Ligands Induce Meridional Metal Stereochemistry to Generate M_8L_{12}, $M_{10}L_{15}$, and $M_{12}L_{18}$ prisms. *J. Am. Chem. Soc.* **2016**, *138* (21), 6813–6821. https://doi.org/10.1021/jacs.6b02445.
(125) Yu. Gitlina, A.; Fadaei-Tirani, F.; Ruggi, A.; Plaice, C.; Severin, K. Acid-Base-Induced *Fac* → *Mer* Isomerization of Luminescent Iridium(III) Complexes. *Chem. Sci.* **2022**, *13* (35), 10370–10374. https://doi.org/10.1039/D2SC02808E.
(126) Coe, B. J.; Glenwright, S. J. Trans-Effects in Octahedral Transition Metal Complexes. *Coord. Chem. Rev.* **2000**, *203* (1), 5–80. https://doi.org/10.1016/S0010-8545(99)00184-8.
(127) Dabb, S. L.; Fletcher, N. C. Mer and Fac Isomerism in Tris Chelate Diimine Metal Complexes. *Dalton Trans.* **2015**, *44* (10), 4406–4422. https://doi.org/10.1039/C4DT03535F.
(128) Howson, S. E.; Allan, L. E. N.; Chmel, N. P.; Clarkson, G. J.; Deeth, R. J.; Faulkner, A. D.; Simpson, D. H.; Scott, P. Origins of Stereoselectivity in Optically Pure Phenylethaniminopyridine Tris-Chelates $M(NN')_3^{n+}$ (M = Mn, Fe, Co, Ni and Zn). *Dalton Trans.* **2011**, *40* (40), 10416. https://doi.org/10.1039/c1dt10588d.
(129) Zysman-Colman, E.; Denis, C. Inorganic and Organometallic Hemicage Podates and Cage Cryptates Incorporating a Benzene Platform. *Coord. Chem. Rev.* **2012**, *256* (15–16), 1742–1761. https://doi.org/10.1016/j.ccr.2012.02.001.
(130) Ruggi, A.; Berenguel Alonso, M.; Reinhoudt, D. N.; Velders, A. H. An Iridium(III)-Caged Complex with Low Oxygen Quenching. *Chem. Commun.* **2010**, *46* (36), 6726. https://doi.org/10.1039/c0cc01178a.
(131) Weizman, H.; Libman, J.; Shanzer, A. A Novel Template Method for Preparing Unidirectional Kinetically Inert Metal Complexes. *J. Am. Chem. Soc.* **1998**, *120* (9), 2188–2189. https://doi.org/10.1021/ja973605c.
(132) Hardie, M. J.; Kilner, C. A.; Halcrow, M. A. {Tris[4-(1 *H* -Pyrazol-3-Yl)-3-Azabut-3-Enyl]Amine}iron(II) Diperchlorate Monohydrate. *Acta Crystallogr. C* **2004**, *60* (4), m177–m179. https://doi.org/10.1107/S010827010400407X.
(133) Francés-Monerris, A.; Magra, K.; Darari, M.; Cebrián, C.; Beley, M.; Domenichini, E.; Haacke, S.; Pastore, M.; Assfeld, X.; Gros, P. C.; Monari, A. Synthesis and Computational Study of a Pyridylcarbene Fe(II) Complex: Unexpected Effects of *Fac* / *Mer* Isomerism in Metal-to-Ligand Triplet Potential Energy Surfaces. *Inorg. Chem.* **2018**, *57* (16), 10431–10441. https://doi.org/10.1021/acs.inorgchem.8b01695.
(134) Francés-Monerris, A.; Magra, K.; Darari, M.; Cebrián, C.; Beley, M.; Domenichini, E.; Haacke, S.; Pastore, M.; Assfeld, X.; Gros, P. C.; Monari, A. Synthesis and Computational Study of a Pyridylcarbene Fe(II) Complex: Unexpected Effects of *Fac* / *Mer* Isomerism in Metal-to-Ligand Triplet Potential Energy Surfaces. *Inorg. Chem.* **2018**, *57* (16), 10431–10441. https://doi.org/10.1021/acs.inorgchem.8b01695.
(135) Magra, K.; Domenichini, E.; Francés-Monerris, A.; Cebrián, C.; Beley, M.; Darari, M.; Pastore, M.; Monari, A.; Assfeld, X.; Haacke, S.; Gros, P. C. Impact of the *Fac* / *Mer* Isomerism on the Excited-State Dynamics of Pyridyl-Carbene Fe(II) Complexes. *Inorg. Chem.* **2019**, *58* (8), 5069–5081. https://doi.org/10.1021/acs.inorgchem.9b00138.
(136) Magra, K.; Darari, M.; Domenichini, E.; Francés-Monerris, A.; Cebrián, C.; Beley, M.; Pastore, M.; Monari, A.; Assfeld, X.; Haacke, S.; Gros, P. C. Photophysical Investigation of Iron(II) Complexes Bearing Bidentate Annulated Isomeric Pyridine-NHC Ligands. *J. Phys. Chem. C* **2020**, *124* (34), 18379–18389. https://doi.org/10.1021/acs.jpcc.0c03638.

(137) Magra, K. PhD thesis, university of Lorraine (France), 2019.
(138) Setzer, T.; Lennartz, C.; Dreuw, A. A Theoretical Study on the Mechanistic Highlights behind the Brønsted-Acid Dependent Mer–Fac Isomerization of Homoleptic Carbenic Iridium Complexes for PhOLEDs. *Dalton Trans.* **2017**, *46* (22), 7194–7209. https://doi.org/10.1039/C7DT01201B.
(139) Wu, B.-H.; Huang, M.-J.; Lai, C.-C.; Cheng, C.-H.; Chen, I.-C. Isomerization Reaction of *Mer* - to *Fac* -Tris(2-Phenylpyridinato-N,C2′)Iridium(III) Monitored by Using Surface-Enhanced Raman Spectroscopy. *Inorg. Chem.* **2018**, *57* (8), 4448–4455. https://doi.org/10.1021/acs.inorgchem.8b00113.
(140) Magra, K.; Darari, M.; Domenichini, E.; Francés-Monerris, A.; Cebrián, C.; Beley, M.; Pastore, M.; Monari, A.; Assfeld, X.; Haacke, S.; Gros, P. C. Photophysical Investigation of Iron(II) Complexes Bearing Bidentate Annulated Isomeric Pyridine-NHC Ligands. *J. Phys. Chem. C* **2020**, *124* (34), 18379–18389. https://doi.org/10.1021/acs.jpcc.0c03638.
(141) Hong, Y.; Jarrige, L.; Harms, K.; Meggers, E. Chiral-at-Iron Catalyst: Expanding the Chemical Space for Asymmetric Earth-Abundant Metal Catalysis. *J. Am. Chem. Soc.* **2019**, *141* (11), 4569–4572. https://doi.org/10.1021/jacs.9b01352.
(142) Onggo, D.; Hook, J. M.; Rae, A. D.; Goodwin, H. A. The Influence of Steric Effects in Substituted 2,2'-Bipyridine on the Spin State of Iron(U) in [FeNJ*+ Systems. 12.
(143) Zang, Y.; Kim, J.; Dong, Y.; Wilkinson, E. C.; Appelman, E. H.; Que, L. Models for Nonheme Iron Intermediates: Structural Basis for Tuning the Spin States of Fe(TPA) Complexes. *J. Am. Chem. Soc.* **1997**, *119* (18), 4197–4205. https://doi.org/10.1021/ja9638521.
(144) Seredyuk, M.; Gaspar, A. B.; Kusz, J.; Bednarek, G.; Gütlich, P. Variable-Temperature X-Ray Crystal Structure Determinations of {Fe[Tren(6-Mepy)$_3$]}(ClO$_4$)$_2$ and {Zn[Tren(6-Mepy)$_3$]}(ClO$_4$)$_2$ Compounds: Correlation of the Structural Data with Magnetic and Mössbauer Spectroscopy Data. *J. Appl. Crystallogr.* **2007**, *40* (6), 1135–1145. https://doi.org/10.1107/S0021889807048571.
(145) Jahro, I. S.; Onggo, D.; Ismunandar; Rahayu, S. I.; Muñoz, M. C.; Gaspar, A. B.; Seredyuk, M.; Gütlich, P.; Real, J. A. Synthesis, Crystal Structure and Magnetic Properties of the Spin Crossover System [Fe(Pq)$_3$]$^{2+}$. *Inorganica Chim. Acta* **2008**, *361* (14–15), 4047–4054. https://doi.org/10.1016/j.ica.2008.03.122.
(146) Abernethy, C. D.; Codd, G. M.; Spicer, M. D.; Taylor, M. K. A Highly Stable N-Heterocyclic Carbene Complex of Trichloro-Oxo-Vanadium(V) Displaying Novel Cl−C$_{\text{carbene}}$ Bonding Interactions. *J. Am. Chem. Soc.* **2003**, *125* (5), 1128–1129. https://doi.org/10.1021/ja0276321.
(147) Ketkaew, R.; Tantirungrotechai, Y.; Harding, P.; Chastanet, G.; Guionneau, P.; Marchivie, M.; Harding, D. J. OctaDist: A Tool for Calculating Distortion Parameters in Spin Crossover and Coordination Complexes. *Dalton Trans.* **2021**, *50* (3), 1086–1096. https://doi.org/10.1039/D0DT03988H.
(148) Loveday, O.; Echeverría, J. Methyl Groups as Widespread Lewis Bases in Noncovalent Interactions. *Nat. Commun.* **2021**, *12* (1), 5030. https://doi.org/10.1038/s41467-021-25314-y.
(149) Magra, K.; Francés-Monerris, A.; Cebrián, C.; Monari, A.; Haacke, S.; Gros, P. C. Bidentate Pyridyl-NHC Ligands: Synthesis, Ground and Excited State Properties of Their Iron(II) Complexes and the Role of the Fac/Mer Isomerism. *Eur. J. Inorg. Chem.* **2022**, *2022* (7). https://doi.org/10.1002/ejic.202100818.
(150) Magra, K.; Francés-Monerris, A.; Cebrián, C.; Monari, A.; Haacke, S.; Gros, P. C. Bidentate Pyridyl-NHC Ligands: Synthesis, Ground and Excited State Properties of Their Iron(II) Complexes and the Role of the *fac/mer* Isomerism. *Eur. J. Inorg. Chem.* **2022**. https://doi.org/10.1002/ejic.202100818.

(151) Volpe, E. C.; Wolczanski, P. T.; Lobkovsky, E. B. Aryl-Containing Pyridine-Imine and Azaallyl Chelates of Iron toward Strong Field Coordination Compounds. *Organometallics* **2010**, 29. 364-377. https://doi.org:10.1021/om900973c.
(152) Tang, Z.; Chang, X.-Y.; Wan, Q.; Wang, J.; Ma, C.; Law, K.-C.; Liu, Y.; Che, C.-M. Bis(Tridentate) Iron(II) Complexes with a Cyclometalating Unit: Photophysical Property Enhancement with Combinatorial Strong Ligand Field Effect. *Organometallics* **2020**, *39* (15), 2791–2802. https://doi.org/10.1021/acs.organomet.0c00149.
(153) Ashley, D. C.; Mukherjee, S.; Jakubikova, E. Designing Air-Stable Cyclometalated Fe(II) Complexes: Stabilization *via* Electrostatic Effects. *Dalton Trans.* **2019**, *48* (2), 374–378. https://doi.org/10.1039/C8DT04402C.
(154) Gravogl, L.; Heinemann, F. W.; Munz, D.; Meyer, K. An Iron Pincer Complex in Four Oxidation States. *Inorg. Chem.* **2020**, *59* (8), 5632–5645. https://doi.org/10.1021/acs.inorgchem.0c00355.
(155) Tomyn, S.; Shylin, S. I.; Bykov, D.; Ksenofontov, V.; Gumienna-Kontecka, E.; Bon, V.; Fritsky, I. O. Indefinitely Stable Iron(IV) Cage Complexes Formed in Water by Air Oxidation. *Nat. Commun.* **2017**, *8* (1), 14099. https://doi.org/10.1038/ncomms14099.
(156) Sinha, N.; Pfund, B.; Wegeberg, C.; Prescimone, A.; Wenger, O. S. Cobalt(III) Carbene Complex with an Electronic Excited-State Structure Similar to Cyclometalated Iridium(III) Compounds. *J. Am. Chem. Soc.* **2022**, *144* (22), 9859–9873. https://doi.org/10.1021/jacs.2c02592.
(157) Sinha, N.; Jiménez, J.; Pfund, B.; Prescimone, A.; Piguet, C.; Wenger, O. S. A Near-Infrared-II Emissive Chromium(III) Complex. *Angew. Chem. Int. Ed.* **2021**, *60* (44), 23722–23728. https://doi.org/10.1002/anie.202106398.
(158) Febrian, R.; Roddy, J. P.; Chang, C. H.; Devall, C. T.; Bracher, P. J. Removal of Paramagnetic Ions Prior to Analysis of Organic Reactions in Aqueous Solutions by NMR Spectroscopy. *ACS Omega* **2021**.
(159) Duchanois, T.; Etienne, T.; Beley, M.; Assfeld, X.; Perpète, E. A.; Monari, A.; Gros, P. C. Heteroleptic Pyridyl-Carbene Iron Complexes with Tuneable Electronic Properties. *Eur. J. Inorg. Chem.* **2014**, *2014* (23), 3747–3753. https://doi.org/10.1002/ejic.201402356.
(160) Khavasi, H. R.; Esmaeili, M. Case Study of the Correlation between Metallogelation Ability and Crystal Packing. *Cryst. Growth Des.* **2019**, *19* (8), 4369–4377. https://doi.org/10.1021/acs.cgd.9b00117.
(161) Braun, J. D.; Lozada, I. B.; Kolodziej, C.; Burda, C.; Newman, K. M. E.; van Lierop, J.; Davis, R. L.; Herbert, D. E. Iron(Ii) Coordination Complexes with Panchromatic Absorption and Nanosecond Charge-Transfer Excited State Lifetimes. *Nat. Chem.* **2019**, *11* (12), 1144–1150. https://doi.org/10.1038/s41557-019-0357-z.
(162) Larsen, C. B.; Braun, J. D.; Lozada, I. B.; Kunnus, K.; Biasin, E.; Kolodziej, C.; Burda, C.; Cordones, A. A.; Gaffney, K. J.; Herbert, D. E. Reduction of Electron Repulsion in Highly Covalent Fe-Amido Complexes Counteracts the Impact of a Weak Ligand Field on Excited-State Ordering. *J. Am. Chem. Soc.* **2021**, *143* (49), 20645–20656. https://doi.org/10.1021/jacs.1c06429.
(163) Bauer, M.; Steube, J.; Päpcke, A.; Bokareva, O.; Reuter, T.; Demeshko, S.; Schoch, R.; Hohloch, S.; Meyer, F.; Heinze, K.; Kühn, O.; Lochbrunner, S. *Janus-Type Dual Emission of a Cyclometalated Iron(III) Complex*; preprint; In Review, 2020. https://doi.org/10.21203/rs.3.rs-64316/v1.
(164) Morris, D. E.; Hanck, K. W.; DeArmond, M. K. Electrochemical and ESR Studies of [Fe(Terpy)2]2+ and [Ru(Terpy)2]2+ and Their Reduction Products. *J. Electroanal. Chem. Interfacial Electrochem.* **1983**, *149* (1–2), 115–130. https://doi.org/10.1016/S0022-0728(83)80562-2.

(165) Dorn, M.; Kalmbach, J.; Boden, P.; Päpcke, A.; Gómez, S.; Förster, C.; Kuczelinis, F.; Carrella, L. M.; Büldt, L. A.; Bings, N. H.; Rentschler, E.; Lochbrunner, S.; González, L.; Gerhards, M.; Seitz, M.; Heinze, K. A Vanadium(III) Complex with Blue and NIR-II Spin-Flip Luminescence in Solution. *J. Am. Chem. Soc.* **2020**, *142* (17), 7947–7955. https://doi.org/10.1021/jacs.0c02122.

(166) Reddy Marri, A.; Marchini, E.; Cabanes, V. D.; Argazzi, R.; Pastore, M.; Caramori, S.; Gros, P. C. Record Power Conversion Efficiencies for Iron(II)-NHC-Sensitized DSSCs from Rational Molecular Engineering and Electrolyte Optimization. *J. Mater. Chem. A* **2021**, *9* (6), 3540–3554. https://doi.org/10.1039/D0TA10841C.

(167) Albrecht, M. Cyclometalation Using D-Block Transition Metals: Fundamental Aspects and Recent Trends. *Chem. Rev.* **2010**, *110* (2), 576–623. https://doi.org/10.1021/cr900279a.

(168) Hübel, W.; Braye, E. H. Organometallic complexes—IV über die reaktion von substituierten acetylenverbindungen mit eisentetracarbonyl. *J. Inorg. Nucl. Chem.* **1959**, *10* (3–4), 250–268. https://doi.org/10.1016/0022-1902(59)80119-6.

(169) Klein, H.-F.; Camadanli, S.; Beck, R.; Leukel, D.; Flörke, U. Cyclometalation of Substrates Containing Imine and Pyridyl Anchoring Groups by Iron and Cobalt Complexes. *Angew. Chem. Int. Ed.* **2005**, *44* (6), 975–977. https://doi.org/10.1002/anie.200460978.

(170) Jiang, S.; Quintero-Duque, S.; Roisnel, T.; Dorcet, V.; Grellier, M.; Sabo-Etienne, S.; Darcel, C.; Sortais, J.-B. Direct Synthesis of Dicarbonyl PCP-Iron Hydride Complexes and Catalytic Dehydrogenative Borylation of Styrene. *Dalton Trans.* **2016**, *45* (27), 11101–11108. https://doi.org/10.1039/C6DT01149G.

(171) Bhattacharya, P.; Krause, J. A.; Guan, H. Iron Hydride Complexes Bearing Phosphinite-Based Pincer Ligands: Synthesis, Reactivity, and Catalytic Application in Hydrosilylation Reactions. *Organometallics* **2011**, *30* (17), 4720–4729. https://doi.org/10.1021/om2005589.

(172) Steube, J.; Burkhardt, L.; Päpcke, A.; Moll, J.; Zimmer, P.; Schoch, R.; Wölper, C.; Heinze, K.; Lochbrunner, S.; Bauer, M. Excited-State Kinetics of an Air-Stable Cyclometalated Iron(II) Complex. *Chem. – Eur. J.* **2019**, *25* (51), 11826–11830. https://doi.org/10.1002/chem.201902488.

(173) Klein, H.-F.; Camadanli, S.; Beck, R.; Flörke, U. Meridional Bicyclometalation with Iron: A Novel Way of Forming Dianionic [C,N,C]-Ligands. *Chem Commun* **2005**, No. 3, 381–382. https://doi.org/10.1039/B413409E.

(174) Estrada-Montaño, A. S.; Ryabov, A. D.; Gries, A.; Gaiddon, C.; Le Lagadec, R. Iron(III) Pincer Complexes as a Strategy for Anticancer Studies. *Eur. J. Inorg. Chem.* **2017**, *2017* (12), 1673–1678. https://doi.org/10.1002/ejic.201601350.

(175) Jackson, B. J.; Najera, D. C.; Matson, E. M.; Woods, T. J.; Bertke, J. A.; Fout, A. R. Synthesis and Characterization of (^{DIPP}CCC)Fe Complexes: A Zwitterionic Metalation Method and CO_2 Reactivity. *Organometallics* **2019**, *38* (15), 2943–2952. https://doi.org/10.1021/acs.organomet.9b00271.

(176) Reilly, S. W.; Webster, C. E.; Hollis, T. K.; Valle, H. U. Transmetallation from CCC-NHC Pincer Zr Complexes in the Synthesis of Air-Stable CCC-NHC Pincer Co(III) Complexes and Initial Hydroboration Trials. *Dalton Trans.* **2016**, *45* (7), 2823–2828. https://doi.org/10.1039/C5DT04752H.

(177) Broere, D. L. J.; Čorić, I.; Brosnahan, A.; Holland, P. L. Quantitation of the THF Content in $Fe[N(SiMe_3)_2]_2 \cdot x$ THF. *Inorg. Chem.* **2017**, *56* (6), 3140–3143. https://doi.org/10.1021/acs.inorgchem.7b00056.

(178) Slanger, D. *Run on Less with Hydrogen Fuel Cells*. RMI. https://rmi.org/run-on-less-with-hydrogen-fuel-cells/ (accessed 2022-11-24).

(179) *The Future of Hydrogen – Analysis*. IEA. https://www.iea.org/reports/the-future-of-hydrogen (accessed 2022-09-30).
(180) Zaccaria, F.; Menendez Rodriguez, G.; Rocchigiani, L.; Macchioni, A. Molecular Catalysis in "Green" Hydrogen Production. *Front. Catal.* **2022**, *2*, 892183. https://doi.org/10.3389/fctls.2022.892183.
(181) Zhang, B.; Sun, L. Artificial Photosynthesis: Opportunities and Challenges of Molecular Catalysts. *Chem. Soc. Rev.* **2019**, *48* (7), 2216–2264. https://doi.org/10.1039/C8CS00897C.
(182) Esswein, A. J.; Nocera, D. G. Hydrogen Production by Molecular Photocatalysis. *Chem. Rev.* **2007**, *107* (10), 4022–4047. https://doi.org/10.1021/cr050193e.
(183) Kellett, R. M.; Spiro, T. G. Cobalt(I) Porphyrin Catalysts of Hydrogen Production from Water. 5. *Inorg. Chem*, **1985**, 24 (15), 2373-2377.
(184) Lazarides, T.; McCormick, T.; Du, P.; Luo, G.; Lindley, B.; Eisenberg, R. Making Hydrogen from Water Using a Homogeneous System Without Noble Metals. *J. Am. Chem. Soc.* **2009**, 131, 9192-9194.
(185) Johansen, O. The anthracenecarboxylate anion as sensitizer for the photoreduction of water. *Chem. Phys. Lett.* **1983**, *91* (1), 6.
(186) Okura, I.; Kita, T.; Aono, S.; Kaji, N. Photoinduced Hydrogen Evolution in a Micellar System. *J. Mol. Catal.* **1985**, *33* (3), 341–343. https://doi.org/10.1016/0304-5102(85)85006-9.
(187) Eckenhoff, W. T. Molecular Catalysts of Co, Ni, Fe, and Mo for Hydrogen Generation in Artificial Photosynthetic Systems. *Coord. Chem. Rev.* **2018**, *373*, 295–316. https://doi.org/10.1016/j.ccr.2017.11.002.
(188) Wass, D.; Robertson, N. Contributions of Inorganic Chemistry to Energy Research. *Dalton Trans.* **2011**, *40* (15), 3775. https://doi.org/10.1039/c1dt90027g.
(189) Chakraborty, S.; Edwards, E. H.; Kandemir, B.; Bren, K. L. Photochemical Hydrogen Evolution from Neutral Water with a Cobalt Metallopeptide Catalyst. *Inorg. Chem.* **2019**, *58* (24), 16402–16410. https://doi.org/10.1021/acs.inorgchem.9b02067.
(190) Metz, S.; Bernhard, S. Robust Photocatalytic Water Reduction with Cyclometalated Ir(Iii) 4-Vinyl-2,2′-Bipyridine Complexes. *Chem. Commun.* **2010**, *46* (40), 7551. https://doi.org/10.1039/c0cc01827a.
(191) Zhang, P.; Wang, M.; Na, Y.; Li, X.; Jiang, Y.; Sun, L. Homogeneous Photocatalytic Production of Hydrogen from Water by a Bioinspired [Fe_2S_2] Catalyst with High Turnover Numbers. *Dalton Trans* **2010**, *39* (5), 1204–1206. https://doi.org/10.1039/B923159P.
(192) Nielsen, M.; Alberico, E.; Baumann, W.; Drexler, H.-J.; Junge, H.; Gladiali, S.; Beller, M. Low-Temperature Aqueous-Phase Methanol Dehydrogenation to Hydrogen and Carbon Dioxide. *Nature* **2013**, *495* (7439), 85–89. https://doi.org/10.1038/nature11891.
(193) Kumar, A.; Daw, P.; Milstein, D. Homogeneous Catalysis for Sustainable Energy: Hydrogen and Methanol Economies, Fuels from Biomass, and Related Topics. *Chem. Rev.* **2022**, *122* (1), 385–441. https://doi.org/10.1021/acs.chemrev.1c00412.
(194) Kowacs, T.; Pan, Q.; Lang, P.; O'Reilly, L.; Rau, S.; Browne, W. R.; Pryce, M. T.; Huijser, A.; Vos, J. G. Supramolecular Bimetallic Assemblies for Photocatalytic Hydrogen Generation from Water. *Faraday Discuss.* **2015**, *185*, 143–170. https://doi.org/10.1039/C5FD00068H.
(195) Barton, B. E.; Rauchfuss, T. B. Hydride-Containing Models for the Active Site of the Nickel−Iron Hydrogenases. *J. Am. Chem. Soc.* **2010**, *132* (42), 14877–14885. https://doi.org/10.1021/ja105312p.

(196) Du, P.; Eisenberg, R. Catalysts Made of Earth-Abundant Elements (Co, Ni, Fe) for Water Splitting: Recent Progress and Future Challenges. *Energy Environ. Sci.* **2012**, *5* (3), 6012. https://doi.org/10.1039/c2ee03250c.
(197) Queyriaux, N.; Jane, R. T.; Massin, J.; Artero, V.; Chavarot-Kerlidou, M. Recent Developments in Hydrogen Evolving Molecular Cobalt(II)–Polypyridyl Catalysts. *Coord. Chem. Rev.* **2015**, *304–305*, 3–19. https://doi.org/10.1016/j.ccr.2015.03.014.
(198) Kaeffer, N.; Chavarot-Kerlidou, M.; Artero, V. Hydrogen Evolution Catalyzed by Cobalt Diimine–Dioxime Complexes. *Acc. Chem. Res.* **2015**, *48* (5), 1286–1295. https://doi.org/10.1021/acs.accounts.5b00058.
(199) Schwarz, J.; Ilic, A.; Johnson, C.; Lomoth, R.; Wärnmark, K. High Turnover Photocatalytic Hydrogen Formation with an Fe(III) N-Heterocyclic Carbene Photosensitiser. *Chem. Commun.* **2022**, *58* (35), 5351–5354. https://doi.org/10.1039/D2CC01016J.
(200) Sahai, R.; Rillema, D. P. A Novel Hetero-Oligomer Containing One Ruthenium(L1)and Three Platinum(11) Metal Centres Bridged by 2,3-Bis(2-Pyridyl)Quinoxaline. *J. Chem. Soc., Chem. Commun.* **1986**, 1133-1134.
(201) Sun, L.; Akermark, B.; Ott, S. Iron Hydrogenase Active Site Mimics in Supramolecular Systems Aiming for Light-Driven Hydrogen Production. *Coord. Chem. Rev.* **2005**, *249* (15–16), 1653–1663. https://doi.org/10.1016/j.ccr.2005.01.013.
(202) Ozawa, H.; Haga, M.; Sakai, K. A Photo-Hydrogen-Evolving Molecular Device Driving Visible-Light-Induced EDTA-Reduction of Water into Molecular Hydrogen. *J. Am. Chem. Soc.* **2006**, *128* (15), 4926–4927. https://doi.org/10.1021/ja058087h.
(203) Fihri, A.; Artero, V.; Razavet, M.; Baffert, C.; Leibl, W.; Fontecave, M. Cobaloxime-Based Photocatalytic Devices for Hydrogen Production. *Angew. Chem. Int. Ed.* **2008**, *47* (3), 564–567. https://doi.org/10.1002/anie.200702953.
(204) Huber-Gedert, M.; Nowakowski, M.; Kertmen, A.; Burkhardt, L.; Lindner, N.; Schoch, R.; Herbst-Irmer, R.; Neuba, A.; Schmitz, L.; Choi, T.; Kubicki, J.; Gawelda, W.; Bauer, M. Fundamental Characterization, Photophysics and Photocatalysis of a Base Metal Iron(II)-Cobalt(III) Dyad. *Chem. – Eur. J.* **2021**, *27* (38), 9905–9918. https://doi.org/10.1002/chem.202100766.
(205) *2,6-Dichloropyridine 98 2402-78-0*. http://www.sigmaaldrich.com/ (accessed 2022-12-06).
(206) *4-Amino-2,6-dichloropyridine 97 2587-02-2*. http://www.sigmaaldrich.com/ (accessed 2022-12-06).
(207) Kulmaczewski, R.; Bamiduro, F.; Shahid, N.; Cespedes, O.; Halcrow, M. A. Structural Transformations and Spin-Crossover in $[FeL_2]^{2+}$ Salts (*L* = 4-{ *Tert* -Butylsulfanyl}-2,6-di{pyrazol-1-yl}pyridine): The Influence of Bulky Ligand Substituents. *Chem. – Eur. J.* **2021**, *27* (6), 2082–2092. https://doi.org/10.1002/chem.202004072.
(208) Ana Maria Garcia Collazo; Martinell Pedemonte, M.; Revez Vilaplana, M.; Lavilla Grifols, R.; Rodrigues Pascau, L.; Cubero Jorda, E. Heteroarylaminoisoquinolines, methods for their preparation and therapeutic uses thereof. WO 2016/120808 A1.
(209) Pukenas, L.; Benn, F.; Lovell, E.; Santoro, A.; Kershaw Cook, L. J.; Halcrow, M. A.; Evans, S. D. Bead-like Structures and Self-Assembled Monolayers from 2,6-Dipyrazolylpyridines and Their Iron(II) Complexes. *J. Mater. Chem. C* **2015**, *3* (30), 7890–7896. https://doi.org/10.1039/C5TC01233C.
(210) Schlosser, M.; Bobbio, C.; Rausis, T. Regiochemically Flexible Substitutions of Di-, Tri-, and Tetrahalopyridines: The Trialkylsilyl Trick. *J. Org. Chem.* **2005**, *70* (7), 2494–2502. https://doi.org/10.1021/jo047962z.
(211) Podolan, G.; Jungk, P.; Lentz, D.; Zimmer, R.; Reissig, H.-U. Studies on the Synthesis of Specifically Fluorinated 4-Amino- Pyridine Derivatives by Regioselective

Nucleophilic Aromatic Substitution and Catalytic Hydrodefluorination. *Adv. Synth. Catal.* **2015**, *357* (14–15), 3215–3228. https://doi.org/10.1002/adsc.201500393.
(212) Hu, J.; Zhao, C.; Zhang, T.; Zhang, X.; Cao, X.; Wu, Q.; Chen, Y.; Zhang, D.; Tao, Y.; Huang, W. Isomeric N-Linked Benzoimidazole Containing New Electron Acceptors for Exciplex Forming Hosts in Highly Efficient Blue Phosphorescent OLEDs. *Adv. Opt. Mater.* **2017**, *5* (13), 1700036. https://doi.org/10.1002/adom.201700036.
(213) Charbonnière, L.; Ziessel, R. PNapuercleophilic Substitution on Polyfluorinated Pyridine and Pyrimidine Rings for Construction of Lanthanide Ligands. *Synthesis,* **2013**, 45, 837-844.
(214) Das, S.; Nugegoda, D.; Qu, F.; Boudreaux, C. M.; Burrow, P. E.; Figgins, M. T.; Lamb, R. W.; Webster, C. E.; Delcamp, J. H.; Papish, E. T. Structure Function Relationships in Ruthenium Carbon Dioxide Reduction Catalysts with CNC Pincers Containing Donor Groups. *Eur. J. Inorg. Chem.* **2020**, *2020* (28), 2709–2717. https://doi.org/10.1002/ejic.202000444.
(215) Jin, T.; Xiong, Y.; Zhu, X.; Tian, Z.; Tao, D.-J.; Hu, J.; Jiang, D.; Wang, H.; Liu, H.; Dai, S. Rational Design and Synthesis of a Porous, Task-Specific Polycarbazole for Efficient CO_2 Capture. *Chem. Commun.* **2016**, *52* (24), 4454–4457. https://doi.org/10.1039/C6CC00573J.
(216) Schlosser, M.; Rausis, T.; Bobbio, C. Rerouting Nucleophilic Substitution from the 4-Position to the 2- or 6-Position of 2,4-Dihalopyridines and 2,4,6-Trihalopyridines: The Solution to a Long-Standing Problem. *Org. Lett.* **2005**, *7* (1), 127–129. https://doi.org/10.1021/ol047826g.
(217) *2,4,6-Trifluoropyridine, 97 %, Thermo Scientific™*. https://www.thermofisher.com/order/catalog/product/L19541.14 (accessed 2022-10-17).
(218) Darari, M.; Francés-Monerris, A.; Marekha, B.; Doudouh, A.; Wenger, E.; Monari, A.; Haacke, S.; Gros, P. C. Towards Iron(II) Complexes with Octahedral Geometry: Synthesis, Structure and Photophysical Properties. *Molecules* **2020**, *25* (24), 5991. https://doi.org/10.3390/molecules25245991.
(219) Duchanois, T.; Etienne, T.; Beley, M.; Assfeld, X.; Perpète, E. A.; Monari, A.; Gros, P. C. Heteroleptic Pyridyl-Carbene Iron Complexes with Tuneable Electronic Properties. *Eur. J. Inorg. Chem.* **2014**, *2014* (23), 3747–3753. https://doi.org/10.1002/ejic.201402356.
(220) Dutta, C.; Rana, S. S.; Choudhury, J. Leveraging Metallotropism-Enabled Substrate Activation in Cobalt-Catalyzed Annulation Chemistry: Protic NHC Template Is the Key. *ACS Catal.* **2019**, *9* (12), 10674–10679. https://doi.org/10.1021/acscatal.9b04125.
(221) Keith, J. M. One Step Conversion of Heteroaromatic-N-Oxides to Imidazolo-Heteroarenes. *J. Org. Chem.* **2008**, *73*, 327–330. https://doi.org/10.1021/jo702038g.
(222) Henwood, A. F. Solubilised Bright Blue-Emitting Iridium Complexes for Solution Processed OLEDs. *J. Mater. Chem. C,* **2016**, 4, 3726.
(223) Labonne, A.; Kribber, T.; Hintermann, L. Highly Active in Situ Catalysts for Anti-Markovnikov Hydration of Terminal Alkynes. *Org. Lett.* **2006**, *8* (25), 5853–5856. https://doi.org/10.1021/ol062455k.
(224) Samanta, S. K.; Rana, A.; Schmittel, M. Reversible Cargo Shipping between Orthogonal Stations of a Nanoscaffold upon Redox Input. *Dalton Trans* **2014**, *43* (25), 9438–9447. https://doi.org/10.1039/C4DT00849A.
(225) Patil, P. H.; Nallasivam, J. L.; Fernandes, R. A. Unimolecular 4-Hydroxypiperidines: New Ligands for Copper-Catalyzed N-Arylation. *Asian J. Org. Chem.* **2015**, *4* (6), 552–559. https://doi.org/10.1002/ajoc.201500062.

(226) Endo, T.; Yoshino, T.; Schneider, U.; Ueno, M. Allylation Reactions of Aldehydes with Allylboronates in Aqueous Media: Unique Reactivity and Selectivity That Are Only Observed in the Presence of Water. *Chem Asian J* **2013**, 13.
(227) Wang, L. Metal-Free Site-Selective C–N Bond-Forming Reaction of Polyhalogenated Pyridines and Pyrimidines. *RSC Adv.* **2015**, 15, 82097. https://doi.org/10.1039/c5ra18653f
(228) Reddy, P. L. Cu(0)@Al2O3/SiO2 NPs: An Efficient Reusable Catalyst for the Cross Coupling Reactions of Aryl Chlorides with Amines and Anilines. *RSC Adv.* **2015**, 7.
(229) Tsukamoto, I.; Koshio, H.; Kuramochi, T.; Saitoh, C.; Yanai-Inamura, H.; Kitada-Nozawa, C.; Yamamoto, E.; Yatsu, T.; Shimada, Y.; Sakamoto, S.; Tsukamoto, S. Synthesis and Structure–Activity Relationships of Amide Derivatives of (4,4-Difluoro-1,2,3,4-Tetrahydro-5H-1-Benzazepin-5-Ylidene)Acetic Acid as Selective Arginine Vasopressin V2 Receptor Agonists. *Bioorg. Med. Chem.* **2009**, *17* (8), 3130–3141. https://doi.org/10.1016/j.bmc.2009.03.001.
(230) Bugaenko, D. I.; Yurovskaya, M. A.; Karchava, A. V. Reaction of Pyridine- *N* -Oxides with Tertiary Sp ^{2} - *N* -Nucleophiles: An Efficient Synthesis of Precursors for *N* -(Pyrid-2-yl)-Substituted *N* -Heterocyclic Carbenes. *Adv. Synth. Catal.* **2020**, *362* (24), 5777–5782. https://doi.org/10.1002/adsc.202001063.
(231) Mangione, M. I.; Spanevello, R. A.; Anzardi, M. B. Efficient and Straightforward Click Synthesis of Structurally Related Dendritic Triazoles. *RSC Adv* **2017**, *7* (75), 47681–47688. https://doi.org/10.1039/C7RA09558A.
(232) Heller, M.; Schubert, U. S. Syntheses of Functionalized 2,2′:6′,2″-Terpyridines. *Eur. J. Org. Chem.* **2003**, *2003* (6), 947–961. https://doi.org/10.1002/ejoc.200390150.
(233) Jayapal, M.; Haque, A.; Al-Busaidi, I. J.; Al-Rasbi, N.; Al-Suti, M. K.; Khan, M. S.; Al-Balushi, R.; Islam, S. M.; Xin, C.; Wu, W.; Wong, W.-Y.; Marken, F.; Raithby, P. R. Dicopper(I) Complexes Incorporating Acetylide-Functionalized Pyridinyl-Based Ligands: Synthesis, Structural, and Photovoltaic Studies. *Inorg. Chem.* **2018**, *57* (19), 12113–12124. https://doi.org/10.1021/acs.inorgchem.8b01684.
(234) Ge, K.; Huang, Y.; Dong, Y.; Guan, G.; Duan, J. Bottom-Up Assembly of a Complex Superstructure from a Simple Low-Symmetry Block and Three Ni Nodes. *Cryst. Growth Des.* **2021**, *21* (5), 2602–2608. https://doi.org/10.1021/acs.cgd.1c00273.
(235) Chevallier, F.; Charlot, M.; Mongin, F.; Champagne, B.; Franz, E.; Clays, K.; Blanchard-Desce, M. Synthetic, Optical and Theoretical Study of Alternating Ethylenedioxythiophene-Pyridine Oligomers: Evolution from Planar Conjugated to Helicoidal Structure towards a Chiral Configuration. *ChemPhysChem* **2016**, *17* (24), 4090–4101. https://doi.org/10.1002/cphc.201601057.
(236) Hübscher, J.; Seichter, W.; Gruber, T.; Kortus, J.; Weber, E. Synthesis and Structural Characterization of Ethynylene-Bridged Bisazines Featuring Various α-Substitution: Ethynylene-Bridged Bisazines Featuring Various α-Substitution. *J. Heterocycl. Chem.* **2015**, *52* (4), 1062–1074. https://doi.org/10.1002/jhet.2122.
(237) Dolomanov, O. V.; Bourhis, L. J.; Gildea, R. J.; Howard, J. A. K.; Puschmann, H. *OLEX2* : A Complete Structure Solution, Refinement and Analysis Program. *J. Appl. Crystallogr.* **2009**, *42* (2), 339–341. https://doi.org/10.1107/S0021889808042726.
(238) Sheldrick, G. M. Crystal Structure Refinement with *SHELXL*. *Acta Crystallogr. Sect. C Struct. Chem.* **2015**, *71* (1), 3–8. https://doi.org/10.1107/S2053229614024218.
(239) Sheldrick, G. M. A Short History of *SHELX*. *Acta Crystallogr. A* **2008**, *64* (1), 112–122. https://doi.org/10.1107/S0108767307043930.

Résumé

Cette thèse de doctorat s'inscrit dans le domaine de la chimie organométallique. D'un point de vue fondamental, nous avons étudié le contrôle de la géométrie moléculaire dans les complexes azine-NHC bidentés de Fe(II) lors de la modification du ligand, accédant sélectivement aux complexes soit faciaux, soit méridiens. En outre, les caractéristiques opto-électroniques peuvent être facilement modifiées en fonction des parties azine et NHC, ce qui entraîne une meilleure absorbance dans le spectre UV-vis. De plus, nous avons exploré l'effet de deux unités de coordination (formellement) anioniques, la N-amido et la C-anionique, en obtenant un ensemble de complexes Fe(III). En ce qui concerne la série N-amido, nous avons rapporté la synthèse de trois complexes, un homoleptique et deux hétéroleptiques. Il est intéressant de noter que les composés homoleptiques et hétéroleptiques semblent présenter un mélange d'orbitales basé sur le métal et sur le ligand, ce qui suggère que ce type de ligands pourrait être utile pour obtenir une "inversion HOMO" complète telle que définie par Jakubikova. En conséquence, les deux séries de complexes ont présenté une absorbance élargie jusqu'à la région IR. Quant à la série C-anionique, nous avons développé une méthodologie qui nous a permis d'obtenir de nouveaux complexes Fe-CCC bis-cyclométallisés, en soulignant que l'utilisation de la boîte à gants, d'un réactif transmétallant ou réducteur a été évitée.

De plus, nous nous sommes lancés dans une chimie plus appliquée comme pour la synthèse de complexes Fe(II) hétéroleptiques pour la production de H_2 dans des réactions de fractionnement de l'eau. Deux complexes ont été obtenus, un homoleptique, et un hétéroleptique qui a été réalisé en suivant une procédure par étapes rapportée par Bauer.

Mots Clés : Complexes de fer, conversion d’énergie solaire, carbènes N-hétérocycliques

Abstract

This doctoral thesis falls within the field of organometallic chemistry. From a fundamental point of view, we have investigated the control of the molecular geometry in bidentate azine-NHC Fe(II) complexes upon ligand modification, accessing selectively either facial or meridional complexes. Additionally, the opto-electronic characteristics can be easily modified as a function of both the azine and the NHC moieties, resulting in an improved absorbance in the UV-vis spectrum. In addition, we explored the effect of two (formally) anionic coordinating units, the N-amido and C-anionic, obtaining a set of Fe(III) complexes. Concerning the N-amido series, we reported the synthesis of three complexes, one homoleptic and two heteroleptic. Interestingly, both homoleptic and heteroleptic compounds seemed to have metal-based and ligand-based orbital mixing, suggesting that this type of ligands could be useful to achieve a full “HOMO inversion” as defined by Jakubikova. As a result, both series of complexes displayed an enlarged absorbance until the IR region. As for the C-anionic series, we developed a methodology that allowed us to get new bis-cyclometalated Fe-CCC complexes, highlighting that the use of glove box, a transmetallating or reducing reagent was avoided.

Furthermore, we dabbled into more applied chemistry dealing with the synthesis heteroleptic Fe(II) complexes towards H_2 production in water splitting reactions. Two complexes were obtained, one homoleptic, and one heteroleptic that was achieved by following a stepwise procedure reported by Bauer.

Keywords: Iron complexes, solar energy conversion, N-heterocyclic carbenes